

|        |                  |
|--------|------------------|
| 申<br>报 | 系列：教师系列<br>科研为主型 |
|        | 专业：热能工程          |
|        | 职称：教授（科<br>研型）   |

## 业绩成果材料

（申报人的业绩成果材料包括论文、科研项目、获奖以及其他成果等）

单 位（二级单位）生物质工程研究院

姓 名 魏国强

材料核对人：

单位盖章：

核对时间：

华南农业大学制

# 目 录

## 一、教学研究业绩

### 1. 教学研究项目

- 1.1 关于教育部《产学研协同育人机制下能源动力类专业基础课程教学改革探索》项目的立项合同及有关佐证材料.....1
- 1.2 关于教育部《“双碳”背景下 AI 与 CDIO 融合的能源动力专业课程教学改革研究与实践》项目的立项通知及有关佐证材料.....5
- 1.3 关于校级教改项目《能源动力类专业课程产教研协同育人模式探索与实践》的立项通知及有关佐证材料.....11
- 2. 教改论文：涉农高校生物质能源领域传热学课程教学改革研究.....14

## 二、科研项目

### 1. 主持

- 1.1 关于国家重点研发课题《双流化床生物质化学链气化关键技术》项目的立项合同及有关佐证材料.....24
- 1.2 关于国家自然科学基金面上项目《碱木质素化学链氧化偶联自催化制备低碳烯烃基础研究》项目的立项合同及有关佐证材料.....28
- 1.3 关于国家自然科学基金面上项目《碱木质素强化煤焦粉化学链气化过程中碱金属的迁移与催化作用机制》项目的立项合同及结题有关佐证材料..... 30
- 1.4 关于中国科学院洁净能源创新联合基金项目《碱木质素强化煤焦粉化学链气化制备高品质合成气关键问题研究》项目的立项合同及结题有关佐证材料..... 34
- 1.5 关于国家重点研发项目子课题《多孔炭复配功能菌制生物有机肥工艺》项目的立项合同及有关佐证材料.....39



|  |    |
|--|----|
| 1.6 关于广东省基础与应用基金区域联合基金粤莞重点项目《天然气化学链制氢耦合燃料电池高效发电新技术》项目的立项合同及有关佐证材料..... | 42 |
| 1.7 关于中国科学院可再生能源重点实验室开放基金《富氮木质废弃物化学链气化制备高品质合成气基础研究》项目的立项合同及有关佐证材料..... | 47 |

## 2. 主参

|   |    |
|---|----|
| 2.1 关于广东省基础与应用基础研究基金杂原子原位负载生物炭的制备及其催化 N <sub>2</sub> 电化学还原机理研究项目的立项合同及有关佐证材料..... | 50 |
|---|----|

## 三、论文、著作等

|              |    |
|--------------|----|
| 1. 检索证明..... | 54 |
|--------------|----|

## 2. 以第一作者发表本专业论文情况

|  |    |
|--|----|
| 2.1. Reaction kinetics and mechanisms for carbon-negative chemical looping gasification of biomass coupled with CO <sub>2</sub> splitting..... | 57 |
|--|----|

|   |    |
|---|----|
| 2.2. Reaction performance of Ce-enhanced hematite oxygen carrier in chemical looping reforming of biomass pyrolyzed gas coupled with CO <sub>2</sub> splitting..... | 70 |
|---|----|

|  |    |
|--|----|
| 2.3. Enhanced chemical looping gasification of biomass coupled with CO <sub>2</sub> splitting based on carbon negative emission. | 83 |
|--|----|

|   |    |
|---|----|
| 2.4. Ca-enhanced hematite oxygen carriers for chemical looping reforming of biomass pyrolyzed gas coupled with CO <sub>2</sub> splitting..... | 96 |
|---|----|

## 3. 以通讯作者发表本专业论文情况

|  |  |
|--|--|
| 3.1. In-situ removal of toluene as a biomass tar model compound using NiFe <sub>2</sub> O <sub>4</sub> for application in chemical looping |  |
|--|--|

|  |     |
|--|-----|
| gasification oxygen carrier.....   | 110 |
| 3.2. Reducing emission of NO <sub>x</sub> and SO <sub>x</sub> precursors while enhancing char production from pyrolysis of sewage sludge by torrefaction pretreatment..... | 124 |

#### 四、科研成果

##### 1. 知识产权

|   |     |
|---|-----|
| 1.1. 专利授权证书：一种垃圾填埋气化学链重整制备低碳烯烃联产高纯一氧化碳的方法.....            | 137 |
| 1.2. 专利授权证书：一种废塑料耦合碱木质素制备低碳烯烃联产高纯氢气的方法.....               | 138 |
| 1.3. 专利授权证书：一种碱木质素化学链氧化偶联制备低碳烯烃的方法.....                   | 139 |
| 1.4. 专利授权证书：一种化学链处理污泥制合成气及高纯 H <sub>2</sub> 同时回收磷的装置..... | 140 |

教育部产学合作协同育人项目

# 立项证书



项目编号：**231001255311634**

项目名称：**产学研协同育人机制下能源动力类专业基础课程  
教学改革探索**

项目负责人：**魏国强**

学校名称：**华南农业大学**

企业名称：**河南轩明实业有限公司**

**该项目入选教育部产学合作协同育人项目2024年第一批次立项项目，特发此证。**



教育部产学合作协同育人项目  
[cxhz.hep.com.cn](http://cxhz.hep.com.cn)

教育部产学合作协同育人项目专家组  
2024年4月

# 项目合作协议

甲方：河南轩明实业有限公司（企业名称）

联系人：郭雨晴

部门：技术部

联系电话：19836999621

通信地址：河南省郑州市金水区文化路 66 号

邮政编码：450003

乙方：华南农业大学（高校名称）

联系人：魏国强

部门：生物质工程研究院

联系电话：13580396927

通信地址：广东省广州市天河区五山路 483 号

邮政编码：510642

依据教育部高等教育司发布的《教育部高等教育司关于征集 2023 年产学研协同育人项目的函》，甲方申报并入选了“2023 年 6 月产学研协同育人项目”（以下简称“项目”）。为确保项目顺利实施，根据《教育部产学研协同育人项目管理办法》，甲乙双方在友好协商的基础上，签署如下项目合作协议。

第一条 乙方接受甲方委托承担的项目名称为产学研协同育人机制下能源动力类专业基础课程教学改革探索。乙方承担的本项目研究应完成甲方项目指南要求的相关任务，具体包括：

（1）形成教改研究报告或论文：以项目研究成果为基础形成教改研究报告或论文，其内容主要涵盖能源动力类教师能力建设、师资培养模式及实施路径创新等问题。

（2）联合公司技术部门，组织专业力量开展能源动力专业方面的技术培训、经验分享、项目研究、企业导师参与开发和指导实践等工作，为大学之间交流搭建桥梁。选派 2 名师生到公司参与技术培训。通过在线学院、企业授课、认证培训、慕课系统等方式，提升大学专业师生的实践能力和水平，为大学培养一支既深谙产业实践应用又精通技术理论的“职业型”队伍。

（3）新增优秀实践基地 1 个。

第二条 本项目所产生的全部作品（简称“本项目成果”，包括但不限于：项目研究总结报告、课程体系、在线课程、教学大纲、教学课件、实验方案、教学案例、软硬件作品等）的知识产权归属约定如下：项目产生作品知识产权归甲方和乙方共同所有。

第三条 当本项目成果为合作作品时，由乙方负责联系取得其合作者的授权。

第四条 乙方保证本项目成果的整体或者素材、软件等不侵犯第三方的合法权益。

第五条 本项目建设周期为1 年。项目各阶段安排如下：

（1）2023.11-2024.01 进行与课题相关资料搜集整理及调查设计工作，并开展调研。

（2）2024.02-2024.05 产学研合作联合确定师资培训的要求，研讨公司现有的智能学习教学软硬件资源，组织展开高校能源动力教师发展的理论与实证依据的设计与建设。



(3) 2024.06-2025.07 以产业发展需求为导向,科学制定翔实可行并符合行业需求的人才培养方案,培养本科生的实践能力。

(4) 2024.08-2024.10 总结经验,寻找和提出问题。通过参加相关的技术开发、经验分享,找到教学设计中存在问题的解决方案。

(5) 2024.11-2024.12 整理项目研究成果,准备结题。

第六条 本项目成果的交付时间为:2025.01,交付方式为:现实交付,师资队伍建设新模式、教改的研究报告或论文与校企合作协议书等资料的形式交付给甲方等。

双方约定,按以下标准对项目成果进行验收:进行验收甲方邀请专家对乙方交付的《产学研协同育人机制下能源动力类专业基础课程教学改革探索》方案资料进行综合评价,确定项目完成情况。

第七条 本项目经费及拨款事宜约定如下:

(1) 本项目经费总额为人民币 5 万元(大写: 伍万元整 )。

(2) 项目经费由甲方 分期 (一次或分期) 支付到乙方指定的账户。  
具体支付方式及时间: 银行转账 2024.09 。

(3) 本项目经费由甲方支付至乙方指定的如下账户:

开户行: 中国工商银行广州五山支行

户 名: 华南农业大学

账 号: 3602-0026-0900-0310-520

(4) 软硬件设备支持情况: 甲方向乙方提供价值人民币 0 万元的软硬件设备,清单如下:

第八条 本协议自签订之日起生效。

第九条 双方应充分、认真地履行本协议。本协议履行过程中如发生争议,双方应友好协商,协商不成时任何一方可将争议提交人民法院依法裁决。

第十条 本协议一式两份,具有同等法律效力,双方各执一份据以履行。本协议条款如需补充、更改,由双方另行签订补充协议。

甲 方(盖章):

法定代表人/委托代理人(签字): 王海鹏

2023 年 11 月 3 日

乙 方(盖章):

法定代表人/委托代理人(签字): 魏国强

2023 年 10 月 30 日

## 业务回单 (收款)

付款人户名: 许昌轩明智能机器人制造有限公司  
付款人开户行: 招商银行股份有限公司郑州未来支行

付款人账号: 371908852110902

收款人户名: 华南农业大学  
收款人开户行: 广州五山支行

收款人账号: 3602002609000310520

币种: 人民币(本位币)  
金额: 伍万圆整

小写: 50,000.00

业务(产品)种类: 跨行收报

凭证号码:

用途:

记账柜员: 00495

渠道: 同业清算互联前置

附言: 往来款

报文种类: 小额客户发起普通贷记业务

业务类型  
(种类): 普通汇兑

凭证种类:

摘要: 往来款

交易机构号: 0360200308

交易代码: 52189

支付交易序  
号: 13087006

委托日期: 2024-11-22

重要提示: 该文件为中国工商银行电子化回单, 请勿重复打印或重复记账。



# 教育部能源与动力工程专业虚拟教研室

## 关于公布“能源与动力工程专业虚拟教研室 2024 年度‘双碳使命 AI 赋能’教改项目”的通知

各项目申请人：

为了探索智慧教学技术深度赋能能源动力类专业人才培养的新模式，教育部能源与动力工程专业虚拟教研室组织开展了“双碳使命 AI 赋能”的教学改革研究项目立项申报工作。经通讯评审及会评审定，评定出能源与动力工程专业虚拟教研室 2024 年度“双碳使命 AI 赋能”教改项目 40 项，推荐“AI 赋能能源与动力工程专业拔尖人才培养模式研究”等 20 个项目为重点项目；评定“‘双碳’战略背景下能动专业多元智能化教学场景的构建与实践”等 20 个项目为一般项目。

现予以公布。

附件：能源与动力工程专业虚拟教研室 2024 年度“双碳使命 AI 赋能”教改项目重点项目和一般项目

教育部能源与动力工程专业虚拟教研室

浙江大学能源工程学院（代章）

2024 年 12 月 3 日



| 能源与动力工程专业虚拟教研室<br>2024 年度“双碳使命 AI 赋能”教改项目 |   |     |         |        |
|---|---|-----|---------|--------|
| 项目编号                                      | 项目名称                                      | 负责人 | 依托单位    | 推荐项目类型 |
| NDZVTRS2024Z-01                           | AI 赋能能源与动力工程专业拔尖人才培养模式研究                  | 饶中浩 | 河北工业大学  | 重点     |
| NDZVTRS2024Z-02                           | 面向航空发动机燃烧学智慧教学的数字化知识图谱建设                  | 王可  | 西北工业大学  | 重点     |
| NDZVTRS2024Z-03                           | 结合 AI 及数字孪生技术的实时互动教学与应用研究                 | 季晨振 | 同济大学    | 重点     |
| NDZVTRS2024Z-04                           | 地方高校能动专业服务本地域“校园-社区-乡村-企业”的师生共建智慧创新实践教学平台 | 李贵敬 | 燕山大学    | 重点     |
| NDZVTRS2024Z-05                           | 能源计量类课程教学资源数字化建设和 AI 赋能教学研究               | 王玉刚 | 中国计量大学  | 重点     |
| NDZVTRS2024Z-06                           | 智慧能源人才知识、能力和素养图谱构建与达成路径                   | 张保生 | 中国矿业大学  | 重点     |
| NDZVTRS2024Z-07                           | AI 赋能增强能源与动力工程专业的发展战略与规划                  | 余昭胜 | 华南理工大学  | 重点     |
| NDZVTRS2024Z-08                           | 《燃气轮机原理》知识图谱建设                            | 陈绍文 | 哈尔滨工业大学 | 重点     |
| NDZVTRS2024Z-09                           | 《燃烧理论》知识图谱建设                              | 翁武斌 | 浙江大学    | 重点     |
| NDZVTRS2024Z-10                           | 《锅炉原理》知识图谱建设                              | 蒲舸  | 重庆大学    | 重点     |
| NDZVTRS2024Z-11                           | 《汽轮机原理》知识图谱建设                             | 王建梅 | 武汉大学    | 重点     |
| NDZVTRS2024Z-12                           | 《制冷与低温原理》知识图谱建设                           | 包士然 | 浙江大学    | 重点     |
| NDZVTRS2024Z-13                           | 《暖通与空调》知识图谱建设                             | 胡雨燕 | 同济大学    | 重点     |
| NDZVTRS2024Z-14                           | 《太阳能》知识图谱建设                               | 祝培旺 | 浙江大学    | 重点     |
| NDZVTRS2024Z-15                           | 《氢能》知识图谱建设                                | 刘建国 | 华北电力大学  | 重点     |



| 项目编号            | 项目名称                      | 负责人 | 依托单位    | 推荐项目类型 |
|-----------------|---------------------------|-----|---------|--------|
| NDZVTRS2024Z-16 | 《风能》知识图谱建设                | 赵爽  | 内蒙古工业大学 | 重点     |
| NDZVTRS2024Z-17 | 《储能》知识图谱建设                | 代鹏程 | 中国石油大学  | 重点     |
| NDZVTRS2024Z-18 | 《碳捕集利用与封存》<br>知识图谱建设      | 王涛  | 浙江大学    | 重点     |
| NDZVTRS2024Z-19 | 《能源动力创新实践》<br>知识图谱与能力图谱建设 | 赵军  | 天津大学    | 重点     |
| NDZVTRS2024Z-20 | 《能动+X》跨学科知识<br>图谱与能力图谱建设  | 郑梦莲 | 浙江大学    | 重点     |

| 项目编号            | 项目名称                                 | 负责人 | 依托单位           | 推荐项目类型 |
|-----------------|--------------------------------------|-----|----------------|--------|
| NDZVTRS2024Y-01 | “双碳”战略背景下能<br>动专业多元智能化教学<br>场景的构建与实践 | 谢宁  | 仲恺农业工程学院       | 一般     |
| NDZVTRS2024Y-02 | 基于问题导向、案例研<br>讨、灵活定制的课程 AI<br>教学资源建设 | 唐玉婷 | 华南理工大学         | 一般     |
| NDZVTRS2024Y-03 | 精准智慧教学模式探究                           | 寇志海 | 沈阳航空航天大学       | 一般     |
| NDZVTRS2024Y-04 | 地方航空特色院校动力<br>工程类课程虚拟仿真<br>教学改革实践研究  | 耿直  | 郑州航空工业管<br>理学院 | 一般     |
| NDZVTRS2024Y-05 | 生物质发电技术<br>教学资源数字化建设                 | 高岩  | 山东建筑大学         | 一般     |
| NDZVTRS2024Y-06 | AI 赋能<br>数字化课程建设                     | 马诗会 | 燕山大学           | 一般     |
| NDZVTRS2024Y-07 | 热力发电厂教学资源<br>数字化建设                   | 王亚辉 | 内蒙古工业大学        | 一般     |
| NDZVTRS2024Y-08 | 能源动力类专业数字化<br>实验教学建设研究               | 孙志利 | 天津商业大学         | 一般     |
| NDZVTRS2024Y-09 | 项目式教学改革<br>探索与实践                     | 胡开永 | 天津商业大学         | 一般     |
| NDZVTRS2024Y-10 | 虚拟仿真实验                               | 程军  | 重庆大学           | 一般     |
| NDZVTRS2024Y-11 | 基于 SBE&S 理念的能<br>动类专业人才仿真思维<br>培养体系  | 卞煜  | 重庆大学           | 一般     |

| 项目编号             | 项目名称                                   | 负责人 | 依托单位     | 推荐项目类型 |
|------------------|--|-----|----------|--------|
| NDZYVTRS2024Y-12 | 基于典型可再生能源工程的数字化科教融合培养能源与动力工程人才         | 尹丽洁 | 同济大学     | 一般     |
| NDZYVTRS2024Y-13 | 基于生成式 AI 的去中心化教学研究                     | 金武  | 南京航空航天大学 | 一般     |
| NDZYVTRS2024Y-14 | 课程智能化教学改革与实践                           | 王春华 | 南京航空航天大学 | 一般     |
| NDZYVTRS2024Y-15 | 深度学习在能源与动力工程测试技术课程项目式教学中的应用            | 康灿  | 江苏大学     | 一般     |
| NDZYVTRS2024Y-16 | 生物质能系列课程思政教学数字资源库“3E”模式构建与实践研究         | 陈豪  | 江苏大学     | 一般     |
| NDZYVTRS2024Y-17 | “双碳”背景下 AI 与 CDIO 融合的能源动力专业课程教学改革研究与实践 | 魏国强 | 华南农业大学   | 一般     |
| NDZYVTRS2024Y-18 | 多模态知识图谱的构建及其在教学模式与教学评价中的应用             | 王坤  | 河北工业大学   | 一般     |
| NDZYVTRS2024Y-19 | 人工智能时代下全链条教学改革探索                       | 李乃良 | 中国矿业大学   | 一般     |
| NDZYVTRS2024Y-20 | 数智技术赋能能源动力类专业课精准教学的实践进路研究              | 杨霄  | 中国矿业大学   | 一般     |

## 2023年拟推荐省级教学改革项目和校级教学改革拟立项项目名单

| 序号 | 项目名称  | 项目负责人 | 拟立项级别 | 备注    |
|----|---|-------|-------|-------|
| 1  | 高阶思维视域下《种子生物学》“四维融合”混合式教学模式改革与实践              | 周玉亮   | 校重点项目 | 拟推荐省级 |
| 2  | 新林科视域下森林培育学知识图谱课程建设与教学模式创新                    | 邱权    | 校重点项目 | 拟推荐省级 |
| 3  | 一流专业建设背景下风景园林规划设计课程教学改革研究                     | 陈崇贤   | 校重点项目 | 拟推荐省级 |
| 4  | 一流农科高校基础实验课程思政教学一体化改革与实践——以大学物理实验课程为例         | 劳媚媚   | 校重点项目 | 拟推荐省级 |
| 5  | 双一流高校“科-教-思”融合培养学生高阶思维的实验教学改革研究——以遗传学实验为例     | 李楠    | 校重点项目 | 拟推荐省级 |
| 6  | 工程结构设计软件课程的“融合+分层”教学                          | 李文雄   | 校重点项目 | 拟推荐省级 |
| 7  | 基于竞赛和创新方法提升大学生创新能力的实证研究                       | 易欣    | 校重点项目 | 拟推荐省级 |
| 8  | 基于创新创业能力培养的“赛教融合”《养羊学》课程改革与实践                 | 柳广斌   | 校重点项目 | 拟推荐省级 |
| 9  | 人工智能赋能生态化大学英语混合教学改革研究                         | 苏君    | 校重点项目 | 拟推荐省级 |
| 10 | 基于创新能力培养的《电路实验》教学改革研究                         | 王建华   | 校重点项目 | 拟推荐省级 |
| 11 | 新时代高校思政课“问题链”教学模式研究——聚焦《习近平新时代中国特色社会主义思想概论》课程 | 何艳玲   | 校重点项目 | 拟推荐省级 |
| 12 | 三产融合理论在《茶叶生物化学》中的应用                           | 张钰乾   | 校重点项目 | 拟推荐省级 |
| 13 | 工程认证背景下基于知识图谱的新工科一流专业建设和提升的研究与实践              | 王金凤   | 校重点项目 | 拟推荐省级 |
| 14 | 融合数据分析思维和学科交叉的《线性代数》课程教学创新与实践                 | 张伟峰   | 校重点项目 | 拟推荐省级 |
| 15 | 基于创新能力培养的统计学专业数据分析类实验课程改革探索与实践                | 周燕    | 校重点项目 | 拟推荐省级 |
| 16 | 基于知识图谱的农业院校课程思政建设探索——以公共数学基础课为例               | 张娜    | 校招标项目 | 拟推荐省级 |
| 17 | 基于新兽医人才培养的《分子生物学》课程改革与实践探索                    | 沈永义   | 校重点项目 | 拟推荐省级 |
| 18 | 思政视角下《国际金融》课程教学改革与实践                          | 周超    | 校重点项目 | 拟推荐省级 |
| 19 | 新农科背景下基于“数字标本”的智慧植保实验体系研究                     | 李云锋   | 校重点项目 | 拟推荐省级 |
| 20 | 低碳农业背景下基于一特两驱教学模式的环境土壤学课程体系构建                 | 林庆祺   | 校重点项目 | 拟推荐省级 |
| 21 | “双一流”建设视野下安全教育模式嵌入环境化学实验室课程体系的实践与优化           | 高婷    | 校重点项目 | 拟推荐省级 |
| 22 | “三台协同，以美育人”——以课程教学为基础的高校舞蹈美育建设研究              | 郑琳喆   | 校重点项目 | 拟推荐省级 |
| 23 | 劳动教育融入设计类专业课程路径探索——以《纤维艺术造型设计》课程为例            | 林汉聪   | 校重点项目 | 拟推荐省级 |
| 24 | 人工智能背景下的新文科艺术专业人才培养研究：以动画专业为例                 | 王柯    | 校招标项目 | 拟推荐省级 |

|    |                                   |     |       |  |
|----|-----------------------------------|-----|-------|--|
| 52 | “食品仪器分析”线上线下混合式一流课程的建设与实践         | 陈运娇 | 校一般项目 |  |
| 53 | 课程思政与“五育并举”融合发展的高校足球课程改革与实践研究     | 陈存志 | 校一般项目 |  |
| 54 | 思政引导的体育课程内容体系改革与实践——以瑜伽课为例        | 何灵捷 | 校一般项目 |  |
| 55 | 新农科背景下的《遗传学》教学改革与实践               | 汪文毅 | 校一般项目 |  |
| 56 | “双一流”背景下基于信息技术的实验室安全教育优化建设        | 陈志民 | 校一般项目 |  |
| 57 | 理论力学多平台混合教学线上线下一体化设计与实践           | 刘新红 | 校一般项目 |  |
| 58 | 《饲料学》线上线下一体化混合教学设计探究              | 朱勇文 | 校一般项目 |  |
| 59 | 新农科背景下融合“课程思政+国际化”的《蚕桑概论》课程改革与实践  | 杨婉莹 | 校一般项目 |  |
| 60 | 多模态话语分析理论下《跨文化交际》课程中中国文化对外传播路径研究  | 杜龙鼎 | 校一般项目 |  |
| 61 | 人工智能赋能英语语言技能课程教学创新实践研究            | 李飞武 | 校一般项目 |  |
| 62 | 基于研究性教学的大学物理实验课程思政实践教学探索          | 杨小红 | 校一般项目 |  |
| 63 | 高校思政课问题式教学的探索研究——以“思想道德与法治”课程为例   | 刘智娴 | 校一般项目 |  |
| 64 | 《果蔬栽培学》课程思政设计与实践                  | 苏钻贤 | 校一般项目 |  |
| 65 | 《园艺种质资源与分类》实验教学内容体系优化的研究与实践       | 张志珂 | 校一般项目 |  |
| 66 | “真人+数字人”的智能教学模式探索与实践——以《数据结构》课程为例 | 梁云  | 校一般项目 |  |
| 67 | 数字化背景下《大学生心理健康教育》课程思政建设与实践        | 严颖  | 校一般项目 |  |
| 68 | 基于创新型人才培养目标对《海洋环境化学》的教学改革研究       | 公晗  | 校一般项目 |  |
| 69 | “四微一体”课堂教学实践与应用——以“水产品质量安全控制”课程为例 | 周爱国 | 校一般项目 |  |
| 70 | 数智时代《财务管理》课程教学改革研究                | 周小春 | 校一般项目 |  |
| 71 | 虚-实二维教学模式在环境监测实践课程中的应用            | 郑芊  | 校一般项目 |  |
| 72 | 能源动力类专业课程产教研协同育人模式探索与实践           | 魏国强 | 校一般项目 |  |
| 73 | 心理资本视域下心理健康课程改革探索                 | 林媛  | 校一般项目 |  |
| 74 | “轻咨询”融入高校心理健康教育课程的实践路径研究          | 刘桂娥 | 校一般项目 |  |
| 75 | 基于可持续创新人才培养的《首饰镶嵌工艺》教学改革与实践       | 潘子广 | 校一般项目 |  |
| 76 | “声动岭南”——音乐与表演专业中的新媒体技术创新教学项目研究与实践 | 冯逸章 | 校一般项目 |  |
| 77 | 人工智能技术背景下影像艺术课程的内容改革：以乡村影像为例      | 程蔚新 | 校一般项目 |  |
| 78 | 《植物学实验》“课程思政”的探索与实践               | 梁祥修 | 校一般项目 |  |

附件2

## 2025 年度本科教学质量与教学改革工程项目

### 中期检查表

|             |                             |
|-------------|-----------------------------|
| 级 别 :       | 一般项目/校级                     |
| 项 目 名 称 :   | 能源动力类专业课程产教研协同<br>育人模式探索与实践 |
| 项 目 负 责 人 : | 魏国强                         |
| 联 系 电 话 :   | 13580396927                 |
| 所 在 单 位 :   | 生物质工程研究院                    |
| 填 表 日 期 :   | 2025.06.03                  |

本科生院制

二、项目研究计划与实际成果

| 计划任务                | 完成情况 | 实际成果   |
|---------------------|------|--|
| 完善能源动力类专业基础课程教学改革方案 | 已完成  | 设计了创新型的教学方案，结合课堂理论与实践，增强了学生的实践操作能力和理论知识的理解。    |
| 增强课堂互动性，提升学生参与度     | 已完成  | 在课堂上采用互动问答、案例分析、分组讨论等多种教学方式，学生的参与度显著提高，课堂气氛活跃。 |
| 开展实验室实训课程，推动产教融合    | 已完成  | 学生参与了实验室设备操作和技术流程的演练，掌握了实际操作技能和工程素养，为就业打下坚实基础。 |
| 邀请企业导师参与教学，提高学生职业素养 | 计划开展 | 企业导师通过课程讲座和实验指导，帮助学生将理论应用于实际，培养了职业素养和团队协作能力。   |
| 撰写研究论文              | 已完成  | 发表教改论文1篇                                       |
| 总结教学改革成果，完成结题报告     | 计划开展 | 准备项目结题   |

二、主要阶段性成果（如有，请填下表，可另加附页）

| 名称                     | 作者             | 成果形式 | 刊物名或出版社、时间             | 字数   | 备注 |
|------------------------|----------------|------|------------------------|------|----|
| 涉农高校生物质能源领域传热学课程教学改革研究 | 魏国强，姚业成，杨希贤，易群 | 期刊论文 | 安徽农学通报，2024，24：114-117 | 5500 |    |
|                        |                |      |                        |      |    |
|                        |                |      |                        |      |    |



### 三、经费及单位审核意见

项目经费使用情况：

项目总预算4000元，支出论文版面费3350元，还剩余650元用于开展下一步研究。

所在单位审核意见：

夏安。

主管领导签名：

谢凡



中国期刊全文数据库全文收录期刊  
中国学术期刊(光盘版)全文收录期刊  
中国学术期刊综合评价数据库统计源期刊  
中国核心期刊(遴选)数据库全文收录期刊

ISSN 1007-7731  
CN 34-1148/S

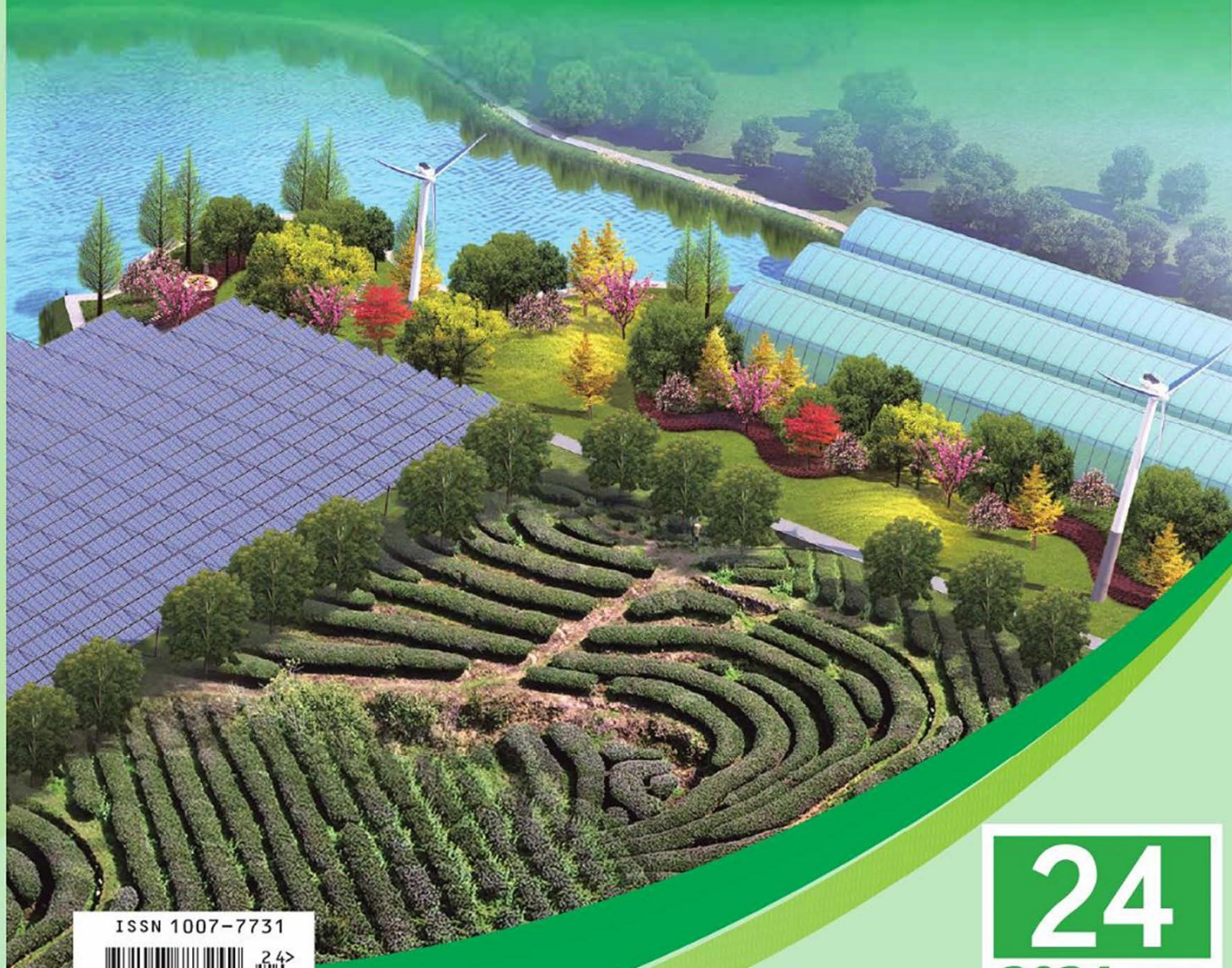
安徽农学通报

第三十卷 第二十四期

二〇二四年十二月

# 安徽农学通报

ANHUI NONGXUE TONGBAO



ISSN 1007-7731



9 771007 773242

24

24

2024 12月



# Anhui Agricultural Science Bulletin

## Vol.30 No.24 Dec. 2024

### Contents

|  |  |
|--|--|
| High yield seed production technology for hybrid rice variety Rong 6 you 5970.....   | WEN Shaoshan JIAO Jun(1)   |
| Cultivation techniques of “six suitability and three high” for regenerated rice<br>.....   | QUE Xinggui LI Juan WANG Zhanwei HE Yingcai PENG Qian WU Xinjun(5)           |
| Analysis of the current situation and strategies of rice industry development in Southern Anhui Province<br>.....  | LI Zhongdong(9)  |
| Main pests and diseases control techniques for corn ..... QIAN Suju ZHU Hongming ZHOU Ping<br>..... CUI Ling WANG Haiyang JIANG Peng CHENG Fangmei SHI Yang GAO Jin WANG Qianqian WANG Wei(13) |  |
| Analysis of the current situation and strategies of summer corn production in Northern Anhui Province<br>.....   | ZHAI Zhengmei(18)  |
| Effects of different sowing dates and densities on characteristics and yield of Wandou 40.....   | LI Yongbin(22)   |
| Effects of leaf structure optimization on tobacco plant growth and tobacco leaf quality in Bin County area<br>.....  | BI Shan LI Ying CHI Peng YAN Peiqiang JIANG Yuzhou WANG Ning WANG Peng(27)   |
| Effects of exogenous gibberellin on fruit quality of blueberry<br>.....  | GUO Xiaolan LI Han YANG Jiawei HU Jinbin WANG Jianbing WANG Dun CAO Yu(33)   |
| Explore on quality stability of feed additive <i>Acremonium terricola</i> culture<br>.....   | XU Juanjuan YUAN Hai TONG Shouli ZHOU Qun ZHOU Juan XU Zhao LI Xiaoxiang(37) |
| Effects of quick dipping with different concentrations of naphthalene acetic acid on rooting of <i>Euonymus fortunei</i> cuttings<br>.....   | WANG Jincheng(42)  |
| Naturalness evaluation of secondary forest based on the mixed management techniques of naturalization and<br>homogenization of pioneer tree species.....                                       | CHANG Huijuan FU Lihua CHENG Shun ZHANG Fei ZHANG Yan(45)                    |
| Progress on seedlings and seeds propagation research of Magnoliaceae plants<br>.....   | HE Yanli XIAO Yaqiong ZHANG Zhilan(50)                                       |
| Investigation and control of piercing-sucking pests in garden plants.....  | SHI Jianyong(54)   |
| Investigation and analysis of plant resources in Guangzhou cultural park<br>.....  | DING Lijun ZHUO Dinglong LI Bingmin LIU Shihan LIANG Jian TAN Guangwen(59)   |
| Research on water quality assurance countermeasures during the flood season of a branch of Yangtze River in Central<br>Jiangsu Province.....   | ZHANG Lei LING Hong JIANG Yeli LI Wanyi TAN Dongxuan DONG Yue LIU Yuan(64)   |
| Research progress of plant lectins in agricultural disease and pest control and biomedical applications<br>.....   | ZHOU Lin WU Lifeng YANG Liuyan ZHANG Yongchun(69)                            |

|   |   |
|---|---|
| Analysis of current situation of damage and control measures of termite in traditional villages in Central Jiangsu Province .....   | DU Shanggen LI Donghu CHEN Zheugfeng GUO Renxia(77)   |
| Termite control technology for small reservoirs and grade 4 and 5 levees .....  | YIN Lizhi(81)   |
| Visualization analysis of soil ecology research hotspots and trends based on CiteSpace .....  | HOU Ruiqi CHEN Yixuan AHE Asha LIU Jingjing XIAO Ximeng YANG Yaojun(85)                         |
| Investigation on the planning strategy of the riverside park .....  | YUAN Xu'an DONG Chenlu LI Yin GUAN Kailang LI Zihua TAN Guangwen(93)                            |
| Analysis on development status and countermeasure of agricultural product processing industry in Huizhou District .....   | WU Runjie ZHANG Jianxi(98)  |
| Research progress on the interaction between dietary polyphenols and intestinal microbiota .....  | WANG Yanzhen(102)   |
| Research on maturity recognition of fresh tobacco leaf bundles in baking chambers based on machine vision .....   | YU Xi LI Hongming DAI En SUN Wusan ZHU Faliang ZHAO Wenjun LI Yueping WANG Jiaxu HU Huixin(106) |
| Exploration and practice of talent cultivation model for Tea Science major under the background of industry education integration and collaborative education between schools and enterprises ..... | ZHENG Shizhong CHEN Xiaohui ZHOU Yinzu ZHOU Ziwei WANG Fang CHEN Meixia CAI Liewei(110)         |
| Research on teaching reform of <i>Heat Transfer</i> course in biomass energy field in agricultural universities .....   | WEI Guoqiang YAO Yecheng YANG Xixian YI Qun(114)  |
| Research on the reform innovation practice of <i>Biochemistry</i> course teaching .....   | HUANG Jing LIU Ying YU Dongmei(118)   |
| Exploration of teaching reform in <i>Grassland</i> practice courses from the perspective of "three innovations" integration .....   | YANG Weiguang QU Shanmin  |
| .....   | JU Xiaofeng LI Guoliang LIU Guofu ZANG Hui ZHAO Lei LI Muyang BAO Fengxuan LIU Xiangping(122)   |
| Research on the teaching reform of <i>Landscape Ecology</i> course from the perspective of green development .....  | ZHAO Dahua(126)   |
| Practice of <i>Microbiology</i> course teaching reform based on "SPOC+flipped classroom" .....  | WANG Chunjuan WANG Jinlong HOU Yu ZHAO Guiyun REN Guihong SUN Haiming(130)                      |
| Optimize and practice of practical teaching system for Landscape major based on the whole industry chain .....  | QIAO Yongxu ZHANG Yongping ZHANG Huimin XIE Rong WANG Zhijie JIANG Yahua LIU Yu ZHANG Nan(133)  |
| Research on strategies for improving the quality of high-quality farmers cultivation under the background of rural revitalization .....   | YANG Qin WU Zhaoming(137)   |
| Research on countermeasures of ecotourism development in X County under the background of "dual carbon target" .....  | HE Guang YAN Zhiming LIU Jiahui PENG Yuxi WANG Yajie(141)                                       |

# 安徽农学通报

(半月刊)

郑之宽 题字

1995 年创刊

2024 年第 24 期

总第 30 卷 488 期

## 目次

### 粮食作物

|   |                         |    |
|---|-------------------------|----|
| 杂交水稻品种 6 优 5970 高产制种技术 .....                      | 文绍山 焦 峻                 | 1  |
| 再生稻“六适三高”栽培技术 .....                               | 阙兴贵 李 娟 王占伟 何英才 彭 乾 吴新军 | 5  |
| 皖南地区水稻产业发展现状与对策分析 .....                           | 李中东                     | 9  |
| 玉米主要病虫害防治技术 .....                                 |                         |    |
| ····· 钱素莉 朱红明 周 萍 崔 玲 王海洋 姜 鹏 程芳梅 施 洋 高 进 王倩倩 王 为 |                         | 13 |
| 皖北地区夏玉米生产现状及策略分析 .....                            | 翟正美                     | 18 |
| 不同播期与密度对皖豆 40 性状及产量的影响 .....                      | 李永宾                     | 22 |

### 经济作物

|                               |                             |    |
|-------------------------------|-----------------------------|----|
| 叶片结构优化对宾县地区烟株生长和烟叶质量的影响 ..... | 毕 璐 李 莹 迟 鹏 颜培强 蒋雨洲 王 宁 王 鹏 | 27 |
| 外源赤霉素对蓝莓果实品质的影响 .....         | 郭小兰 李 瀚 杨嘉蔚 胡进彬 王建兵 王 盾 曹 瑜 | 33 |

### 动物科学

|                             |                             |    |
|-----------------------------|-----------------------------|----|
| 饲料添加剂地衣芽孢杆菌培养物质量稳定性探究 ..... | 徐娟娟 袁 海 童守礼 周 群 周 娟 徐自奥 李晓祥 | 37 |
|-----------------------------|-----------------------------|----|

### 林业科学

|                                    |                         |    |
|------------------------------------|-------------------------|----|
| 速生不同浓度的蔡乙酸对扶芳藤插穗生根的影响 .....        | 王金成                     | 42 |
| 基于先锋树种自然化和均质化混交经营技术的次生林自然度评价 ..... | 常慧娟 付立华 程 顺 张 菲 张 岩     | 45 |
| 木兰科植物种苗及种子繁殖研究进展 .....             | 何艳丽 肖亚琼 张志兰             | 50 |
| 园林植物刺吸式害虫种类调查及防治 .....             | 施剑勇                     | 54 |
| 广州文化公园植物资源调查与分析 .....              | 丁丽君 卓定龙 李冰敏 刘世晗 梁 建 谭广文 | 59 |

期刊基本参数: CN34—1148/S\*1995\*5\*A4\*144\*zh\*P\*¥20.00\*1000\*32\*2024-12

## 资源·环境·植保

|                                    |                             |    |
|------------------------------------|-----------------------------|----|
| 苏中地区某通江河道汛期水质保障策略分析 .....          | 张 蕾 凌 虹 江野立 李婉逸 谭东炬 董 悦 刘 媛 | 64 |
| 植物凝集素在农业病虫害防治和生物医药学应用中的研究进展 .....  | 周 琳 吴立峰 杨柳燕 张永春             | 69 |
| 苏中地区传统村落白蚁为害现状及防治对策分析 .....        | 杜尚根 李冬虎 陈正峰 郭仁霞             | 77 |
| 小型水库及4、5级堤防白蚁防治技术 .....            | 尹立志                         | 81 |
| 基于CiteSpace的土壤生态研究热点与趋势可视化分析 ..... | 侯蕊琪 陈佚暄 阿合阿沙 刘静婷 肖析蒙 杨瑶君    | 85 |
| 滨河生态公园规划设计策略研究 .....               | 袁徐安 董晨露 李 银 关开朗 李子华 谭广文     | 93 |

## 农产品加工·检验检测

|                           |         |    |
|---------------------------|---------|----|
| 徽州区农产品加工产业发展现状及对策分析 ..... | 吴润杰 张建喜 | 98 |
|---------------------------|---------|----|

## 药食同源

|                            |     |     |
|----------------------------|-----|-----|
| 膳食多酚与肠道微生物群的相互作用研究进展 ..... | 王艳珍 | 102 |
|----------------------------|-----|-----|

## 农业信息·农业气象

|                             |                                     |     |
|-----------------------------|-------------------------------------|-----|
| 基于机器视觉的烤房成杆鲜烟叶成熟度判别研究 ..... | 喻 曦 李洪明 戴 恩 孙五三 朱法亮 赵文军 李跃平 王家绪 胡慧新 | 106 |
|-----------------------------|-------------------------------------|-----|

## 农业教育

|                                     |   |     |
|-------------------------------------|---|-----|
| 产教融合背景下校企协同育人的茶学专业人才培养模式探索与实践 ..... | 郑世仲 陈晓慧 周银珠 周子维 王 芳 陈美霞 蔡烈伟             | 110 |
| 涉农高校生物质能源领域传热学课程教学改革研究 .....        | 魏国强 姚业成 杨希贤 易 群                         | 114 |
| 生物化学课程教学改革创新实践研究 .....              | 黄 静 刘 莹 于冬梅                             | 118 |
| “三创”融合视域下草学类实践课教学改革探究 .....         | 杨伟光 曲善民 鞠晓峰 李国良 刘国富 臧 辉 赵 磊 李沐阳 包凤轩 刘香萍 | 122 |
| 绿色发展视域下园林生态学课程教学改革研究 .....          | 赵大华                                     | 126 |
| 基于“SPOC+翻转课堂”的微生物学课程教学改革实践 .....    | 王春娟 王金龙 侯 宇 赵桂云 任桂红 孙海明                 | 130 |
| 基于全产业链的园林专业实践教学体系优化与实践 .....        | 乔永旭 张永平 张惠敏 谢 荣 王志杰 蒋亚华 刘 宇 张 楠         | 133 |

## 农业经济·管理

|                              |                     |     |
|------------------------------|---------------------|-----|
| 乡村振兴背景下高素质农民培育质量提升策略研究 ..... | 杨 琴 吴兆明             | 137 |
| “双碳”背景下X县生态旅游发展策略研究 .....    | 何 广 闫志明 刘家辉 彭宇茜 王雅捷 | 141 |

|                              |   |
|------------------------------|---|
| 《安徽农学通报》第30卷(2024年)总目录 ..... | I |
|------------------------------|---|

|                                   |    |
|-----------------------------------|----|
| 宿州市:打造全要素产业链条,推动绿色食品产业高质量发展 ..... | 封二 |
| 安徽地方特色农产品巡礼 .....                 | 封三 |

本刊声明:凡被本刊录用的稿件,即视为作者同意授权本刊及本刊合作单位(中国知网、万方、维普等数据库)使用其作品,授权权利包括但不限于复制权、发行权、信息网络传播权、表演权、翻译权、汇编权及改编权等权利。所刊论文稿费已包含上述著作权使用费。作者对上述声明有异议的来稿请说明,本刊将做适当处理。

# 安徽农学通报 编委会

主任委员：卢仕仁

副主任委员：(按拼音字母为序)

操海群 郭 亮 姜道宏 李升和 李泽福 刘万程 王加启 魏 骅  
夏伦平 袁维海

委 员：(按拼音字母为序)

曹成茂 崔广荣 丁 凯 范 涛 韩仁长 花日茂 华金玲 江 河  
李绍稳 舒英杰 汪建飞 汪建来 汪社宽 王贵春 王华君 王立克  
夏加发 夏伦志 殷宗俊 余海兵 袁文业 张从合 左光之

主 编：卢仕仁

社长/执行主编：郑丹丹

副 主 编：马世堂

## 安徽农学通报

Anhui Nongxue Tongbao

1995年创刊 半月刊

第30卷 第24期 2024年

## Anhui Agricultural Science Bulletin

Started in 1995, Semimonthly

Volume 30, Issue 24, 2024

主管单位 安徽省科学技术协会

主办单位 安徽省农学会

编辑出版 安徽农学通报

主 编 卢仕仁

地 址 合肥市滨湖新区洞庭湖路3355号

电 话 0551-62675980、0551-62678400

电子邮箱 anhuixtb1995@163.com

网 址 <http://www.ahnxtb.cn>

邮 编 230091

印刷单位 合肥华苑印刷包装有限公司

发行单位 中国邮政集团有限公司

安徽省邮政报刊发行局

Administrated by Anhui Association of Science and Technology

Sponsored by Anhui Association of Agricultural Science Societies

Edited and published by Anhui Agricultural Science Bulletin

Chief editor LU Shiren

Address No. 3355 Dongtinghu Road, Binhu New District, Hefei

Tel 0551-62675980, 0551-62678400

E-mail anhuixtb1995@163.com

Web site <http://www.ahnxtb.cn>

Postal code 230091

Printed by Hefei Huayuan Printing and Packaging Co., Ltd.

Distributed by Anhui Postal Newspaper and Publication Distribution

Bureau of China Post Group Co., Ltd.

本期执行编辑 杨 欢

法 律 顾 问 夏跃东[上海建纬(合肥)律师事务所 13637059816]

ISSN 1007-7731

CN 34-1148/S

2024年12月30日出版

邮发代号 26-146

定 价 20.00元



封面图片源自安徽应时农业设计院有限公司



# 涉农高校生物质能源领域传热学课程教学改革研究

魏国强<sup>1</sup> 姚业成<sup>1</sup> 杨希贤<sup>1</sup> 易群<sup>2</sup>

(<sup>1</sup>华南农业大学,广东广州 510642;

<sup>2</sup>武汉工程大学,湖北武汉 430073)

**摘要** 为适应能源产业发展需求,培养能适应和引领新一轮能源科技革命和产业变革的卓越工程科技人才,本文对涉农高校生物质能源领域的必修课程传热学进行教学改革研究。针对该课程教学内容复杂、教学模式单一和考核评价方式有待优化等教学现状,结合CDIO教育理念,提出相应的教学改革措施。具体包括“线上+线下”融合,实施翻转课堂;引入CDIO教育理念,强化案例教学;以赛促学,激发学习热情;融入思政元素,增强思政觉悟;改革考核方式,加大过程性考核力度。通过具体的工程案例提高学生的课堂参与度,加强师生互动,有利于培养学生的批判性思维。为类似课程教学改革创新研究提供参考。

**关键词** 传热学;生物质能源;生物质材料;CDIO教学

中图分类号 G642.0;S216

文献标识码 A

文章编号 1007-7731(2024)24-0114-04

DOI号 10.16377/j.cnki.issn1007-7731.2024.24.025

## Research on teaching reform of *Heat Transfer* course in biomass energy field in agricultural universities

WEI Guoqiang<sup>1</sup> YAO Yecheng<sup>1</sup> YANG Nixian<sup>1</sup> YI Qun<sup>2</sup>

(<sup>1</sup>South China Agricultural University, Guangzhou 510642, China;

<sup>2</sup>Wuhan Institute of Technology, Wuhan 430073, China)

**Abstract** To meet the development needs of the energy industry and cultivate outstanding engineering and technological talents who can adapt to and lead the new round of energy technology revolution and industrial transformation, conducted teaching reform research on the compulsory course of *Heat Transfer* in the field of biomass energy in agricultural universities. In response to the complex teaching content, single teaching model, and need for optimization of assessment and evaluation methods in this course, combined with the CDIO educational concept, corresponding teaching reform measures were proposed. Specifically, it includes the integration of “online+offline” and the implementation of flipped classrooms; introducing CDIO educational concept and strengthening case teaching; promoting learning through competitions and stimulating enthusiasm for learning; integrating ideological and political elements to enhance ideological and political awareness; reforming the assessment method and increasing the intensity of process based assessment. Through specific engineering cases, students’ classroom participation had been improved, teacher-student interaction had been strengthened, and it was conducive to cultivating students’ critical thinking. Provides a reference for research on teaching reform and innovation in similar courses.

**Keywords** *Heat Transfer*; biomass energy; biomass materials; CDIO education

姜未汀等<sup>[1]</sup>研究表明,为加快清洁能源的综合利用与高效转化,能源动力类学科承担着重要的发展任务。实践中,随着能源产业面临新一轮的变革与挑战,亟需培养一大批能适应和引领新一轮能源

**基金项目** 教育部产学合作育人项目(231001255311634);教育部能源与动力工程专业虚拟教研室“双碳使命AI赋能”教学改革研究项目(NDZYVTRS2024Y-17)。

**作者简介** 魏国强(1981—),男,河北石家庄人,博士,副教授,从事生物基有机固废热化学转化及高值化利用研究。

**通信作者** 姚业成(1993—),男,广东广州人,博士,助理研究员,从事农林有机固废热解气化研究。

**收稿日期** 2024-10-12

科技革命和产业变革的卓越工程科技人才,有必要进一步从人才培养方案着手,加大力度挖掘课程思政元素,结合绿色发展理念,深化课程教学改革。张嘉杰等<sup>[2]</sup>研究认为,传热学研究的一项重要内容是热量传递规律,其是涉农高校生物质能源领域和能源动力专业的必修课程之一。CDIO (Conceive, Design, Implement, Operate)是一种基于工程教育的理念,旨在培养学生的核心能力,包括构思(Conceive)、设计(Design)、实现(Implement)和操作(Operate)。将该理念应用于传热学课程,可为学生提供更加综合和更具实践性的学习体验。

关于传热学课程,相关学者进行了一系列教学改革探索与实践工作。李文强等<sup>[3]</sup>研究提出,通过新媒体技术将前沿科学实验引入线下理论课堂,极大激发了学生的学习热情和创新思维。胡艳鑫等<sup>[4]</sup>根据课程“应用范围广、知识覆盖面广和时间跨度大”的特点,基于翻转课堂,使用多元化的教学资源与新媒体技术,对教学模式进行改革。冯耀勋等<sup>[5]</sup>探索了网络教学模式与常规教学法相结合的教学方法,发现网络教学可以大幅提高学生的学习兴趣。朱群志等<sup>[6]</sup>研究优化教材体系,提出了调整课程结构与教学内容、创新专题讨论及实验教学等措施,提高教学效果,增强实践和创新能力。尚琳琳等<sup>[7]</sup>研究提出了调整实验教学体系的教学方案,结合开放性实验室的管理模式,优化实验考核与奖励等实施办法,对于本科实验教学过程创新能力培养进行新的尝试和探索。

本文针对传热学课程教学内容复杂,教学模式单一、考核评价有待多元化等问题,提出采用翻转课堂教学模式,结合CDIO教育理念,通过具体的工程案例提高了学生的课堂参与度,加强师生互动,促使学生进行批判性思考。通过对传热学课程教学模式的改革,以培养适应和引领新一轮能源科技革命和产业变革的卓越工程科技人才。

## 1 生物质能源领域传热学课程教学现状分析

当前,生物质能源转化方式以催化热解为主,热量在生物质之间传递的机制、规律和影响因素等十分复杂。传热学的核心内容之一是探讨

生物质热量传递规律,该课程知识框架清晰,主要包括导热、对流换热和辐射换热3种基本传热过程及其综合应用。

### 1.1 教学内容与模式方面

传热学是能源与动力专业的基础课,王杰等<sup>[8]</sup>研究认为,其具有理论性和抽象性的特点,如基本概念和原理过多,容易混淆;公式多,推导过程复杂,难以记忆;教学内容复杂,抽象的内容难以理解,应用灵活,学生较难掌握。实践中,该课程教学形式较为生硬且教学内容枯燥,部分学生学习的积极主动性不高。部分教师对教学内容的理解和把握程度有待提高,在教学过程中较为注重对概念、定理和公式推导过程的介绍,而对于如何在未来的专业课程中深入应用这些知识点,以及如何利用专业知识解决实际工程问题等的讲解有待深入;对建立起理论和实际工程应用之间联系的主动性不足,学生较难更全面理解课程知识体系。解丹等<sup>[9]</sup>研究认为,这可能导致学生重视对知识点的客观记忆,而学以致用能力有待进一步增强。同时,教学中对课程思政元素的融入不够自然,教学内容与绿色低碳发展理念的结合度不够深入,有待融入工匠精神。

### 1.2 考核评价方面

在该课程考核中,期末成绩占70%,平时成绩占30%。成绩构成有待多元化,评价方法单一,过程性考核评价方法有待应用。李雪梅<sup>[10]</sup>研究认为,有必要改革考核评价模式,以真实反映学生的能力和水平。尚琳琳等<sup>[7]</sup>研究指出,为鼓励学生主动锻炼动手能力和创新思维,有必要进一步加强对其实操水平和问题分析能力的考量,优化综合成绩构成。

## 2 传热学课程教学改革措施分析

针对该课程教学形式较生硬、教学内容抽象复杂,思政元素融入不足,考核评价方式有待多元化等现状,提出应用翻转课堂、案例教学和以赛促学等教学模式与方法。

### 2.1 “线上+线下”融合,实施翻转课堂

传热学在生产技术中发挥重要作用,在该课程教学的概念化阶段,可以帮助学生理解传热的基本原理和概念,包括传热的机制、传热方程和热导率

等。通过深入挖掘优质在线资源,利用慕课等网络平台的在线学习资源,特别是农业生物质材料热转化方面,让学生建立起对传热学的概念性认识。同时,建立热传导课程的在线题库资源,通过学习群讨论课题和作业,使学生能及时巩固和实践线下所学知识。学期初,课题组教师从各章节中选取合适的教学内容,通过在线学习平台,将相关学习视频推送给学生进行课前预习,通过翻转课堂的形式,开展教学活动。翻转课堂的课件制作要求精美,知识点讲解要求清晰,以使大部分学生能掌握授课内容,并在课堂练习和讲解上分配一定学时。充分利用在线题库资源,通过互动式教学、课前在线交流、课内小组讨论和课后习题评价等方式,将教学模式转变为“先学后教”,让学生及时巩固和实践线下所学知识。谢新奇等<sup>[11]</sup>研究认为,这有利于进一步激发学生的学习主动性,有效活跃了课堂气氛,实现了良好的师生互动。另外,搭建生活小场景实验,为学生提供动手操作的平台,并涉及传热设备的操作和维护等内容,以检验其对专业知识的掌握程度。

2.2 引入 CDIO 教育理念,强化案例教学

借鉴张贺磊等<sup>[12]</sup>的研究成果,引入 CDIO 教育理念,结合相关工程案例,按照基础—综合—创新的多维度思路,进行该课程的教学改革。对实际工程所涉及的复杂传热、传质过程进行剖析,引导学生对相应的传热过程、知识进行串联学习。依据学科前沿动态和经济发展动态,更新知识结构,设计教学项目,丰富教学内容,使学生充分认识到课程内容的技术革新,增强其专业认同感。杨建平等<sup>[13]</sup>研究探索“案例引入—理论学习—案例剖析—创新实践”的渐进启发式教学方法,注重将“双碳”元素引入教学案例中。在对新概念、新原理、新结构、新技术和新应用的求知过程中,结合实际案例,提高学生对知识点的认知,锻炼其分析和解决问题的能力,进而为创新型人才的培养奠定基础。将 CDIO 教育培训理念融入课堂教学(表 1),逐步实现从基础到综合,再到创新的多维度能力培养。

表 1 CDIO 教育理念融入课堂教学

| 例子   | 内容   | 层次 |
|------|--|----|
| 生活常识 | (1)探讨壶柄用橡胶包裹的原因;分析塑料和不锈钢的不同之处<br>(2)把勺子放进热水里,判断哪个勺子里的黄油融化得更快 | 基础 |
| 工程案例 | 建筑节能材料   | 综合 |
| 改进措施 | (1)结构改造<br>(2)选择导热系数小的材料<br>(3)增加厚度                          | 创新 |

2.3 以赛促学,激发学习热情

借鉴杨建平等<sup>[13]</sup>的研究成果,开展课前课中课后、线上线下的“全时空”教学。实践中,教研组对接“全国高校人工环境科学奖”专业基础竞赛与各大高校考研典型传热试题,将相关内容有机整合到教学中,将竞赛试题以平时作业的形式分发给学生,在学期末组织传热课堂知识竞赛,以激发学生的学习热情,提高课堂趣味性和参与度。为提高学生的课外学习能力,将教学过程分为课前准备、课中教学和课后拓展 3 个阶段。课前通过线上视频,培养学生自主学习能力;课中注重发挥教师的引导作用,采用任务驱动等方法,剖析案例中的传热问题,完成相应的教学任务,帮助学生探索新知识;课后将所学的理论知识运用到学科竞赛、大创项目中,以提高学生创新能力和综合素质。

2.4 融入思政元素,增强思政觉悟

全方位、深度挖掘绿色发展理念下的传热学课程中蕴含的思政元素,并与课堂教学进行高度融合,形成协同育人效应。在理论课堂教学过程中,从专业理论知识的认知、案例的剖析和实践环节的锻炼 3 个过程入手,结合能源动力行业领域的发展现状,深入挖掘关键知识点,与碳达峰、碳中和案例中的思政元素进行有机融合。将课程体系理论知识与思政元素进行有机结合,让学生在职业发展中贯彻绿色发展理念。

马衍坤等<sup>[14]</sup>研究指出,在教学设计过程中,将时事热点、社会新闻案例与教学内容进行有机结合,将思政元素、专业素质与教学内容进行有机结合。例如,对于传热过程的控制,可以结合新的节能材料和节能措施,帮助学生树立节能减排意识,培养其社会责任感;对于傅里叶定律,可以融入工匠精神,结合



大量的实验实例获得可靠的数据;对于大型容器的沸腾换热,可以结合临界热流密度的概念进行安全

教育,强调安全生产的重要性。该课程思政元素的映射和融合如表2所示。

表2 该课程思政元素的映射和融合

| 知识点         | 思政元素的映射与融合               |
|-------------|--------------------------|
| 传热在生产技术中的应用 | 贯彻碳中和发展理念                |
| 热导率         | 培养技术创新意识                 |
| 傅里叶定律       | 培养科学、严谨的工作精神             |
| 传热的发展历史     | 培养掌握真理,敢于挑战权威的精神         |
| 凝结换热        | 培养技术创新意识                 |
| 沸腾换热        | 突出培养安全生产理念               |
| 强化/弱化传热     | 树立节能环保意识,培养能源转换效率提升的思维模式 |
| 临界绝缘直径      | 培养辩证思维                   |

## 2.5 改革考核方式,加大过程性考核力度

为突出应用型人才的培养力度,结合王任远等<sup>[15]</sup>和赵亮等<sup>[16]</sup>的研究成果,对考核方式进行优化,进一步加强对学生的实操能力的考核,增加实验课考核成绩占比,总体考试成绩由期末考试(65%)、实验课(15%)和平时成绩(20%)组成。同时,将阶段测试、在线学习和课程分组评分等纳入过程性考核,定期实时更新学生的平时成绩,激发其学习积极性。

综上,本文开展传热学课程教学改革。采用多种现代教学方式,如翻转课堂、线上线下混合式教学等,形成活泼的课堂教学氛围。通过师生互动讨论,增强了课堂吸引力和学生注意力。结合CDIO教育培训理念,通过具体的工程案例,让学生组成团队,不断进行批判性思考,提高其发现、分析和解决问题的能力。依托本课程,教师在思政教学比赛和青年教师演讲比赛中多次获奖。

## 参考文献

- [1] 姜未汀,张莉,袁薇,等.《传热学》课程建设研究[J].中国电力教育,2021(增刊1):97-98.
- [2] 张嘉杰,马素霞,庞晓敏,等.以社会主义核心价值观和马克思主义科学方法论为引领的专业课程思政体系构建:以传热学课程为例[J].化工高等教育,2024,41(4):132-136.
- [3] 李文强,冯喜平,惠卫华.新媒体结合工科教学的探索:以“传热学”教学实践为例[J].科技风,2022(8):90-92.
- [4] 胡艳鑫,吴婷婷,王长宏.基于翻转课堂的创新教学模式在《传热学》中的实践[J].广东化工,2020,47(22):209-211.

- [5] 冯耀勋,郑晓峰.一般本科院校能源与动力工程专业锅炉原理课程教学设计方法探讨[J].广东化工,2019,46(19):207-208.
- [6] 朱群志,姜未汀,张莉,等.研究生课程“高等传热学”教学改革初探[J].中国电力教育,2014(30):49-50.
- [7] 尚琳琳,郭煜,马利敏,等.传热学实验创新能力培养的探索与实践[J].中国教育技术装备,2014(18):144-145.
- [8] 王杰,张素平.提高传热学课程教学效果的探讨[J].化工高等教育,2021,38(6):146-150.
- [9] 解丹,王浩全,杨喜旺,等.案例驱动教学法的实践探索[J].工业和信息化教育,2024(1):82-85.
- [10] 李雪梅.传热学课程教学改革的探讨与实践[J].科技信息,2011(30):75.
- [11] 谢新奇,赵鑫博,商佳棋,等.新工科背景下新能源专业传热学教学模式探讨[J].中国新通信,2022,24(6):149-151.
- [12] 张贺磊,耿直,单晨晨,等.案例式教学在传热学课程教学中的应用[J].中国电力教育,2022(2):57-58.
- [13] 杨建平,杨莺,孔凡红,等.“双碳”背景下“传热学”课程教学改革实践[J].中国电力教育,2024(8):67-68.
- [14] 马衍坤,刘静,唐明云,等.立足“四个面向”的基础课程思政元素挖掘方法与应用:以“传热学”课程为例[J].中国地质教育,2022,31(1):57-61.
- [15] 王任远,张敏.新工科背景下流体力学与传热学课程教学改革探讨[J].时代汽车,2021(15):85-86.
- [16] 赵亮,田玉兰,潘亚娣.建设一流能源类课程教学模式的创新与实践:以“生物质能”为例[J].化工时刊,2021,35(3):47-49.

(责任编辑:杨欢)

课题编号：2024YFB4206101

密 级：公开

国家重点研发计划  
课题任务书

|           |                           |
|-----------|---------------------------|
| 课题名称：     | 双流化床生物质化学链气化关键技术          |
| 所属项目：     | 生物质化学链气化制汽柴油关键技术与示范       |
| 所属专项：     | 可再生能源技术                   |
| 项目牵头承担单位： | 中国科学院广州能源研究所              |
| 课题承担单位：   | 华南农业大学                    |
| 课题负责人：    | 魏国强                       |
| 执行期限：     | 2024 年 12 月 至 2028 年 11 月 |

中华人民共和国科学技术部制

2024 年 12 月 18 日



课题基本信息表

|                         |              |  |             |                 |                    |
|-------------------------|--------------|--|-------------|-----------------|--------------------|
| 课题名称                    |              | 双流化床生物质化学链气化关键技术   |             |                 |                    |
| 课题编号                    |              | 2024YFB4206101   |             |                 |                    |
| 所属项目                    |              | 生物质化学链气化制汽柴油关键技术与示范  |             |                 |                    |
| 所属专项                    |              | 可再生能源技术  |             |                 |                    |
| 密级                      |              | <input checked="" type="checkbox"/> 公开 <input type="checkbox"/> 秘密 <input type="checkbox"/> 机密   |             | 单位总数            | 4                  |
| 课题类型                    |              | <input type="checkbox"/> 基础前沿 <input checked="" type="checkbox"/> 重大共性关键技术 <input type="checkbox"/> 应用示范研究 <input type="checkbox"/> 其他 |             |                 |                    |
| 课题活动类型                  |              | <input type="checkbox"/> 基础前沿 <input checked="" type="checkbox"/> 应用研究 <input type="checkbox"/> 试验发展                                   |             |                 |                    |
| 课题研究<br>所属学科            |              | 能源科学技术<br>一次能源   |             |                 |                    |
| 课题成果应<br>用的主要国<br>民经济行业 |              | 电力、热力、燃气及水生产和供应业<br>燃气生产和供应业<br>燃气生产和供应业   |             |                 |                    |
| 课题的社会<br>经济目标           |              | 能源生产、分配和合理利用<br>可再生能源  |             |                 |                    |
| 经费预算                    |              | 总需求 530.00 万元，其中中央财政专项资金需求 530.00 万元   |             |                 |                    |
| 课题周期节点                  |              | 起始时间   | 2024 年 12 月 | 结束时间            | 2028 年 11 月        |
|                         |              | 实施周期   | 共 48 个月     | 预计中期时间点         | 2026 年 11 月        |
| 课题<br>承担<br>单位          | 单位名称         | 华南农业大学   |             | 单位法定<br>代表人姓名   | 薛红卫                |
|                         | 单位性质         | 大专院校   |             | 组织机构代码          | 124400004554165634 |
|                         | 单位主管部门       |  |             | 隶属关系            | 地方                 |
|                         | 单位所属地区       | 广东省  |             | 地市（市、自<br>治州、盟） | 广州市 天河区            |
|                         | 通信地址         | 广州市天河区五山路 483 号  |             | 邮政编码            | 510642             |
|                         | 单位开户名称       | 中国工商银行广州五山支行   |             |                 |                    |
|                         | 开户银行<br>（全称） | 中国工商银行股份有限公司<br>广州五山支行   |             | 汇入地点            | 广东省 广州<br>市        |





项目牵头承担单位（甲方）：

法定代表人签字（签章）：

吕建成



2024年12月24日

项目负责人签字（签章）：

李峰

2024年12月24日

课题承担单位（乙方）：

法定代表人签字（签章）：

薛红已



2024年12月24日

课题负责人签字（签章）：

魏国强

2024年12月24日





|        |                    |
|--------|--------------------|
| 项目批准号  | 52276191           |
| 申请代码   | E0607              |
| 归口管理部门 |                    |
| 依托单位代码 | 51064208A0499-0932 |



522761911004595

# 国家自然科学基金 资助项目计划书 (预算制项目)

资助类别: 面上项目

亚类说明:

附注说明:

项目名称: 碱木质素化学链氧化偶联自催化制备低碳烯烃基础研究

直接费用: 54万元 执行年限: 2023.01-2026.12

负责人: 魏国强

通讯地址: 广东省广州市天河区五山街道五山路483号

邮政编码: 510642 电 话: 020-87057716

电子邮件: weigq@scau.edu.cn

依托单位: 华南农业大学

联系人: 唐家林 电 话: 020-85280070

填表日期: 2022年09月15日

国家自然科学基金委员会制



## 项目组主要成员

| 编号  | 姓名  | 出生年月    | 性别 | 职称    | 学位 | 单位名称           | 电话            | 证件号码               | 项目分工    | 每年工作时间（月） |     |  |     |  |
|-----|-----|---------|----|-------|----|----------------|---------------|--------------------|---------|-----------|-----|--|-----|--|
| 1   | 魏国强 | 1981.09 | 男  | 副研究员  | 博士 | 华南农业大学         | 020-87057716  | 130182198109134818 | 项目负责人   | 8         |     |  |     |  |
| 2   | 邓丽芳 | 1982.11 | 女  | 副研究员  | 博士 | 华南农业大学         | 020-87013240  | 431022198211203429 | 化学链气化研究 | 6         |     |  |     |  |
| 3   | 吴鹏飞 | 1991.04 | 男  | 助理研究员 | 博士 | 中国科学院大连化学物理研究所 | 0411-84379866 | 210102199104223451 | 催化偶联制烯烃 | 6         |     |  |     |  |
| 4   | 毕桂灿 | 1983.11 | 男  | 实验师   | 博士 | 华南农业大学         | 13826012528   | 440182198311221213 | 实验研究    | 6         |     |  |     |  |
| 总人数 |     |         | 高级 |       | 中级 |                | 初级            |                    | 博士后     |           | 博士生 |  | 硕士生 |  |
| 10  |     |         | 2  |       | 2  |                | 0             |                    | 0       |           | 3   |  | 3   |  |





|        |                    |
|--------|--------------------|
| 项目批准号  | 51976226           |
| 申请代码   | E060702            |
| 归口管理部门 |                    |
| 依托单位代码 | 51064008B1273-2371 |



# 国家自然科学基金委员会 资助项目计划书

资助类别：面上项目

亚类说明：

附注说明：常规面上项目

项目名称：碱木质素强化煤焦粉化学链气化过程中碱金属的迁移与催化作用机制

直接费用：63万元      执行年限：2020.01-2023.12

负责人：魏国强

通讯地址：广州市天河区五山能源路2号生物质大楼403

邮政编码：510640      电      话：020-87057716

电子邮件：weigq@ms.giec.ac.cn

依托单位：中国科学院广州能源研究所

联系人：汪丛伟      电      话：020-87057632

填表日期：2019年09月03日

国家自然科学基金委员会制





简表

|        |                |                                |     |   |      |                       |     |               |
|--------|----------------|--------------------------------|-----|---|------|-----------------------|-----|---------------|
| 申请者信息  | 姓 名            | 魏国强                            | 性 别 | 男 | 出生年月 | 1981年09月              | 民 族 | 汉族            |
|        | 学 位            | 硕士                             |     |   | 职称   | 助理研究员                 |     |               |
|        | 是否在站博士后        | 否                              |     |   | 电子邮件 | weigq@ms.giec.ac.cn   |     |               |
|        | 电 话            | 020-87057716                   |     |   | 个人网页 |                       |     |               |
|        | 工 作 单 位        | 中国科学院广州能源研究所                   |     |   |      |                       |     |               |
|        | 所 在 院 系 所      | 废弃物处理与资源化利用研究室                 |     |   |      |                       |     |               |
| 依托单位信息 | 名 称            | 中国科学院广州能源研究所                   |     |   |      |                       | 代码  | 51064008B1273 |
|        | 联 系 人          | 汪丛伟                            |     |   | 电子邮件 | wangcw@ms.giec.ac.cn  |     |               |
|        | 电 话            | 020-87057632                   |     |   | 网站地址 | http://www.giec.ac.cn |     |               |
| 合作单位信息 | 单 位 名 称        |                                |     |   |      |                       |     |               |
|        | 中国科学院山西煤炭化学研究所 |                                |     |   |      |                       |     |               |
| 项目基本信息 | 项 目 名 称        | 碱木质素强化煤焦粉化学链气化过程中碱金属的迁移与催化作用机制 |     |   |      |                       |     |               |
|        | 资 助 类 别        | 面上项目                           |     |   |      | 亚 类 说 明               |     |               |
|        | 附 注 说 明        | 常规面上项目                         |     |   |      |                       |     |               |
|        | 申 请 代 码        | E060702:生物质能                   |     |   |      | E060404:煤与其他固体燃料的燃烧   |     |               |
|        | 基 地 类 别        | 可再生能源与天然气水合物实验室                |     |   |      |                       |     |               |
|        | 执 行 年 限        | 2020.01-2023.12                |     |   |      |                       |     |               |
|        | 直 接 费 用        | 63万元                           |     |   |      |                       |     |               |

## 国家自然科学基金 资助项目准予结题通知

魏国强 同志：

您承担的国家自然科学基金项目：（碱木质素强化煤焦粉化学链气化过程中碱金属的迁移与催化作用机制），批准号：（51976226）按有关规定已审核完毕，准予结题。

与本项目资助有关的后续成果，请您继续及时报送。

祝您在研究工作中取得更好的成绩！

国家自然科学基金委员会

工程与材料科学部

2024年3月26日

——原始邮件——

发件人:工程热物理与能源利用学科 <[ete@nsfc.gov.cn](mailto:ete@nsfc.gov.cn)>

发送时间:2024-12-25 11:20:16 (星期三)

收件人: [weig@scau.edu.cn](mailto:weig@scau.edu.cn)

抄送:

主题: 2024年工程热物理与能源利用学科国家自然科学基金项目结题综合评价结果

国家自然科学基金面上项目负责人:

2024年10月-12月,工程热物理与能源利用学科分领域组织了基金项目进展交流会。对2023年底结题和执行到中期的所有E06申请代码下的面上项目、青年科学基金项目 and 地区科学基金项目实现了全覆盖。

根据参会项目负责人的评议结果,您负责的基金项目“碱木质素强化煤焦粉化学链气化过程中碱金属的迁移与催化作用机制”,(项目批准号:51976226)综合评价等级为:优秀。

期待您未来在基础研究方面取得更多更大的突破和成果!

---

国家自然科学基金委员会

工程热物理与能源利用学科

电话:010-62327131



## 中国科学院洁净能源创新研究院-榆林学院 联合基金项目计划书

项目名称:

碱木质素强化煤焦粉化学链气化制备高品质合成  
气关键问题研究

项目负责人:

魏国强

所在单位:

中国科学院广州能源研究所

手机和 E-mail:

13580396927; weigq@ms.giec.ac.cn

合作研究单位 1:

榆林学院

手机和 E-mail:

13720697676; ylyanlong@126.com

合作研究单位 2:

武汉工程大学

手机和 E-mail:

15103400721; yiqun@tyut.edu.cn

填报时间:

2021 年 06 月 03 日

中国科学院洁净能源创新研究院-榆林学院  
二〇二一年制

## 一、项目简表

|                       |                 |   |      |                     |      |            |              |      |
|-----------------------|-----------------|---|------|---------------------|------|------------|--------------|------|
| 项目基本信息                | 项目名称            | 碱木质素强化煤焦粉化学链气化制备高品质合成气关键问题研究  |      |                     |      |            |              |      |
|                       | 摘要<br>(限 400 字) | 榆林资源优势突出, 炼焦及沙柳造纸业发达, 但工业副产物煤焦粉及碱木质素尚未充分利用, 存在环境风险。常规煤焦粉利用方式存在条件苛刻、转化率低、催化剂易失活的问题。本研究从榆林地区工业副产物煤焦粉及碱木质素协同资源化利用角度出发, 提出采用碱木质素作为可弃型催化剂, 通过强化化学链气化的方式来处理煤焦粉, 突破常规反应动力学限制, 改善氧载体晶格结构及离子传递, 获取高品质合成气。研究过程中聚焦高性能氧载体设计构筑理论与碱金属催化强化反应机理, 解析流化床多相反应体系质能传递协同匹配与优化规律, 构建多相反应历程定向调控机制, 实现燃料 C/H/O 元素向 CO/H <sub>2</sub> 转化, 获取高品质合成气。该反应过程具有氧源廉价、烟损低、反应高效、无需型煤的优点, 还避免了常规碱金属催化剂易失活、难以循环利用的问题, 有望开辟工业副产物协同资源化利用新途径, 具有较好的应用前景。 |      |                     |      |            |              |      |
|                       | 中文关键词           | 化学链气化; 氧载体; 沙柳; 煤焦粉; 碱木质素   |      |                     |      |            |              |      |
|                       | 所属领域            | <input type="checkbox"/> 环保废物处理 <input type="checkbox"/> 新能源技术<br><input type="checkbox"/> 能源化工 <input checked="" type="checkbox"/> 生物质转化   |      |                     |      |            |              |      |
|                       | 研究期限            | 2021 年 7 月 至 2023 年 6 月   |      |                     |      | 资助金额       | 100 (万元)     |      |
|                       | 资助经费分配方案        | 申请单位经费<br>中国科学院广州能源研究所  |      | 40 (万元)             |      |            |              |      |
|                       |                 | 合作研究单位 1 经费<br>榆林学院   |      | 30 (万元)             |      |            |              |      |
| 合作研究单位 2 经费<br>武汉工程大学 |                 | 30 (万元)   |      |                     |      |            |              |      |
| 项目负责人信息               | 姓名              | 魏国强   | 性别   | 男                   | 出生年月 | 1981.09    | 职称           | 副研究员 |
|                       | 手机              | 13580396927   | 电子邮件 | weigq@ms.giec.ac.cn |      | 单位<br>(全称) | 中国科学院广州能源研究所 |      |
| 合作研究单位 1 负责人信息        | 姓名              | 闫龙  | 性别   | 男                   | 出生年月 | 1980.05    | 职称           | 教授   |
|                       | 手机              | 13720697676   | 电子邮件 | ylyanlong@126.com   |      | 单位<br>(全称) | 榆林学院         |      |
| 合作研究单位 2 负责人信息        | 姓名              | 易群  | 性别   | 男                   | 出生年月 | 1985.09    | 职称           | 教授   |
|                       | 手机              | 15103400721   | 电子邮件 | yiqun@tyut.edu.cn   |      | 单位<br>(全称) | 武汉工程大学       |      |



## 七、项目负责人承诺签字及所在单位资格审查

本人郑重承诺：我保证本报告内容的真实性。我将履行项目负责人职责，严格遵守国家相关法律法规、中科院及榆林学院的相关规定和《中国科学院洁净能源创新研究院-榆林学院联合基金管理实施细则（试行）》，我承诺在项目执行过程中，尊重科研规律，弘扬科学家精神，严谨求实，追求卓越；遵守科研伦理道德和作风学风诚信要求，切实保证研究工作时间，认真开展科学研究工作；严格遵守本项目经费管理实施细则，项目经费严格按照规定的开支范围全部用于与项目研究工作相关的支出，厉行勤俭节约，不用于与科学研究无关的支出，不截留、挪用、侵占项目经费；项目结题时，同意在单位内部公开项目经费决算和项目结题/成果报告，接受监督；按时报送有关材料。若填报失实和违反规定及违背上述承诺，本人将承担全部责任，愿意接受中国科学院洁净能源创新研究院-榆林学院联合基金管理办公室做出的各项处理决定。

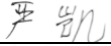

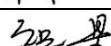
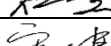
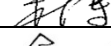
项目负责人（签字） 魏国强 2021年 7月 2日

已对该项目负责人的资格和计划书内容进行了审核。我单位保证对项目研究提供或创造一切必要的条件，严格遵守国家相关法律法规、中科院及榆林学院的相关规定和《中国科学院洁净能源创新研究院-榆林学院联合基金管理实施细则（试行）》，督促项目负责人和项目组成员以及本单位科研管理部门遵守相关规定并及时报送有关材料，确保各项经费开支按照规定专项用于合作基金项目。

申请单位(公章)

年 月 日

### 验收意见

|        |   |       |   |
|--------|---|-------|---|
| 项目类别   | 中科院洁净能源创新研究院-榆林学院联合基金   | 编号    | YLU-DNL Fund 2021021  |
| 项目名称   | 碱木质素强化煤焦粉化学链气化制备高品质合成气关键问题研究  | 项目负责人 | 魏国强   |
| 项目牵头单位 | 中国科学院广州能源研究所  | 时间    | 2023.09.13  |
| 专家组意见  | <p>由中国科学院广州能源研究所牵头，榆林学院、武汉工程大学共同承担的中国科学院洁净能源创新研究院-榆林学院联合基金项目“碱木质素强化煤焦粉化学链气化制备高品质合成气关键问题研究”，项目编号 YLU-DNL Fund 2021021，进行了项目结题验收绩效评价。专家组听取了项目组汇报，查阅了相关材料，进行了质询与讨论，形成意见如下：</p> <ol style="list-style-type: none"> <li>1. 本项目从榆林地区工业副产物煤焦粉及碱木质素协同资源化利用角度出发，采用碱木质素作为可弃型催化剂，开发了高性能载氧体，构建了碱木质素强化煤焦粉化学链气化反应体系，改善了载氧体晶格氧传递，获取了高品质合成气，完成了考核指标，达到预期目标，为解决煤焦粉/碱木质素高效回收利用技术难题提了支撑。</li> <li>2. 本项目构建了 Fe/Ni 基高活性复合载氧体，解析了晶格氧传递机理，构建了碱金属强化化学链反应体系，制备合成气有效组成超过 84%。进一步构建了化学链气化-高值化利用新系统：焦炉煤气和焦粉耦合化学链制氢联产甲醇和氨系统（PCCLHG-CGTMA），比传统煤气化-高值化系统能效提高 14.1~18.7%。</li> <li>3. 本项目发表 SCI 收录论文 22 篇，申请 PCT 专利 1 项，中国发明 3 项，培养研究生 6 名，参加高水平学术会议 4 次。</li> <li>4. 项目组织管理规范，经费使用合理。</li> <li>5. 建议加快成果在榆林及其他地区转化与技术推广工作。</li> </ol> |       |   |
| 综合验收意见 | <input checked="" type="checkbox"/> 通过<br><input type="checkbox"/> 不通过  |       |   |
| 专家签认   | 工作单位  | 职称/职务 | 专家确认  |
| 严凯     | 中山大学  | 教授    |  |
| 杜朕屹    | 太原理工大学  | 教授    |  |
| 祝星     | 昆明理工大学  | 教授    |  |
| 宋涛     | 南京师范大学  | 教授    |  |
| 余昭胜    | 华南理工大学  | 副教授   |  |

牵头单位意见

同意

负责人（签字）：魏国强 单位（盖章）：



2023年09月25日

合作单位意见

同意  
负责人（签字）：杨群



2023年09月25日

关于国家重点研发计划“循环经济关键技术与装备”重点专项

“8.1 种养产业集聚区多源种养废物耦合利用集成技术及示范

（应用示范类）”组织实施协议

甲方：中山大学

法定地址：广东省广州市海珠区新港西路 135 号

乙方：华南农业大学

法定地址：广东省广州市天河区五山路 483 号

依据《中华人民共和国科技进步法》、《中华人民共和国民法典》、《中华人民共和国著作权法》、《中华人民共和国专利法》、《中华人民共和国促进科技成果转化法》、《关于改进加强中央财科研政项目和资金管理若干的意见》等法律和管理办法，经甲、乙双方协商一致，为按时高质量完成双方联合承担的国家重点专项“8.1 种养产业集聚区多源种养废物耦合利用集成技术及示范（应用示范类）”（项目编号：2023YFC3905800）之课题 4. 沼渣及种养废物协同热解制备矿区土壤生态修复材料及装备，经过平等协商，在真实、充分地表达各自意愿的基础上，达成如下协议。由签约双方共同遵守。

一、甲、乙双方承诺按课题要求，团结协作，按期，保质完成课题各阶段任务。

为本课题研究工作做出贡献。

二、甲方的责任：

1. 甲方为本课题牵头单位，负责本课题的组织与实施，为乙方完成本课题任务提供必要的支持。
2. 根据科技部的相关管理办法及政策，为保证整个课题的成功实施，甲方对乙方科研活动，完成任务的进度情况等负有监督和建议的责任。

三、乙方的责任：

1. 乙方承诺按照课题要求配备满足要求的资源，确保按要求完成研究任务和目标。
2. 乙方采取的研究方法，技术路线。实施进度等应按照国家科技部审批的课题任务书执行。

3. 乙方按课题任务书要求完成自己所承担课题主要考核指标(包括示范工程,应达到的主要技术指标,应发表的论文、获得的发明专利等知识产权,以及其他应考核的指标)。
4. 乙方应提供有关资料,并积极配合甲方完成本课题的年度报告、中期检查、课题结题验收、审计等各项工作。
5. 乙方承诺与甲方及其他参与课题工作的单位密切合作,相互支持,在课题工作中接受甲方的统一安排和协调。乙方相关工作出现于课题规定不相符情况下,乙方承诺按规定接受科技部管理部门、专家、甲方、审计部门等相关部门的要求,改进工作,并承担相关责任。

#### 四、经费与财务

甲乙双方按照科技部批准的任务书、经费预算书进行经费(包括国拨经费和配套经费)的管理、分配和使用,并遵照国家科研项目资金管理规定建立相应的财务管理制度。乙方必须根据任务分工和课题任务书约定,将获得的经费全部用于所承担的课题研发工作。双方承诺无条件接受科技部项目或课题管理方要求的财务审计,并根据审计要求进行整改,直至符合国家相关规定。双方预算如下(金额单位:万元):

| 序号 | 预算科目名称    | 华南农业大学 |
|----|-----------|--------|
| 1  | 一、经费支出    | 60.00  |
| 2  | (一) 直接费用  | 47.31  |
| 3  | 1、设备费     | 8.00   |
| 4  | 其中: 设备购置费 | 5.00   |
| 5  | 2、业务费     | 31.31  |
| 6  | 3、劳务费     | 8.00   |
| 7  | (二) 间接费用  | 12.69  |
| 8  | 二、其他来源资金  | 0      |
| 9  | 三、合计      | 60.00  |

五、双方本着相互合作的精神,在课题执行过程中涉及的知识产权按以下方式处理:

1. 双方在执行本课题之前各自所获得的知识产权及相关权益均归各自所有,



十、附表

表 1 乙方具体任务、成果指标、负责人及经费表

| 课题名称   | 任务内容                              | 成果指标  | 负责人 | 国拨经费<br>(万元) | 自筹经费<br>(万元) |
|--|-----------------------------------|---|-----|--------------|--------------|
| 课题 4. 沼渣<br>及种养废物协<br>同热解制备矿<br>区土壤生态修<br>复材料及装备 | 任务四: 多孔<br>炭复配功能<br>菌制生物有<br>机肥工艺 | 生物有机肥 1 种, 生<br>产装备 1 套; 申请专<br>利 $\geq 1$ 件, 培养研究<br>生 $\geq 1$ 名。 | 魏国强 | 60.0         | 0            |

甲方(公章):

法定代表人(签章):

课题负责人签字:

日期: 2023.11.22

乙方(公章):

法定代表人(签章):

课题参与人签字:

日期: 2023.11.17

受理编号: c232019102500000087

项目编号: 2023B1515120062

文件编号: 粤基金字(2024)4号

## 广东省基础与应用基础研究基金项目 任务书

项目名称: 天然气化学链制氢耦合燃料电池高效发电新技术应用基础研究

项目类别: 区域联合基金-重点项目

项目起止时间: 2023-11-01 至 2026-10-31

管理单位(甲方): 广东省基础与应用基础研究基金委员会

依托单位(乙方): 中国科学院广州能源研究所

通讯地址: 广东省广州市天河区广东省广州市天河区五山能源路2号

邮政编码: 510640

单位电话: 020-37029825

项目负责人: 黄振

联系电话: 020-87057716



(广东科技微信公众号)



(查看任务书信息)



(受理纸质材料二维码)

广东省基础与应用基础研究  
基金委员会  
二〇二〇年制

## 六、工作分工及财政经费分配

| 承担/参与单位名称<br>(盖章) | 工作分工                                   | 省级财政科技资金分配<br>(万元) |
|-------------------|--|--------------------|
| 中国科学院广州能源研究所      | 开展多功能复合载氧体的设计理论方法、<br>天然气化学链重整反应基础理论研究 | 40.00              |
| 华南农业大学            | 负责开展化学链制氢变换过程调控规律研<br>究工作              | 35.00              |
| 东莞理工学院            | 开展燃料电池电化学特性及耦合系统集成<br>优化研究             | 25.00              |
|                   | 合计                                     | 100.00             |



# 广东省基础与应用基础研究基金 区域联合基金项目合作协议

项目名称：天然气化学链制氢耦合燃料电池高效发电新技术  
应用基础研究

项目主持单位（甲方）：中国科学院广州能源研究所

项目负责人：黄振

联系方式：13265006815

项目参与单位（乙方）：华南农业大学

项目负责人：魏国强

联系方式：13580396927

项目参与单位（丙方）：东莞理工学院

项目负责人：康世民

联系方式：13433630966

2023 年 9 月

具体研发进度如下：

①本合同生效两周内，进行试验研究前期准备工作；

②乙方、丙方收到研究经费算起 2 个月内，提出实验方案并开展研究工作；

③12 个月内，乙方、丙方按总项目中期考核要求，完成相应中期考核目标，提交中期考核成果；

④依据项目的具体年度研究计划完成该合同签署的委托研究内容，进行分析总结。

3.三方通过紧密合作，各展所长，推动广东省氢能产业发展升级研发；通过技术共享，促进各自研究水平与研究手段的提升；双方共同指导博士生、硕士生，实现异地交流，拓展研究视野，更好地以本项目为依托完成博士和硕士论文。

## 二、项目经费分配

合作双方就该项目的国拨专项经费分配比例金额如下：

| 项目单位名称       | 负责人 | 国拨专项经费分配比例 |
|--------------|-----|------------|
|              |     | 经费总额       |
| 中国科学院广州能源研究所 | 黄振  | 40%        |
| 华南农业大学       | 魏国强 | 35%        |
| 东莞理工学院       | 康世民 | 25%        |

具体拨付方式和时间如下：

项目主持单位在收到资金拨付后 90 日内给参与单位拨付。

参与单位（乙方）开户银行名称、地址和帐号为：

单位名称： 华南农业大学

开户银行： 中国工商银行广州五山支行

地 址： 广州市天河区五山路 483 号

帐 号： 3602-0026-0900-0310-520

税务登记号： 1244-0000-4554-1656-34

参与单位（丙方）开户银行名称、地址和帐号为：



2.合作三方确定，执行合同中如遇不可抗力和技术风险等因素导致协议不能继续履行时，应及时通知其他两方以将损失控制在最小的范围并共同协商变更或解除本协议。

3.除上述情形外，任何一方欲变更、解除本协议，应该 30 日前书面通知其他两方，由签约三方协商一致后，签署书面文件，报送项目主管部门进行处理。

## 五、项目违约责任

三方确定：任何一方违反本合同约定，造成研究开发工作停滞、延误或失败的，按约定承担违约责任；三方因履行本合同而发生的争议，应协商、调解解决。协商、调解不成的，提交仲裁委员会仲裁。

## 六、其他

1.本合同自三方签字盖章后生效。对本合同任何条款的修改、补充或更改，需三方签订书面协议并签字盖章后方可生效。

2.本合同正本一式九份，双方各持三份，各份具有同等法律效力。

3.本合同未尽事宜，按所属科技计划合同和国家颁布的相关管理办法执行。

项目主持单位（甲方盖章）



项目负责人（签章）：

李永

2023年 9 月 15 日

项目参与单位（丙方盖章）



项目负责人（签章）：

傅世

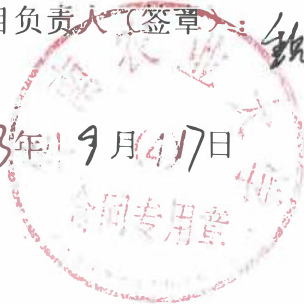
2023年 9 月 12 日

项目参与单位（乙方盖章）

项目负责人（签章）：

张国强

2023年 9 月 17 日



任务书编号：E229kf0501

密级：公开

中国科学院可再生能源重点实验室

## 开放基金项目任务书

项目名称：富氮木质废弃物化学链气化制备高品质合成气  
基础研究

项目负责人：魏国强

所在单位：华南农业大学

通讯地址：广州市天河区五山街道五山路 483 号

邮政编码：510642

联系电话及电子邮件：13580396927/weigq@scau.edu.cn

起止年限：2022 年 09 月至 2024 年 08 月

中国科学院广州能源研究所

二〇一〇年十二月

# 五、项目的经费预算

单位：万元

| 经费来源预算      |      | 经费支出预算   |      |
|-------------|------|----------|------|
| 科 目         | 预算数  | 科 目      | 预算数  |
| 来源预算合计      | 3.00 | 支出预算合计   | 3.00 |
| 一、重点实验室开放基金 |      | 一、人员费    | 1.00 |
|             |      | 其中：项目负责人 | 0.50 |
|             |      | 主要研究人员   | 0.50 |
|             |      | 二、设备费    | 0.00 |
|             |      | 1、购置费    | 0.00 |
|             |      | 2、试制费    | 0.00 |
|             |      | 三、相关业务费  | 2.00 |
|             |      | 1、材料费    | 1.00 |
|             |      | 2、燃料及动力费 | 0.00 |
|             |      | 3、测试及化验费 | 0.50 |
|             |      | 4、会议差旅费  | 0.50 |
|             |      | 四、其他费用   |      |
|             |      |          |      |
|             |      |          |      |
|             |      |          |      |

## 六、任务书签订各方意见

项目组织单位（甲方）

负责人（签字）



财务负责人（签字）

刘丽敏

项目负责人所在单位（乙方）

（公 章）

单位负责人（签字）



项目负责人（签字）

魏国强

2022 年 9 月 16 日

中国科学院广州能源研究所审定意见

负责人（签字）



受理编号: c22140500000660

项目编号: 2022A1515010941

文件编号: 粤基金字(2022)3号

## 广东省基础与应用基础研究基金项目 任务书

项目名称: 杂原子原位负载生物炭的制备及其催化N<sub>2</sub>电化学还原机理研究

项目类别: 广东省自然科学基金-面上项目

项目起止时间: 2022-01-01 至 2024-12-31

管理单位(甲方): 广东省基础与应用基础研究基金委员会

依托单位(乙方): 华南农业大学

通讯地址: 广东省广州市天河区五山路483号

邮政编码: 510642

单位电话: 020-85283435

项目负责人: 邓丽芳

联系电话: 020-87013240



(广东科技微信公众号)



(查看任务书信息)



(受理纸质材料二维码)

广东省基础与应用基础研究  
基金委员会  
二〇二〇年制



## 五、人员信息

| 项目负责人 |                    |    |    |      |       |           |        |     |
|-------|--------------------|----|----|------|-------|-----------|--------|-----|
| 姓名    | 证件号码               | 年龄 | 性别 | 职称   | 学历    | 在项目中承担的任务 | 所在单位   | 签名  |
| 邓丽芳   | 431022198211203429 | 40 | 女  | 副研究员 | 博士研究生 | 项目负责人     | 华南农业大学 | 邓丽芳 |

| 项目组主要成员 |                    |    |    |      |       |           |        |     |
|---------|--------------------|----|----|------|-------|-----------|--------|-----|
| 姓名      | 证件号码               | 年龄 | 性别 | 职称   | 学历    | 在项目中承担的任务 | 所在单位   | 签名  |
| 魏国强     | 130182198109134818 | 41 | 男  | 副研究员 | 博士研究生 | 生物炭调制     | 华南农业大学 | 魏国强 |
| 钟家伟     | 44138119880604471X | 34 | 男  | 副研究员 | 博士研究生 | 催化机理研究    | 华南农业大学 | 钟家伟 |
| 韩冰      | 211011199704285519 | 25 | 男  | 未取得  | 本科    | 样品采集及制备   | 华南农业大学 | 韩冰  |
| 张止戈     | 420204199404144912 | 28 | 男  | 未取得  | 本科    | 产物检测      | 华南农业大学 | 张止戈 |

## 六、工作分工及经费分配

| 承担/参与单位名称<br>(盖章) | 工作分工        | 总经费分摊<br>(万元) | 省基金委经费分配<br>(万元) |
|-------------------|-------------|---------------|------------------|
| 华南农业大学            | 负责整个项目的具体实施 | 10.00         | 10.00            |
|                   | 合计          | 10.00         | 10.00            |

## 八、本任务书签约各方

管理单位（甲方）：

广东省基础与应用基础研究基金委员会（盖章）



法定代表人（或法人代理）：

曾路

（签章）

2022 年 04 月 21 日

依托单位（乙方）： 华南农业大学

（盖章）

法定代表人（或法人代理）： 刘雅红



（签章）

联系人（项目主管）姓名： 倪慧群

（签章）

Email: kjcgxk@scau.edu.cn

电话： 020-85283435 / 15920301530

开户单位名称： 华南农业大学

开户银行名称： 广东广州工行五山支行

开户银行帐号： 3602002609000310520

2022 年 4 月 24 日

联系人（项目负责人）姓名： 邓丽芳

（签名）

邓丽芳

Email: denglf@scau.edu.cn

电话： 020-87013240

2022 年 4 月 22 日

## 检索证明

根据委托人提供的论文材料，委托人华南农业大学生物质工程研究院 魏国强 7 篇论文收录情况如下表。

| 序号 | 论文名称  | 发表刊物及发表的年月卷期/页码等  | 作者排名   | 论文等级 | 作者文中单位       | 收录情况 | 影响因子                                       | 中科院大类分区                         |
|----|---|---|--------|------|--------------|------|--|---------------------------------|
| 1  | Reaction kinetics and mechanisms for carbon-negative chemical looping gasification of biomass coupled with CO <sub>2</sub> splitting                              | INDUSTRIAL CROPS AND PRODUCTS<br>出版年: 2024<br>出版日期: DEC 15<br>卷期: 222 页码: -<br>文献号: 120083<br>文献类型: Article | 第一作者   | T2 类 | 华南农业大学       | SCI  | IF2-year=6.2<br>IF5-year=6.2<br>(2024)     | 农林科学 1 区<br>Top 期刊: 是<br>(2025) |
| 2  | Reaction performance of Ce-enhanced hematite oxygen carrier in chemical looping reforming of biomass pyrolyzed gas coupled with CO <sub>2</sub> splitting         | ENERGY<br>出版年: 2021<br>出版日期: JAN 15<br>卷期: 215 页码: -<br>文献号: 119044<br>文献类型: Article                        | 第一作者   | T2 类 | 中国科学院广州能源研究所 | SCI  | IF2-year=8.857<br>IF5-year=8.234<br>(2021) | 工程技术 1 区<br>Top 期刊: 是<br>(2021) |
| 3  | In-situ removal of toluene as a biomass tar model compound using NiFe <sub>2</sub> O <sub>4</sub> for application in chemical looping gasification oxygen carrier | ENERGY<br>出版年: 2020<br>出版日期: JAN 1<br>卷期: 190 页码: -<br>文献号: 116360  | 共同通讯作者 | T2 类 | 中国科学院广州能源研究所 | SCI  | IF2-year=7.147<br>IF5-year=6.845<br>(2020) | 工程技术 1 区<br>Top 期刊: 是<br>(2020) |

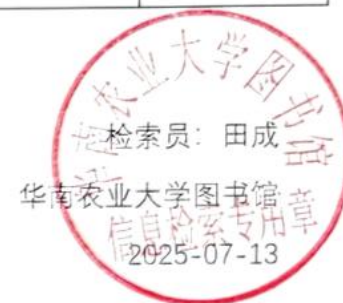
|   |   |  |      |     |              |      |  |                                 |
|---|---|--|------|-----|--------------|------|--|---------------------------------|
|   |   | 文献类型: Article  |      |     |              |      |  |                                 |
| 4 | Enhanced chemical looping gasification of biomass coupled with CO2 splitting based on carbon negative emission          | ENERGY CONVERSION AND MANAGEMENT<br>出版年: 2022<br>出版日期: MAY 15<br>卷期: 260 页码: -<br>文献号: 115597<br>文献类型: Article | 第一作者 | T2类 | 华南农业大学       | SCI  | IF2-year=10.4<br>IF5-year=10.3<br>(2022)   | 工程技术 1 区<br>Top 期刊: 是<br>(2022) |
| 5 | Ca-enhanced hematite oxygen carriers for chemical looping reforming of biomass pyrolyzed gas coupled with CO2 splitting | FUEL<br>出版年: 2021<br>出版日期: FEB 1<br>卷期: 285 页码: -<br>文献号: 119125<br>文献类型: Article                              | 第一作者 | T2类 | 中国科学院广州能源研究所 | SCI  | IF2-year=8.035<br>IF5-year=7.621<br>(2021) | 工程技术 1 区<br>Top 期刊: 是<br>(2021) |
| 6 | 涉农高校生物质能源领域传热学课程教学改革研究  | 安徽农学通报<br>出版年: 2024<br>出版日期: 2024.12<br>卷期: 30 24 页码: -<br>文献号:<br>文献类型:                                       | 第一作者 |     | 华南农业大学       | CNKI | 无  | 无                               |



|   |  |   |               |      |              |     |  |                                 |
|---|--|---|---------------|------|--------------|-----|--|---------------------------------|
| 7 | Reducing emission of NOx and SOx precursors while enhancing char production from pyrolysis of sewage sludge by torrefaction pretreatment | ENERGY<br>出版年: 2020<br>出版日期: FEB 1<br>卷期: 192 页码: -<br>文献号: 116620<br>文献类型: Article | 共同通讯作者 (倒数第一) | T2 类 | 中国科学院广州能源研究所 | SCI | IF2-year=7.147<br>IF5-year=6.845<br>(2020) | 工程技术 1 区<br>Top 期刊: 是<br>(2020) |
|---|--|---|---------------|------|--------------|-----|--|---------------------------------|

说明: 论文等级和中科院大类分区按《华南农业大学学术论文评价方案(试行)》划分。

报告免责声明: 如未盖章, 报告无效



# INDUSTRIAL CROPS AND PRODUCTS

VOLUME 222P5

15 December 2024

## Contents

Abstracted/indexed in: Agricola; CAB Abstracts; CABS; Chemical Abstracts; Current Contents; AB & ES; EMBASE; Embiology Elsevier BIOBASE/Current Awareness in Biological Sciences; Elsevier/Geobase; Environmental Abstracts. Also covered in the abstract and citation database SCOPUS®. Full text available on ScienceDirect®

### Fats and oils

Recyclable polyurethane from castor oil based on dynamic disulfide bonds and multiple hydrogen bonds as adhesive and photothermal conversion materials  
*Y. Fang, Q. Li, Z. Kou, Y. Ma, M. Zhang, Y. Hu, P. Jia and Y. Zhou (China)*

120027

Assessment of seed and biochemical traits in neem germplasm for sustainable agriculture and industrial applications  
*R. Garg, A. Bhatt, A. Kumar, Y.C. Tripathi and R. Kant (India)*

120018

Improving the performance of lipases in the full hydrolysis of residual coconut oil by immobilization on hydrophobic supports

*R.R.C. Monteiro, F.M.T. de Luna, D. Lomonaco (Brazil), R. Fernandez-Lafuente (Spain) and R.S. Vieira (Brazil)*

120014

Uncovering key genes associated with protein and oil in soybeans based on transcriptomics and proteomics

*W. Mo, P. Wang, Q. Shi, X. Zhao, X. Zheng, L. Ji, L. Zhang, M. Geng, Y. Wang, R. Wang, M. Bian, X. Meng, Z. Zuo and Z. Yang (China)*

119981

Impact of microwave pretreatment on yield, quality and lipid composition of *Acer truncatum* Bunge seed oil  
*L. Wu, X. Shen, W. Xue, Q. Chen, W. Hu, Q. Yang and H. Pang (China)*

120086

Genomic region linked to gray mold resistance in castor (*Ricinus communis* L.)

*S. Senthilvel, R.D. Prasad, R. Sathishkumar, M. Shaik and M.D. Mohanrao (India)*

120080

Chemical ingredient variation relation to climatic factors of cold-pressed rapeseed oil in the Yangtze River Basin  
*N. Ning, A. Rasool, M. Qin, J. Mo, H. Lou, Z. Wang, Z. Xu, B. Wang, J. Wang, J. Kuai, J. Zhao, C. Jia and G. Zhou (China)*

120063

Tung oil-based modifier strengthening and toughening epoxy resin by sacrificial bond

*K. Zhang, P. Fu, Y. Wang, Q. Chang, W. Yang, Z. You, J. Huang, X. Nie and J. Chen (China)*

120116

(Contents continued on inside back cover)

Available online at [www.sciencedirect.com](http://www.sciencedirect.com)

ScienceDirect

Have you visited the journal's website recently? New FREE Online Features:  
Tables of Contents NOW WITH ABSTRACTS. Full Search on Abstracts, Authors and Keywords, Author and Subject Index  
Visit the Industrial Crops and Products website today! Bookmark: <http://www.elsevier.com/locate/indcrop>



0926-6690(20241215)222:1P5;1-2



Volume 222P5, 15 December 2024

ISSN 0926-6690

# INDUSTRIAL CROPS AND PRODUCTS

AN INTERNATIONAL JOURNAL



## Aims and Scope

*Industrial Crops and Products*, an *International Journal*, publishes papers reporting the results of original research, short communications and critical reviews on all aspects of industrial crops and products.

This covers a wide range of aspects of cultivation, crop improvement, crop compounds, processing and integrated chain control, all focusing on the exploitation of agricultural crops for industrial use.

The scope of the journal covers a vast range of crops and research disciplines. Crops should contain significant renewable resources such as:

- fibres and fibre compounds;
- carbohydrates;
- oils and fatty acids;
- waxes, resins, gums, rubber and other polymers;
- proteins;
- essential oils for ink, lubricants, plastics, cosmetics;
- biologically active compounds for pharmaceuticals, herbicides and insecticides, and preservatives.

Examples of new or potential crops are agave, cassava, crambe, cuphea, elephant grass, fibre hemp, flax, guar, guayule, jojoba, kenaf, lesquerella, maize, meadowfoam, oil palm, peas, plantago, potato, pyrethrum, rape seed, safflower, soybean, Stokes aster, sugar beet, sunflower, veronia and wheat. Papers within the above indicated frame-work will be accepted if they cover or integrate research on:

- agronomic production and modelling;
- breeding, genetics and biotechnology;
- post-harvest treatment and storage;
- (bio)process technology;
- (bio)chemistry;
- product testing, development and marketing;
- economics, and systems analysis and optimization;
- bioenergy.

**Publication information:** *Industrial Crops and Product* (ISSN 0926-6690). For 2024, volumes 207–222 (16 issues) are scheduled for publication. Subscription prices are available upon request from the Publisher or from the Elsevier Customer Service Department nearest you or from this journal's website (<http://www.elsevier.com/locate/indcrop>). Further information is available on this journal and other Elsevier products through Elsevier's website (<http://www.elsevier.com>). Subscriptions are accepted on a prepaid basis only and are entered on a calendar year basis. Issues are sent by standard mail (surface within Europe, air delivery outside Europe). Priority rates are available upon request. Claims for missing issues should be made within six months of the date of dispatch.

**Submission of manuscripts:** Manuscripts should be submitted online by using the Elsevier Editorial System at [ees.elsevier.com/indcrop](http://ees.elsevier.com/indcrop). Authors will be guided step-by-step through uploading files directly from their computers. Authors should select a set of classifications for their papers from a given list, as well as a category designation (Original Research Paper, Short Communication, and so on). Electronic PDF proof will be automatically generated from uploaded files, and used for subsequent reviewing.

Authors submitting hard copy papers will be asked to resubmit using Elsevier Editorial System.

Submission of an article is understood to imply that the article is original and unpublished and is not being considered for publication elsewhere. Upon acceptance of an article, the author(s) will be asked to transfer the copyright of the article to the publisher. This transfer will ensure the widest possible dissemination of information.

**Language (Usage and Editing services).** Please write your text in good English (American or British usage is accepted, but not a mixture of these). Authors who feel their English language manuscript may require editing to eliminate possible grammatical or spelling errors and to conform to correct scientific English may wish to use the English Language Editing service available from Elsevier's WebShop (<http://webshop.elsevier.com/languageediting>) or visit our customer support site (<http://service.elsevier.com>) for more information.

**Author inquiries:** You can track your submitted article at <http://www.elsevier.com/track-submission>. You can track your accepted article at <http://www.elsevier.com/trackarticle>. You are also welcome to contact Customer Support via <http://service.elsevier.com>

**Orders, claims, and journal inquiries:** Please visit our Support Hub page <https://service.elsevier.com> for assistance.

**Advertising information:** If you are interested in advertising or other commercial opportunities please e-mail [Commercialsales@elsevier.com](mailto:Commercialsales@elsevier.com) and your inquiry will be passed to the correct person who will respond to you within 48 hours.

**Funding body agreements and policies:** Elsevier has established agreements and developed policies to allow authors who publish in Elsevier journals to comply with potential manuscript archiving requirements as specified as conditions of their grant awards. To learn more about existing agreements and policies please visit <http://www.elsevier.com/fundingbodies>.

© 2024 Elsevier B.V.

This journal and the individual contributions contained in it are protected under copyright, and the following terms and conditions apply to their use in addition to the terms of any Creative Commons or other user license that has been applied by the publisher to an individual article:

### Photocopying

Single photocopies of single articles may be made for personal use as allowed by national copyright laws. Permission is not required for photocopying of articles published under the CC BY license nor for photocopying for non-commercial purposes in accordance with any other user license applied by the publisher. Permission of the publisher and payment of a fee is required for all other photocopying, including multiple or systematic copying, copying for advertising or promotional purposes, resale, and all forms of document delivery. Special rates are available for educational institutions that wish to make photocopies for non-profit educational classroom use.

### Derivative Works

Users may reproduce tables of contents or prepare lists of articles including abstracts for internal circulation within their institutions or companies. Other than for articles published under the CC BY license, permission of the publisher is required for resale or distribution outside the subscribing institution or company.

For any subscribed articles or articles published under a CC BY-NC-ND license, permission of the publisher is required for all other derivative works, including compilations and translations.

### Storage or Usage

Except as outlined above or as set out in the relevant user license, no part of this publication may be reproduced, stored in a retrieval system or transmitted in any form or by any means, electronic, mechanical, photocopying, recording or otherwise, without prior written permission of the publisher.

### Permissions

For information on how to seek permission visit [www.elsevier.com/permissions](http://www.elsevier.com/permissions).

### Author rights

Author(s) may have additional rights in their articles as set out in their agreement with the publisher (more information at <http://www.elsevier.com/authorsrights>).

### Notice

Practitioners and researchers must always rely on their own experience and knowledge in evaluating and using any information, methods, compounds or experiments described herein. Because of rapid advances in the medical sciences, in particular, independent verification of diagnoses and drug dosages should be made. To the fullest extent of the law, no responsibility is assumed by the publisher for any injury and/or damage to persons or property as a matter of products liability, negligence or otherwise, or from any use or operation of any methods, products, instructions or ideas contained in the material herein. Although all advertising material is expected to conform to ethical (medical) standards, inclusion in this publication does not constitute a guarantee or endorsement of the quality or value of such product or of the claims made of it by its manufacturer.

© The paper used in this publication meets the requirements of ANSI NISO Z39.48-1992 (Permanence of Paper).

Printed by CPI Antony Rowe, Pegasus Way, Melksham, UK

A full and complete Guide for Authors, can be found on the World Wide Web: access under <http://www.elsevier.com/locate/indcrop>

(Contents continued from outside back cover)

## Non-food bioactive products

Diversity of chemical compounds in lily fragrance and identification of key sensory markers

Y. Zhou, F. Wang, Q. Wang, Y. Chen, J. Dong, Y. Ye, G. Zhu, Y. Fan and Y. Xu (China)

120034

120089

Melatonin-mediated alleviation of drought stress via modulation of physio-biochemical and soil bacterial community structure in *Diospyros lotus* L.

P. Zhang, X. Lyu, Y. Hu, R. Zhou, F. Hao, H. Hu and D. Lang (PR China)

120002

120111

Manipulating flavonoid biosynthesis in *Trigonella persica* through controlled spectral lighting

E. Bakhshy, F. Zarinkamar, B. Mohammad Soltani and M. Nazari (Iran)

120016

120118

Allelopathic characterization and allelochemicals identification of hemp (*Cannabis sativa* L.) leaf residue

T. Poonsawat, N. Srilasak and I. Koodkaew (Thailand)

120003

120140

Corrigendum to "Integrated transcriptomics and metabolomics unravel the molecular mechanisms governing flavonoid synthesis in *Torreya grandis* under low phosphorus stress" [Ind. Crops Prod. 210 (2024) 118080]

Q. Wang, Y. Wang, Q. Xie, L. Wang, W. Dai, C. Yu and J. Wu (China)

120037

120147

Effect of cultivar type, ontogeny and extraction methods as determinant factors of olive leaf metabolome: A case study in 8 Egyptian cultivars as analyzed using LC/MS-based metabolomics

N.M. Fayek, A. Zayed, H.A. Zahran, N.S. Ramadan (Egypt), E. Capanoglu (Türkiye), Z. Li, Y. Fang (China), I. Khalifa (Egypt) and M.A. Farag (Egypt, China)

120085

120023

Integrated metabolome and transcriptome analyses reveal the critical role of alpha-linolenic acid metabolism in *Panax notoginseng* root rot disease

Y. Zhu, M. Li, K. Li, J. Li, X. Liu, S. Yang, F. Wei, Y. Xia and G. Liu (China)

120072

120075

Chemical profiling and bioactivities of common commercial essential oils against larvae and adults of *Tribolium castaneum*: Insecticidal, behavioral, and biochemical effects

H. Annaz (Morocco), A. Gonzalez-Coloma (Spain), M. Moullamri, A. Ajaha, A. Laglaoui, N. Bouayad and K. Rharrahe (Morocco)

120082

120103

Melatonin alleviates drought stress and increases lutein and zeaxanthin industrial pigments in African marigold by some physiological regulations

M. Mohammadi, G. Eghlima, F. Aghamir, D. Nezamdoost, M. Bagnazari (Iran) and S.S. Bidabadi (USA)

Discovery of new insecticidal cyclic hexapeptides from *Fusarium tricinctum* HM76 and their biosynthesis

M. Ren, R. Huo, W. Han, Z. Wang, Y. Wang, J. Song, J. Wang, L. Su, T. Cao, J. Zhang and D. Luo (China)

Chemical composition and bioactivities of *Eucalyptus* essential oils from selected pure and hybrid species: A review

S.C. Yip, L.Y. Ho (Malaysia), T.-Y. Wu (Taiwan) and N.W. Sit (Malaysia)

Sustainable ultrasound-assisted extraction of osthole from *Cnidium monnieri* (L.) Cuss based on natural deep eutectic solvents and switchable hydrophilicity solvents

H. Zhang, Y. Zhang, Y. Wang, X. Wang, F. Zhao, X. Jing and J. Han (China)

2-(2-Phenylethyl)chromone dimers as melanin production inhibitors from agarwood of *Gyrinops walla* Gaertn

L.-Y. Chen, W.-L. Mei, L. Yang, F. Wu, C.-H. Cai, J.-Z. Yuan, H.-Q. Chen and H.-F. Dai (China)

Nano cellulose-crystals: Isolation and their promising application as reinforcement in vulcanized natural rubber compounds

F.L. Silva, C.A. Correia, L.M. Oliveira, H. Ribeiro and T.S. Valera (Brazil)

New insights into ethylene-induced latex flow in a dose-dependent manner in rubber tree

J. Wan, R. Fan, W. Yang, F. Wei, H. Gao, H. Wei and J. Qiu (China)

Quality aspects during pine resin storage: Appearance deterioration, turpentine chemical components change, kinetic model and insights into isomerization mechanisms

X. Luo, B. Qin, X. Chen, X. Li, J. Liang, X. Wei and L. Wang (PR China)

Effect of spatial distribution of rubber powder on ductility of rubber asphalt from mesoscopic mechanical perspective: For bio-based materials recycling

H. Li, Y. Zhang, F. Yang, M. Zhang, H. Jing, Z. Li, A.I. Bature and Q. Ma (China)

(Contents continued on Back Matter)

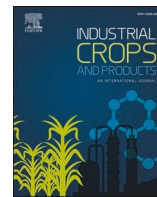
(Contents continued from inside back cover)

- Unveiling the spatial distribution of plant defense metabolites in *Dracaena cambodiana* Pierre ex Gagnep under wound stress  
Y. Zhang, Y. Liu, B. Wang, H. Wu, P. Liu and J.-h. Wei (China)
- Bioenergy - crops and processing**
- First chromosome-scale genome of Indian tea (*Camellia assamica* Masters; syn *C. sinensis* var *assamica*) cultivar TV 1 reveals its evolution and domestication of caffeine synthesis  
H.C. Rawal, S. Borchetia, M. Rohilla, A. Mazumder, M. Gogoi, P.K. Patel, R.V.J. Ilango, B. Das, A.B. Mazumder, T. Bandyopadhyay, P.M. Kumar, S. Soundararajan, B. Bera, P. Mahadani, G. Saha, S. Mukherjee, S. Sabhapondit, A.K. Barooah, T.R. Sharma, N.K. Singh and T.K. Mondal (India)
- Method development and application for multi-phenolic components in the processing of *Dendrobium officinale* using UPLC coupled with mass spectrometry and chemometric analysis  
X. Yang, P. Liu, F. Wang, T. Zhang, N. Li, C. Lu, L. Tong, J. Liu, J. Sun and B. Fan (China)
- Effect of drying technology on the physical, rehydration, flavor, and allicin content of single-clove garlic  
Y. Xie, J. Geng, J. Han, Z. Wang, Y. Zhao, H. Yang and P. Li (PR China)
- Hydrangea-like NiMn layered double hydroxide grown on biomass-derived porous carbon as a high-performance supercapacitor electrode  
Y. Wang, Y. Jin, W. Tian, B. Fan, D. Ding, Z. Zhao, Z. Chen, Z. Guo and P. Ren (PR China)
- Identification and characterization of genes regulating flowering time in apricots  
M. Liu, R. Yang, G. Chen, W. Li, Y. Liu, C. Chang, Y. Wang, D. Ma, H. Wang, J. Cai and C. Fu (China)
- Hydrogen-rich gas generation from enhanced catalytic cracking of biomass tar and related model compounds on Ni-Fe/ASA@HZSM-5 catalyst: Pathways and mechanisms  
X. Li, Z. Wang, P. Liu, D. Wan, S. Wu, Y. Wu and T. Lei (China)
- Unveiling oak leaves-derived biochar/ $\text{Fe}_3\text{O}_4/\text{CuO}$  nanocatalyst for biodiesel production and declining tractor engine exhaust emissions  
T. Li and H. Liang (PR China)
- Pre-digestion of corn straw with kitchen waste improves synergistic methanogenic profiles at different carbon-to-nitrogen ratios  
D. Hua, X. Hou, Y. Zhao, H. Xu, G. Meng, F. Jin and Y. Li (China)
- Real cost and profitability of Virginia fanpetals production for solid biofuel under various propagation methods in north-eastern Poland  
E. Olba-Zięty, J. Kwiatkowski and M.J. Stolarski (Poland)
- Effect and mechanism of short time ball milling on physicochemical characteristics and pyrolysis kinetics of *Pennisetum giganteum*  
Y. Yang, X. Bai, S. Yang, D. Xu and W. Li (China)
- Reaction kinetics and mechanisms for carbon-negative chemical looping gasification of biomass coupled with  $\text{CO}_2$  splitting  
G. Wei, Y. Yao, X. Wu, X. Yang, H. Yuan, Z. Huang, Z. Gao (PR China), S. Peng, Y. Cai and Z. Kang (China)
- Sequential pretreatment of lignocellulosic biomass employing hydrothermal treatment and ball milling to improve the efficiency of enzymatic hydrolysis  
E.-J. Lee, Y.-J. Shin, H. Kim and J.-W. Lee (Republic of Korea)
- A novel homologous acid ferric chloride/5-sulfosalicylic acid coordinated catalytic pretreatment for high-efficiency selective separation of poplar hemicellulose  
M. Yao, Y. Liu, L. Qin, X. Li, X. Long, C. Qin, C. Liang, C. Huang and S. Yao (PR China)
- Enhancing biomass fuel properties of municipal sewage sludge with carbon-rich and low ash energy crops common reed and miscanthus  
M. Yurten and S. Ozdemir (Turkey)



Contents lists available at ScienceDirect

## Industrial Crops &amp; Products

journal homepage: [www.elsevier.com/locate/indcrop](http://www.elsevier.com/locate/indcrop)

# Reaction kinetics and mechanisms for carbon-negative chemical looping gasification of biomass coupled with CO<sub>2</sub> splitting

Guoqiang Wei<sup>a</sup>, Yecheng Yao<sup>a</sup>, Xiaoyan Wu<sup>a</sup>, Xixian Yang<sup>a,\*</sup>, Haoran Yuan<sup>b</sup>, Zhen Huang<sup>b</sup>, Zhongwang Gao<sup>a</sup>, Shuai Peng<sup>c</sup>, Yingjie Cai<sup>c</sup>, Zhanxiao Kang<sup>d</sup>

<sup>a</sup> Institute of Biomass Engineering, Key Laboratory of Energy Plants Resource and Utilization, South China Agricultural University, Guangzhou 510642, PR China

<sup>b</sup> Guangzhou Institute of Energy Conversion, Chinese Academy of Sciences (CAS), Guangzhou 510640, PR China

<sup>c</sup> Hubei Provincial Engineering Laboratory for Clean Production and High Value Utilization of Bio-based Textile Materials, Wuhan Textile University, Wuhan 430200, China

<sup>d</sup> School of Fashion and Textiles, Hong Kong Polytechnic University, Kowloon, Hong Kong 999077, China

## ARTICLE INFO

### Keywords:

Biomass  
CO<sub>2</sub> splitting  
CLGCS  
Reaction kinetic  
Lattice oxygen  
Oxygen carrier

## ABSTRACT

Chemical looping gasification of biomass coupled with CO<sub>2</sub> splitting (CLGCS) was proposed to produce high-quality syngas from biomass and split CO<sub>2</sub> into CO by using Fe/Ni mixed oxygen carrier without extra catalyst and excessive energy consumption, providing a carbon negative emission technology for the cascade utilization of biomass and greenhouse gas. In this work, the reaction kinetic and the activation energy were investigated based on the non-model kinetic model and the lattice oxygen migration mechanism was revealed by the valence evolution of oxygen carriers. The chemical looping gasification (CLG) involved four stages based on the activation energy distribution, which are dehydration, pyrolysis, gas reforming, and char reacting. Ni provided an active site in pyrolysis stage, resulting in a rapid decline activation energy. The higher energy barrier of 341.38 kJ/mol needed to be overcome in char reacting due to the solid-solid reaction. The reaction activation energy exhibited a rising trend as the oxygen vacancies decrease in CO<sub>2</sub> splitting stage (CS), where the internal lattice oxygen transfer resistance increases. The lattice oxygen O<sup>2-</sup> dissociated into chemisorbed oxygen O<sup>2-</sup>/O<sup>-</sup>, which was further converted into molecular O<sub>2</sub> on the surface of the carrier. Ni<sup>2+</sup> from Ni-Fe is preferentially converted to Ni-O in the reduction reaction, and then reduced to Ni<sup>0</sup>. The Ni/Fe intermetallic synergies were also confirmed by the difference in Ni-Ni and Ni-O electron binding energies of Ni2p. The transfer mechanism for CLG was expressed as: O<sub>(lattice)</sub><sup>2-</sup>  $\xrightarrow{e^-}$  O<sub>2</sub><sup>-</sup>/O<sub>(chemical)</sub><sup>-</sup>  $\xrightarrow{e^-}$  O<sub>2(phy)}</sub>  $\xrightarrow{e^-}$  O<sub>2(g)}</sub>. The lattice oxygen migration displayed an opposite trend for CO<sub>2</sub> splitting reaction, where Ni played a catalytic activation role, facilitating the transfer of lattice oxygen rather than participating in the reaction.

## 1. Introduction

According to the International Energy Agency (IEA), global CO<sub>2</sub> emissions reached 36.3 billion tons in 2021, representing a 6 % increase compared with the previous year. The rapid increase in CO<sub>2</sub> contributes to the greenhouse effect, which leads to extreme weather events and environmental threats, including melting glaciers, rising sea levels, desertification, and acid rain. Against this backdrop, the development of clean renewable energy and the large-scale utilization of CO<sub>2</sub> are

effective approaches to addressing environmental issues from both incremental and stock perspectives (Lu et al., 2024).

In terms of reducing CO<sub>2</sub> emissions, using clean renewable energy to replace traditional fossil fuels can fundamentally reduce carbon emissions and mitigate environmental threats. Biomass, as a typical clean and renewable resource, offers several advantages such as extensive sources, abundant reserves, carbon neutrality, low nitrogen, and sulfur content, which is an ideal candidate for replacing fossil energy (Li et al., 2024). Biomass gasification, which converts biomass into syngas, is an effective method for clean energy production. However, the traditional

**Abbreviation:** CLG, Chemical looping gasification; CLGCS, Chemical looping gasification of biomass coupled with CO<sub>2</sub> splitting; FWO, Flynn-Wall-Ozawa formula; IEA, International Energy Agency; HV, Low heating value MJ/kg; MFK, Non-model free kinetics; TGA, Thermogravimetric analysis; XPS, X-ray Photoelectron Spectroscopy.

\* Corresponding author.

E-mail address: [yangxx@scau.edu.cn](mailto:yangxx@scau.edu.cn) (X. Yang).

<https://doi.org/10.1016/j.indcrop.2024.120083>

Received 16 July 2024; Received in revised form 23 October 2024; Accepted 13 November 2024

Available online 21 November 2024

0926-6690/© 2024 Elsevier B.V. All rights reserved, including those for text and data mining, AI training, and similar technologies.



### Nomenclature

|       |                                      |
|-------|--------------------------------------|
| $A$   | Pre-exponential factor ( $s^{-1}$ )  |
| $E$   | Apparent activation energy (kJ/mol)  |
| $m$   | Mass                                 |
| $R$   | Gas constant                         |
| $r^2$ | Coefficient of determination         |
| $T$   | Reaction temperature ( $^{\circ}C$ ) |

### Greek Symbols

|          |                                  |
|----------|----------------------------------|
| $\alpha$ | The reaction conversion          |
| $\beta$  | heating rate ( $^{\circ}C/min$ ) |

### Subscripts

|     |                        |
|-----|------------------------|
| $f$ | Final mass of sample   |
| $t$ | Mass of sample at time |

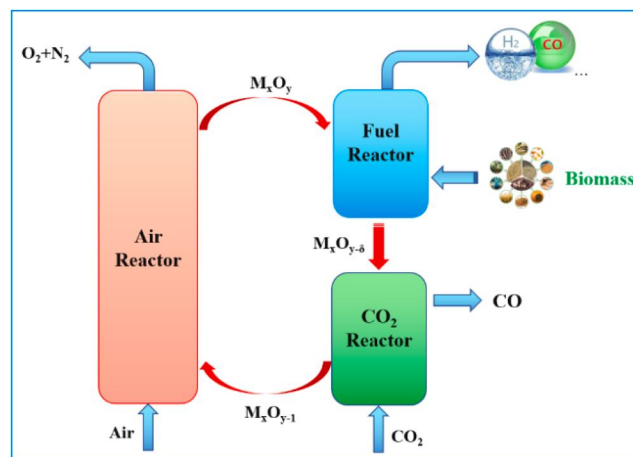


Fig. 1. Schematic diagram of the CLGCS system.

biomass gasification process requires the preparation of pure oxygen as a gasification agent, which involves complex equipment and high energy consumption. When air is directly used as the gasification agent, the resulting syngas products are diluted by inert gas, posing challenges in subsequent Fischer-Tropsch synthesis. To overcome these issues, chemical looping gasification (CLG) of biomass using the lattice oxygen of oxygen carriers instead of molecular oxygen has been developed (Wei et al., 2019). The CLG process offers several advantages over traditional biomass gasification: it eliminates the need for gasification agent preparation, reduces complexity, and energy consumption, avoids the inert dilution of syngas products, and results in high-quality syngas (Wei et al., 2022). Additionally, the oxygen carriers used in CLG have a catalytic cracking effect on tar formation, leading to clean syngas products. Therefore, the CLG is considered an ideal method for obtaining high-quality syngas from renewable biomass resources.

From the perspective of reducing CO<sub>2</sub> stocks, geological CO<sub>2</sub> storage is a promising method to achieve the net-negative target by 2060. However, there are concerns regarding challenges that arise from CO<sub>2</sub>-brine-rock interactions and their implications on reservoir properties, storage process efficiency, and reservoir behavior. Furthermore, geological CO<sub>2</sub> storage is limited by available storage sites, space, and other factors, posing challenges for large-scale CO<sub>2</sub> storage (Galina et al., 2019; S. Zhang et al., 2019). While the physical utilization of CO<sub>2</sub>, such as its use in food refrigerants, welding protective gas, oilfield fillers, and fire extinguishing agents, contributes to carbon emission reduction, the total amount of CO<sub>2</sub> available is limited. To achieve the net-negative target, it is crucial to develop chemical utilization of CO<sub>2</sub>, including the production of urea, ammonia bicarbonate, and other compounds. However, due to the linear symmetrical molecule structure of CO<sub>2</sub> with two equal C=O bonds, breaking the C=O bond for CO<sub>2</sub> activation requires significant energy input. There are two main methods for CO<sub>2</sub> activation: forming M-CO<sub>2</sub> coordination complex compounds with transition metals and triggering subsequent reactions through Lewis bases (Qu et al., 2019). This activation process demands not only substantial energy input but also the involvement of catalysts to enable the chemical utilization of CO<sub>2</sub>, thus limiting large-scale resource utilization of CO<sub>2</sub>. Efficiently and cost-effectively activating CO<sub>2</sub> molecules is a major challenge that must be overcome in the current chemical synthesis industry (Kayaki et al., 2009; Kimura et al., 2012; Yang et al., 2011). Chemical looping splitting of CO<sub>2</sub> offers a new solution to address this challenge without requiring excessive energy input or a specific catalyst.

Current studies have shown that the multi-system coupling of chemical looping reactions can achieve multi-energy complementarity, improve overall system efficiency, and yield high-value products. Given the increasing impact of carbon emissions from fossil energy

combustion, previous research proposed chemical looping gasification of biomass coupled with CO<sub>2</sub> splitting (CLGCS) as a means to produce high-quality syngas and split CO<sub>2</sub> into CO without the need for specific catalysts or excessive energy consumption (Wei et al., 2021, 2022). In this field, numerous researchers have conducted extensive studies, providing important insights that have advanced the understanding and optimization of key processes and technologies. Shen et al. explored the oxidation and reduction properties of the LaFe<sub>0.5</sub>Mn<sub>0.5</sub>O<sub>3</sub> (M=Mn, Co, Ni, Cu) perovskites as oxygen carrier in the CLGCS system (Shen et al., 2022). Guo et al. used the multiphase particle-in-cell method integrated with thermochemical sub-models to optimize the reactor of the CLGCS system (Guo et al., 2024). He et al. optimized the experimental conditions and received bio-syngas with adjustable H<sub>2</sub> to CO ratios ranging from 1:1–2.2:1 (He et al., 2019).

As depicted in Fig. 1, the CLGCS system comprises three components: the air reactor, fuel reactor, and CO<sub>2</sub> reactor. Initially, biomass is introduced into the fuel reactor, where it produces high-quality syngas using the lattice oxygen from the oxygen carrier instead of molecular oxygen. Subsequently, the reduced oxygen carrier and biomass char are transferred to the CO<sub>2</sub> reactor, where they react with CO<sub>2</sub> to generate CO and partially recover the lattice oxygen of the oxygen carrier. Finally, the resulting oxygen carrier fully recovers its lattice oxygen in the air reactor through calcination in an air atmosphere. The oxygen carrier flows between the three reactors, transferring lattice oxygen and reaction heat to ensure the progress of the CLGCS reaction cycle.

The function of an oxygen carrier in lattice oxygen and heat transfer makes it key to realizing the CLG and combustion system process. Currently, research on oxygen carriers for the chemical looping reaction process primarily focuses on synthetic metal oxides, natural ore, and industrial waste residue (Chen et al., 2024; Son et al., 2019). Among these options, iron-based mixed oxygen carriers have several advantages, including high oxygen carrying capacity, resistance to sintering, and good reaction selectivity (Lan et al., 2024).

Considering the high cost of raw materials, the complex preparation process, and the low mechanical strength, synthetic iron-based oxygen carriers find it difficult to meet the requirements for large-scale industrial applications in chemical looping conversion. This difficulty is due to the need to replenish a large amount of oxygen carriers to compensate for quality loss caused by sintering, wear, and other factors. Although natural iron ore oxygen carriers have advantages such as abundant sources, low prices, and high mechanical strength, their reactivity is low. An effective approach to achieving ideal oxygen carriers for large-scale chemical looping processes is to use inexpensive iron ore as the base matrix and introduce active metal components to enhance lattice oxygen transfer and improve fuel conversion efficiency (Wei et al., 2018; Zhang et al., 2024). Oxygen carriers prepared using this method balance

**Table 1**  
Ultimate analysis and proximate analysis of pine sawdust.

| Proximate analysis |          |              |          |       | Ultimate analysis |      |      |                |  | Lower heating value |
|--------------------|----------|--------------|----------|-------|-------------------|------|------|----------------|--|---------------------|
| wt%, ad            |          |              |          |       | wt%, daf          |      |      |                |  | MJ/kg               |
| Ash                | Volatile | Fixed carbon | Moisture | C     | H                 | N    | S    | O <sup>d</sup> |  | 19.52               |
| 0.93               | 79.32    | 14.14        | 5.60     | 49.60 | 6.46              | 0.05 | 0.04 | 43.85          |  |                     |

Note: O<sup>d</sup> : By difference

reactivity and preparation cost, showing great potential for industrial applications. In the previous study, hematite ore particles were used as the oxygen carrier matrix and added NiO, Co<sub>2</sub>O<sub>3</sub>, CeO<sub>2</sub>, and CaO as exogenous metals to prepare mixed oxygen carriers. The CLGCS were investigated for producing high-quality syngas from biomass and splitting CO<sub>2</sub> into CO using these mixed oxygen carriers (Wei et al., 2021). The synergistic interaction between the metals was analyzed, and the reactivity improvement order of different exogenous metals on the hematite matrix was determined. However, the reaction kinetic performance and lattice oxygen migration mechanism of the oxygen carriers have not been revealed, thus hampering the development of novel and improved oxygen carriers.

In this study, a detailed kinetic analysis of CLGCS over Fe/Ni oxygen carriers at different heating rates was performed. The activation energy and pre-exponential factors for each stage of CLGCS were examined to identify the rate-limiting step. The evolution of the element content and the valence distribution of oxygen carriers at different reaction stages were monitored by X-ray Photoelectron Spectroscopy (XPS) to elucidate the lattice oxygen migration mechanism of the oxygen carriers.

## 2. Experimental

### 2.1. Materials

Hematite ore (Fe<sub>2</sub>O<sub>3</sub> L.) from China was utilized as an oxygen carrier matrix after being crushed and sieved into 60–80 mesh particles. The elemental composition includes O, Fe, Si, Al, Ca, Zn, P, Mg, K, Mn, Ti, Cl, and so on. NiO, derived from analytical grade Ni (NO<sub>3</sub>)<sub>2</sub>·6 H<sub>2</sub>O, was used to modify the hematite matrix. The intermediate product was produced using the incipient impregnation method. After drying at 120 °C for 24 h and calcination at 950 °C for 3 h, the Fe-based mixed oxygen carrier with a mass fraction of 10 % NiO was achieved. In the experiment, pine sawdust (Pinus spp. L.) with a particle size of 80–100 mesh from Guangzhou, China, was used as the biomass material. The ultimate analysis and proximate analysis of the pine sawdust are shown in Table 1.

### 2.2. Apparatus and methods

In this work, the thermogravimetric analysis reactor (Mettler TGA/DSC3+) was utilized to investigate the reaction kinetic performance of biomass in CLGCS at different heating rates. The non-dynamic model method was employed to determine the reaction kinetics parameters. Oxygen carrier and pine sawdust were mixed in a 1:1 mass ratio and then uniformly ground before being placed into the TGA reactor for testing. The tests were conducted under the N<sub>2</sub> atmosphere with flow rate of 30 mL/min. The CLG stage reaction took place within a temperature range of 30–950 °C with heating rate of 5 °C/min, 10 °C/min, 15 °C/min, 20 °C/min, and 25 °C/min, respectively. After the CLG reaction stage, N<sub>2</sub> continues to enter, where the reaction sample began to cool down. To facilitate the splitting reaction, CO<sub>2</sub> (with a mole fraction of 99.99 %) was injected at a flow rate of 30 mL/min. The splitting reaction was performed within the temperature range of 180–950 °C, employing the same heating rates as before.

The activation energy kinetic parameters of the reaction process were determined using the non-model Free Kinetics (MFK) method (Huang et al., 2022), which involved calculating the parameters based on the Arrhenius formula (Lin et al., 2020).

$$\frac{d\alpha}{dt} = A(\alpha)f(\alpha)\exp\left(-\frac{E_a}{RT}\right) \quad (1)$$

Where  $T$  is the reaction temperature and  $A$  is the pre-exponential factor (s<sup>-1</sup>).  $E_a$  is the apparent activation energy (kJ/mol), and  $R$  is the gas constant (8.314 J/mol/K). The  $f(\alpha)$  is the reaction mechanism function (Ma et al., 2023), and the reaction conversion,  $\alpha$ , can be represented by the Eq. (2).

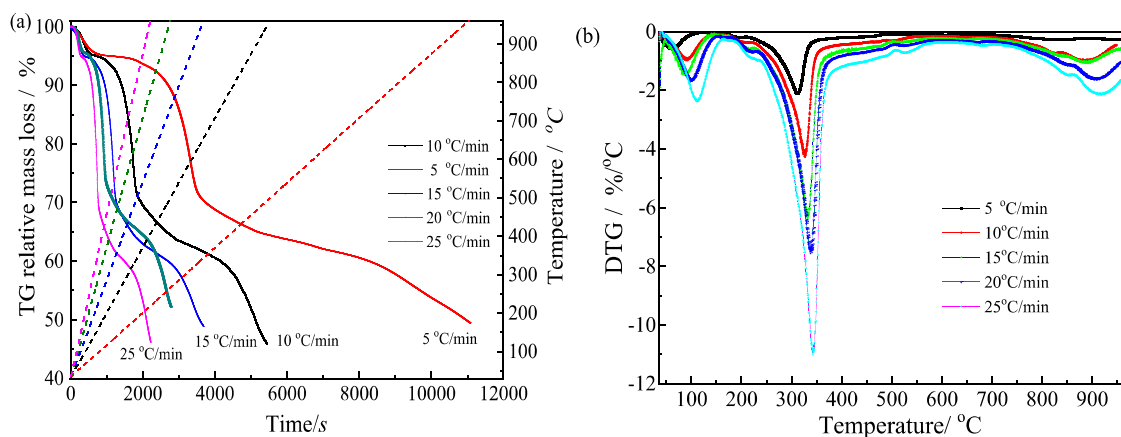
$$\alpha = (m_i - m_t) / (m_i - m_f) \quad (2)$$

Where  $m_i$  is the initial mass of the sample.  $m_t$  is the mass of sample at time  $t$ .  $m_f$  is the final mass of sample.

Furthermore, the integral formula (1) can be expressed as (3),

$$g(\alpha) = A \int \exp\left(-\frac{E_a}{RT}\right) dt \quad (3)$$

When the heating rate is defined as  $\beta = dT/dt$ , the equation can be



**Fig. 2.** Thermogravimetric curves of CLG stage (a) TGA curves (b) DTG curves.

converted into Eqs. (4) and (5), which consists the basic equation of non-isothermal kinetic analysis.

$$\frac{d\alpha}{dT} = \frac{A}{\beta} f(\alpha) \exp\left(-\frac{E_a}{RT}\right) \quad (4)$$

$$g(\alpha) = \frac{A}{\beta} \int \exp\left(-\frac{E_a}{RT}\right) dT \quad (5)$$

When  $g(\alpha)$  is the integral form of reaction model.

Flynn-Wall-Ozawa formula (6) was adopted to obtain more accurate and reliable analysis results (Ma et al., 2023).

$$\log \beta = \log \left[ \frac{AE_a}{Rg(\alpha)} \right] - 2.315 - 0.4567 \frac{E_a}{RT} \quad (6)$$

$$\ln \left( \beta \frac{d\alpha}{dT} \right) = \ln[Af(\alpha)] - \frac{E_a}{RT} \quad (7)$$

The activation energy of the reaction can be calculated by obtaining the algebraic relationship between  $\lg(\beta)$  or  $\ln(\beta d\alpha/dT)$  and  $1/T$ , where  $T$  is the reaction temperature at equal conversion. Then, the apparent activation energy  $E_a$  can be achieved by linear fitting calculation.

In addition, X-ray Photoelectron Spectroscopy (Thermo ESCALAB 250XI) was used to detect the element composition and the valence distribution of oxygen carrier at different reaction stages, obtaining the migration mechanism of lattice oxygen during the CLGCS process. The total spectrum and single element spectra of C, Fe, Ni, and O were obtained using an Al K $\alpha$  ray excitation source (20 kV, 10 mA) under the conditions of 20 eV and 100 eV. The fresh oxygen carrier was reduced by biomass pyrolysis gas at 900 °C, with gas flow rate of 60 mL/min with the reduction time of 5 min, 10 min, 15 min, 25 min, 35 min, and 45 min, respectively. Then, the reduced samples were cooled in N<sub>2</sub> atmosphere.

### 3. Results and discussion

#### 3.1. Thermal reaction performance of CLG process

Fig. 2 indicates the thermal reaction performance of CLG process for biomass and Fe/Ni mixed oxygen carrier at different heating rates. The thermal reaction curves show three major weight loss peaks within specific temperature ranges of 60–120 °C, 300–400 °C, and 800–900 °C, respectively. The weight loss peak below 150 °C is primarily attributed to the dehydration weight loss of the sample. The weight loss peak between 300 °C and 400 °C corresponds to the thermal decomposition of biomass, which removes small molecules of volatile components. The weight loss peak between 800 °C and 900 °C represents the CLG reaction of sawdust char and oxygen carrier. For the different heating rates of 5 °C/min, 10 °C/min, 15 °C/min, 20 °C/min, and 25 °C/min, the maximum weight loss reaction rate is similar and the total weight loss ranges from 47.9 % to 54.1 %. The reaction equilibrium time is shortened as the rising heating rate. The maximum weight loss reaction rate of 0.44 %/°C is obtained at 343.3 °C for the weight loss curve with heating rate of 25 °C/min. While the maximum weight loss rate of 0.42 %/°C is achieved at 312.9 °C of the weight loss curve with heating rate of 5 °C/min. Obviously, the temperature of maximum weight loss peak shifts to the right and increases with the rising heating rate. High temperature increases the sample's reaction rate and promotes its transformation. The entire reaction process consists three main steps: dehydration, pyrolysis, and char chemical looping gasification. The heating rate and conversion rate do not have a perfectly linear relationship, leading to variations in final weight loss. At high heating rates, a temperature gradient exists between the sample particles and the reactor, resulting in hysteresis effects on heat and mass transfer during the reaction. Achieving reaction equilibrium quickly within a short period of time becomes challenging. Consequently, as the heating rate increases, the maximum weight loss reaction rate in each section of the sample shifts towards the higher

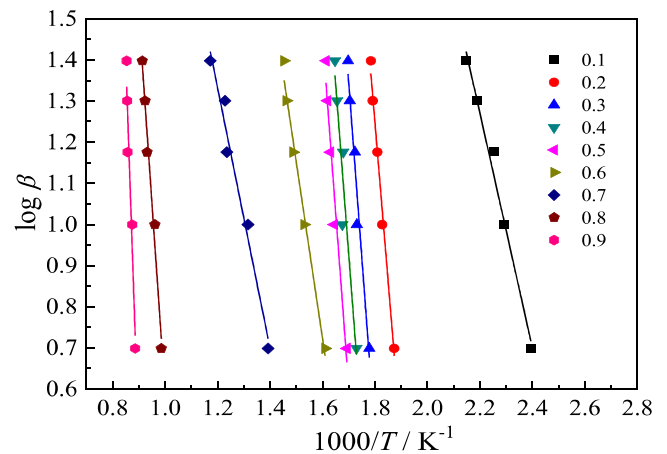


Fig. 3. The relationship between  $\log \beta$  and  $1/T$  at different heating rates.

**Table 2**  
Kinetics parameters of CLG stage.

| $\alpha$ | $E_a$<br>kJ/mol | $r^2$ |
|----------|-----------------|-------|
| 0.1      | 51.88           | 0.98  |
| 0.2      | 140.38          | 0.99  |
| 0.3      | 155.02          | 0.96  |
| 0.4      | 151.40          | 0.89  |
| 0.5      | 154.99          | 0.95  |
| 0.6      | 78.10           | 0.98  |
| 0.7      | 57.62           | 0.97  |
| 0.8      | 167.62          | 0.98  |
| 0.9      | 341.38          | 0.92  |

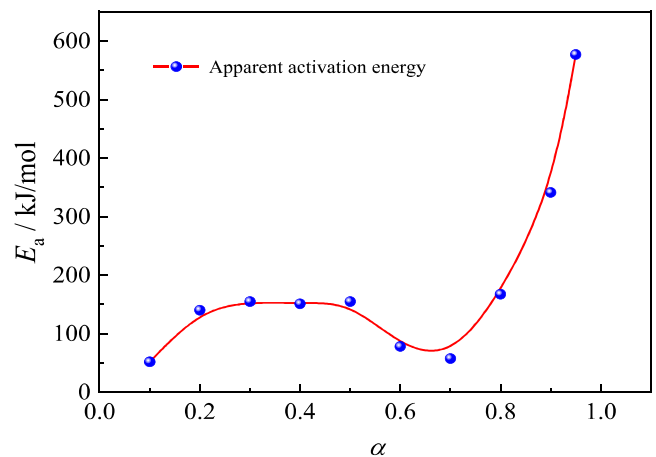


Fig. 4. Activation energy distribution of CLG reaction with pine sawdust (Ozawa).

temperature area.

#### 3.2. Reaction kinetics performance of CLG process

It is proved that the model-free kinetics method can avoid the error caused by the selection of mechanism function and improve the calculation accuracy of apparent activation energy. Based on Ozawa or Friedman calculation method, the apparent activation energy of the reaction can be calculated by obtaining the algebraic relationship between  $\lg(\beta)$  or  $\ln(\beta d\alpha/dT)$  and  $1/T$ , where  $T$  is the equal conversion reaction temperature, and then the apparent activation energy  $E_a$  was calculated by linear fitting. In this study, Ozawa method was used to

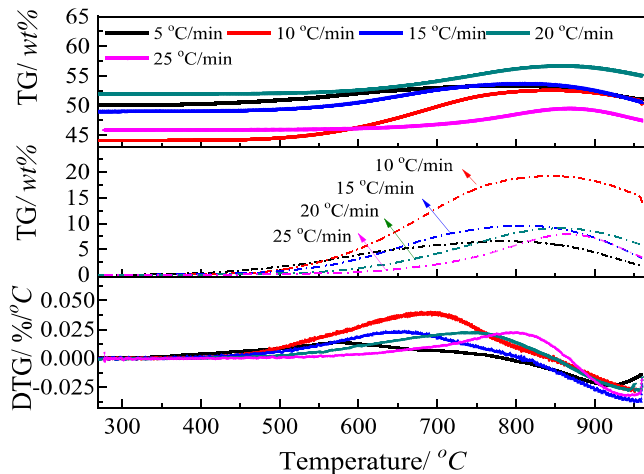


Fig. 5. Thermogravimetric analysis of CO<sub>2</sub> splitting stage.

calculate the kinetic parameters of biomass CLG reaction process. According to Eq. (6),  $\alpha$  was used between 0.1 and 0.9 with a step size of 0.1, and the Ozawa method was utilized to fit the TG data at various heating rates. Then, the activation energy distribution under various conversion conditions of biomass chemical looping gasification various was achieved. The correlation coefficients in the fitting process was exhibited in Table 2. Fig. 3 displays the  $E_a$  calculated from the slope of the curve of  $\log\beta$  versus  $1/T$ , while Table 2 presents the pyrolysis kinetics with varying mixing ratios. The  $r^2$  values, ranging 0.92–0.99, demonstrate a strong linear correlation.

The activation energy distribution of CLG reaction with pine sawdust calculated by Ozawa method was shown in Fig. 4. It can be observed that the activation energy distribution calculated by Ozawa method displayed a trend of fluctuation, indicating that the CLG reaction of biomass included four stages: dehydration, pyrolysis, gas reforming, and char reacting with oxygen carrier. When the conversion rate  $\alpha$  was less than 0.1, this stage mainly was attributed to the separation of free water or water molecules in biomass, where indicated the lowest activation energy  $E_a$ . The  $E_a$  appeared 51.88 kJ/mol with a conversion rate  $\alpha$  of 0.1. As the increase of  $\alpha$ , hemicellulose, cellulose and some lignin in the sawdust began to pyrolysis into small molecule compound, escaping the biomass. Consequently, the apparent activation energy  $E_a$  increased, and a higher energy barrier of the pyrolysis reaction needed to be overcome. However, with the further increasing of the reaction conversion rate  $\alpha$ , the apparent activation energy  $E_a$  showed a downward trend. The lower  $E_a$  appeared at an  $\alpha$  of 0.7, corresponding to 57.62 kJ/mol. This reaction process was mainly ascribed to the reactions of small molecular substances produced in the pyrolysis with NiO and Fe<sub>2</sub>O<sub>3</sub> in oxygen carrier. Owing to the medium temperature stage, the pyrolysis product molecules and active atoms in oxygen carrier were in an excited state, and the chemical bond energy was weakened. Moreover, NiO in oxygen carrier reacted with CO and CH<sub>4</sub> gases of pyrolysis production to generate Ni elemental substance, which provides an active site for the reduction of Fe<sub>2</sub>O<sub>3</sub> in the oxygen carrier, and enhances the intermetallic synergism, resulting in a rapid decline in the activation energy of the reaction (Wei et al., 2022, 2019). At the same time, NiO reacts with CO and CH<sub>4</sub> gas produced by pine pyrolysis to produce Ni elemental, which supplied the active sites for the lattice oxygen migration, strengthening the intermetallic synergism, and reducing the reaction activation energy rapidly. Correspondingly, with the increase of the reaction conversion rate  $\alpha$ , the pyrolysis process of pine powder was completed basically, and the apparent activation energy  $E_a$  showed a trend of rapid rise. The main reaction of the system was the solid-solid reaction between biomass char and oxygen carrier, and the reaction needed to overcome the energy barrier rapidly increased. When  $\alpha$  was 0.8, the activation energy  $E_a$  reached 167.62 kJ/mol. Therefore, Fe<sub>2</sub>O<sub>3</sub> in oxygen carrier

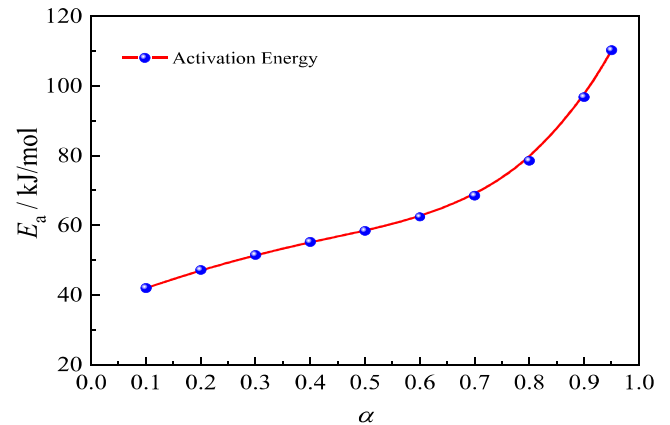


Fig. 6. Activation energy distribution of CO<sub>2</sub> splitting reaction.

was successively transformed into Fe<sub>3</sub>O<sub>4</sub>, FeO, and Fe, NiO was also transformed into Ni elemental in the CLG process with the reaction activation energy further increasing. when  $\alpha$  was 0.9, the reaction activation energy was 341.38 kJ/mol. To achieve high reaction conversion rates, higher energy barriers and larger  $E_a$  must be overcome.

### 3.3. Thermal reaction performance of CO<sub>2</sub> splitting reaction

After the CLG stage, the reduced oxygen carrier sample was cooled to 180 °C in N<sub>2</sub> atmosphere and injected with CO<sub>2</sub> for splitting reaction. The reaction mainly involved the splitting reaction of CO<sub>2</sub> with the reduced oxygen carrier and the disproportionation reaction of CO<sub>2</sub> and biomass char, as described by Eqs. 8 and 9, where the heating rate was set as 5 °C/min, 10 °C/min, 15 °C/min, 20 °C/min, and 25 °C/min, respectively.

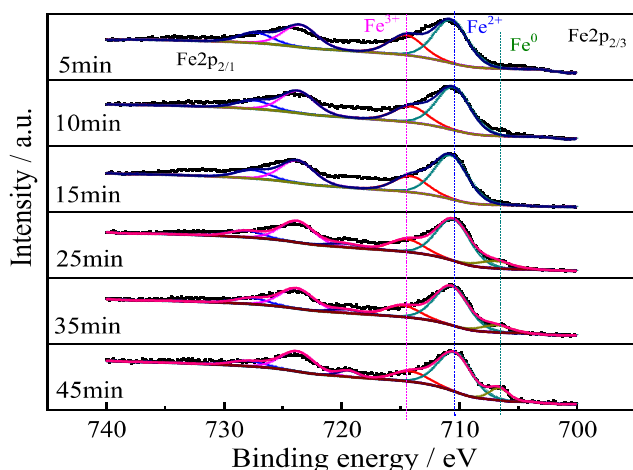


Fig. 5 shows the thermogravimetric curves obtained at various heating rates during the CO<sub>2</sub> splitting stage. Since the CO<sub>2</sub> splitting reaction was carried out after the CLG process, the vertical axis of the initial thermogravimetric curve did not start at zero. In this study, the thermogravimetric data at the beginning of CO<sub>2</sub> input was used as the starting point for data analysis to facilitate comparison. Results indicated that the weight of sample increased as the reaction between CO<sub>2</sub> and the oxygen carrier, with the recovery of lattice oxygen occurring after the temperature of 500 °C. As  $\beta$  increases from 10 °C/min to 25 °C/min, the maximum weight difference decreased from 19.15 % to 7.87 %. The curves of DTG illustrated that the temperature at which the maximum weight loss rises from 574.2 °C to 811.3 °C and maximum gain weight rate increases from 0.013 %/°C to 0.021 %/°C as  $\beta$  increases from 10 °C/min to 25 °C/min. The sample adequately reacted at a lower heating rate. It is obvious that the reduced oxygen carrier splitted CO<sub>2</sub> to recover lattice oxygen with the introduction of CO<sub>2</sub>, and the temperature of maximum peak increased with the rising heating rate. Due to the thermal hysteresis effect, the high heating rate leads to insufficient heat and mass transfer time of the sample, and the hysteresis phenomenon occurs when the equilibrium temperature is reached. Consequently, the heat and mass transfer of the sample are sufficient with lower heating rate, where the highest instantaneous reaction rate were obtained at 10 °C/min. As the increasing of temperature, reaction rate of TG curve decreased gradually, which was attributed to the disproportionation reaction between CO<sub>2</sub> and biomass char consumed continuously at this stage. While, the heating rates have little effect on the disproportionation reaction as the temperature exceeds 850 °C, and the DTG curves indicated similar reaction rates.



**Table 3**  
Kinetics parameters of CO<sub>2</sub> splitting reaction.

| $\alpha$ | $E_a$<br>kJ/mol | $r^2$ |
|----------|-----------------|-------|
| 0.1      | 42.00           | 0.96  |
| 0.2      | 47.18           | 0.92  |
| 0.3      | 51.49           | 0.94  |
| 0.4      | 55.21           | 0.92  |
| 0.5      | 58.40           | 0.92  |
| 0.6      | 62.41           | 0.95  |
| 0.7      | 68.50           | 0.90  |
| 0.8      | 78.55           | 0.96  |
| 0.9      | 96.79           | 0.89  |
| 0.95     | 110.27          | 0.92  |



**Fig. 7.** Fe element valence distribution in different processes.

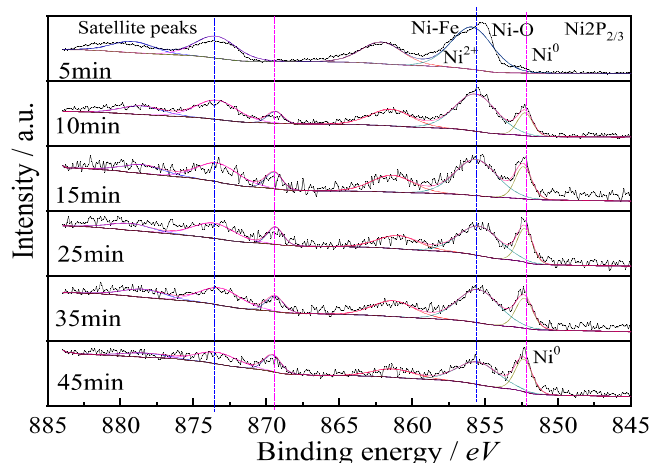
### 3.4. Reaction kinetics performance of CO<sub>2</sub> splitting reaction

The Ozawa method was used to calculate the kinetic parameters of the CO<sub>2</sub> splitting reaction and the activation energy was obtained and shown in Fig. 6 and Table 3. Results show that the low conversion rate with  $\alpha = 0.1$  has a lower activation energy compared with  $\alpha = 0.95$ . In the initial stage, CO<sub>2</sub> reacted with iron to form CO and FeO, the reduced oxygen carrier had sufficient oxygen vacancies, where the activation energy barrier in the splitting reaction was low, enabling an easy reaction. The activation energy  $E_a$  was 42.00 kJ/mol, corresponding to  $\alpha=0.1$ . The oxygen vacancy gradually decreased as the conversion rate  $\alpha$  increasing rapidly, which led to the higher energy barrier that needed to be overcome in the reaction. As the sample conversion increases, Fe is converted to FeO and starts to undergo deeper conversion to Fe<sub>3</sub>O<sub>4</sub>. At this stage, it becomes more challenging for CO<sub>2</sub> to be cleaved on the surface of the oxygen carrier and transfer lattice oxygen to the particle. Consequently, the reaction requires overcoming a higher energy barrier, leading to a continuous improvement in the activation energy of the reaction. When the conversion rate  $\alpha$  was 0.4, the activation energy  $E_a$  reached 55.21 kJ/mol. In addition, the sawdust char that was not completely transformed in the CLG stage also participated in the CO<sub>2</sub> splitting process, which improved the activation energy of the whole reaction. The activation energy reached 110.27 kJ/mol with  $\alpha$  0.95. Table 3 indicated that the fitting results had a good linear correlation.

### 3.5. The lattice oxygen migration mechanism of oxygen carriers

#### 3.5.1. The CLG process

Furthermore, XPS analysis was used to analyze and characterize the elemental valence and distribution evolution of oxygen carriers in the



**Fig. 8.** Ni element valence distribution in different processes.

CLG process, revealing the lattice oxygen migration mechanism. In the formation of NiO modified iron-based oxygen carrier, Fe and Ni were the main active elements related to the lattice oxygen transfer, and their distribution and valence changes in the reaction have important correlations with the lattice oxygen transfer. The valence states of Fe elements in different processes were characterized by XPS analysis and the Fe2p<sub>2/3</sub> spectra are shown in Fig. 7. It was observed that the binding energy peak of the Fe2p<sub>3/2</sub> orbit of Fe elements was wider and stronger than that of the Fe2p<sub>1/2</sub> orbit, which was mainly due to the coupling in the spin orbit (j-j) (Peng et al., 2017; Yamashita et al., 2008). In the XPS spectrum of reduced Fe2p<sub>2/3</sub>, two main peaks were observed at binding energies of 714.56 eV and 710.78 eV, and representing Fe<sup>3+</sup> and Fe<sup>2+</sup>, respectively (Pradhan et al., 2012). In addition, the binding energy peak of 706.9 eV corresponded to the formation of Fe<sup>0</sup> metal. In the fresh oxygen carrier, the atomic ratios of Fe<sup>3+</sup> and Fe<sup>2+</sup> were 61.32 % and 38.52 %, respectively, with no Fe<sup>0</sup> detected. After 15 min of reaction, the atomic ratios of Fe<sup>3+</sup> decreased to 26.45 % and Fe<sup>2+</sup> increased to 73.55 %. During 45 min, the atom ratios of Fe<sup>3+</sup>, Fe<sup>2+</sup> and Fe<sup>0</sup> are 18.26 %, 69.10 % and 12.64 %, respectively. It can be observed that Fe<sup>3+</sup> in the oxygen carrier is reduced to Fe<sup>2+</sup> and further converted to Fe<sup>0</sup> during the reaction, following the reduction path of Fe<sup>3+</sup>→Fe<sup>2+</sup>→Fe<sup>0</sup> (Wei et al., 2018).

The binding energy spectra of Ni element and the valence distribution of the NiO modified oxygen carrier in different processes were investigated by XPS analysis, exhibited in Fig. 8. By comparing the electron binding energy spectra of Ni2p in XPS spectra, it was found that three electron binding energy peaks of Ni elements appear on the electron spectra with the process of reaction. The binding energy of metal Ni at Ni2p<sub>3/2</sub> corresponds to 852.6 eV, while the binding energy of NiO and Ni (OH) at Ni2p<sub>3/2</sub> corresponds to 853.7 eV and 855.6 eV. In addition, according to the NIST X-ray Photoelectron Spectroscopy Database, the peak of electron binding energy of Ni elements shifts in the case of synergistic interaction with Fe elements, and Ni elements in NiFe<sub>2</sub>O<sub>4</sub> bind to 855.4 eV in the Ni2p<sub>3/4</sub> orbital. Therefore, three spectral peaks of Ni elements are attributed to the electron binding energy peaks of Fe-Ni, Ni-O and Ni<sup>0</sup> in this study. In Fig. 8, the Ni2p spectra are displayed, and the results revealed that the Ni-Fe and Ni-O bonds, with proportions of 62.27 % and 37.73 % respectively, appear at 855.90 eV. Additionally, corresponding satellite peaks were observed at 873.46 eV and 879.2 eV for the Ni-Fe and Ni-O bonds, respectively. The elemental binding energy peak of Ni<sup>0</sup> was observed at 852.26 eV, confirming that Ni<sup>0</sup> was reduced to elemental Ni in the oxygen carrier. As the reduction reaction proceeded from 10 min to 45 min, the ratios of Ni-Fe and Ni-O binding decreased from 59.77 % to 50.87 % and 26.76–19.01 %, respectively. Simultaneously, the ratios of Ni<sup>0</sup> increased from 13.47 % to 30.03 %. Apparently, Ni element on the surface of oxygen carrier was



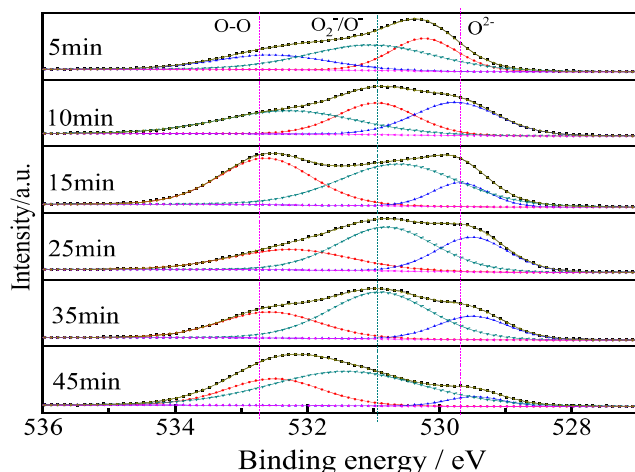


Fig. 9. O element valence distribution in different reactions.

preferentially converted from Ni-Fe to Ni-O in the reduction reaction, and then reduced to Ni<sup>0</sup>. The difference between Ni-Ni and Ni-O electron binding energy of Ni2p also confirmed that Ni-modified iron ore oxygen carrier can produce intermetallic synergies and improve the lattice oxygen reactivity of oxygen carrier.

The experimental results and XPS spectra of O1s of NiO modified oxygen carrier at different reduction times are shown in Fig. 9 and Table 4. The surface of the fresh oxygen carrier contains three oxygen species: the lattice oxygen (O<sup>2-</sup>) a binding energy range of 529.64–531.09 eV, the chemisorbed oxygen (O<sub>2</sub><sup>-</sup>/O<sup>-</sup>) a binding energy range of 530.0–532.69 eV and hydroxide and/or carbonate oxygen (O<sub>2</sub>) with a higher binding energy peak on the catalyst surface. The oxygen species on the surface of oxygen carrier can be divided into three categories: lattice oxygen, chemisorptive oxygen and physical adsorption oxygen according to the difference of electron binding energy. The different oxygen species were indentified based on the O1s electron binding energy. The electron binding energy in the range of

529.64–531.09 eV was attributed to lattice oxygen O<sup>2-</sup>, while the electron binding energy in the range of 531.0–532.69 eV was chemisorbed oxygen O<sup>-</sup>/O<sub>2</sub><sup>-</sup>. This oxygen species was related to the adsorption of organic matter and metal ions. Carbonates, hydroxyl groups and C-O, H-O formed by adsorbed water on the surface of oxygen carriers contributed to chemisorbed oxygen-related electron binding peaks (Sutthiumporn et al., 2011). The oxygen species with electron binding energy higher than 532.0 eV was specified as adsorbed molecular oxygen O<sub>2</sub>.

As shown in Table 4, the rates of O<sup>2-</sup>, O<sub>2</sub><sup>-</sup>/O<sup>-</sup>, and O<sub>2</sub> in the fresh surface of oxygen carrier are 44.49 %, 51.25 %, and 24.26 % respectively. The surface lattice oxygen O<sup>2-</sup> decreased gradually with the reaction, while the molecular adsorbed oxygen remained basically stable in the process. As the reaction progresses to 45 min, the surface lattice oxygen O<sup>2-</sup> decreases from 44.49 % to 6.58 %, while the rates of O<sub>2</sub><sup>-</sup>/O<sup>-</sup> and O<sub>2</sub> increase to 62.66 % and 30.76 %, respectively. The proportion of lattice oxygen on the surface of oxygen carrier gradually decreased in the reduction process, while the proportion of chemisorbed oxygen gradually increased. In the chemical looping reaction, chemisorbed oxygen O<sup>2-</sup>/O<sup>-</sup> is primarily converted by lattice oxygen primarily and then regenerated into physical adsorbed oxygen generated O<sub>2</sub> (Gao et al., 2020). Due to the weak intermolecular interaction between physical adsorption oxygen and the surface of oxygen carrier, it is easy to escape the surface of oxygen carrier and react with fuel, so the physical adsorbed oxygen basically remain stable. The oxygen element reaction path in the oxygen carrier can be expressed as follows: O<sub>2(lattice)</sub>  $\xrightarrow{e^-}$  O<sup>2-</sup>/O<sup>-</sup>(chemical)  $\xrightarrow{e^-}$  O<sub>2(phy)}</sub>  $\xrightarrow{e^-}$  O<sub>2(g)}</sub> (Feng et al., 2024).

Overall, the conversion of NCF can be summarized as shown in Fig. 10. The chemisorption of oxygen (O<sup>2-</sup>/O<sup>-</sup>) is dissociated by lattice oxygen (O<sup>2-</sup>) and transported from the bulk phase to the reaction surface. Additionally, the chemisorbed oxygen (O<sup>2-</sup>/O<sup>-</sup>) is further converted into (O<sup>2-</sup>) and reacts with fuel. During the reaction, the Fe<sup>3+</sup>/Fe<sup>2+</sup> and Ni<sup>2+</sup> lose lattice oxygen and are gradually reduced to low-valence metal elements. The dissociation rate of Ni-Fe bond was lower than that of Ni-O bond. This phenomenon can be confirmed by the fact that the atomic ratio of Ni-O decreases faster in CLG process than that of

Table 4  
Elements valence and content of oxygen carrier in chemical looping reaction.

| Sample<br>/Chemical looping<br>reaction | Fe 2p <sub>3/2</sub> / Atomic ratio<br>(%) |                  |                 | Ni 2p <sub>3/2</sub> / Atomic ratio<br>(%) |                            |                 | 1s/ Atomic ratio<br>(%) |                                 |                |
|---|--|------------------|-----------------|--|----------------------------|-----------------|-------------------------|---------------------------------|----------------|
|   | Fe <sup>3+</sup>                           | Fe <sup>2+</sup> | Fe <sup>0</sup> | Ni <sup>2+</sup><br>(Ni-Fe)                | Ni <sup>2+</sup><br>(Ni-O) | Ni <sup>0</sup> | O <sup>2-</sup>         | O <sup>2-</sup> /O <sup>-</sup> | O <sub>2</sub> |
| Fresh                                   | 61.32                                      | 38.52            | -               | 62.27                                      | 37.73                      | -               | 44.49                   | 51.25                           | 24.26          |
| 5 min                                   | 31.76                                      | 68.24            | -               | 65.28                                      | 33.86                      | -               | 35.63                   | 40.76                           | 23.61          |
| 10 min                                  | 29.51                                      | 70.49            | -               | 59.77                                      | 26.76                      | 13.47           | 33.24                   | 42.33                           | 24.43          |
| 15 min                                  | 26.45                                      | 73.55            | -               | 55.23                                      | 25.57                      | 19.19           | 29.60                   | 46.97                           | 23.43          |
| 25 min                                  | 20.62                                      | 67.55            | 11.83           | 53.47                                      | 24.05                      | 22.48           | 26.98                   | 46.50                           | 26.52          |
| 35 min                                  | 20.22                                      | 68.69            | 11.09           | 52.16                                      | 23.75                      | 24.09           | 18.66                   | 52.80                           | 28.54          |
| 45 min                                  | 18.26                                      | 69.10            | 12.64           | 50.87                                      | 19.01                      | 30.03           | 6.58                    | 62.66                           | 30.76          |

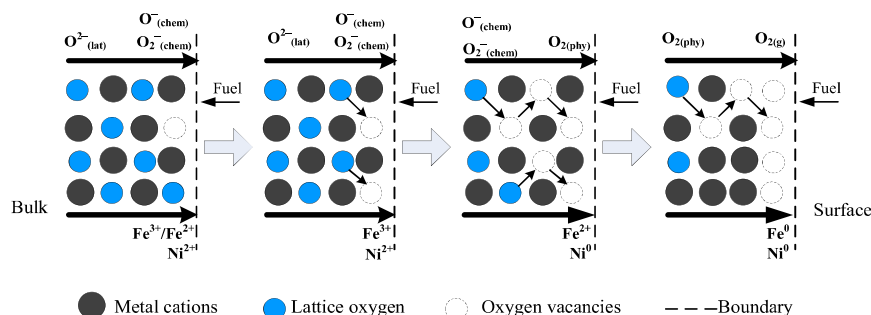


Fig. 10. Lattice oxygen migration path in chemical looping reaction.

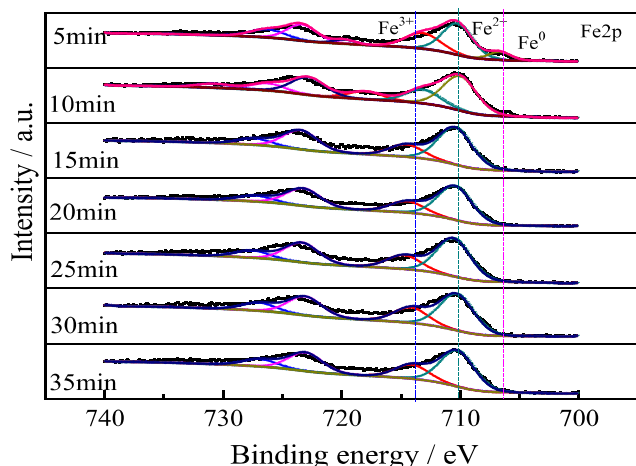


Fig. 11. Fe element valence distribution in CO<sub>2</sub> splitting processes.

Ni-Fe in Table 4. The difference in the Ni2p electron binding energy between the Fe-Ni and Ni-O phases in Fig. 8 also supports this transformation.

### 3.5.2. The CO<sub>2</sub> splitting reaction process

The reduced oxygen carrier was further used for CO<sub>2</sub> splitting reaction, and the oxygen carrier elements and valence state distribution at different reaction times were test by XPS to investigate the lattice oxygen transfer mechanism. Fig. 11 to Fig. 13 revealed the valence states and distributions of Fe, Ni, and O elements on the surface of oxygen carriers, the corresponding atomic distribution exhibited as Table 5. Fig. 11 displayed the percentages of Fe<sup>3+</sup>, Fe<sup>2+</sup>, and Fe<sup>0</sup> on the surface of oxygen carrier during the initial splitting reaction, which were 18.26 %, 69.10 %, and 12.64 %, respectively. As the reaction progresses, CO<sub>2</sub> splited on the surface of the oxygen carrier to generate CO, and the active lattice oxygen enters the bulk phase through the surface of the oxygen carrier. As a result, Fe<sup>0</sup> metal on the surface of oxygen carrier decreased and the content of Fe<sup>2+</sup> and Fe<sup>3+</sup> atoms increased. The binding energy peak of Fe elemental disappears after 15 min, indicating that the reaction between Fe elemental and CO<sub>2</sub> is basically completed. After 35 min, the ratio of Fe<sup>3+</sup> and Fe<sup>2+</sup> on the surface of oxygen support is 30.15 % and 69.85 %, respectively. This reveals that the reaction path of the Fe element valence state on the surface of the oxygen support in the CO<sub>2</sub> cleavage reaction can be represented as follows: Fe<sup>0</sup> → Fe<sup>2+</sup> → Fe<sup>3+</sup>.

The evolution behaviors of the Ni elements of oxygen carrie during the CO<sub>2</sub> splitting process were are shown in Fig. 12. Results indicated that Ni peak appears at the binding energy of 852.3 eV and remains stable on the surface of the oxygen carrier though the subsequent re-actions. The presence of Ni elements played a catalytic activation role in the CO<sub>2</sub> splitting reaction, facilitating the transfer of lattice oxygen to the oxygen carrier, but it did not directly participate in the reaction,

resulting in its atomic ratio remaining basically stable. As the CO<sub>2</sub> splitting reaction proceeds, lattice oxygen was continuously transferred to the interior of the oxygen carrier. The increasing Fe<sup>2+</sup> and Fe<sup>3+</sup> atoms enhanced the interaction between Ni and Fe bonds, while decreasing the interaction between Ni and O bonds in the oxygen carrier. Furthermore, the total sum of Ni-Fe and Ni-O bonds remained relatively stable during the reaction.

The O1s orbital electron energy spectrum of the oxygen carrier in the CO<sub>2</sub> splitting reaction was illustrated in Fig. 13, and the atomic

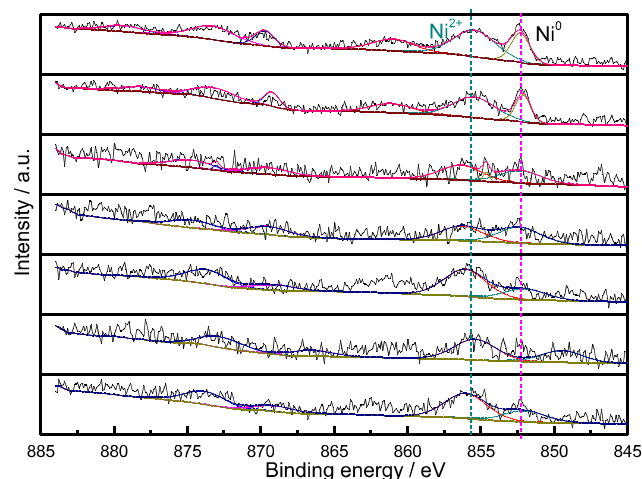


Fig. 12. Ni element valence distribution in CO<sub>2</sub> splitting processes.

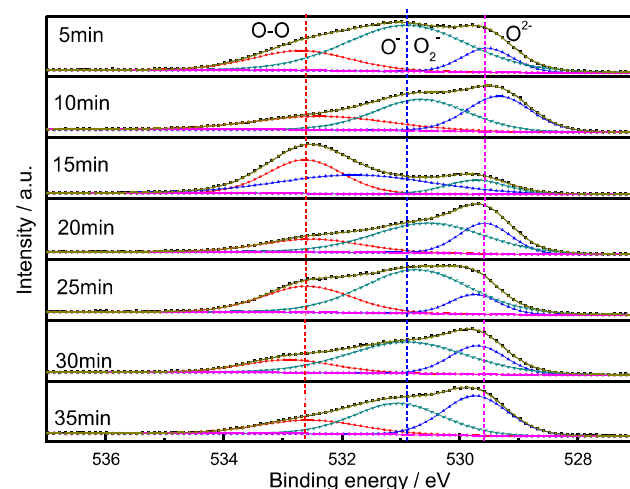


Fig. 13. O element valence distribution in CO<sub>2</sub> splitting processes.

Table 5

Evolution of elements valence and ratio of oxygen carrier in CO<sub>2</sub> splitting reaction.

| Sample<br>/CO <sub>2</sub><br>splitting | Fe 2p <sub>3/2</sub> / Atomic ratio |                  |                 | Ni 2p <sub>3/2</sub> / Atomic ratio |                            |                 | 1s/ Atomic ratio(%) |                                 |                |
|---|-------------------------------------|------------------|-----------------|-------------------------------------|----------------------------|-----------------|---------------------|---------------------------------|----------------|
|   | Fe <sup>3+</sup>                    | Fe <sup>2+</sup> | Fe <sup>0</sup> | Ni <sup>2+</sup><br>(Ni-Fe)         | Ni <sup>2+</sup><br>(Ni-O) | Ni <sup>0</sup> | O <sup>2-</sup>     | O <sup>2-</sup> /O <sup>-</sup> | O <sub>2</sub> |
| 5 min                                   | 22.99                               | 46.19            | 10.82           | 23.00                               | 51.76                      | 25.24           | 14.07               | 64.30                           | 21.63          |
| 10 min                                  | 24.14                               | 68.55            | 7.31            | 23.59                               | 52.05                      | 24.36           | 32.50               | 41.70                           | 25.80          |
| 15 min                                  | 24.98                               | 75.02            | -               | 38.87                               | 32.73                      | 28.40           | 33.70               | 46.30                           | 20.00          |
| 20 min                                  | 25.13                               | 74.87            | -               | 36.20                               | 36.05                      | 27.75           | 25.73               | 53.74                           | 20.53          |
| 25 min                                  | 26.69                               | 73.31            | -               | 50.77                               | 20.88                      | 28.35           | 20.23               | 59.05                           | 20.72          |
| 30 min                                  | 29.74                               | 70.26            | -               | 50.08                               | 23.70                      | 26.22           | 24.54               | 57.59                           | 17.88          |
| 35 min                                  | 30.15                               | 69.85            | -               | 54.47                               | 16.25                      | 29.28           | 38.35               | 41.05                           | 20.60          |

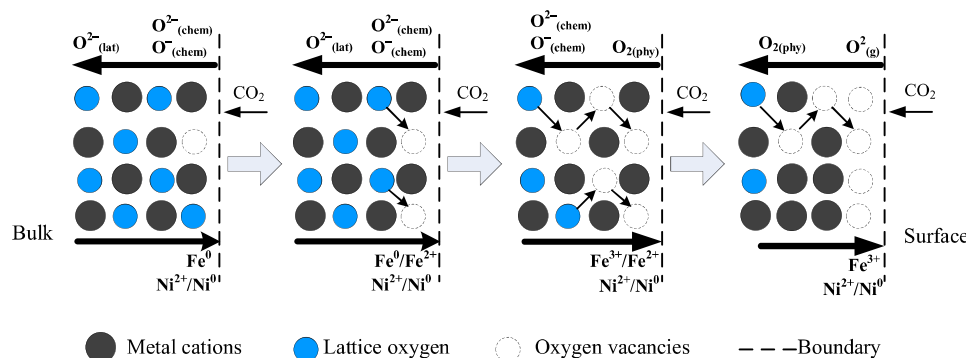


Fig. 14. Lattice oxygen migration path in CO<sub>2</sub> splitting reaction.

proportion distribution is listed in Table 5. The lattice oxygen transferred from the surface of oxygen carrier to the bulk phase in the CO<sub>2</sub> splitting process. The atomic ratios of oxygen O<sup>2-</sup>, O<sup>2-</sup>/O<sup>-</sup>, and O<sup>0</sup> on the surface of the oxygen carrier changed from 6.58 %, 62.66 %, and 30.76 % at the initial reaction to 14.07 %, 64.30 %, and 21.63 % after 5 min reaction, where the contents of lattice oxygen and chemisorbed oxygen of the oxygen carrier gradually increased with the reaction process. The physical adsorbed oxygen remained basically stable. Initially, a significant number of oxygen vacancies and active oxygen molecules get adsorbed onto the surface of the oxygen carrier, leading to an increase in the proportion of O<sup>0</sup>. As the reaction progresses, the O<sup>0</sup> species on the surface of the oxygen carrier gradually converted into O<sup>2-</sup> and O<sup>2-</sup>/O<sup>-</sup>. After 35 min, the atomic ratios of O<sup>2-</sup>, O<sup>2-</sup>/O<sup>-</sup>, and O<sup>0</sup> are measured to be 38.35 %, 41.05 %, and 20.60 %, respectively. The lattice oxygen migration path in CO<sub>2</sub> splitting reaction was as follows: CO<sub>2(g)</sub>  $\xrightarrow{e}$  O<sub>2(phy)</sub>  $\xrightarrow{e}$  O<sub>2</sub>/O<sub>(chemical)</sub>  $\xrightarrow{e}$  O<sub>(lattice)</sub>.

Based on the above analysis, the lattice oxygen migration mechanism of oxygen carriers in CO<sub>2</sub> splitting reaction was exhibited in Fig. 14. In this reaction, CO<sub>2</sub> decomposed on the surface of the oxygen carrier within oxygen vacancies, providing active oxygen to the oxygen carrier. This active oxygen accumulated on the surface, forming O<sub>2</sub>, which further converted into O<sup>2-</sup>/O<sup>-</sup> and lattice oxygen. The valence state of the Fe element increased within the oxygen carrier, while the Ni element remained relatively stable, as the oxygen vacancies in the carrier were partially recovered.

#### 4. Conclusion

In this paper, reaction kinetics and mechanisms for the CLGCS were systematically discussed. The main conclusions are as follows:

(1) The biomass CLG reaction process involved four stages based on the activation energy distribution calculated with Ozawa method: dehydration, pyrolysis, gas reforming, and char reacting with oxygen carrier. Ni provided an active site for the reduction of Fe<sub>2</sub>O<sub>3</sub>, resulting in a rapid decline in the activation energy of pyrolysis stage. The solid-solid reaction in char reacting stage needed to overcome the higher energy barrier, which exhibited the maximum activation energy 341.38 kJ/mol with  $\alpha=0.9$ . The activation energy of CO<sub>2</sub> splitting reaction increased steadily, indicating that the transfer resistance of lattice oxygen to the interior increased and the reaction energy barrier augmented correspondingly, where the apparent activation energy appeared 110.27 kJ/mol with  $\alpha=0.95$ .

(2) For the CLG reaction, the lattice oxygen O<sup>2-</sup> in the oxygen carrier initially dissociated into chemisorbed oxygen O<sup>2-</sup>/O<sup>-</sup>, which then converted physically adsorbed oxygen O<sub>2</sub> in surface of oxygen carrier from the bulk phase. The dissociation rate of Ni-Fe bond was lower than that of Ni-O bond. The transfer mechanism of lattice oxygen in CLG reaction was expressed as: O<sub>(lattice)</sub>  $\xrightarrow{e}$  O<sub>2</sub>/O<sub>(chemical)</sub>  $\xrightarrow{e}$  O<sub>2(phy)</sub>  $\xrightarrow{e}$  O<sub>2(g)</sub>. The lattice oxygen migration displayed an opposite trend in the process of CO<sub>2</sub>

splitting reaction. The presence of Ni played a catalytic activation role, facilitating the transfer of lattice oxygen rather than participating in the reaction, resulting in a relatively stable atomic content.

#### CRediT authorship contribution statement

**Haoran Yuan:** Writing – review & editing, Supervision, Resources, Methodology. **Xiaoyan Wu:** Validation, Investigation. **Yecheng Yao:** Visualization, Investigation, Data curation. **Guoqiang Wei:** Writing – original draft, Investigation, Funding acquisition, Conceptualization. **Yingjie Cai:** Visualization, Resources. **Zhanxiao Kang:** Data curation, Validation. **Shuai Peng:** Visualization, Formal analysis. **Zhongwang Gao:** Visualization, Software, Project administration. **Zhen Huang:** Validation, Resources, Funding acquisition. **Xixian Yang:** Supervision, Resources, Investigation, Conceptualization.

#### Declaration of Competing Interest

The authors declare that they have no known competing financial interests or personal relationships that could have appeared to influence the work reported in this paper

#### Acknowledgement

The financial support of National Natural Science Foundation of China (No. 52276191) is gratefully acknowledged. This work is also supported by the National Key Research and Development Program of China (No.2023YFC3905800), Guang Dong Basic and Applied Basic Research Foundation (No.2023B1515120062), the National Founded Postdoctoral Researcher Program of China (No. GZC20230856), the Foundation of State Key Laboratory of Clean and Efficient Coal Utilization, Taiyuan University of Technology (No. MJNYSKL202310) and the Foundation of State Key Laboratory of Coal Conversion (No. J24-25-101).

#### Data Availability

Data will be made available on request.

#### References

- Feng, Z., Dai, C., Shi, P., Lei, X., Guo, R., Wang, B., You, J., 2024. Seven mechanisms of oxygen evolution reaction proposed recently: a mini review. *Chem. Eng. J.* 485, 149992. <https://doi.org/10.1016/j.cej.2024.149992>.
- Galina, N.R., Arce, G.L.A.F., Ávila, I., 2019. Evolution of carbon capture and storage by mineral carbonation: Data analysis and relevance of the theme. *Min. Eng.* 142, 105879. <https://doi.org/10.1016/j.mineng.2019.105879>.
- Gao, E., Sun, G., Zhang, W., Bernards, M.T., He, Y., Pan, H., Shi, Y., 2020. Surface lattice oxygen activation via Zr<sup>4+</sup> cations substituting on A<sup>2+</sup> sites of MnCr<sub>2</sub>O<sub>4</sub> forming Zr<sub>x</sub>Mn<sub>1-x</sub>Cr<sub>2</sub>O<sub>4</sub> catalysts for enhanced NH<sub>3</sub>-SCR performance. *Chem. Eng. J.* 380, 122397. <https://doi.org/10.1016/j.cej.2019.122397>.

- Guo, M., Lin, J., Yu, J., Wang, S., Luo, K., Fan, J., 2024. Configuration optimization of a biomass chemical looping gasification (CLG) system combined with CO<sub>2</sub> absorption. *Renew. Energy* 237, 121459. <https://doi.org/10.1016/j.renene.2024.121459>.
- He, F., Huang, Z., Wei, G., Zhao, K., Wang, G., Kong, X., Feng, Y., Tan, H., Hou, S., Lv, Y., Jiang, G., Guo, Y., 2019. Biomass chemical-looping gasification coupled with water/CO<sub>2</sub>-splitting using NiFe<sub>2</sub>O<sub>4</sub> as an oxygen carrier. *Energy Convers. Manag.* 201, 112157. <https://doi.org/10.1016/j.enconman.2019.112157>.
- Huang, Z., Gao, N., Lin, Y., Wei, G., Zhao, K., Zheng, A., Li, H., 2022. Exploring the migration and transformation of lattice oxygen during chemical looping with NiFe<sub>2</sub>O<sub>4</sub> oxygen carrier. *Chem. Eng. J.* 429, 132064–132078. <https://doi.org/10.1016/j.cej.2021.132064>.
- Kayaki, Y., Yamamoto, M., Ikariya, T., 2009. N-heterocyclic carbenes as efficient organocatalysts for CO<sub>2</sub> fixation reactions. *Angew. Chem. Int. Ed. Engl.* 48 (23), 4194–4197. <https://doi.org/10.1002/anie.200901399>.
- Kimura, T., Kamata, K., Mizuno, N., 2012. A bifunctional tungstate catalyst for chemical fixation of CO<sub>2</sub> at atmospheric pressure. *Angew. Chem. Int. Ed. Engl.* 51 (27), 6700–6703. <https://doi.org/10.1002/anie.201203189>.
- Lan, T., Sun, W., Shi, X., Lu, Y., 2024. Na<sub>2</sub>WO<sub>4</sub>-doped Mn<sub>2</sub>O<sub>3</sub>-TiO<sub>2</sub> oxygen carrier catalyst for chemical looping OCM: redox catalysis and mechanistic insight. *Chem. Eng. J.* 484. <https://doi.org/10.1016/j.cej.2024.149368>.
- Li, J., Zeng, K., Zhong, D., Chen, X., Nzihou, A., Yang, H., Chen, H., 2024. Algae pyrolysis in alkaline molten salt: products transformation. *Fuel* 358, 129868. <https://doi.org/10.1016/j.fuel.2023.129868>.
- Lin, Y., Wang, H., Huang, Z., Liu, M., Wei, G., Zhao, Z., Fang, Y., 2020. Chemical looping gasification coupled with steam reforming of biomass using NiFe<sub>2</sub>O<sub>4</sub>: kinetic analysis of DAEM-TI, thermodynamic simulation of OC redox, and a loop test. *Chem. Eng. J.* 395, 125046. <https://doi.org/10.1016/j.cej.2020.125046>.
- Lu, J., Mao, X., Liu, Z., Liu, Y., Zhang, Q., Song, P., Tu, K., 2024. The global environmental impacts of China's accession to the WTO: a 20-year review. *Environ. Sci. Technol.* 58 (13), 5760–5771. <https://doi.org/10.1021/acs.est.3c10159>.
- Ma, C., Zhang, F., Hu, J., Wang, H., Yang, S., Liu, H., 2023. Co-pyrolysis of sewage sludge and waste tobacco stem: Gas products analysis, pyrolysis kinetics, artificial neural network modeling, and synergistic effects. *Bioresour. Technol.* 389, 129816. <https://doi.org/10.1016/j.biortech.2023.129816>.
- Peng, Q., Wang, J., Feng, Z., Du, C., Wen, Y., Shan, B., Chen, R., 2017. Enhanced photoelectrochemical water oxidation by fabrication of p-LaFeO<sub>3</sub>/n-Fe<sub>2</sub>O<sub>3</sub> heterojunction on hematite nanorods. *J. Phys. Chem. C* 121 (24), 12991–12998. <https://doi.org/10.1021/acs.jpcc.7b01817>.
- Pradhan, G., Parida, K., 2012. Dramatic enhancement of catalytic activity over transition metal substituted hematite. *J. Ind. Eng. Chem.* 18 (5), 1612–1619. <https://doi.org/10.1016/j.jiec.2012.02.022>.
- Qu, M., Qin, G., Du, A., Fan, J., Sun, Q., 2019. B80 fullerene: A promising metal-free photocatalyst for efficient conversion of CO<sub>2</sub> to HCOOH. *J. Phys. Chem. C* 123 (39), 24193–24199. <https://doi.org/10.1021/acs.jpcc.9b07562>.
- Shen, X., Wu, Y., Xu, X., Su, J., He, Z., Jiang, E., Ren, Y., Sun, Y., 2022. Torrefaction enhanced biomass chemical-looping gasification coupled with CO<sub>2</sub>-splitting via half doped LaFe<sub>0.5</sub>Mn<sub>0.5</sub>O<sub>3</sub> perovskite. *Fuel Process. Technol.* 234, 107314. <https://doi.org/10.2139/ssrn.4017527>.
- Son, E.N., Baek, S.H., Lee, R., Baek, J.I., Ryu, H.J., Yoo, D.J., Sohn, J.M., 2019. Study on the redox characteristics of CaCo based oxygen carrier for chemical looping combustion. *Chem. Eng. J.* 377, 121522. <https://doi.org/10.1016/j.cej.2019.04.102>.
- Sutthiumporn, K., Kawi, S., 2011. Promotional effect of alkaline earth over Ni-La<sub>2</sub>O<sub>3</sub> catalyst for CO<sub>2</sub> reforming of CH<sub>4</sub>: Role of surface oxygen species on H<sub>2</sub> production and carbon suppression. *Int. J. Hydrog. Energy* 36 (22), 14435–14446. <https://doi.org/10.1016/j.ijhydene.2011.08.022>.
- Wei, G., Huang, J., Fan, Y., Huang, Z., Zheng, A., He, F., Li, H., 2019. Chemical looping reforming of biomass based pyrolysis gas coupling with chemical looping hydrogen by using Fe/Ni/Al oxygen carriers derived from LDH precursors. *Energy Convers. Manag.* 179 304–313. <https://doi.org/10.1016/j.enconman.2018.10.065>.
- Wei, G., Feng, J., Hou, Y.L., Li, F.-Z., Li, W.Y., Huang, Z., Li, H., 2021. Ca-enhanced hematite oxygen carriers for chemical looping reforming of biomass pyrolyzed gas coupled with CO<sub>2</sub> splitting. *Fuel* 285, 119125–119134. <https://doi.org/10.1016/j.fuel.2020.119125>.
- Wei, G., Yang, M., Huang, Z., Bai, H., Chang, G., He, F., Lin, Y., 2022. Syngas production from lignite via chemical looping gasification with hematite oxygen carrier enhanced by exogenous metals. *Fuel* 321. <https://doi.org/10.1016/j.fuel.2022.124119>.
- Wei, G.Q., Zhao, W.N., Meng, J.G., Feng, J., Li, W.Y., He, F., Li, H.B., 2018. Hydrogen production from vegetable oil via a chemical looping process with hematite oxygen carriers. *J. Clean. Prod.* 200, 588–597. <https://doi.org/10.1016/j.jclepro.2018.07.263>.
- Yamashita, T., Hayes, P., 2008. Analysis of XPS spectra of Fe<sup>2+</sup> and Fe<sup>3+</sup> ions in oxide materials. *Appl. Surf. Sci.* 254 (8), 2441–2449. <https://doi.org/10.1016/j.apsusc.2007.09.063>.
- Yang, Z.Z., He, L.N., Zhao, Y.N., Li, B., Yu, B., 2011. CO<sub>2</sub> capture and activation by superbase/polyethylene glycol and its subsequent conversion. *Energy Environ. Sci.* 4 (10), 3971–3975. <https://doi.org/10.1039/C1EE02156G>.
- Zhang, H.X., Yu, X.Y., Su, X., Gao, X., Huang, Z.Q., Yang, B., Chang, C.R., 2024. Dopant-Enhanced harmonization of  $\alpha$ -Fe<sub>2</sub>O<sub>3</sub> oxygen migration and surface catalytic reactions during chemical looping reforming of methane. *Chem. Eng. J.* 481, 148446. <https://doi.org/10.1016/j.cej.2023.148446>.
- Zhang, S., Zhuang, Y., Liu, L., Zhang, L., Du, J., 2019. Risk management optimization framework for the optimal deployment of carbon capture and storage system under uncertainty. *Renew. Sust. Energ. Rev.* 113, 109280. <https://doi.org/10.1016/j.rser.2019.109280>.

CONTENTS

Full Length Articles

- Continuous modelling of cyclic ageing for lithium-ion batteries  
**D. Šeruga, A. Gosar, C.A. Sweeney, J. Jaguemont, J. Van Mierlo and M. Nagode** 119079
- Investigation on the limiting oxygen concentration of combustible gas at high pressures and temperatures during oil recovery process  
**P. Li, Z. Liu, M. Li, Y. Zhao, X. Li, S. Wan, Y. Ma and Y. He** 119157
- Planning renewable energy introduction for a microgrid without battery storage  
**S. Obara, S. Fujimoto, K. Sato and Y. Utsugi** 119176
- Experimental air/particle flow characteristics of an 80,000 Nm<sup>3</sup>/h fly ash entrained-flow gasifier with different multi-burner arrangements  
**N. Fang, Z. Li, S. Liu, C. Xie, L. Zeng and Z. Chen** 119160
- Spark and flame kernel interaction with dual-pulse laser-induced spark ignition in a lean premixed methane–air flow  
**L. Wermer, J.K. Lefkowitz, T. Ombrello and S.-k. Im** 119162
- Influence of Al<sub>2</sub>O<sub>3</sub> nano additives in ternary fuel (diesel-biodiesel-ethanol) blends operated in a single cylinder diesel engine: Performance, combustion and emission characteristics  
**H. Venu, V.D. Raju, S. Lingesan and M. Elahi M Soudagar** 119091
- A high efficiency stirling-type pulse tube refrigerator for cooling above 200 K  
**B. Wang, Y. Chao, Q. Zhao, H. Wang, Y. Wang and Z. Gan** 119120
- Methodological analysis of variable geometry turbine technology impact on the performance of highly downsized spark-ignition engines  
**J.R. Serrano, P. Piqueras, J. De la Morena, A. Gómez-Vilanova and S. Guilain** 119122
- Debottlenecking cogeneration systems under process variations: Multi-dimensional bottleneck tree analysis with neural network ensemble  
**S.Y. Teng, W.D. Leong, B.S. How, H.L. Lam, V. Máša and P. Stehlik** 119168
- Terminalia chebula* as a novel green source for the synthesis of copper oxide nanoparticles and as feedstock for biodiesel production and its application on diesel engine  
**K.V. Yatish, R.M. Prakash, C. Ningaraju, M. Sakar, R. GeethaBalakrishna and H.S. Lalithamba** 119165
- Rotation improvement of vertical axis wind turbine by offsetting pitching angles and changing blade numbers  
**X. Sun, J. Zhu, Z. Li and G. Sun** 119177
- The survey of the combined heat and compressed air energy storage (CH-CAES) system with dual power levels turbomachinery configuration for wind power peak shaving based spectral analysis  
**P. Zhao, P. Wang, W. Xu, S. Zhang, J. Wang and Y. Dai** 119167
- Risk-constrained stochastic market operation strategies for wind power producers and energy storage systems  
**O. Lak, M. Rastegar, M. Mohammadi, S. Shafiee and H. Zareipour** 119092
- Heterogeneous effects of energy efficiency and renewable energy on economic growth of BRICS countries: A fixed effect panel quantile regression analysis  
**R. Akram, F. Chen, F. Khalid, G. Huang and M. Irfan** 119019
- Development and performance assessment power generating systems using clean hydrogen  
**O. Oruc and I. Dincer** 119100

CONTENTS— continued on inside back cover

Abstracted/indexed in: Applied Sci. & Tech. Index, Biosis Data, Cam. Sci. Abstr. Chem. Abstr. Serv. Curr. Cont. Eng. Tech. & Applied Sci., Elsevier BIOBASE/Current Awareness in Biological Sciences; Eng. Ind., Environ. Per. Bibl., INSPEC Data, Res. Alert, Curr. Cont. Sci. Cit. Indx., Curr. Cont. SCISEARCH Data. Also covered in the abstract and citation database SCOPUS®. Full text available on ScienceDirect®



ELSEVIER



0360-5442(20210115)215:PB;1-E

ISSN 0360-5442

Printed by Henry Ling in the United Kingdom

483



TECHNOLOGIES

RESOURCES

RESERVES

DEMAND



IMPACT

CONSERVATION

MANAGEMENT

POLICY

The International Journal

Available online at [www.sciencedirect.com](http://www.sciencedirect.com)

ScienceDirect



## AIMS AND SCOPE

*Energy* is an international, multi-disciplinary journal in energy engineering and research. The journal aims to be a leading peer-reviewed platform and an authoritative source of information for analyses, reviews and evaluations related to energy. The journal covers research in mechanical engineering and thermal sciences, with a strong focus on energy analysis, energy modelling and prediction, integrated energy systems, energy planning and energy management. The journal also welcomes papers on related topics such as energy conservation, energy efficiency, biomass and bioenergy, renewable energy, electricity supply and demand, energy storage, energy in buildings, and on economic and policy issues, provided such topics are within the context of the broader multi-disciplinary scope of *Energy*.

© 2020 Elsevier Ltd. All rights reserved.

This journal and the individual contributions contained in it are protected under copyright, and the following terms and conditions apply to their use in addition to the terms of any Creative Commons or other user license that has been applied by the publisher to an individual article:

### Photocopying

Single photocopies of single articles may be made for personal use as allowed by national copyright laws. Permission is not required for photocopying of articles published under the CC BY license nor for photocopying for non-commercial purposes in accordance with any other user license applied by the publisher. Permission of the publisher and payment of a fee is required for all other photocopying, including multiple or systematic copying, copying for advertising or promotional purposes, resale, and all forms of document delivery. Special rates are available for educational institutions that wish to make photocopies for non-profit educational classroom use.

### Permissions

For information on how to seek permission visit [www.elsevier.com/permissions](http://www.elsevier.com/permissions)

### Derivative works

Users may reproduce tables of contents or prepare lists of articles including abstracts for internal circulation within their institutions or companies. Other than for articles published under the CC BY license, permission of the publisher is required for resale or distribution outside the subscribing institution or company.

For any subscribed articles or articles published under a CC BY-NC-ND license, permission of the publisher is required for all other derivative works, including compilations and translations.

### Electronic storage or usage

Permission of the Publisher is required to store or use electronically any material contained in this journal, including any article or part of an article (please consult [www.elsevier.com/permissions](http://www.elsevier.com/permissions)).

Except as outlined above or as set out in the relevant user license, no part of this publication may be reproduced, stored in a retrieval system or transmitted in any form or by any means, electronic, mechanical, photocopying, recording or otherwise, without prior written permission of the publisher.

### Author rights

Author(s) may have additional rights in their articles as set out in their agreement with the publisher (more information at <http://www.elsevier.com/authorsrights>).

### Notice

Practitioners and researchers must always rely on their own experience and knowledge in evaluating and using any information, methods, compounds or experiments described herein. Because of rapid advances in the medical sciences, in particular, independent verification

of diagnoses and drug dosages should be made. To the fullest extent of the law, no responsibility is assumed by the publisher for any injury and/or damage to persons or property as a matter of products liability, negligence or otherwise, or from any use or operation of any methods, products, instructions or ideas contained in the material herein.

Although all advertising material is expected to conform to ethical (medical) standards, inclusion in this publication does not constitute a guarantee or endorsement of the quality or value of such product or of the claims made of it by its manufacturer.

**Funding body agreements and policies:** Elsevier has established agreements and developed policies to allow authors who publish in Elsevier journals to comply with potential manuscript archiving requirements as specified as conditions of their grant awards. To learn more about existing agreements and policies please visit <http://www.elsevier.com/funding-bodies>.

**Publication information:** *Energy* (ISSN 0360-5442). For 2021 volumes 214-237 (24 issues) are scheduled for publication. Subscription prices are available upon request from the Publisher or from the Elsevier Customer Service Department nearest you or from this journal's website (<http://www.elsevier.com/locate/energy>). Further information is available on this journal and other Elsevier products through Elsevier's website (<http://www.elsevier.com>). Subscriptions are accepted on a prepaid basis only and are entered on a calendar year basis. Issues are sent by standard mail (surface within Europe, air delivery outside Europe). Priority rates are available upon request. Claims for missing issues should be made within six months of the date of dispatch.

**Orders, claims, and journal inquiries:** Please visit our Support Hub page <https://service.elsevier.com> for assistance.

### Author inquiries:

You can track your submitted article at <http://www.elsevier.com/track-submission>. You can track your accepted article at <http://www.elsevier.com/trackarticle>. You are also welcome to contact Customer Support via <http://support.elsevier.com>.

### Advertising information:

If you are interested in advertising or other commercial opportunities please e-mail [Commercialsales@elsevier.com](mailto:Commercialsales@elsevier.com) and your inquiry will be passed to the correct person who will respond to you within 48 hours.

### Language (usage and editing services)

Please write your text in good English (American or British usage is accepted, but not a mixture of these). Authors who feel their English language manuscript may require editing to eliminate possible grammatical or spelling errors and to conform to correct scientific English may wish to use the English Language Editing service available from Elsevier's WebShop <http://webshop.elsevier.com/languageediting/> or visit our customer support site <http://support.elsevier.com> for more information.

### Illustration services

Elsevier's WebShop (<http://webshop.elsevier.com/illustrationservices/>) offers Illustration Services to authors preparing to submit a manuscript but concerned about the quality of the images accompanying their article. Elsevier's expert illustrators can produce scientific, technical and medical-style images, as well as a full range of charts, tables and graphs. Image "polishing" is also available, where our illustrators take your image(s) and improve them to a professional standard. Please visit the website to find out more.

For a full and complete Guide for Authors, please go to: <http://www.elsevier.com/locate/energy>

Printed by Henry Ling in the United Kingdom

The paper used in this publication meets the requirements of ANSI/NISO Z39.48-1992 (Permanence of Paper)

## CONTENTS—continued from outside back cover

Distribution Network Reconfiguration based on LMP at DG connected busses using game theory and self-adaptive FWA

E. Azad-Farsani, I.G. Sardou and S. Abedini

119146

Stability study of hydrogen-air flame in a conical porous burner

V. Zangeneh and A. Alipoor

119140

Research on energy conversion efficiency of the reconfigurable reconnection electromagnetic launcher

G. Fan, Y. Wang, K. Hou, Y. Miao, Y. Hu and Z. Yan

119088

Using long short-term memory model to study risk assessment and prediction of China's oil import from the perspective of resilience theory

S. Chen, Y. Song, Y. Ding, M. Zhang and R. Nie

119152

Gender differences and productive use of energy fuel in Ghana's rural non-farm economy

M.O. Asibey, K.A. Ocloo and O. Amponsah

119068

Investigation of the performance of a hybrid PV/thermal system using water/silver nanofluid-based optical filter

A.S. Abdelrazik, R. Saidur and F.A. Al-Sulaiman

119172

Improving the environment begins at home: Revisiting the links between FDI and environment

R.M. Adeel-Farooq, M.F. Riaz and T. Ali

119150

Study on fundamental link between mixing efficiency and entrainment performance of a steam ejector

Y. Tang, Z. Liu, Y. Li, Z. Huang and K.J. Chua

119128

Volatile-char interactions during biomass pyrolysis: Effect of char preparation temperature

B. Li, L. Zhao, X. Xie, D. Lin, H. Xu, S. Wang, Z. Xu, J. Wang, Y. Huang, S. Zhang, X. Hu and D. Liu

119189

Reliability assessment and congestion management of power system with energy storage and uncertain renewable resources

V.K. Prajapati and V. Mahajan

119134

In-situ synchrotron characterisation of fracture initiation and propagation in shales during indentation

L. Ma, A.-L. Fauchille, M.R. Chandler, P. Dowe, K.G. Taylor, J. Mecklenburgh and P.D. Lee

119161

Corrosion performance of candidate boiler tube alloys under advanced pressurized oxy-fuel combustion conditions

K. Li, Y. Zeng and J.-L. Luo

119178

Analysis of factors influencing actual absorption of solar energy by building walls

H. Li, H. Jia, K. Zhong and Z. Zhai

118988

Do economic development and human capital decrease non-renewable energy consumption? Evidence for OECD countries

R. Alvarado, Q. Deng, B. Tillaguango, P. Méndez, D. Bravo, J. Chamba, M. Alvarado-Lopez and M. Ahmad

119147

Energy saving potential for space heating in Chinese airport terminals: The impact of air infiltration

X. Liu, T. Zhang, X. Liu, L. Li, L. Lin and Y. Jiang

119175

Energy utilization and disposal of herb residue by an integrated energy conversion system: A pilot scale study

L. Dong, J. Tao, Z. Zhang, B. Yan, Z. Cheng and G. Chen

119192

Numerical research on combustion and emissions behaviors of a medium compression ratio direct-injection twin-spark plug synchronous ignition methanol engine under steady-state lean-burn conditions

C. Gong, J. Sun and F. Liu

119193

Investigation on the EGR effect to further improve fuel economy and emissions effect of Miller cycle turbocharged engine

K. Shen, Z. Xu, H. Chen and Z. Zhang

119116

Comparison of activated carbons prepared by one-step and two-step chemical activation process based on cotton stalk for supercapacitors application

J. Cheng, S.-C. Hu, G.-T. Sun, K. Kang, M.-Q. Zhu and Z.-C. Geng

119144

Testing the persistence of shocks on renewable energy consumption: Evidence from a quantile unit-root test with smooth breaks

C.-C. Lee, O. Ranjbar and C.-C. Lee

119190

Development of physical-chemical surrogate models and skeletal mechanism for the spray and combustion simulation of RP-3 kerosene fuels

Y. Bai, Y. Wang, X. Wang, Q. Zhou and Q. Duan

119090

CONTENTS—continued on Back Matter

*CONTENTS– continued from inside back cover*

Experimental electro-hydrodynamic investigation of flag-based energy harvesting in the wake of inverted C-shape cylinder

**U. Latif, E. Uddin, M.Y. Younis, J. Aslam, Z. Ali, M. Sajid and A. Abdelkefi**

Energy cooperation between Myanmar and China under One Belt One Road: Current state, challenges and perspectives

**B. Yang, T. Swe, Y. Chen, C. Zeng, H. Shu, X. Li, T. Yu, X. Zhang and L. Sun**

Lateral comparison of the coupling parameters on the novel hexagonal shaped cross flow thermoelectric generator

**R. Zhang, H. Zhang and X. Wang**

Reaction performance of Ce-enhanced hematite oxygen carrier in chemical looping reforming of biomass pyrolyzed gas coupled with CO<sub>2</sub> splitting

**G. Wei, H. Zhou, Z. Huang, A. Zheng, K. Zhao, Y. Lin, G. Chang, Z. Zhao, H. Li and Y. Fang**

Energy cost and efficiency analysis of building resilience against power outage by shared parking station for electric vehicles and demand response program

**M.-W. Tian and P. Talebizadehsardari**

Stochastic synergies of urban transportation system and smart grid in smart cities considering V2G and V2S concepts

**M. Jafari, A. Kavousi-Fard, T. Niknam and O. Avatefipour**

Experimental investigation of exergetic efficiency of 3 side concave dimple roughened absorbers

**V. Kumar Dr.**

CO<sub>2</sub> capture performance and mechanism of blended amine solvents regulated by N-methylcyclohexylamine

**R. Wang, S. Liu, Q. Li, S. Zhang, L. Wang and S. An**

A hybrid deep transfer learning strategy for short term cross-building energy prediction

**X. Fang, G. Gong, G. Li, L. Chun, W. Li and P. Peng**

Low return temperature from domestic hot-water system based on instantaneous heat exchanger with chemical-based disinfection solution

**T. Benakopoulos, M. Tunzi, R. Salenbien, D. Vanhoudt and S. Svendsen**

An integrative approach for evaluating the environmental economic efficiency

**B. Singpai and D.D. Wu**

118940

119195 Assessment of the energy recovery potential of oil sludge through gasification aiming electricity generation

**Y. Castillo Santiago, A. Martínez González, O.J. Venturini and D.M. Yepes Maya**

119210

119130 Thermodynamic carbon pump 2.0: Elucidating energy efficiency through the thermodynamic cycle

**S. Li, S. Deng, L. Zhao, R. Zhao and X. Yuan**

119155

119163 A two-stage multi-objective optimal scheduling in the integrated energy system with We-Energy modeling

**N. Zhang, Q. Sun and L. Yang**

119121

119044 How does cleaner energy transition influence standard of living and natural resources conservation? A study of households' perceptions in rural Odisha, India

**S.S. Swain and P. Mishra**

119135

119058 Wind speed modeling for cascade clusters of wind turbines Part 2: Wind speed reduction and aggregation superposition

**X. Dong, J. Li, D. Gao and K. Zheng**

119145

119054 Development of biochar from the refuse derived fuel (RDF) through organic / inorganic sludge mixed with rice straw and coconut shell

**S. Shangdiar, Y.-C. Lin, P.-C. Cheng, F.-C. Chou and W.-D. Wu**

119151

119039 Experimental investigation of the exact role of large-molecule guest substances (LMGSs) in determining phase equilibria and structures of natural gas hydrates

**J. Lee, D. Lee and Y. Seo**

119219

119209 Ceiling thermal impingement spread characteristics induced by wall-attached fires under various sub-atmospheric pressures

**F. Tang, P. Hu and C. Shi**

119127

119208 Short-term wind speed time series forecasting based on a hybrid method with multiple objective optimization for non-convex target

**Y. Dong, J. Wang, L. Xiao and T. Fu**

119180

119211 Ranking PCMs for building façade applications using multi-criteria decision-making tools combined with energy simulations

**T. Mukhamet, S. Kobeyev, A. Nadeem and S.A. Memon**

119102

*CONTENTS– continued on Next Page*



# Reaction performance of Ce-enhanced hematite oxygen carrier in chemical looping reforming of biomass pyrolyzed gas coupled with CO<sub>2</sub> splitting

Guoqiang Wei <sup>a, b</sup>, Huan Zhou <sup>a, b</sup>, Zhen Huang <sup>a, \*</sup>, Anqing Zheng <sup>a, \*\*</sup>, Kun Zhao <sup>a</sup>, Yan Lin <sup>a</sup>, Guozhang Chang <sup>d</sup>, Zengli Zhao <sup>a</sup>, Haibin Li <sup>a</sup>, Yitian Fang <sup>c</sup>

<sup>a</sup> Guangzhou Institute of Energy Conversion, Chinese Academy of Sciences (CAS), Key Laboratory of Renewable Energy, CAS, Guangzhou, 510640, China

<sup>b</sup> Training Base of State Key Laboratory of Coal Science and Technology Jointly Constructed By Shanxi Province and Ministry of Science and Technology, Taiyuan University of Technology, Taiyuan, 030024, China

<sup>c</sup> State Key Laboratory of Coal Conversion, Institute of Coal Chemistry, Chinese Academy of Sciences, Taiyuan, 030001, China

<sup>d</sup> State Key Laboratory of High-efficiency Utilization of Coal and Green Chemical Engineering, Ningxia University, Yinchuan, 750021, China

## ARTICLE INFO

### Article history:

Received 27 July 2020

Received in revised form

29 September 2020

Accepted 7 October 2020

Available online 8 October 2020

### Keywords:

Biomass pyrolyzed gases

Oxygen carrier

FeCeO<sub>3</sub>

Chemical looping reforming

CO<sub>2</sub> splitting

## ABSTRACT

Hematite enhanced by CeO<sub>2</sub> were investigated in chemical looping reforming (CLR) coupled with CO<sub>2</sub> splitting to achieve high quality synthesis gas and recycle CO<sub>2</sub> into CO. CeO<sub>2</sub>, Fe<sub>2</sub>O<sub>3</sub> and CeFeO<sub>3</sub> solid solution generated from integration of Fe<sup>3+</sup> and CeO<sub>2</sub> lattice were detected in mixed oxygen carriers as major components. Owing to the charge compensation and oxygen defects formation in lattice rearrangement, CeFeO<sub>3</sub> solid solution contributed to promoting oxygen mobility and creating oxygen vacancies. Fe<sub>2</sub>O<sub>3</sub> particles helped provide oxygen spillover pathway from subsurface to surface and improve lattice oxygen transfer through direct contact with the surface of CeFeO<sub>3</sub> solid solution. CeO<sub>2</sub> enhanced metallic interaction and catalytic oxidation reactivity. The highest gas product amount and H<sub>2</sub>/CO in CLR process increased by 43.46% and 51.31%, respectively. Also, the instantaneous CO productivity of 2.47 mmol/min/g with 86.13% CO<sub>2</sub> conversion was realized in CO<sub>2</sub> splitting. Reaction parameters including temperature, CeO<sub>2</sub> content and M<sub>CO2</sub>/m<sub>OC</sub> indicated positive correlation with CO productivity. The mixed oxygen carrier maintained its reactivity and stability after 15 cycles reaction following the pathway of Ce<sub>2</sub>O<sub>3</sub>/Fe<sub>2</sub>O<sub>3</sub>/CeFeO<sub>3</sub> → Ce<sub>2</sub>O<sub>3</sub>/Fe → CeFeO<sub>3</sub>/CeO<sub>2</sub>/Fe<sub>3</sub>O<sub>4</sub>, though sintering behavior was observed in reacted sample. Fe–Ce interactions and oxygen mobility were improved by successive redox reactions, which can offset the negative effects of sintering.

© 2020 Published by Elsevier Ltd.

## 1. Introduction

The emission of CO<sub>2</sub> from the burning of fossil fuels has made an unprecedented challenge to the climate change and caused wide concern in the recent years. Nations around the world are making efforts to reduce CO<sub>2</sub> emission and control the global temperature rise below 2 °C based the implementation of Paris Agreement. In fact, there are several alternative ways to reduce the CO<sub>2</sub> accumulation in atmosphere [1]. One way to reduce CO<sub>2</sub> emissions is the carbon capture and storage technology, which captures CO<sub>2</sub> in the

emission sources and stores it in geological formations, such as depleted oil fields or deep saline aquifers. This technology helps reduce carbon emission, but requires extra huge investment in infrastructure and enough storage space [2,3]. Moreover, Chemical Looping Combustion (CLC) is viewed as an effective option to reduce CO<sub>2</sub> emission with avoiding N<sub>2</sub> dilution in products and easy sequestration of pure CO<sub>2</sub>, which oxidizes fuel through lattice oxygen of oxygen carrier instead of molecular oxygen [4]. Actually, the CLC process has been investigated extensively over the past three decades as a new technology for power generation with CO<sub>2</sub> capture. However, this technology has not yet involved in the utilization of CO<sub>2</sub>, which has an important role in reducing anthropogenic CO<sub>2</sub> emissions. A good example is the chemical conversion of CO<sub>2</sub> into useable fuels or other chemicals via F-T synthesis or fuel preparation processes where CO<sub>2</sub> is used as feedstock. Although the

\* Corresponding author.

\*\* Corresponding author.

E-mail addresses: [weigq@ms.giec.ac.cn](mailto:weigq@ms.giec.ac.cn) (G. Wei), [huangzhen@ms.giec.ac.cn](mailto:huangzhen@ms.giec.ac.cn) (Z. Huang), [zhengaq@ms.giec.ac.cn](mailto:zhengaq@ms.giec.ac.cn) (A. Zheng).

**Notation list**

|                                |                                     |
|--------------------------------|-------------------------------------|
| AR                             | air reactor                         |
| CR                             | carbon reactor                      |
| Ar                             | argon                               |
| Fe <sup>3+</sup>               | ferric ion                          |
| CeO                            | cerium oxide                        |
| Fe <sub>2</sub> O <sub>3</sub> | iron oxide                          |
| CCS                            | CO <sub>2</sub> capture and storage |
| Fe <sub>3</sub> O <sub>4</sub> | ferroferric oxide                   |
| CH <sub>4</sub>                | methane                             |
| FR                             | fuel reactor                        |
| CLC                            | chemical looping combustion         |
| H <sub>2</sub>                 | hydrogen                            |
| CLG                            | chemical looping gasification       |
| [O]                            | lattice oxygen                      |

|                                   |   |
|-----------------------------------|---|
| CLR                               | chemical looping reforming                      |
| SEM                               | scanning electron microscopy                    |
| CO                                | carbon monoxide                                 |
| TPR                               | H <sub>2</sub> temperature programmed reduction |
| CO <sub>2</sub>                   | carbon dioxide                                  |
| XRD                               | X-ray diffraction                               |
| Ce <sup>2+</sup>                  | cerium ion                                      |
| XRF                               | X-ray fluorescence                              |
| Ce <sub>2</sub> FeO <sub>4</sub>  | cerium iron oxide                               |
| η <sub>CH4</sub>                  | CH <sub>4</sub> conversion                      |
| CaFeO <sub>3</sub>                | cerium iron oxide                               |
| η <sub>CO2</sub>                  | CO <sub>2</sub> conversion                      |
| Ce(NO <sub>3</sub> ) <sub>3</sub> | cerium nitrate                                  |
| ξ                                 | H <sub>2</sub> /CO molar ratio                  |
| Ce <sup>4+</sup>                  | cerium ion–                                     |

chemical conversion process helps recycle CO<sub>2</sub> into high value chemicals [5,6], there is still a key challenge for this process in activation or splitting CO<sub>2</sub> owing to its extremely stable molecular structure. The splitting process requires not only energy input but also appropriate catalyst [7]. Therefore, a novel process needs to be developed to facilitate the splitting of CO<sub>2</sub> into small molecule compounds (eg. CO) with high efficiency, low cost and catalyst free.

Additionally, using clean renewable energy instead of fossil fuels is another effective way to reduce carbon emissions. Biomass is an ideal alternative energy to the fossil fuels with the advantages of carbon neutral, low pollution and widespread distribution [8,9]. Owing to the pressing demand for power generation and F-T synthesis, biomass gasification to produce synthesis gas with gasifying agent like air, steam or oxygen carriers is viewed a promising utilization method. Intensive studies have been performed on the biomass gasification covering the topic of gasifying agent, reaction process, product composition, energy consumption, etc [10,11]. It is noted that Chemical Looping Gasification (CLG) of biomass reveals advantages in avoiding N<sub>2</sub> dilution, improving gas heating value, reducing tar content and cutting gasification cost, which produces synthesis gas from biomass by using lattice oxygen of oxygen carriers instead of molecular oxygen [12]. Although fundamental knowledge and significant insights for the potential breakthroughs have been achieved in the previous researches focusing on biomass CLG process, there are still some challenges for this process in coupling of F-T synthesis directly due to the presence of impurity gases (e.g. CO<sub>2</sub>, CH<sub>4</sub>) in synthesis gas products [13,14]. Traditionally, the separation of impurity gas from synthesis gas needs high energy consumption. A novel approach without removing impurity gases and high separation energy consumption is needed to be further investigated to integrate F-T synthesis directly.

Therefore, Chemical Looping Reforming (CLR) of biomass pyrolyzed gas coupled with CO<sub>2</sub> splitting process was proposed to improve biomass pyrolyzed gas product quality and achieve CO from CO<sub>2</sub> with low cost, high efficiency and simple operation. This process reveals better advantage on meeting the F-T synthesis requirement and utilizing greenhouse gas. As depicted in Fig. 1, a typical CLR coupled with CO<sub>2</sub> splitting system is composed of FR (fuel reactor), CR (carbon reactor), AR (air reactor), forming a redox looping system. The biomass pyrolyzed gas CLR reaction and CO<sub>2</sub> splitting reaction occur in FR and CR separately, then the used oxygen carrier is recovered to its initial state in AR. The oxygen carrier (Me<sub>x</sub>O<sub>y</sub>) circulates between the three reactors to transport lattice oxygen and reaction heat. High quality synthesis gas and pure CO are generated successively from the FR and CR without intensive

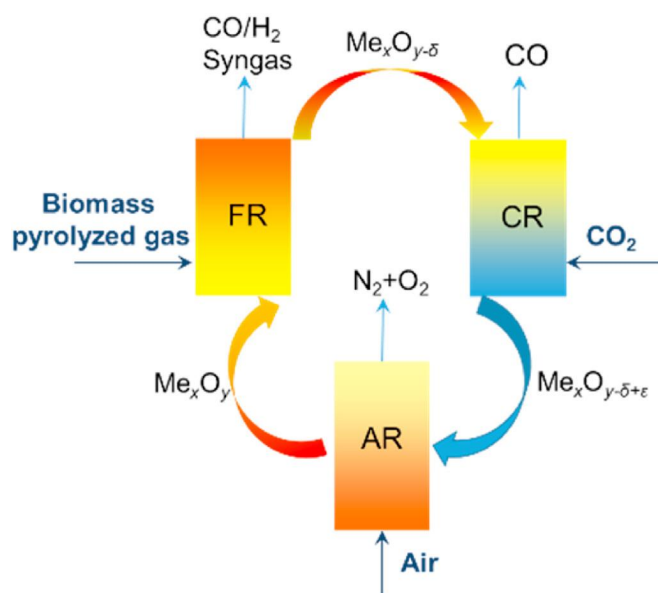


Fig. 1. CLR of biomass pyrolyzed gases coupled with CO<sub>2</sub> splitting process.

energy input and specific catalyst. Obviously, this reaction process reveals better advantages in high quality synthesis gas production, CO<sub>2</sub> recycling and low cost operation.

In view of the significant role of oxygen carriers in transfer lattice oxygen and reaction heat, the design and evaluation of oxygen carriers are key factors to the CLR of biomass pyrolyzed gases coupled with CO<sub>2</sub> splitting process. In fact, oxygen carriers related to Fe, Mn, Cu, Ni, Co, Ce, CaSO<sub>4</sub>, etc. have been extensively investigated in the past decades [15–20]. It is noted that the design and application of oxygen carriers are gradually focused on Fe-based oxygen carriers among these types of oxygen carriers in the recent years. There are many excellent advantages for the Fe-based oxygen carriers in low preparation cost, good thermal stability, high mechanical strength, anti-sintering, high oxygen content and environmental protection, which are beneficial to the large scale industrial application of fluidized bed [21]. A recent research by Barnali Bhui et al. [22] displays that low cost Fe<sub>2</sub>O<sub>3</sub> using as oxygen carrier for the North East Indian coal can achieve highest CO<sub>2</sub> yield of 96% in CLC reaction conditions. Another investigation by



Guoqiang Wei et al. [23] reveals that nature hematite can be used as oxygen carrier in the CLG of lignite to achieve high purity synthesis gas. Also, Laihong Shen et al. [24] report that the CLG process of coal has been carried out in a 5 kW<sub>th</sub> interconnected fluidized bed with a two-stage fuel reactor and natural hematite oxygen carrier. The maximum gasification efficiency and syngas yield at 915 °C reach to 75.2% and 0.97 Nm<sup>3</sup>/kg of coal, respectively. Whereas, there are still some shortcomings for the single Fe-base oxygen carriers in reactivity, lattice oxygen transfer, fuel conversion efficiency and product selectivity. It has been proved to be an effective way to construct mixed oxygen carrier based on the synergistic effects between metals [25,26]. Multiple investigations can be found in literatures about the Fe-based mixed oxygen carriers. Ce–Fe mixed oxygen carriers exhibit good reactivity and stability during the chemical looping redox cycles [27–29]. Actually, Kongzhai Li et al. [30–32] have shown in their researches that Fe<sub>2</sub>O<sub>3</sub> can be enhanced by CeO<sub>2</sub> in chemical looping process to maintain high reactivity and stability mainly based on the formation of Fe–Ce solid solution which brings about abundant oxygen vacancies and promotes oxygen mobility. Also, the presence of CeO<sub>2</sub> helps improve the carbon deposition resistance of oxygen carrier. In additionally, Wenguo Xiang et al. [33] also demonstrate that CeO<sub>2</sub> is excellent alternative support for Fe-based oxygen carrier in chemical looping hydrogen generation process, which enhances oxygen mobility, redox reactivity and carbon deposition resistance. Haoquan Hu et al. [34] find that Ce doping to Fe<sub>2</sub>O<sub>3</sub> could increase the heavy oil conversion and yields of gasoline in chemical looping partial oxidation of vacuum residue, which is attributed to the formation of solid solution, increasing specific surface area and oxygen vacancy concentration. Nicholas C. Means et al. [35] evaluate the redox performance of Fe<sub>2</sub>O<sub>3</sub>/CeO<sub>2</sub>/ZrO<sub>2</sub> oxygen carriers under high temperature in situ gasification CLC conditions. They point out the Fe–Ce oxygen carrier has the highest oxygen transport capability owing to the formation of CeFeO<sub>3</sub>. Fang liu et al. [36] also report the promotional role of the CeO<sub>2</sub> additive in iron based oxygen carrier, creating oxygen vacancies in a solid solution.

Therefore, this study aims to achieve high quality biomass synthesis gas and recycle CO<sub>2</sub> into CO via biomass pyrolyzed gas CLR coupled with CO<sub>2</sub> splitting process by using Ce-enhanced hematite oxygen carriers based on the favorable characteristic of Ce–Fe solid solution which increases oxygen vacancies and promotes the lattice oxygen mobility in reaction process.

## 2. Experimental and apparatus

### 2.1. Materials

The Ce–Fe mixed oxygen carriers were synthesized by chemical impregnation method, which used natural ore as supporting matrix and Ce(NO<sub>3</sub>)<sub>3</sub>·6H<sub>2</sub>O analytical pure as external cerium ion source. In a typical preparation process of Ce–Fe mixed oxygen carriers, natural hematite ore obtained from China was crushed into particles with grain size of 0.18–0.25 mm and the Ce(NO<sub>3</sub>)<sub>3</sub>·6H<sub>2</sub>O samples were weighed with the CeO<sub>2</sub>/hematite mass ratio of 5 wt%, 10 wt%, 15 wt% and 20 wt%. Next, the weighted Ce(NO<sub>3</sub>)<sub>3</sub>·6H<sub>2</sub>O analytical pure samples were dissolved into aqueous solution, respectively. The hematite ore particles were incipient impregnated by the above Ce(NO<sub>3</sub>)<sub>3</sub>·6H<sub>2</sub>O solution samples separately and evaporated water in a thermostatic oscillator at 60 °C to synthesized well-mixed samples. The resulting metal oxides were dried in drying oven for 12 h and calcined in muffle furnace for 4 h at 950 °C in air atmosphere. Consequently, Ce–Fe mixed oxygen carriers were synthesized with the CeO<sub>2</sub>/hematite mass ratio of 5 wt%, 10 wt%, 15 wt% and 20 wt%, which were marked as CH0, CH5, CH10, CH15 and CH20, respectively. The principal elements component of

nature hematite ore were detected by X Ray Fluorescence and the results were shown as follows, 63.50 wt%Fe, 33.88 wt%O, 2.63 wt% Si, 1.44 wt% Al, 0.13 wt% Ca, 0.09 wt% P, 0.08 wt% Mg, 0.05 wt% Mn, 0.04 wt%Ti and 0.01 wt%Cr. Moreover, the gas mixture consisting of 15 vol% H<sub>2</sub>, 30 vol% CO, 12.5 vol% CH<sub>4</sub>, 5 vol% CO<sub>2</sub>, 37.5 vol% N<sub>2</sub> was used as biomass pyrolyzed model gas. CO<sub>2</sub> analytical pure with the volume fraction more than 99.99 vol% was adopted as reactant gas to generate CO.

### 2.2. Method and apparatus

X-ray fluorescence (XRF, AXIOSMAX- PETRO) measurement was carried out to test the elements content of nature hematite ore. X-ray diffraction (XRD, X'Pert PRO MPD) analysis with Cu K $\alpha$  radiation (40 kV, 40 mA) was performed to characterize the crystalline evolution of fresh and used oxygen carriers at scan rate 2°/min and step size 0.0167°. H<sub>2</sub>-temperature-programmed reduction (TPR, ASIQAIV200-2) was used to investigate the lattice oxygen releasing reactivity with heating rate of 10 °C/min and the gas flow rate 120 ml/min (5 vol% H<sub>2</sub>/He). Furthermore, the scanning electron microscopy (SEM, A Hitachi S4800) instrument was implemented to observe the micromorphology of oxygen carrier. The composition of the gaseous production was analyzed by gas chromatography after purification process. Additionally, the batch test of CLR of biomass pyrolyzed gas coupled with CO<sub>2</sub> splitting process were carried out in a fixed bed reactor system which was composed of electric furnace, quartz tube, temperature control system, gas flow control system and clarification unit. The schematic diagram of the fixed bed reactor with the quartz tube of 800 mm length and 23 mm inner diameter was illustrated in Fig. 2. A typical experimental procedure was presented as follows. Quartz cotton was tiled in the quartz tube before experiment and 1 g mixed oxygen carrier was added into quartz tube. Then, the reaction system was heated to the set value with Ar injecting to replace air at gas flow rate of 150 ml/min. Subsequently, the biomass pyrolyzed model gas was introduced to react with oxygen carrier for 30 min at gas flow rate of 60 ml/min. Following the CLR process, the CO<sub>2</sub> splitting reaction was carried out with CO<sub>2</sub> gas flow rate of 50 ml/min after 20 min purge by Ar. The CO<sub>2</sub> splitting reaction lasted for 30 min and the reacted oxygen carriers were regenerated in air atmosphere for 60 min to recover their initial state. The gaseous products were collected by the airbags and then analyzed by gas chromatography.

### 2.3. Data evaluation

The composition of gaseous product is calculated with formula (1),

$$c_i = \frac{\int_0^t v x_i dt}{\int_0^t v (x_{CO} + x_{CO_2} + x_{H_2} + x_{CH_4} + x_{N_2}) dt} \quad (1)$$

In this equation,  $v$  and  $x_i$  represent gas flow rate, volume fraction of species  $i$ , respectively. Moreover, the Ar balance is used to calculate the total amount of each gas products. The conversion ( $\eta$ , %) of CO<sub>2</sub> and CH<sub>4</sub> in CLR stage are defined as follows,

$$\eta_{CO_2} = \frac{\int_0^t v \times x_{CO_2} dt - c_{CO_2} \times G_{out}}{\int_0^t v x_{CO_2} dt} \quad (2)$$



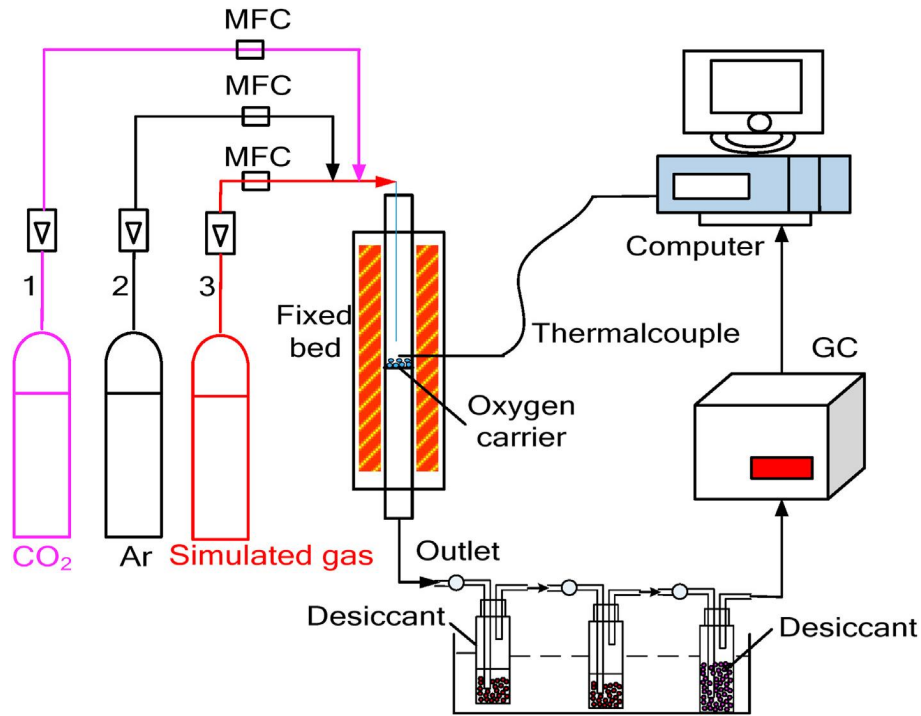


Fig. 2. The schematic diagram of fixed bed reaction system.

$$\eta_{CH_4} = \frac{\int_0^t v \times x_{CH_4} dt - c_{CH_4} \times G_{out}}{\int_0^t v x_{CH_4} dt} \quad (3)$$

The  $H_2/CO$  molar ratio ( $\xi$ ) in the gas products is evaluated as:

$$\xi = \frac{c_{H_2}}{c_{CO}} \quad (4)$$

In addition, equation (2) is also adopted to calculate the conversion ( $\eta$ , %) of  $CO_2$  in splitting stage and the  $CO$  yield is achieved by the gas products analysis.

### 3. Results and discussion

#### 3.1. Characterization of mixed oxygen carriers

The XRD patterns of fresh hematite and Ce–Fe mixed oxygen carrier were displayed in Fig. 3. The crystalline phases of  $Fe_2O_3$  (JCPDS: 00-013-0534),  $Al_2O_3$  (JCPDS: 00-004-0877) and  $SiO_2$  (JCPDS: 01-082-0511) were detected from the single hematite oxygen carrier. It has been proved that  $Fe_2O_3$  is the active component to release lattice oxygen in chemical looping process.  $Al_2O_3$  and  $SiO_2$  are used as inert carrier to prevent sintering of oxygen carrier. Moreover, the  $CeFeO_3$  (JCPDS: 00-022-0166),  $CeO_2$  (JCPDS: 03-065-5923) and  $Fe_2O_3$  (JCPDS: 01-084-0308) are also observed in the XRD pattern of Ce–Fe mixed oxygen carrier. Comparing the two XRD patterns, it is indicated that the  $Fe^{3+}$  in oxygen carrier integrates into the lattice of  $CeO_2$  to generate  $CeFeO_3$  solid solution based on the larger ionic radius of  $Ce^{4+}$  (0.101 nm) than that of  $Fe^{3+}$  (0.064 nm) [29]. Also, some  $CeO_2$  and  $Fe_2O_3$  crystalline phases that have not formed solid solution are also detected in the mixed oxygen carrier. In fact, it is difficult for all the  $Fe^{3+}$  in hematite into  $CeO_2$  lattice due to the mismatch in ionic radius, valence equilibrium and the resulting

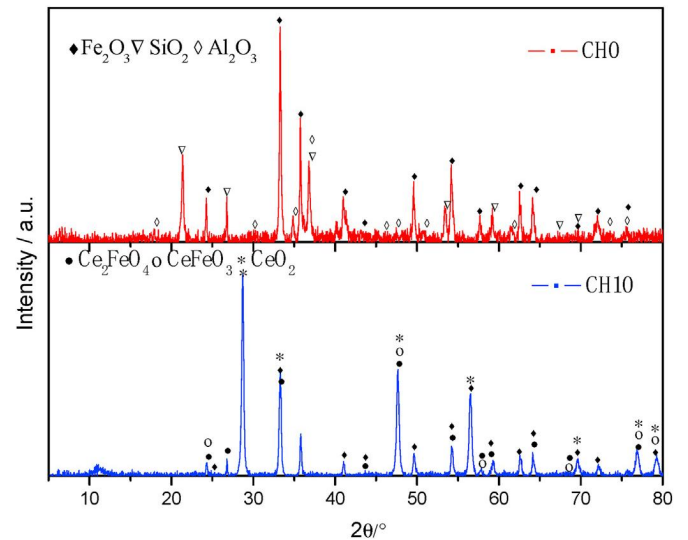


Fig. 3. XRD patterns of single hematite and Ce–Fe mixed oxygen carrier.

crystallographic relaxation effects between host and dopant cations. While, for the  $CeFeO_3$  solid solution, the original lattice structure and charge balance are disturbed as the  $Fe^{3+}$  in diffusing in  $CeO_2$  lattice, leading to charge compensation and oxygen defects formation [31]. That is why the  $CeFeO_3$  solid solution facilitates creating more oxygen vacancies and promoting oxygen ion migration. Furthermore, some trace elements are too little to be neglected in the XRD pattern.

Furthermore, the releasing reactivity of lattice oxygen was characterized by the  $H_2$ -TPR analysis, as depicted in Fig. 4. Three  $H_2$  absorption peaks at 476.8 °C, 625.1 °C and 844.9 °C are observed in the TPR profile of hematite oxygen carrier. Whereas, there are four reduction peaks at 448.9 °C, 573.7 °C, 726.5 °C and 770.1 °C

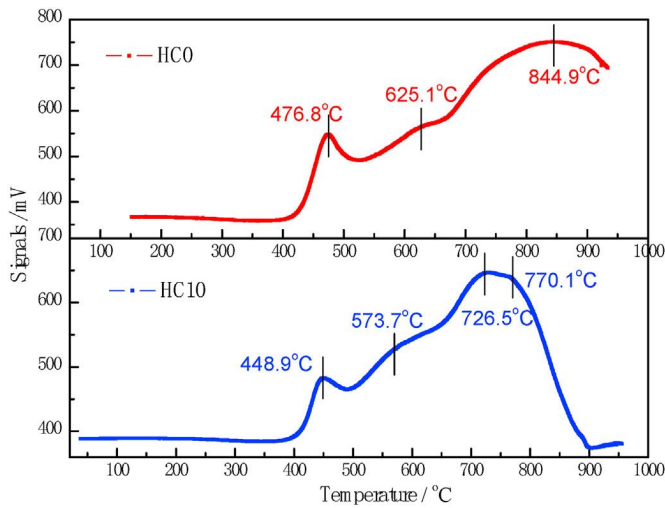
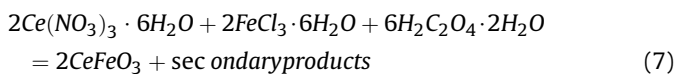


Fig. 4. TPR profiles of single hematite and Ce–Fe mixed oxygen carrier.

appearing in the TPR curve of Ce–Fe mixed oxygen carrier. For the hematite oxygen carrier, it is generally accepted that the  $\text{Fe}_2\text{O}_3$  is reduced by  $\text{H}_2$  through the path of  $\text{Fe}_2\text{O}_3 \rightarrow \text{Fe}_3\text{O}_4 \rightarrow \text{FeO} \rightarrow \text{Fe}^0$ , corresponding to the three  $\text{H}_2$  reduction peaks at 476.8 °C, 625.1 °C and 844.9 °C, respectively [37]. By contrast, the Ce–Fe binary oxygen carrier indicates good lattice oxygen releasing reactivity at lower temperature attributed to the metallic synergistic interactions and solid solution formation. The crystalline phases of  $\text{CeFeO}_3$ ,  $\text{CeO}_2$  and  $\text{Fe}_2\text{O}_3$  in mixed oxygen carrier have been confirmed by XRD analysis. It is reported that pure  $\text{CeO}_2$  exhibits two  $\text{H}_2$  absorption peaks in TPR curve, which are the low temperature reduction peak in the range of 300 °C–500 °C (522 °C) and the high temperature reduction peak at 780 °C–788 °C, corresponding to the reduction of surface oxygen and bulk oxygen of  $\text{CeO}_2$  [38,39]. Moreover,  $\text{Fe}_2\text{O}_3$  in hematite also appears two  $\text{H}_2$  reduction peaks at 476.8 °C and 844.9 °C. Therefore, it is inferred that the reduction peaks at 448.9 °C and 770.1 °C of Ce–Fe mixed oxygen carrier are attributed to the consumption of surface oxygen and bulk oxygen of  $\text{CeO}_2$ , respectively, overlapping the crystalline phase transformation of  $\text{Fe}_2\text{O}_3$  to  $\text{Fe}_3\text{O}_4$  and  $\text{FeO}$  to  $\text{Fe}^0$ , separately [40,41]. Although  $\text{H}_2$  absorption peaks overlap in TPR curve, the reduction temperatures of mixed oxygen carrier are lower than that of single hematite and pure  $\text{CeO}_2$ , indicating that there is an obviously chemical interaction between hematite and  $\text{CeO}_2$  to promote lattice oxygen transfer. Furthermore, the  $\text{H}_2$  absorption peaks at 573.7 °C and 726.5 °C are ascribed to the reduction of  $\text{CeFeO}_3$ , overlapping the phase transformation of  $\text{Fe}_3\text{O}_4$  to  $\text{FeO}$  [36]. The  $\text{CeFeO}_3$  is generated from the Fe species integration into  $\text{CeO}_2$ , following equations (5)–(7) [35,42],

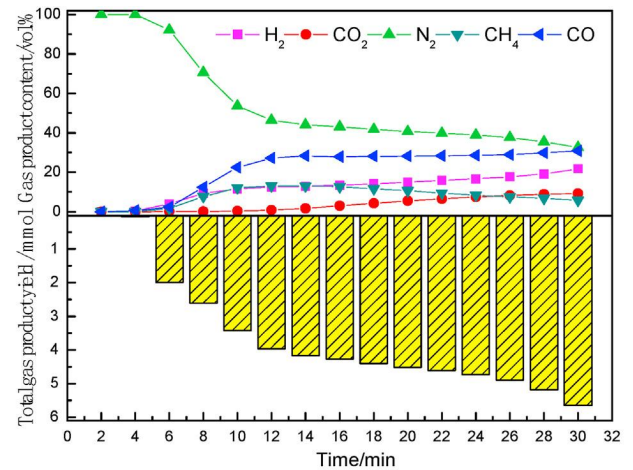
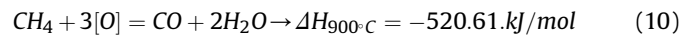
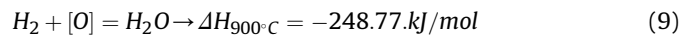
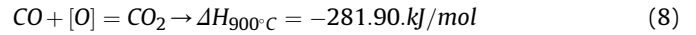


The  $\text{H}_2$  reduction analysis exhibits that there is obviously metallic interaction in oxygen carrier. Also, the formation of  $\text{CeFeO}_3$  solid solution is beneficial to reduce reaction temperature and increase oxygen vacancy concentration, enhancing the lattice oxygen transfer.

### 3.2. Evaluation of CLR coupled with $\text{CO}_2$ splitting process

#### 3.2.1. Gas production as a function of reaction time in CLR stage

The CLR experimental results of biomass pyrolyzed model gas with HC10 oxygen carrier in fixed bed reactor at 900 °C were shown in Fig. 5. It is found that the total gas yield in CLR process indicates upward trend ascribing to the oxidation reaction of lattice oxygen and dry reforming reaction of  $\text{CH}_4$ . Actually, the primary chemical reactions involved in CLR of biomass pyrolyzed gas can be summarized as follows:



(a) Gas composition evolution and yield in CLR stage

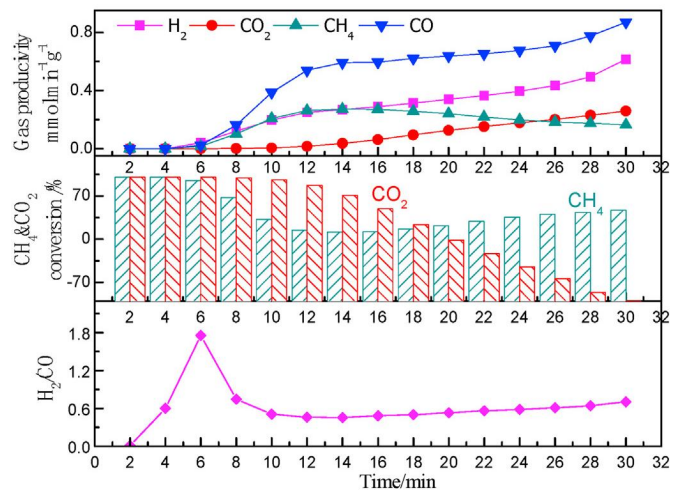
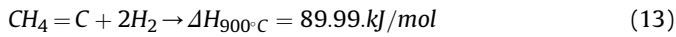


Fig. 5. CLR reaction of biomass pyrolyzed gases as a function of time.



Correspondingly, the gas productivity of CO and H<sub>2</sub> increase steadily with reaction time proceeding based on the reforming reactions of CH<sub>4</sub> with CO<sub>2</sub> or H<sub>2</sub>O, as shown in equations (11), (12). The H<sub>2</sub>/CO ratio of gas products reaches the maximum value of 1.76 at 6th minutes of reaction process then decreases slowly nearly to the initial value 0.5. Owing to the sufficient supply of lattice oxygen, the reactions (10)–(12) become the main reactions in the early stage of CLR process, resulting in higher H<sub>2</sub> productivity than CO. As the reaction progress, H<sub>2</sub> is consumed more quickly based on reaction (9) due to the lower activation energy than CO in the reaction with lattice oxygen [O], leading to the decrease of H<sub>2</sub>/CO. In the later stage of CLR reaction, the dry reforming reaction of CH<sub>4</sub> with CO<sub>2</sub> becomes main reaction as the lattice oxygen consumption. Therefore, the initial conversion efficiency of CO<sub>2</sub> reaches nearly 100% then decreases slowly with the proceeding of reaction. The CH<sub>4</sub> concentration reveals a similar trend to CO<sub>2</sub>. After 18 min of reaction, the CH<sub>4</sub> decomposition reaction (13) and steam reforming reactions (14), (15) are accelerated with the catalyst of reduced oxygen carrier in lattice oxygen deficiency condition, which leads to the increase of CH<sub>4</sub> conversion efficiency and further decrease of CO<sub>2</sub> conversion in the later stage of CLR reaction. Ce-based oxygen carrier exhibits good performance in anti-carbon deposition according to the published literatures, the reactions (13) and (14) are not the main reactions in CLR process. In summary, the maximum H<sub>2</sub>/CO ratio 1.76 with 94.92% CH<sub>4</sub> conversion and nearly 100% CO<sub>2</sub> conversion in biomass pyrolyzed gas were achieved at the 6th minute of CLR reaction.

### 3.2.2. Effect of CeO<sub>2</sub> content in oxygen carrier on CLR reaction process

The effects of CeO<sub>2</sub> content in oxygen carrier on the gas productivity and H<sub>2</sub>/CO as well as the conversion efficiency of CH<sub>4</sub> and CO<sub>2</sub> were shown in Fig. 6. The reaction time lasted for 30 min and reaction temperature was 900 °C. It is observed that the gas product composition of H<sub>2</sub>, CO increases from 10.02 vol%, 26.64 vol% to 22.85 vol%, 30.21 vol% and the H<sub>2</sub>, CO gas productivity rise to 0.58, 0.76 mmol/min/g (oxygen carrier) from 0.39, 0.55 mmol/min/g

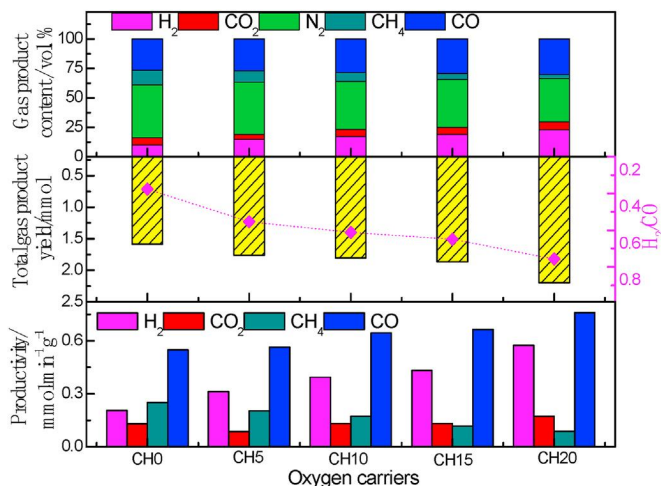
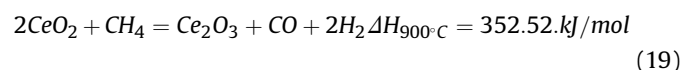
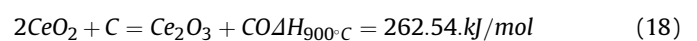
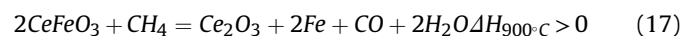
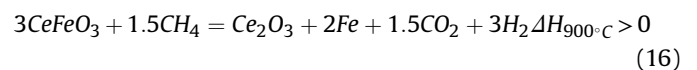


Fig. 6. The effect of CeO<sub>2</sub> content in oxygen carriers on CLR process.

(oxygen carrier) respectively with the content of CeO<sub>2</sub> varying from 0 wt% to 20 wt%. While, the gas product composition and productivity of CH<sub>4</sub> decrease from 12.20 vol%, 0.25 mmol/min/g (oxygen carrier) to 3.48 vol%, 0.09 mmol/min/g (oxygen carrier) respectively with the increasing of CeO<sub>2</sub> content in oxygen carrier. Furthermore, compared with the original gas input, the total gas product amount and H<sub>2</sub>/CO reveal an upward trend with the addition of CeO<sub>2</sub> in oxygen carrier. The highest total gas product amount and H<sub>2</sub>/CO after CLR process have increased 43.46%, 51.31% respectively than that of initial input gas by using with CH20 oxygen carrier. This can be ascribed to the formation of CeFeO<sub>3</sub> solid solution, increasing oxygen vacancies and enhancing lattice oxygen releasing [40]. Actually, owing to the relatively smaller energy barriers, oxide species can hop readily through passages near interstitial sites in the lattice of CeO<sub>2</sub>. Ce<sup>4+</sup> site and interstitial site in CeO<sub>2</sub> are replaced by Fe<sup>3+</sup> during the formation of CeFeO<sub>3</sub> solid solution, which results in oxygen vacancies are essential for the charge balance and excess oxygen species, respectively. These factors play an important role in enhancing the oxygen species migration in mixed oxygen carrier [43]. In addition, Ce–Fe mixed oxides contributes to the catalytic oxidation of CH<sub>4</sub> as catalyst in CLR process. It is also reported that the lattice distortion of CeO<sub>2</sub> conduces to promote the catalytic activity by tuning oxygen mobility and enhancing the adsorption capacity of reactants [38]. Also, the Fe<sub>2</sub>O<sub>3</sub> species on the surface of CeFeO<sub>3</sub> solid solution could provide pathway of oxygen spillover from subsurface to surface, further improving the oxygen mobility [44]. Therefore, the addition of CeO<sub>2</sub> promotes the increase of CO, H<sub>2</sub> productivity and decrease of CH<sub>4</sub> composition in CLR process following the reaction formulas (10)–(12). As for the CO<sub>2</sub>, small amount of CeO<sub>2</sub> is beneficial to inhibit the production of CO<sub>2</sub> based on the reaction (11). However, excessive CeO<sub>2</sub> in hematite oxygen carrier can promote the CO<sub>2</sub> product due to the high catalytic oxidization reactivity of mixed oxides. The lowest CO<sub>2</sub> concentration is obtained by using CH5 oxygen carrier with 5 wt % CeO<sub>2</sub> content.

### 3.2.3. Investigation on CO<sub>2</sub> splitting performance of mixed oxygen carrier

Following the CLR process, CO<sub>2</sub> splitting reaction performance was evaluated with CH10 oxygen carrier in fixed bed reactor to obtain high purity CO at 900 °C, which also lasted for 30 min. Then the reduced oxygen carrier was regenerated in air atmosphere at 900 °C for 60 min. The crystalline phase evolution of CH10 oxygen carrier at different reaction stages was shown in Fig. 7. Ce<sub>2</sub>O<sub>3</sub> (00-023-1048) and Fe (01-087-0722) are detected in the reduced oxygen carrier sample after CLR reaction, indicating that CeO<sub>2</sub>, Fe<sub>2</sub>O<sub>3</sub> and CeFeO<sub>3</sub> solid solution are reduced to Ce<sub>2</sub>O<sub>3</sub> and Fe separately in CLR process, which supply lattice oxygen to oxidize biomass pyrolyzed gas. The main chemical reactions involved in this process are inferred as follows.





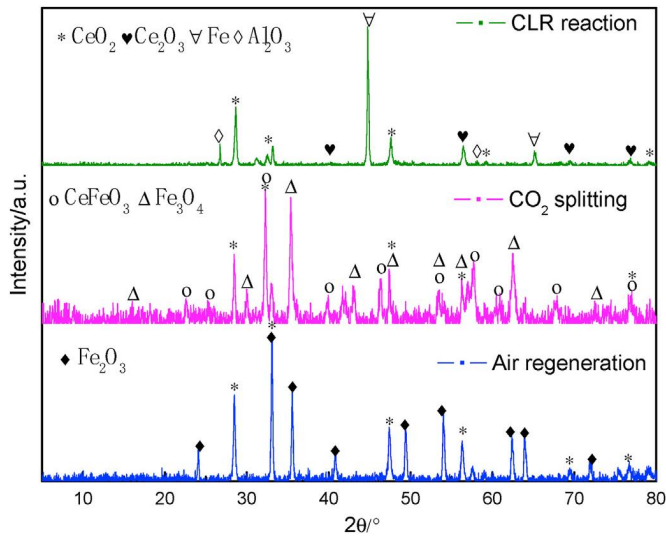
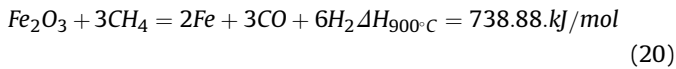
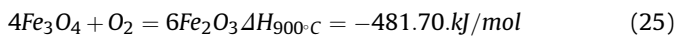


Fig. 7. XRD pattern of mixed oxygen carrier at different reaction stage.



There are  $\text{CeFeO}_3$ ,  $\text{CeO}_2$  and  $\text{Fe}_3\text{O}_4$  (JCPDS:01-087-2334) crystal-line phases in the oxygen carrier sample after  $\text{CO}_2$  splitting stage, revealing the  $\text{CeFeO}_3$  solid solution and lattice oxygen of oxygen carrier can be partially regenerated. The  $\text{CO}_2$  splitting process can be summarized as the reactions (23–24). Moreover, lattice oxygen of mixed oxygen carrier can be completely recovered via air regeneration stage, which has been confirmed by detecting  $\text{CeO}_2$  and  $\text{Fe}_2\text{O}_3$  (00-024-0072) based on XRD analysis, following the reaction (25).



The  $\text{CO}_2$  conversion and CO productivity as function of reaction time in  $\text{CO}_2$  splitting stage were exhibited in Fig. 8. As shown in reaction (23)–(24), the  $\text{CO}_2$  is split into CO in reaction process and releases lattice oxygen to reduced oxygen carrier at the same time. The instantaneous CO productivity and  $\text{CO}_2$  conversion efficiency decrease from the peak value of 2.47 mmol/min/g (oxygen carrier) and 86.13% at 3rd minute of reaction gradually to 0.04 mmol/min/g (oxygen carrier) and 1.25% respectively at 39th minute. At the initial stage of  $\text{CO}_2$  splitting, there are abundant oxygen vacancies in reduced oxygen carrier due to the consumption of lattice oxygen in CLR stage, which leads to high reaction chemical potential and reaction rate.  $\text{CO}_2$  is prone to split to generate CO and supplement from surface of oxygen carrier to bulk phase. As the reaction proceeding, oxygen vacancy concentration of oxygen carrier gradual declines, which results in the decrease of CO productivity and  $\text{CO}_2$  conversion. The reaction process is limited by mass transfer and kinetically controlling regimes. Furthermore, the formation of  $\text{Fe}_3\text{O}_4$  makes lattice reorients and oxygen vacancies arrangement,

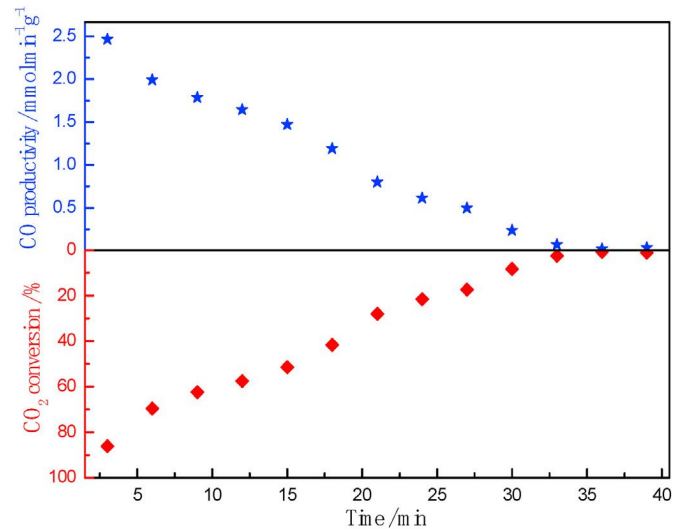


Fig. 8.  $\text{CO}_2$  conversion and CO productivity as function of reaction time.

increasing the difficulty of lattice oxygen recover. Oxygen carrier transformation pathway in CLR coupled with  $\text{CO}_2$  splitting process can be summarized as  $\text{Fe}_2\text{O}_3/\text{CeO}_2/\text{CeFeO}_3 \rightarrow \text{Ce}_2\text{O}_3/\text{Fe} \rightarrow \text{CeFeO}_3/\text{CeO}_2/\text{Fe}_3\text{O}_4 \rightarrow \text{Fe}_2\text{O}_3/\text{CeO}_2$ .

### 3.2.4. $\text{CO}_2$ splitting behavior with variable reaction parameters

To further investigate the  $\text{CO}_2$  splitting process, the effect of reaction parameters including reaction temperature and  $\text{CeO}_2$  content in oxygen carrier were evaluated. Besides, a reaction parameter of  $M_{\text{CO}_2}/m_{\text{OC}}$  which represented the ratio of mole amount of  $\text{CO}_2$  involved in reaction process to the mass of oxygen carrier was also defined and examined. This parameter were directly correlated to the reaction load of unit mass oxygen carrier in  $\text{CO}_2$  splitting stage. The experimental results were shown in Fig. 9. Owing to the endothermic reaction (24) in  $\text{CO}_2$  splitting process, high temperature shifts the reaction equilibrium and enhances reaction rate, which causes the CO productivity and  $\text{CO}_2$  conversion increase from 0.84 mmol/min/g (oxygen carrier), 40.93% to 1.22 mmol/min/g (oxygen carrier), 59.78% respectively with the increasing temperature. Although the  $\text{CO}_2$  splitting reaction with  $\text{Ce}_2\text{O}_3$  (23) is exothermic, the influence of  $\text{CeO}_2$  content in oxygen carrier on  $\text{CO}_2$  conversion and CO productivity displays a

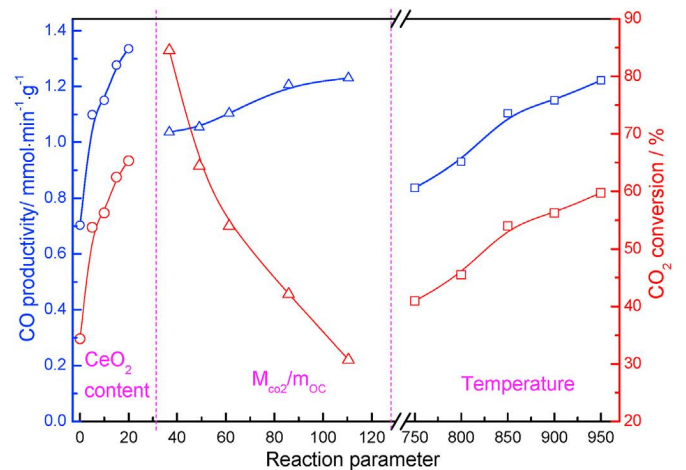


Fig. 9.  $\text{CO}_2$  splitting behavior with variable reaction parameters.

similar upward trend to the effect of increasing temperature, indicating that cerium oxide is more helpful to improve the reactivity of iron than split  $\text{CO}_2$  directly. The CO productivity and  $\text{CO}_2$  conversion by using unmodified hematite oxygen carrier in  $\text{CO}_2$  splitting reaction were only 0.70 mmol/min/g (oxygen carrier) and 34.38%, respectively. By comparison, 1.34 mmol/min/g (oxygen carrier) CO productivity and 65.32%  $\text{CO}_2$  conversion were achieved with  $\text{CH}_2\text{O}$  oxygen carrier including 20 wt% content of  $\text{CeO}_2$ . Obviously, the addition of  $\text{CeO}_2$  in oxygen carrier reveals a significant influence on enhancing  $\text{CO}_2$  splitting reaction. Moreover, though the reaction (23) is not the main reaction in  $\text{CO}_2$  splitting process, it contributes to the generation of CO from  $\text{CO}_2$ , promoting  $\text{CO}_2$  conversion. As for the effect of  $M_{\text{CO}_2}/m_{\text{OC}}$  on  $\text{CO}_2$  splitting behavior, there are two different reaction curves for the CO productivity and  $\text{CO}_2$  conversion with the increasing of  $M_{\text{CO}_2}/m_{\text{OC}}$  in reaction process. The CO productivity curve increases steadily with the increasing of  $M_{\text{CO}_2}/m_{\text{OC}}$ , whereas, the  $\text{CO}_2$  conversion curve manifests an opposite trend. As mentioned above,  $M_{\text{CO}_2}/m_{\text{OC}}$  actually represents the mole amount of  $\text{CO}_2$  flows though per unit mass of oxygen carrier in  $\text{CO}_2$  splitting reaction. It is a key factor for the  $\text{CO}_2$  splitting gas-solid reaction to make reactant gas diffuse into the surface and internal pores of oxygen carrier. With the  $M_{\text{CO}_2}/m_{\text{OC}}$  increasing from 36.81 mmol/g (oxygen carrier) to 110.42 mmol/g (oxygen carrier), the CO productivity varies from 1.04 mmol/min/g (oxygen carrier) to 1.23 mmol/min/g (oxygen carrier). At the same time,  $\text{CO}_2$  conversion decreases from 84.51% to 30.72%. It is apparent that increasing  $M_{\text{CO}_2}/m_{\text{OC}}$  in the early stage are beneficial to generation of CO. However, with the rising of  $M_{\text{CO}_2}/m_{\text{OC}}$ , more  $\text{CO}_2$  flows directly through the outer space of oxygen carrier without participation in reaction, reducing the  $\text{CO}_2$  conversion. As can be observed in Fig. 9, the CO productivity varies little when  $M_{\text{CO}_2}/m_{\text{OC}}$  exceeds 85.89 mmol/g, which is an optimal reaction parameter for the  $\text{CO}_2$  splitting process.

### 3.3. Successive cycle evaluation for CLR coupled with $\text{CO}_2$ splitting process

Cyclic reaction evaluation of CLR coupled with  $\text{CO}_2$  splitting process was conducted further with  $\text{CH}_2\text{O}$  oxygen carrier at 900 °C by using biomass pyrolyzed gas,  $\text{CO}_2$  and air alternately. Fig. 10 illustrates the cyclic reaction results associated with gas yield,  $\text{H}_2/\text{CO}$  and  $\text{CO}_2$  splitting stage. It is found that the  $\text{H}_2$  and CO yield rate as

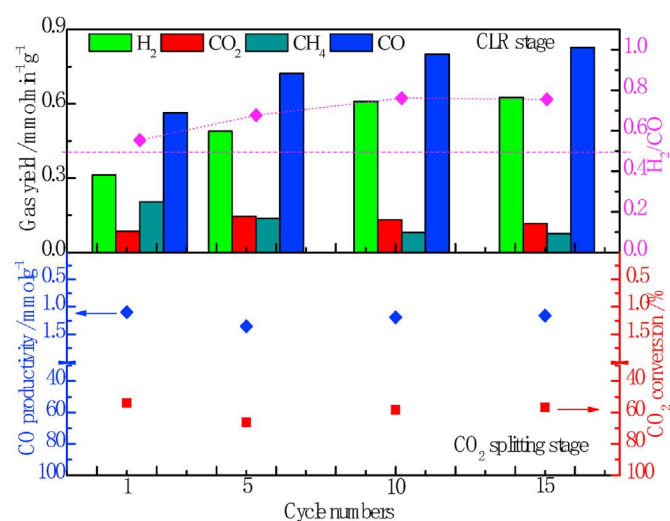


Fig. 10. Multiple cyclic redox performance of mixed oxygen carrier.

well as  $\text{H}_2/\text{CO}$  in CLR stage increase after 5 cycles reaction then gradually stabilize at the values of 0.63 mmol/min/g (oxygen carrier), 0.83 mmol/min/g (oxygen carrier) and 0.76 after 15 cycles reaction.  $\text{CH}_4$  conversion in CLR stage decreases from 0.20 mmol/min/g (oxygen carrier) to 0.08 mmol/min/g (oxygen carrier), indicating the cracking reaction and dry reforming reaction of  $\text{CH}_4$  are accelerated with the cyclic reaction. The CO productivity and  $\text{CO}_2$  conversion in  $\text{CO}_2$  splitting stage increase steadily to 1.35 mmol/min/g (oxygen carrier) and 66.08% after 5 cycles reaction then keep stability in the later 10 cycles. These results provide some insights that the reactivity of mixed oxygen carrier is improved after 5 cycles reaction compared to the 1st cycle, then gradually stabilize with the cyclic reaction. It can be interpreted that successive redox reaction enhances Fe–Ce interactions at the contact interfaces between iron oxide species and Ce oxide species, promoting  $\text{Fe}^{3+}$  diffuse into the interstitial site in  $\text{CeO}_2$  lattice and charge compensation in solid solution [40,45]. Accordingly, the oxygen vacancy concentration and lattice oxygen mobility of the mixed oxygen carrier are strengthened by cyclic reaction, which can counteract or even exceeds the negative effects of material sintering on oxygen carrier [46]. Moreover, the micro-pore diameter and lattice structure of oxygen carrier will be distorted as lattice oxygen releasing and recovering alternately in cyclic reaction. This also contributed to the diffusion of reactant gas into the bulk of oxygen carrier, dynamically improving the reactions between oxygen carrier and biomass pyrolyzed gas or  $\text{CO}_2$ . The Fe–Ce mixed oxygen carrier reveals relatively high reactivity and stability in CLR coupled with  $\text{CO}_2$  splitting cyclic reaction due to the combination effects of Fe–Ce interactions enhancement, lattice oxygen mobility improvement and lattice structure rearrangement.

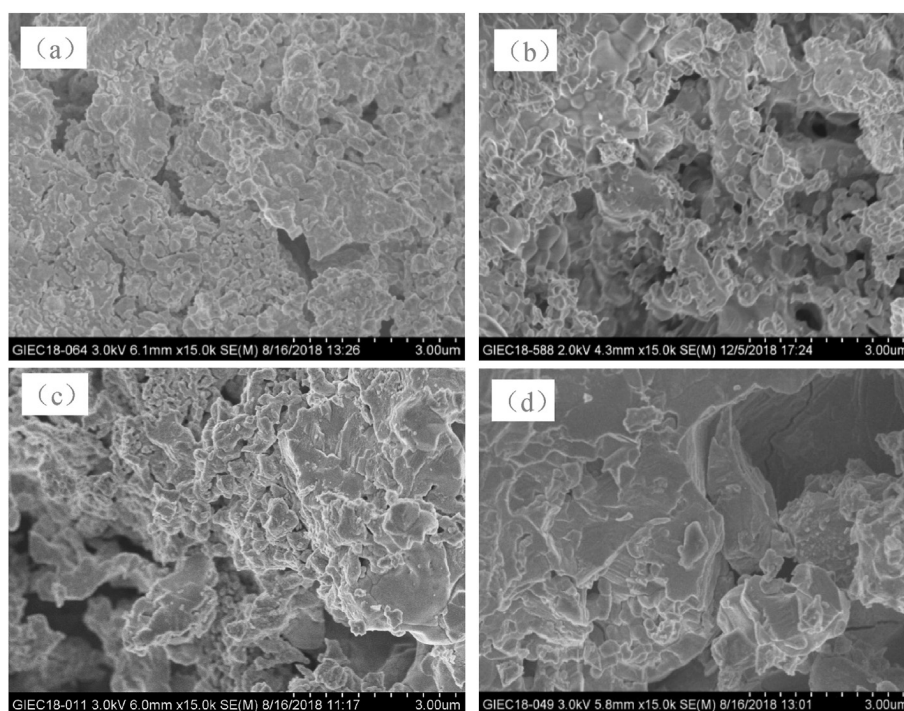
### 3.4. Morphology analysis of oxygen carrier in multi-cycling reaction

Fig. 11 displays the SEM photographs of oxygen carrier in multi-cycling reaction. Irregular blocks with particle size over 3  $\mu\text{m}$  are observed in fresh mixed oxygen carrier. Although agglomeration occurs, there are still pore structures between the particles, which contributes to the diffusion of reactant gas. The XRD analysis in Fig. 3 reveals that the irregular particles mainly consist of  $\text{Fe}_2\text{O}_3$ ,  $\text{CeO}_2$  and  $\text{CeFeO}_3$  solid solution, exhibiting good dispersion and uniformity in mixed oxygen carrier. High dispersion can enhance the interaction between  $\text{Fe}_2\text{O}_3$  and  $\text{CeO}_2$  in mixed oxygen carrier, promoting the oxygen mobility and improving reactivity in reaction process. After releasing lattice oxygen in CLR stage and recovering lattice oxygen in air regeneration, the oxygen carrier pore structures are larger than the fresh sample, though the agglomeration is still observed. This leads to improvement of oxygen carrier reactivity in the initial cycles reaction of CLR and  $\text{CO}_2$  splitting. Sintering occurs in the oxygen carrier sample after 15 cycles reaction, which has a negative effect on the CLR coupled  $\text{CO}_2$  splitting process. However, the gas yield in CLR stage and  $\text{CO}_2$  conversion in splitting stage do not increase significantly in 15 cycles reaction according to the experimental results in Fig. 10. A reasonable inference is that the improvement of porous structure, oxygen vacancy concentration and oxygen mobility of oxygen carrier after cyclic reaction can offset the negative effects of sintering on reactivity of oxygen carrier.

## 4. Conclusions

This study investigated the CLR of biomass pyrolyzed gas coupled with  $\text{CO}_2$  splitting process to achieve high quality biomass synthesis gas and recycle  $\text{CO}_2$  into CO by using Ce-enhanced hematite oxygen carrier. Main components of  $\text{CeO}_2$ ,  $\text{Fe}_2\text{O}_3$  and  $\text{CeFeO}_3$





**Fig. 11.** SEM photographs of oxygen carrier at multiple redox cycles: (a) fresh oxygen carrier (b) reduced sample after CLR (c) air regeneration (d) 15 cycles reaction.

solid solution formed by  $\text{Fe}^{3+}$  integration into the lattice of  $\text{CeO}_2$  were confirmed in Ce–Fe mixed oxygen carrier. The  $\text{CeFeO}_3$  solid solution facilitated to create more oxygen vacancies and promote oxygen ion migration. The  $\text{Fe}_2\text{O}_3$  particles in contact with the surface of  $\text{CeFeO}_3$  solid solution could provide a pathway of oxygen spillover from subsurface to surface to improve lattice oxygen releasing of oxygen carrier. The enhancing role of  $\text{CeO}_2$  in oxygen carrier is exhibited in promoting metallic synergistic interaction and improving catalytic oxidation reactivity of oxygen carrier, which confirmed by  $\text{H}_2$ -TPR analysis and CLR reaction process. The maximum  $\text{H}_2/\text{CO}$  ratio 1.76 with 94.92%  $\text{CH}_4$  conversion and nearly 100%  $\text{CO}_2$  conversion in biomass pyrolyzed gas are achieved at the 6th minute of CLR reaction. Also, the instantaneous CO productivity 2.47 mmol/min/g (oxygen carrier) with 86.13%  $\text{CO}_2$  conversion efficiency were obtained in the 3rd minute of  $\text{CO}_2$  splitting reaction. Reaction temperature,  $\text{CeO}_2$  addition and  $M_{\text{CO}_2}/m_{\text{OC}}$  show positive correlation with instantaneous CO productivity, while the  $M_{\text{CO}_2}/m_{\text{OC}}$  parameter reveals negative correlation with  $\text{CO}_2$  conversion. Gas yield in CLR stage and  $\text{CO}_2$  conversion in splitting stage remained stable in the 15 cycles reaction, though sintering occurred in oxygen carrier sample. This can be inferred that cyclic redox reaction enhances Fe–Ce interactions and increases oxygen mobility in oxygen carrier, offsetting the negative effects of sintering on reactivity of oxygen carrier.

#### Credit author statement

Guoqiang Wei, Conceptualization, Data curation, Writing - original draft. Huan Zhou, Experiment. Zhen Huang, Conceptualization, Supervision. Anqing Zheng, Methodology, Writing-Review. Kun Zhao, Project administration. Yan Lin, Resources. Guozhang Chang, Resources. Zengli Zhao, Methodology. Haibin Li, Funding acquisition. Yitian Fang, Funding acquisition.

#### Declaration of competing interest

The authors declare that they have no known competing financial interests or personal relationships that could have appeared to influence the work reported in this paper.

#### Acknowledgements

The financial support of DNL Cooperation Fund, Chinese Academy of Sciences (DNL180205) is gratefully acknowledged. The authors gratefully acknowledge the financial support of National Key Research and Development Program of China (No.2016YFB0901401), Natural Science Foundation of Guangdong Province (2018A0303130012), Science & Technology Research Project of Guangdong Province (2017A020216009), Science & Technology Project of Guangzhou (201707010202) and the Foundation of State Key Laboratory of High-efficiency Utilization of Coal and Green Chemical Engineering (2020-KF-04).

#### References

- [1] Zhang ZE, Pan SY, Li H, Cai JC, Olabi AG, Anthony EJ, Manovic V. Recent advances in carbon dioxide utilization. *Renew Sustain Energy Rev* 2020;125: 109799–815. <https://doi.org/10.1016/j.rser.2020.109799>.
- [2] Zhang S, Zhuang Y, Liu LL, Zhang L, Du J. Risk management optimization framework for the optimal deployment of carbon capture and storage system under uncertainty. *Renew Sustain Energy Rev* 2019;113:109280–92. <https://doi.org/10.1016/j.rser.2019.109280>.
- [3] Gomes J. Carbon dioxide sequestration technologies. New York: Nova Publishers Inc. Eds.; 2013. 978-1-62257-187-1.
- [4] Song T, Shen LH. Review of reactor for chemical looping combustion of solid fuels. *Int J Greenh Gas Control* 2018;76:92–110. <https://doi.org/10.1016/j.jggc.2018.06.004>.
- [5] Blumberg T, Morosuk T, Tsatsaronis G.  $\text{CO}_2$ -utilization in the synthesis of methanol: potential analysis and exergetic assessment. *Energy* 2019;175: 730–44. <https://doi.org/10.1016/j.energy.2019.03.107>.
- [6] Mobley PD, Peters JE, Akunuri N, Hlebak J, Gupta V, Zheng QH, Zhou SJ, Lail M. Utilization of  $\text{CO}_2$  for ethylene oxide. *Energy Procedia* 2017;114:7154–61. <http://creativecommons.org/licenses/by-nc-nd/4.0/>.

- [7] Alper E, Yuksel Orhan O. CO<sub>2</sub> utilization: developments in conversion processes. *Petroleum* 2017;3(1):109–26. <https://doi.org/10.1016/j.petlm.2016.11.003>.
- [8] Mendiara T, García-Labiano F, Abad A, Gayán P, de Diego LF, Izquierdo MT, Adán J. Negative CO<sub>2</sub> emissions through the use of biofuels in chemical looping technology: a review. *Appl Energy* 2018;232:657–84. <https://doi.org/10.1016/j.apenergy.2018.09.201>.
- [9] Zhao X, Zhou H, Sikarwar VS, Zhao M, Park Ah A, Fennell PS, Shen LH, Fan LS. Biomass-based chemical looping technologies: the good, the bad and the future. *Energy Environ Sci* 2017;10(9):1885–910. <https://doi.org/10.1039/C6EE03718F>.
- [10] AlNouss A, McKay G, Al-Ansari T. Production of syngas via gasification using optimum blends of biomass. *J Clean Prod* 2020;242:118499–513. <https://doi.org/10.1016/j.jclepro.2019.118499>.
- [11] Maria Sepe A, Li J, Paul MC. Assessing biomass steam gasification technologies using a multi-purpose model. *Energy Convers Manag* 2016;129:216–26. <https://doi.org/10.1016/j.enconman.2016.10.018>.
- [12] Wei GQ, He F, Zhao WN, Huang Z, Zhao K, Zhao ZL, Zheng AQ, Wu XS, Li HB. Experimental investigation of Fe–Ni–Al oxygen carrier derived from hydrotalcite-like precursors for the chemical looping gasification of biomass char. *Energy Fuels* 2017;31(5):5174–82. <https://doi.org/10.1021/acs.energyfuels.7b00208>.
- [13] Wei GQ, He F, Zhao ZL, Huang Z, Zheng AQ, Zhao K, Li HB. Performance of Fe–Ni bimetallic oxygen carriers for chemical looping gasification of biomass in a 10 kW<sub>th</sub> interconnected circulating fluidized bed reactor. *Int J Hydrogen Energy* 2015;40(46):16021–32. <https://doi.org/10.1016/j.ijhydene.2015.09.128>.
- [14] Huang Z, Deng ZB, Feng YH, Chen TJ, Chen DZ, Zheng AQ, Wei GQ, He Fang, Zhao ZL, Wu JH, Li HB. Exploring the conversion mechanisms of toluene as a biomass tar model compound on NiFe<sub>2</sub>O<sub>4</sub> oxygen carrier. *ACS Sustainable Chem Eng* 2019;7(19):16539–48. <https://doi.org/10.1021/acssuschemeng.9b03831>.
- [15] Wei GQ, Huang J, Fan YY, Huang Z, Zheng AQ, He F, Meng JG, Zhang DY, Zhao Kun, Zhao ZL, Li HB. Chemical looping reforming of biomass based pyrolysis gas coupling with chemical looping hydrogen by using Fe/Ni/Al oxygen carriers derived from LDH precursors. *Energy Convers Manag* 2019;179:304–13. <https://doi.org/10.1016/j.enconman.2018.10.065>.
- [16] Huang Z, Deng ZB, Chen DZ, Wei GQ, He F, Zhao K, Zheng AQ, Zhao ZL, Li HB. Exploration of reaction mechanisms on hydrogen production through chemical looping steam reforming using NiFe<sub>2</sub>O<sub>4</sub> oxygen carrier. *ACS Sustainable Chem Eng* 2019;7(13):11621–32. <https://doi.org/10.1021/acssuschemeng.9b01557>.
- [17] Miller DD, Smith M, Shekhawat D. Interaction of manganese with aluminosilicate support during high temperature (1100 °C) chemical looping combustion of the Fe–Mn-based oxygen carrier. *Fuel* 2020;263:116738–47. <https://doi.org/10.1016/j.fuel.2019.116738>.
- [18] Dai J, Whitty KJ. Impact of fuel-derived chlorine on CuO-based oxygen carriers for chemical looping with oxygen uncoupling. *Fuel* 2020;263:116780–8. <https://doi.org/10.1016/j.fuel.2019.116780>.
- [19] Wang BW, Li J, Ding N, Mei DF, Zhao HB, Zheng CG. Chemical looping combustion of a typical lignite with a CaSO<sub>4</sub>–CuO mixed oxygen carrier. *Energy Fuels* 2017;31(12):13942–54. <https://doi.org/10.1021/acs.energyfuels.7b02584>.
- [20] Tian X, Wang K, Zhao HB, Su MZ. Chemical looping with oxygen uncoupling of high-sulfur coal using copper ore as oxygen carrier. *Proc Combust Inst* 2017;36(3):3381–8. <https://doi.org/10.1016/j.proci.2016.08.056>.
- [21] Zhang S, Xiao R. Comparison of pyrite cinder with synthetic and natural iron-based oxygen carriers in coal-fueled chemical-looping combustion. *Greenhouse Gases: Sci Technol* 2018;8(1):106–19. <https://doi.org/10.1002/ghg.1724>.
- [22] Bhui B, Vairakannu P. Experimental and kinetic studies on in-situ CO<sub>2</sub> gasification based chemical looping combustion of low ash coal using Fe<sub>2</sub>O<sub>3</sub> as the oxygen carrier. *J CO<sub>2</sub> Util* 2019;29:103–16. <https://doi.org/10.1016/j.jccou.2018.11.012>.
- [23] Wei GQ, wang HT, Zhao WN, Huang Z, Yi Q, He F, Zhao K, Zheng AQ, Meng JG, Deng ZB, Chen J, Zhao ZL, Li HB. Synthesis gas production from chemical looping gasification of lignite by using hematite as oxygen carrier. *Energy Convers Manag* 2019;185:774–82. <https://doi.org/10.1016/j.enconman.2019.01.096>.
- [24] Shen T, Wu J, Shen LH, Yan JC, Jiang SX. Chemical looping gasification of coal in a 5 kW<sub>th</sub> interconnected fluidized bed with a two-stage fuel reactor. *Energy Fuels* 2017;32(4):4291–9. <https://doi.org/10.1021/acs.energyfuels.7b03111>.
- [25] Feng YC, Wang NN, Guo X, Zhang SX. Dopant screening of modified Fe<sub>2</sub>O<sub>3</sub> oxygen carriers in chemical looping hydrogen production. *Fuel* 2020;262:116489. <https://doi.org/10.1016/j.fuel.2019.116489>.
- [26] Tijani MM, Aqsha A, Mahinpey N. Synthesis and study of metal-based oxygen carriers (Cu, Co, Fe, Ni) and their interaction with supported metal oxides (Al<sub>2</sub>O<sub>3</sub>, CeO<sub>2</sub>, TiO<sub>2</sub>, ZrO<sub>2</sub>) in a chemical looping combustion system. *Energy* 2017;138:873–82. <https://doi.org/10.1016/j.energy.2017.07.100>.
- [27] Zhu YY, Liu RL, Sun XY, Ma XX, Wang XD, Tian HJ. Metal modified hexaaluminates for syngas generation and CO<sub>2</sub> utilization via chemical looping. *Int J Hydrogen Energy* 2019;44(21):10218–31. <https://doi.org/10.1016/j.ijhydene.2019.02.187>.
- [28] Tian D, Li KZ, Wei YG, Zhu X, Zeng CH, Cheng XM, Zheng Y, Wang H. DFT insights into oxygen vacancy formation and CH<sub>4</sub> activation over CeO<sub>2</sub> surfaces modified by transition metals (Fe, Co and Ni). *Phys Chem Chem Phys* 2018;20(17):11912–29. <https://doi.org/10.1039/C7CP08376A>.
- [29] Zhu X, Wei YG, Wang H, Li KZ. Ce–Fe oxygen carriers for chemical-looping steam methane reforming. *Int J Hydrogen Energy* 2013;38(11):4492–501. <https://doi.org/10.1016/j.ijhydene.2013.01.115>.
- [30] Zheng Y, Li KZ, Wang H, Tian D, Wang YH, Zhu X, Wei YG, Zheng M, Luo YM. Designed oxygen carriers from macroporous LaFeO<sub>3</sub> supported CeO<sub>2</sub> for chemical-looping reforming of methane. *Appl Catal B Environ* 2017;202:51–63. <https://doi.org/10.1016/j.apcatb.2016.08.024>.
- [31] Li K, Wang H, Wei YG, Yan DX. Transformation of methane into synthesis gas using the redox property of Ce–Fe mixed oxides: effect of calcination temperature. *Int J Hydrogen Energy* 2011;36(5):3471–82. <https://doi.org/10.1016/j.ijhydene.2010.12.038>.
- [32] Gu ZH, Li KZ, Wang H, Qing S, Zhu X, Wei YG, Chen XM, Yu H, Cao Y. Bulk monolithic Ce–Zr–Fe–O/Al<sub>2</sub>O<sub>3</sub> oxygen carriers for a fixed bed scheme of the chemical looping combustion: reactivity of oxygen carrier. *Appl Energy* 2016;163:19–31. <https://doi.org/10.1016/j.apenergy.2015.10.177>.
- [33] Ma Sw, Chen SY, Soomro A, Zhu M, Xiang WG. Characterization of Fe<sub>2</sub>O<sub>3</sub>/CeO<sub>2</sub> oxygen carriers for chemical looping hydrogen generation. *Int J Hydrogen Energy* 2018;43(6):3154–64. <https://doi.org/10.1016/j.ijhydene.2017.12.111>.
- [34] Wang DC, Jin LJ, Li Y, Yao DM, Wang JF, Hu HQ. Upgrading of vacuum residue with chemical looping partial oxidation over Ce doped Fe<sub>2</sub>O<sub>3</sub>. *Energy* 2018;162:542–53. <https://doi.org/10.1016/j.energy.2018.08.038>.
- [35] Means NC, Hammache S, Burgess WA, Howard BH, Smith MW. Evaluation of the redox performance and characterization of Fe<sub>2</sub>O<sub>3</sub>/CeO<sub>2</sub>/ZrO<sub>2</sub> oxygen carriers under high temperature in situ gasification chemical-looping combustion conditions. *Energy Fuels* 2020;34(1):871–8. <https://doi.org/10.1021/acs.energyfuels.9b03018>.
- [36] Liu F, Chen LY, Neathery JK, Saito K, Liu KL. Cerium oxide promoted iron-based oxygen carrier for chemical looping combustion. *Ind Eng Chem Res* 2014;53(42):16341–8. <https://doi.org/10.1021/ie501360b>.
- [37] Hosseini SY, Khosravi-Nikou MR, Shariati A. Production of hydrogen and syngas using chemical looping technology via cerium-iron mixed oxides. *Chem Eng Process* 2019;139:23–33. <https://doi.org/10.1016/j.cep.2019.03.018>.
- [38] Li DY, Li KZ, Xu RD, Zhu X, Wei YG, Tian D, Chen XM, Wang H. Enhanced CH<sub>4</sub> and CO oxidation over Ce<sub>1-x</sub>Fe<sub>x</sub>O<sub>2-δ</sub> hybrid catalysts by tuning the lattice distortion and the state of surface iron species. *ACS Appl Mater Interfaces* 2019;11(21):19227–41. <https://doi.org/10.1021/acsami.9b05409>.
- [39] Ma SW, Chen SY, Zhu M, Zhao ZH, Hu J, Wu MD, Toan S, Xiang WG. Enhanced sintering resistance of Fe<sub>2</sub>O<sub>3</sub>/CeO<sub>2</sub> oxygen carrier for chemical looping hydrogen generation using core-shell structure. *Int J Hydrogen Energy* 2019;44(13):6491–504. <https://doi.org/10.1016/j.ijhydene.2019.01.167>.
- [40] Zhu X, Zhang MY, Li KZ, Wei YG, Zheng Y, Hu JH, Wang H. Chemical-looping water splitting over ceria-modified iron oxide: performance evolution and element migration during redox cycling. *Chem Eng Sci* 2018;179:92–103. <https://doi.org/10.1016/j.ces.2018.01.015>.
- [41] Galvita V, Sundmacher K. Redox behavior and reduction mechanism of Fe<sub>2</sub>O<sub>3</sub>–CeZrO<sub>2</sub> as oxygen storage material. *J Mater Sci* 2007;42(22):9300–7. <https://doi.org/10.1007/s10853-007-1872-7>.
- [42] Petschnig LL, Fuhrmann G, Schildhammer D, Tribus M, Schottenberger H, Huppertz H. Solution combustion synthesis of CeFeO<sub>3</sub> under ambient atmosphere. *Ceram Int* 2016;42(3):4262–7. <https://doi.org/10.1016/j.ceramint.2015.11.102>.
- [43] Li GS, Smith JRRL, Inomata H. Synthesis of nanoscale Ce<sub>1-x</sub>Fe<sub>x</sub>O<sub>2</sub> solid solutions via a low-temperature approach. *J Am Chem Soc* 2001;123:11091–2. <https://doi.org/10.1021/ja016502+>.
- [44] Li KZ, Haneda M, Ning Ph, Wang H, Ozawa M. Microstructure and oxygen evolution of Fe–Ce mixed oxides by redox treatment. *Appl Surf Sci* 2014;289:378–83. <https://doi.org/10.1016/j.apsusc.2013.10.170>.
- [45] Li KZ, Wang H, Wei YG, Yan DX. Direct conversion of methane to synthesis gas using lattice oxygen of CeO<sub>2</sub>–Fe<sub>2</sub>O<sub>3</sub> complex oxides. *Chem Eng J* 2010;156(3):512–8. <https://doi.org/10.1016/j.cej.2009.04.038>.
- [46] Li KZ, Wang H, Wei YG, Yan DX. Partial oxidation of methane to syngas with air by lattice oxygen transfer over ZrO<sub>2</sub>-modified Ce–Fe mixed oxides. *Chem Eng J* 2011;173(2):574–82. <https://doi.org/10.1016/j.cej.2011.08.006>.

## ENERGY CONVERSION AND MANAGEMENT

Volume 260

2022

### CONTENTS

#### Energy Conservation and Efficient Utilization

- Comprehensive energy, exergy, and economic analysis of the scenario of supplementing pumped thermal energy storage (PTES) with a concentrated photovoltaic thermal system B. KURŞUN and K. KTEK 115592
- Thermodynamic analysis and optimization of a novel hybrid system using thermoacoustic cycle to harvest waste heat of high temperature PEMFC X. GUO, Y. GUO, J. WANG, B. XIAO, Y. CAO and C. WU 115572
- Performance investigation and evaluation of a new three-piston pump energy recovery device for small scale desalination system D. SONG, Y. ZHANG, H. WANG, X. LI, Y. XIAO, C. WANG, S. WANG, Q. ZHANG and J. HU 115576
- Towards time-effective optimization: Enviro-economic study of the C3MR LNG process P. FURDA, M. VARINY and Z. LABOVSKA 115602
- CO<sub>2</sub> capture-driven thermal battery using functionalized solvents for plus energy building application S. KIM, J.W. LEE, H.W. CHOI, G.J. LEE, R. XU, S.H. YOON, Z. XU, R. WANG and Y. TAE KANG 115606
- Optimal design of heat pump integrated low-grade heat utilization systems J. HU, S. FAN, B. ZHANG, C. HE, Z. LIU and Q. CHEN 115619
- Thermodynamic analysis of a novel combined cooling, heating, and power system consisting of wind energy and transcritical compressed CO<sub>2</sub> energy storage Y. ZHANG, Y. LIN, F. LIN and K. YANG 115609
- Potential of applying the thermochemical recuperation in combined cooling, heating and power generation: New concept and energy analysis Z. BAI, Y. YUAN, S. ZHOU, B. ZHENG and W. HU 115582
- Thermodynamic assessment of a geothermal power and cooling cogeneration system with cryogenic energy storage T.H. ÇETIN, J. ZHU, E. EKICI and M. KANOGLU 115616
- A novel design, implementation and performance evaluation of the first electronic expansion ejector for energy saving of a mini split air conditioner controlled by inverter A.M. ELSAID 115603

- Wickability-optimized textured liquid-desiccant air dehumidifiers for independent moisture management in energy-efficient buildings M. AHMADI, B. AHMADI and S. BIGHAM 115637
- Performance evaluation of small scale solar organic Rankine cycle using MWCNT + R141b nanorefrigerant A. KUMAR, P.R. GUPTA, A.K. TIWARI and Z. SAID 115631
- Optimal integration of organic Rankine cycles into process heat exchanger networks: A simultaneous approach S. WATANAPANICH, S.-T. LI and J.-Y. LEE 115604
- Soft faults in residential heat pumps: Possibility of evaluation via on-field measurements and related degradation of performance F. PELELLA, L. VISCITO and A.W. MAURO 115646
- Clean Energy and Sustainability**
- A novel hybrid control strategy of wind turbine wakes in tandem configuration to improve power production M.E. NAKHCHI, S. WIN NAUNG and M. RAHMATI 115575
- A comparative techno-economic and sensitivity analysis of Power-to-X processes from different energy sources D. BELLOTTI, M. RIVAROLO and L. MAGISTRI 115565
- Maximization of photo-voltaic array power output through Lo Sho Square shade dispersion technique based re-configuration scheme MANJUNATH, SURESH H.N. and RAJANNA S. 115588
- Enhanced chemical looping gasification of biomass coupled with CO<sub>2</sub> splitting based on carbon negative emission** G. WEI, L. DENG, H. YUAN, X. YANG, Z. HUANG, A. ZHENG and L. XU 115597
- Floating solar PV to reduce water evaporation in water stressed regions and powering water pumping: Case study Jordan L.W. FARRAR, A.S. BAHAI, P. JAMES, A. ANWAR and N. AMDAR 115598
- Productivity and economy prediction for a solar-powered natural vacuum desalination system via water-filling and air-releasing in Asia M. WEI, C. ZHONG, J. LIU, H. XU, J. CHEN, J. XIANG, K. WANG and H. ZHENG 115570

(Contents continued on inside back cover)

Energy Convers. Mgmt is indexed/abstracted in Res. Alert, Biosis Data, CAB Inter., Cam. Sci. Abstr., Chem. Abstr. Serv., Curr. Cont./Eng. Tech. & Applied Sci., Eng. Ind., Environ. Per. Bibl., INSPEC Data., Curr. Cont. Sci. Cit. Ind., Curr. Cont. SCISEARCH Data., SSSA/CISA/ECA/ISMEC, Applied Sci. & Tech. Ind., Applied Sci. & Tech. Abstr. Also covered in the abstract and citation database Scopus®. Full text available on ScienceDirect®.



ELSEVIER

Printed in the Netherlands

269



0196-8904(20220515)260:1-W

260

ENERGY CONVERSION AND MANAGEMENT

Vol. 260 (2022)

ELSEVIER



Volume 260, 15 May 2022

ISSN 0196-8904

# Energy Conversion AND Management



**Editor-in-Chief:**  
Moh'd Ahmad Al-Nimr

**Editors:**  
Marc A. Rosen  
Keat T. Lee  
Nesreen Ghaddar  
Kwan-Soo Lee  
Jincan Chen

generation • utilization • conservation • efficiency • storage • transmission



## AIMS AND SCOPE

The journal *Energy Conversion and Management* provides a forum for publishing original contributions and comprehensive technical review articles of interdisciplinary and original research on all important energy topics.

The topics considered include energy generation, utilization, conversion, storage, transmission, conservation, management and sustainability. These topics typically involve various types of energy such as mechanical, thermal, nuclear, chemical, electromagnetic, magnetic and electric. These energy types cover all known energy resources, including renewable resources (e.g., solar, bio, hydro, wind, geothermal and ocean energy), fossil fuels and nuclear resources.

Papers are welcome that investigate or consider the prospects of energy technologies, devices, systems, materials, processes, operation, performance, maintenance and control. Priority may be given to interdisciplinary energy subjects that deal with advanced technologies and that consider more than one of these methodologies: modeling, experimental, analysis and optimization, with appropriate verifications of the findings.

**Publication information:** *Energy Conversion and Management* (ISSN 0196-8904). For 2022, volumes 251-274 (24 issues) are scheduled for publication. Subscription prices are available upon request from the Publisher or from the Elsevier Customer Service Department nearest you or from this journal's website (<http://www.elsevier.com/locate/enconman>). Further information is available on this journal and other Elsevier products through Elsevier's website (<http://www.elsevier.com>). Subscriptions are accepted on a prepaid basis only and are entered on a calendar year basis. Issues are sent by standard mail (surface within Europe, air delivery outside Europe). Priority rates are available upon request. Claims for missing issues should be made within six months of the date of dispatch.

**Orders, claims, and journal inquiries:** please contact the Elsevier Customer Service Department nearest you:

**St. Louis:** Elsevier Customer Service Department, 3251 Riverport Lane, Maryland Heights, MO 63043, USA; phone: (877) 8397126 [toll free within the USA]; (+1) (314) 4478878 [outside the USA]; fax: (+1) (314) 4478077; e-mail: [JournalCustomerService-usa@elsevier.com](mailto:JournalCustomerService-usa@elsevier.com)

**Oxford:** Elsevier Customer Service Department, The Boulevard, Langford Lane, Kidlington, Oxford OX5 1GB, UK; phone: (+44) (1865) 843434; fax: (+44) (1865) 843970; e-mail: [JournalsCustomerServiceCMEA@elsevier.com](mailto:JournalsCustomerServiceCMEA@elsevier.com)

**Tokyo:** Elsevier Customer Service Department, 4F Higashi-Azabu, 1-Chome Bldg, 1-9-15 Higashi-Azabu, Minato-ku, Tokyo 106-0044, Japan; phone: (+81) (3) 5561 5037; fax: (+81) (3) 5561 5047; e-mail: [JournalsCustomerServiceJapan@elsevier.com](mailto:JournalsCustomerServiceJapan@elsevier.com)

**The Philippines:** Elsevier Customer Service Department, 2nd Floor, Building H, UP-Ayalaland Technohub, Commonwealth Avenue, Diliman, Quezon City, Philippines 1101; phone: (+65) 6349 0222; fax: (+63) 2 352 1394; e-mail: [JournalsCustomerServiceAPAC@elsevier.com](mailto:JournalsCustomerServiceAPAC@elsevier.com)

**Advertising information:** If you are interested in advertising or other commercial opportunities please e-mail [Commercialsales@elsevier.com](mailto:Commercialsales@elsevier.com) and your inquiry will be passed to the correct person who will respond to you within 48 hours.

**Author inquiries:** You can track your submitted article at <http://www.elsevier.com/track-submission>. You can track your accepted article at <http://www.elsevier.com/trackarticle>. You are also welcome to contact Customer Support via <http://service.elsevier.com>.

**Language (usage and editing services):** Please write your text in good English (American or British usage is accepted, but not a mixture of these). Authors who feel their English language manuscript may require editing to eliminate possible grammatical or spelling errors and to conform to correct scientific English may wish to use the English Language Editing service available from Elsevier's WebShop <http://webshop.elsevier.com/languageediting/> or visit our customer support site <http://service.elsevier.com> for more information.

**Illustration services:** Elsevier's WebShop (<http://webshop.elsevier.com/illustrationservices>) offers Illustration Services to authors preparing to submit a manuscript but concerned about the quality of the images accompanying their article. Elsevier's expert illustrators can produce scientific, technical and medical-style images, as well as a full range of charts, tables and graphs. Image 'polishing' is also available, where our illustrators take your image(s) and improve them to a professional standard. Please visit the website to find out more.s

© 2022 Elsevier Ltd.

This journal and the individual contributions contained in it are protected under copyright, and the following terms and conditions apply to their use in addition to the terms of any Creative Commons or other user license that has been applied by the publisher to an individual article:

**Photocopying:** Single photocopies of single articles may be made for personal use as allowed by national copyright laws. Permission is not required for photocopying of articles published under the CC BY license nor for photocopying for non-commercial purposes in accordance with any other user license applied by the publisher. Permission of the publisher and payment of a fee is required for all other photocopying, including multiple or systematic copying, copying for advertising or promotional purposes, resale, and all forms of document delivery. Special rates are available for educational institutions that wish to make photocopies for non-profit educational classroom use.

**Derivative Works:** Users may reproduce tables of contents or prepare lists of articles including abstracts for internal circulation within their institutions or companies. Other than for articles published under the CC BY license, permission of the publisher is required for resale or distribution outside the subscribing institution or company.

For any subscribed articles or articles published under a CC BY-NC-ND license, permission of the publisher is required for all other derivative works, including compilations and translations.

**Storage or Usage:** Except as outlined above or as set out in the relevant user license, no part of this publication may be reproduced, stored in a retrieval system or transmitted in any form or by any means, electronic, mechanical, photocopying, recording or otherwise, without prior written permission of the publisher.

**Permissions:** For information on how to seek permission visit [www.elsevier.com/permissions](http://www.elsevier.com/permissions).

**Author rights:** Author(s) may have additional rights in their articles as set out in their agreement with the publisher (more information at <http://www.elsevier.com/authorsrights>).

**Notice:** Practitioners and researchers must always rely on their own experience and knowledge in evaluating and using any information, methods, compounds or experiments described herein. Because of rapid advances in the medical sciences, in particular, independent verification of diagnoses and drug dosages should be made. To the fullest extent of the law, no responsibility is assumed by the publisher for any injury and/or damage to persons or property as a matter of products liability, negligence or otherwise, or from any use or operation of any methods, products, instructions or ideas contained in the material herein.

Although all advertising material is expected to conform to ethical (medical) standards, inclusion in this publication does not constitute a guarantee or endorsement of the quality or value of such product or of the claims made of it by its manufacturer.

**Funding Body Agreements and Policies:** Elsevier has established agreements and developed policies to allow authors whose articles appear in journals published by Elsevier, to comply with potential manuscript archiving requirements as specified as conditions of their grant awards. To learn more about existing agreements and policies please visit <http://www.elsevier.com/fundingbodies>

© The paper used in this publication meets the requirements of ANSI/NISO Z39.48-1992 (Permanence of Paper)

For a full and complete Guide for Authors, please go to:  
<http://www.elsevier.com/locate/enconman>

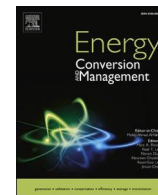
(Contents continued from outside back cover)

|  |        |   |        |
|--|--------|---|--------|
| Economic, environmental and exergy analysis of the decarbonisation of cement production cycle<br>V. MANCINI, N. VERDONE, A. TRINCA and G. VILARDI  | 115577 | <b>Thermodynamics and Thermofluid Processes</b>   |        |
| A combined heating and power system based on compressed carbon dioxide energy storage with carbon capture: Exploring the technical potential<br>W. XU, P. ZHAO, F. GOU, W. WU, A. LIU and J. WANG  | 115610 | Comprehensive comparative analysis of Metal-Oxide nanoaditives impacts on Oil-Filled Finemet and Vitroperm alloy core transformers HST concerning nanofluid thermophysical properties accurate estimation<br>Z. TAGHIKHANI, M.A. TAGHIKHANI and G.B. GHAREHPETIAN | 115594 |
| Neural network genetic algorithm optimization of a transient hybrid renewable energy system with solar/wind and hydrogen storage system for zero energy buildings at various climate conditions<br>A. IZADI, M. SHAHAFVE and P. AHMADI             | 115593 | Modified Stirling cycle thermodynamic model IPD-MSM and its application<br>C. YANG, N. ZHUANG, W. DU, H. ZHAO and X. TANG   | 115630 |
| Remote areas and islands power generation: A review on diesel engine performance and emission improvement techniques<br>A.G.M.B. MUSTAYEN, M.G. RASUL, X. WANG, M. NEGNEVITSKY and J.M. HAMILTON   | 115614 | <b>Fuels, Combustion, and Chemical Processes</b>  |        |
| Conceptual design of novel He-SCO <sub>2</sub> Brayton cycles for ultra-high-temperature concentrating solar power<br>Q. LI, E. E. Y. QIU, J. WANG and Y. ZHANG  | 115618 | Developing a novel gasification-based sludge-to-methanol utilization process and exergy-economic-environmental (3E) analysis<br>T. SHI, Y. LIU, A. YANG, S. SUN, W. SHEN and J. REN   | 115600 |
| The reliability of photovoltaic power generation scheduling in seventeen European countries<br>H. ZSIBORACS, G. PINTER, A. VINCEZ, N.H. BARANYAI and M.J. MAYER  | 115641 | A machine learning model to predict the pyrolytic kinetics of different types of feedstocks<br>S. WANG, Z. SHI, Y. JIN, L.N. ZAINI, Y. LI, C. TANG, W. MU, Y. WEN, J. JIANG, P.G. JONSSON and W. YANG   | 115613 |
| Photothermal bio-based membrane via spectrum-tailoring and dual H-bonding networks strategies for seawater treatment and crude oil viscosity reduction<br>Z. WEI, C. CAI and Y. FU   | 115645 | Multizone model of a refused derived fuel gasification: A thermodynamic Semi-empirical approach<br>P. SHARMA, S. SEN, P.N. SHETH and B.N. MOHAPATRA   | 115621 |
| A two-stage framework for site selection of underground pumped storage power stations using abandoned coal mines based on multi-criteria decision-making method: An empirical study in China<br>X. YONG, W. CHEN, Y. WU, Y. TAO, J. ZHOU and J. HE | 115608 | <b>Articles from the Special Issue on Sustainable Development of Energy, Water and Environment Systems Edited by Prof. Dr. Neven Duic and Prof. Goran Krajacic</b>  |        |
|  |        | A retrofitting control system design suitable for deep borehole drilling using legacy draw-works mechanical brake hardware<br>D. PAVKOVIĆ, M. CIPEK, M. KRZNAR and J. BENIĆ   | 115589 |
|  |        | A novel smart energy network paradigm integrating combined heat and power, photovoltaic and electric vehicles<br>F. CALISE, F.L. CAPPIELLO, M. DENTICE D'ACCADIA and M. VICIDOMINI  | 115599 |



Contents lists available at ScienceDirect

## Energy Conversion and Management

journal homepage: [www.elsevier.com/locate/enconman](http://www.elsevier.com/locate/enconman)Enhanced chemical looping gasification of biomass coupled with CO<sub>2</sub> splitting based on carbon negative emissionGuoqiang Wei<sup>a,d</sup>, Lifang Deng<sup>a</sup>, Haoran Yuan<sup>a,b,\*</sup>, Xixian Yang<sup>a</sup>, Zhen Huang<sup>b</sup>, Anqing Zheng<sup>b</sup>, Li Xu<sup>c</sup><sup>a</sup> Institute of Biomass Engineering, Key Laboratory of Energy Plants Resource and Utilization, Ministry of Agriculture and Rural Affairs, South China Agricultural University, Guangzhou 510642, PR China<sup>b</sup> Guangzhou Institute of Energy Conversion, Chinese Academy of Sciences (CAS), Guangzhou 510640, PR China<sup>c</sup> Institute of Circular Economy, Faculty of Materials and Manufacturing, Beijing University of Technology, Beijing 100124, PR China<sup>d</sup> State Key Laboratory of High-efficiency Utilization of Coal and Green Chemical Engineering, School of Chemistry and Chemical Engineering, Ningxia University, Yinchuan 750021, China

## ARTICLE INFO

## Keywords:

Biomass  
CO<sub>2</sub> splitting  
CLGCS  
Oxygen carrier  
Carbon negative emission  
Heterologous metal

## ABSTRACT

Under the background of fossil fuel consumption and global climate change, an enhanced chemical looping gasification of biomass coupled with CO<sub>2</sub> splitting (CLGCS) was proposed in this work to produce high-quality syngas from biomass and split CO<sub>2</sub> into CO by using Fe-based mixed oxygen carriers (OCs) without extra catalyst and excessive energy consumption, which provided a carbon negative emission technology for the cascade conversion of biomass and resource utilization of greenhouse gas. The reaction equilibrium and regulation mechanism of CLGCS were analyzed in Ellingham diagrams via theoretical calculation. Variable conditions were designed and performed to investigate the reaction performance of OCs. The intermetallic synergy was analyzed, and the improvement order of heterologous metal on lattice oxygen transfer of OCs was Co<sub>2</sub>O<sub>3</sub> > NiO > CeO<sub>2</sub> > CaO. The NiO modified sample exhibited excellent reaction behavior in CLGCS, which provided active sites for catalytic cracking of tar in CLG stage and activating CO<sub>2</sub> molecules in splitting stage. Syngas with heating value 13.32 MJ/m<sup>3</sup> and carbon conversion 74.18% were achieved in CLG stage, corresponding to CO<sub>2</sub> conversion 64.09% and CO yield 23.59 mmol/g in splitting stage. High temperature enhanced the endothermic reactions in CLGCS process, and the biomass occurrence ratio indicated a positive correlation with CO<sub>2</sub> splitting. Although some OC particles agglomerated in reaction process, the pore structure and reactivity remained stable. After 20 cyclic reaction tests, the carbon conversion in CLG stage and CO<sub>2</sub> conversion in splitting stage were kept at 67.52% and 73.5%, respectively. The reaction path of CLGCS with NiO modified OC was summarized as: Fe<sub>2</sub>O<sub>3</sub>/NiFe<sub>2</sub>O<sub>4</sub> → Fe/FeO/Ni → Fe<sub>3</sub>O<sub>4</sub>/Ni → Fe<sub>2</sub>O<sub>3</sub>/NiFe<sub>2</sub>O<sub>4</sub>.

## 1. Introduction

In recent years, the energy consumption grows rapidly with the development of global economy and industry, resulting in a rapid increase of CO<sub>2</sub> emission. According to the Statistical Review of World Energy 2021 (70th Edition) published by British Petroleum, the global CO<sub>2</sub> emission maintained continuous growth since 2013, reaching a record of 34.36 billion tons in 2019. The carbon emission fell by over 6% in 2020, which was mainly attribute to the declining energy demand driven by an unprecedented COVID-19 pandemic and the development of renewable energy. Whereas, the carbon emission was still exceeded

32 billion tons in 2020, leading to serious global climate change and environmental problems such as greenhouse effect, glacier melting, sea level rising, land desertification and so on. The development of clean and renewable resource instead of fossil fuels is the fundamental way to reduce carbon emissions and improve ecological environment.

Biomass is a clean renewable resource with abundant reserves, various sources, low sulfur content and carbon neutral, which can absorb CO<sub>2</sub> in atmosphere during the growth process. The efficient development and utilization of biomass resources contributes greatly to reduce carbon emissions and alleviate current environmental problems. Biomass can be easily converted into solid fuels, liquid fuels, gaseous

\* Corresponding author.

E-mail address: [yuanhaoran81@gmail.com](mailto:yuanhaoran81@gmail.com) (H. Yuan).<https://doi.org/10.1016/j.enconman.2022.115597>

Received 17 January 2022; Received in revised form 25 March 2022; Accepted 6 April 2022

Available online 13 April 2022

0196-8904/© 2022 Elsevier Ltd. All rights reserved.



fuels and industrial raw materials [1,2]. Gasification is an effective way of high-value utilization of biomass resources, which can transfer the biomass into high quality syngas, being subsequently used for power generation or F-T synthesis of liquid fuels and chemicals. Chemical looping gasification (CLG) has been extensively investigated and proven to generate high quality syngas without the preparation of pure oxygen, water steam and other gasification agents [3,4]. Due to the avoidance of  $N_2$  dilution and the catalysis of oxygen carriers (OCs), syngas production from CLG process reveals higher heating value and lower tar content than that from the conventional gasification process [5–8]. A good example is the sawdust CLG process with Mn/Fe-based oxygen carrier in fluidized bed, reported by Shen, et al. [9], where the Mn/Fe-based oxygen carrier exhibits beneficial effect on catalytic cracking of PAHs.

Moreover, it is not enough to reduce  $CO_2$  emissions and realize carbon neutrality by carbon capture technology alone. Actually, the  $CO_2$  capture and storage (CCS) technology has been intensively investigated over the past 20 years, which contributes to preventing the  $CO_2$  emission into atmosphere by capturing and storing the  $CO_2$  underground or in ocean [10]. However, there are some challenges in capture cost and storage space for the CCS process. Some  $CO_2$  capture technologies, such as pre-combustion capture and post-combustion capture, which involve  $CO_2$  separation process and consume more energy, resulting in higher carbon capture cost [11]. Though the goal of oxy-fuel combustion processes is to reduce the energy consumption of  $CO_2$  separation process, it requires separation of oxygen from atmosphere, which is also expensive [12]. Chemical looping combustion (CLC) indicates advantages in carbon capture cost, avoiding the separation process of  $O_2$  from air and  $CO_2$  from flue gas [13,14]. Xiao et al. [15] evaluated the life cycle assessment of hydrogen production via Fe-based chemical looping process using non-aqueous phase bio-oil as fuel. The results displayed that non-aqueous phase bio-oil production consumed the largest fossil energy and contributed the largest global warming potential while the chemical looping hydrogen production played a critical role in lessening greenhouse gas emission. However, the utilization of  $CO_2$  has not yet been involved in the CLC process under the current circumstances. Obviously, the chemical utilization via F-T synthesis or hydrogenation to convert  $CO_2$  into liquid fuels and chemicals has greater application potential than the traditional physical utilization such as dry ice, welding and refrigeration [16,17].

One challenge is that the  $CO_2$  is not easy to convert into liquid fuels and chemicals owing to the thermodynamic limitation and molecular structure stability. The  $CO_2$  is a triatomic molecule with two equal C = O

bonds arranged in a linear arrangement around the central carbon atom. This symmetrical arrangement structure makes it a nonpolar molecule, requiring a lot of energy to break the C = O bond [18]. Therefore, the first step for  $CO_2$  to participate in organic reaction is to activate  $CO_2$  molecule through input of energy or catalytic pathway, breaking the C = O bond. The activation of  $CO_2$  usually occurs in two ways. The first pathway is to form M- $CO_2$  coordination complex compound with the transition metals, which is considered to be an effective way of  $CO_2$  activation. The first fully characterized M- $CO_2$  complex ( $PCy_3)_2Ni(CO_2)$  was reported by Aresta in 1971 [19]. So far, many transition metals have been found for the activation of  $CO_2$ , such as  $Fe^0$ ,  $Rh^I$ ,  $Pd^0$  and  $Pd^{II}$  [20]. Another pathway of  $CO_2$  activation is mainly through the Lewis base and trigger subsequent reactions, which involves strong bases (1, 8-diazabicyclic undecarbonyl-7-ene, DBU), tungstate radical, azabicyclic carbene (NHC), azabicyclic carbene (NHO) and compounds containing hydroxyl groups [21–23]. Therefore, the current chemical conversion process of  $CO_2$  inevitably involves energy input and transition metal or strong base catalyst, which poses a great threat to the ecological environment.

Based on our previous research [24,25], the CLG of biomass coupled with  $CO_2$  splitting (CLGCS) is proposed in this study to produce high-quality syngas and split  $CO_2$  into CO without specific catalyst and excessive energy consumption, which can also realize the cascade conversion of carbon in fuel. The schematic diagram of CLGCS process is shown in Fig. 1.

The CLGCS process consists of fuel reactor, air reactor and  $CO_2$  reactor. Biomass reacts with the lattice oxygen of OCs in fuel reactor to generate syngas, then the reduced OCs and biomass char are transferred to the  $CO_2$  reactor, where the  $CO_2$  reacts with the reduced OCs and biomass char to produce CO. The reduced OCs are partially oxidized and then transported to air reactor, recovering lattice oxygen and releasing reaction heat. The resulting syngas and CO can be used for power generation, hydrogen production and F-T synthesis of liquid fuels [26]. The CLGCS process produces high quality syngas from biomass meanwhile splitting  $CO_2$  into CO without specific catalysis and high energy consumption. The biomass is converted to gaseous product in a cascade of fuel reactor and  $CO_2$  reactor, achieving higher carbon conversion efficiency. Moreover, the mass and heat balance analysis in our previous study indicated that the reaction system can realize auto-thermal operation under certain conditions, where the reaction heat from air reactor was supplied through the oxygen carrier to fuel reactor and  $CO_2$  reactor, maintaining the operation of whole system [24]. Therefore, the CLGCS process reveals advantages in syngas preparation and  $CO_2$

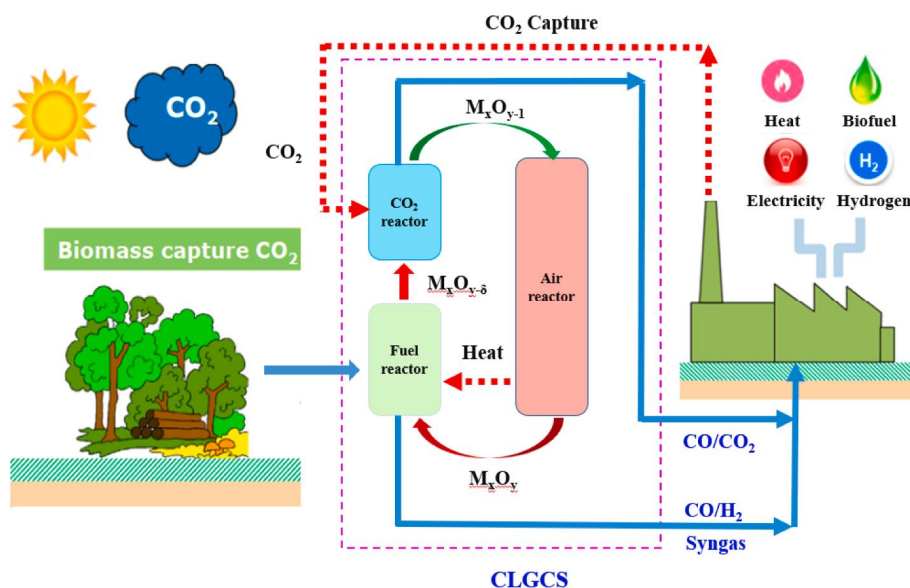


Fig. 1. Schematic diagram of the CLGCS process.

splitting with low-cost oxygen source, high carbon conversion efficiency and low activation energy consumption, which provides a carbon negative emission technology for the resource utilization of renewable biomass and greenhouse gas CO<sub>2</sub>.

OCs play an important role in transferring lattice oxygen and reaction heat in CLGCS process. In a variety of OCs, Fe-based OCs have exhibited numerous applications in heterogeneous OCs due to its remarkable sintering resistance, high oxygen storage capacity and low cost [13,27,28]. Nevertheless, the low reactivity and poor lattice oxygen transfer performance restrict its large-scale application in CLGCS process. Previous studies have proved that the Fe-based OCs modified by exogenous active metal revealed excellent reactivity, sintering resistance and redox capacity [29]. In particular, the mixed OCs with low cost, good reaction selectivity and high mechanical strength can be obtained by using iron ore as the matrix, which then were modified by Ni, Co, Cu, Mn and other exogenous metals [30,31]. Dennis Y. Lu [32] et al. studied the enhanced performance of ilmenite modified by ZrO<sub>2</sub> and NiO, as OCs in CLC process, demonstrating that the addition of metal oxides had a positive effect on the Fe-based OCs, such as accelerating reactivity towards methane reduction and enhancing resistance to agglomeration. Zhu, et al. [33] reported that Ce-modified iron OCs exhibited high redox performance superior to that of pure iron OCs in chemical looping water splitting process, which can inhibit the deactivation caused by sintering of materials. Zhou, et al. [34] investigated the CLG reactivity of coal with iron-manganese based OCs, confirming that the migration and reactivity of lattice oxygen were enhanced by the synergistic effect between Fe and Mn active components. Zhao [35] et al. evaluated the reactivity of Cu-Fe OCs in CLG process of biomass, where the Cu promoted the decomposition of small molecular compounds in tar, while the Fe reduced the yield of large molecular compounds. Furthermore, Ni and Ca also exhibited good synergistic effect with Fe in mixed oxides among the exogenous modified metals, which also improved the carbon conversion efficiency in reaction process [36]. Guo, et al. [37] found that remarkable synergistic effect was observed for bimetallic Fe-Ni oxides in coal gasification, increasing the CH<sub>4</sub> yield in syngas. Moreover, Wang, et al. [38] and Huang, et al. [39] also reported that Fe/Ca mixed OCs and NiFe<sub>2</sub>O<sub>4</sub> sample promoted tar vapor/ model compound toluene cracking into carbon and small molecular gas.

Therefore, the CLGCS process is proposed to realize high quality syngas production and carbon negative emission via splitting CO<sub>2</sub> to CO with hematite OC matrix modified by exogenous metals. The reaction equilibrium theory, zone division and regulation mechanism of CLGCS process are further evaluated by thermodynamic calculation. The reaction evolution process was investigated by fixed bed coupled with multidimensional analysis methods. The reaction path and micromorphology evolution of OCs as well as the cyclic reaction tests were also analyzed to evaluate the reaction behavior of CLGCS process.

## 2. Experimental

### 2.1. Materials

Hematite ore from China was used as the OC matrix after being crushed and screened into 60–80 mesh particles. The purpose of adopting this particle size was to match the particle size of pine sawdust, which promoted the transfer of heat and mass. The analytical reagent of Ce(NO<sub>3</sub>)<sub>3</sub>·6H<sub>2</sub>O, Ni (NO<sub>3</sub>)<sub>2</sub>·6H<sub>2</sub>O, Co(NO<sub>3</sub>)<sub>2</sub>·6H<sub>2</sub>O and Ca(NO<sub>3</sub>)<sub>2</sub>·4H<sub>2</sub>O were used to modify the hematite particles as exogenous metal. Analytical reagent samples were weighed with the mass ratio of metallic oxide and hematite 10%, and then dissolved in 150 mL deionized water to form solution. The hematite matrix particles were incipiently impregnated into the above solution. The obtained mixture was oscillated in 60 °C water bath for 24 h to ensure complete impregnation. After that, the resulting mixture was then dried at 120 °C for 24 h and calcined at 950 °C for 3 h in muffle furnace, achieving the exogenous metal modified OCs. The elemental composition of hematite was

characterized by X-ray fluorescence (XRF, AXIOSMAX-PETRO), as shown in Table 1. Pine from Guangzhou, China was used as biomass material in this study after being grinded and screened into 40–60 mesh sawdust particles. The proximate and ultimate analysis of pine sawdust were displayed in Table 2. Accordingly, the molecular formula of pine sawdust can be represented by CH<sub>1.6</sub>O<sub>0.7</sub> in the case of ignoring N and S content.

### 2.2. Apparatus and methods

The schematic diagram of the experimental apparatus for CLGCS process is exhibited in Fig. 2. The experimental apparatus consists of quartz tube, heating furnace, gas control unit, gas purification unit and control system. The quartz tube reactor is 800 mm in length and 23 mm in diameter. The reaction temperature is measured by a thermocouple in the quartz tube and controlled by a feedback control system. The upper hopper is used to storage pine sawdust, which connects with ball valves to control the sawdust feeding rate. Before the experiment, an amount of quartz cotton is placed into quartz tube and spread evenly. Then the reactor begins to heat up with replacing the air by N<sub>2</sub> at a flow rate of 100 mL/min. The CLG stage begins first when the temperature reaches set point, which lasts for 50 min. After CLG reaction, N<sub>2</sub> is purged for 20 min, then CO<sub>2</sub> splitting reaction is carried out for 30 min. The reaction temperature range is 750–900 °C. The cyclic redox experiment is performed at 900 °C with biomass/OC (B/O) mass ratio 0.5 and CO<sub>2</sub> flow rate of 30 mL/min. The air flow rate is 150 mL/min in regeneration process, lasting for 60 min.

### 2.3. Characterization

Gas chromatography (GC, Agilent 7890A) is adopted to analyze the composition of gaseous product. The crystalline phase of OCs is characterized by X-ray diffraction (XRD, X'Pert PRO MPD) with Cu Kα (40kv, 40 mA) at scanning rate 2° /min and step 0.0167°. The micromorphology of oxygen carrier is detected by scanning electron microscopy (SEM, A Hitachi S4800) and the reactivity of lattice oxygen is analyzed by H<sub>2</sub> temperature programmed reduction (TPR, Quantachrome, CPB-1) at a gas flow rate of 120 mL/min (5% H<sub>2</sub>/N<sub>2</sub>) and heating rate of 6 °C/min. Elemental composition of oxygen carriers are characterized by X-ray fluorescence (XRF, AXIOSMAX-PETRO).

### 2.4. Data evaluation

The molecular composition (*c<sub>i</sub>*) of gaseous products in CLG stage is calculated by formula 1.

$$c_i = \frac{\int_0^t v x_i dt}{\int_0^t v (x_{CO} + x_{CO_2} + x_{H_2} + x_{CH_4} + x_{C_2H_4} + x_{N_2}) dt} \quad (1)$$

Where the *x<sub>i</sub>*, *v* indicate the mole fraction of species *i* and syngas flow rate. *x<sub>CO</sub>*, *x<sub>H<sub>2</sub></sub>*, *x<sub>CH<sub>4</sub></sub>* and *x<sub>C<sub>2</sub>H<sub>4</sub></sub>* are the mole fraction of CO, H<sub>2</sub>, CH<sub>4</sub> and C<sub>2</sub>H<sub>4</sub>. The symbols *x<sub>CO</sub>*, *x<sub>H<sub>2</sub></sub>*, *x<sub>CH<sub>4</sub></sub>* and *x<sub>C<sub>2</sub>H<sub>4</sub></sub>* represent the mole fractions of carbon monoxide, hydrogen, methane and ethylene, respectively.

The syngas yield *Y* (m<sup>3</sup>/kg) is evaluated by N<sub>2</sub> balance, as shown in formula 2. The gas flow rate of N<sub>2</sub> and the mass of biomass are expressed by *v<sub>N2</sub>* and *m<sub>b</sub>*.

$$Y = \int_0^t \frac{v_{N_2} (c_{in,N_2} - c_{out,N_2})}{m_b c_{out,N_2}} dt \quad (2)$$

The low heating value of syngas (*LHV*, kJ/Nm<sup>3</sup>) and carbon conversion efficiency (*η<sub>c</sub>*, %) are calculated by the formulas (3) ~ (4).

$$LHV = 126x_{CO} + 108x_{H_2} + 359x_{CH_4} + 635x_{C_2H_4} \quad (3)$$

$$\eta_c = \frac{12 \times (x_{CO_2} + x_{CO} + x_{CH_4} + 2x_{C_2H_4}) \times Y}{22.4 \times (303/273) \times M_c \%} \times 100\% \quad (4)$$

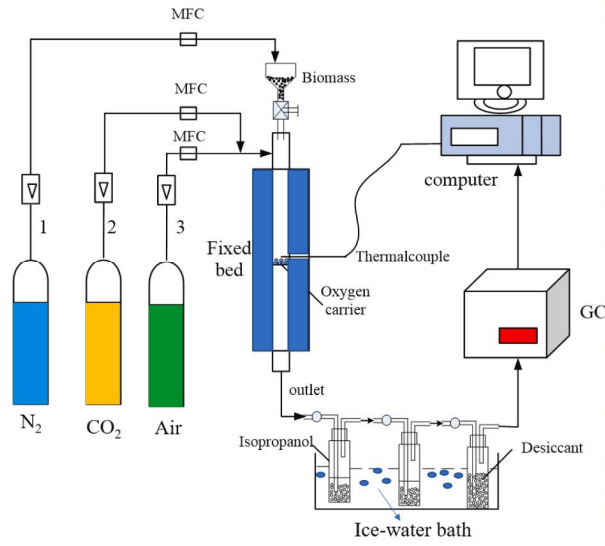
**Table 1**  
Elemental composition of hematite ore.

| Elements | O    | Fe    | Si   | Al  | Ca   | Zn   | P   | Mg   | K    | Ti   | Mn   | Cl   |
|----------|------|-------|------|-----|------|------|-----|------|------|------|------|------|
| Conc. %  | 30.1 | 64.61 | 2.83 | 1.4 | 0.09 | 0.53 | 0.1 | 0.08 | 0.02 | 0.03 | 0.05 | 0.02 |

**Table 2**  
Proximate and ultimate analysis of pine sawdust.

| Proximate analysis<br>wt.%, air dried basis |           |              |          | Ultimate analysis wt.%, dry ash-free basis |      |      |      |       |  | LHV<br>MJ/kg |
|---|-----------|--------------|----------|--|------|------|------|-------|--|--------------|
| Ash   | Volatiles | Fixed carbon | Moisture | C  | H    | N    | S    | O*    |  | 19.52        |
| 0.93  | 79.32     | 14.14        | 5.60     | 49.60                                      | 6.46 | 0.05 | 0.04 | 43.85 |  |              |

Note: O\*: By difference.



**Fig. 2.** Schematic diagram of experimental apparatus for CLGCS process.

Where,  $M_c$  (%) represents the mass fraction of carbon in biomass. The selectivity ( $\epsilon_i$ ) of  $\text{CH}_4$ ,  $\text{CO}$  and  $\text{CO}_2$  in syngas is evaluated by formula (5).

$$\epsilon_i = \frac{12 \times Y_i \int_0^t x_i dt}{22.4 \times (303/273) \times M_c \%} \times 100\% \quad (5)$$

The selectivity ( $\epsilon_i$ ) of  $\text{C}_2\text{H}_4$  is  $2\epsilon_i$  and the selectivity of  $\text{H}_2$  is calculated by formula (6).

$$\epsilon_{\text{H}_2} = \frac{2Y_{\text{H}_2} \int_0^t x_{\text{H}_2} dt}{22.4 \times (303/273) \times M_H \%} \times 100\% \quad (6)$$

Where, the  $M_H$  % represents the mass fraction of hydrogen in biomass. The conversion efficiency of  $\text{CO}_2$  in splitting stage is calculated by formula 7.

$$\eta_{\text{CO}_2} = \frac{\int_0^t v \times x_{\text{CO}_2} dt - c_{\text{CO}_2} \times G_{\text{out}}}{\int_0^t v x_{\text{CO}_2} dt} \quad (7)$$

Where, the  $x_{\text{CO}_2}$  is the composition of  $\text{CO}_2$  in reactant gas,  $C_{\text{CO}_2}$  is the composition of  $\text{CO}_2$  in gaseous product and  $G_{\text{out}}$  represents the volume of gaseous product. Moreover, the  $\text{CO}$  gas yield ( $P_{\text{co}}$ , mmol/g OC) is defined by formula 8.

$$P_{\text{co}} = \frac{273 \times \int_0^t v \times x_{\text{co}} dt}{298 \times 22.4 \times m_{\text{oc}}} \quad (8)$$

Where  $x_{\text{co}}$   $v$  is the molecular composition and flow rate of gaseous product  $\text{CO}$ ,  $m_{\text{oc}}$  is the mass of OCs,  $t$  is the reaction time.

### 3. Results and discussion

#### 3.1. Reaction performance of lattice oxygen in modified OCs

Our previous studies have confirmed that the heterologous metal can improve the oxygen vacancy of OCs and enhance lattice oxygen transfer by generating the complex compound/solid solution such as  $\text{CaFe}_2\text{O}_5$ ,  $\text{CeFe}_2\text{O}_3$ ,  $\text{CoFe}_2\text{O}_4$  and  $\text{NiFe}_2\text{O}_4$  with the hematite ore, which increases fuel conversion efficiency of chemical looping reaction [39,40].  $\text{H}_2$ -TPR is used to further investigate the lattice oxygen transfer process of OCs modified by exogenous metals, as exhibited in Fig. 3. There are two hydrogen reduction peaks at 474.7 °C and 846.2 °C in the TPR curve of fresh hematite OC, indicating a crystal transformation path of  $\text{Fe}_2\text{O}_3 \rightarrow \text{Fe}_3\text{O}_4 \rightarrow \text{FeO} \rightarrow \text{Fe}^0$  [41]. By contrast, the TPR curve of  $\text{Co}_2\text{O}_3$  modified sample exhibits three hydrogen absorption peaks at 380 °C, 539.8 °C and 754.9 °C, respectively. The first hydrogen absorption peak is ascribed to the reduction process of  $\text{Co}_3\text{O}_4$ , while the second and third hydrogen absorption peaks are mainly attributed to the hydrogen reduction of  $\text{CoFe}_2\text{O}_4$  and  $\text{CoO}$ . The reduction temperature of  $\text{Co}_2\text{O}_3$  modified sample is significantly lower than that of fresh hematite, promoting the lattice oxygen transfer. Moreover, three  $\text{H}_2$  reduction peaks of  $\text{NiO}$  modified OC were observed at 482 °C, 540.1 °C and 710.1 °C, corresponding to the reduction process of  $\text{NiO}$ ,  $\text{NiFe}_2\text{O}_4$  and  $\text{Fe}_2\text{O}_3$ , respectively. The hydrogen reduction temperature of  $\text{NiFe}_2\text{O}_4$  in modified OC is close to that of  $\text{CoFe}_2\text{O}_4$ , while the reduced temperature of  $\text{Fe}^0$  crystal phase in deep reduction process is apparently lower than that of  $\text{Co}_2\text{O}_3$  modified

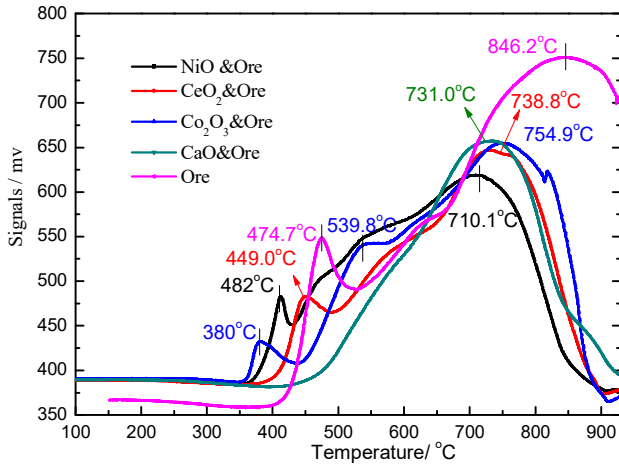
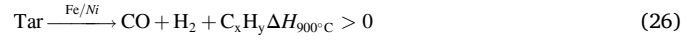
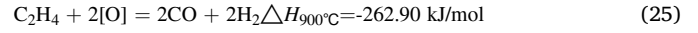
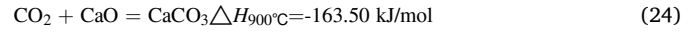
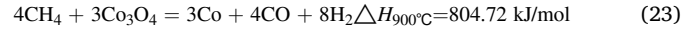
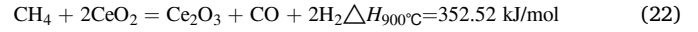
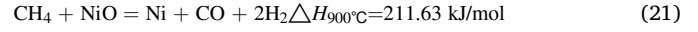
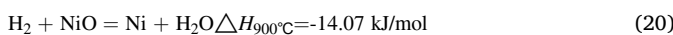
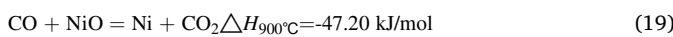
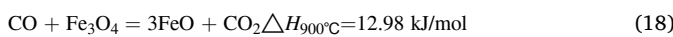
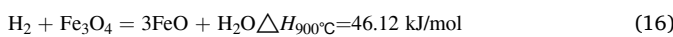
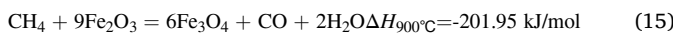
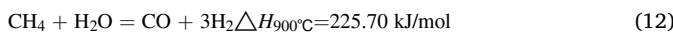
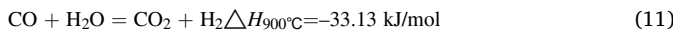
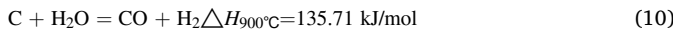


Fig. 3. TPR analysis pattern of hematite OCs with exogenous metal.

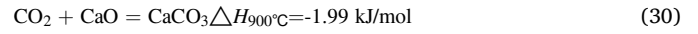
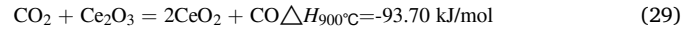
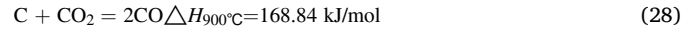
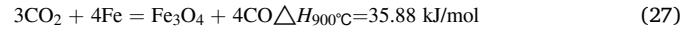
sample, which displays better reactivity. There are four reduction peaks at 448.9 °C, 573.7 °C, 738.8 °C and 770.1 °C on the TPR curve of CeO<sub>2</sub> modified sample. The improvement of CeO<sub>2</sub> on hematite OC is mainly attributed to the synergistic effect of Fe-Ce metal and the formation of CeFeO<sub>3</sub> solution, which increases the oxygen vacancy concentration and enhances the transfer behavior of lattice oxygen. Though the CaO cannot react with H<sub>2</sub> directly, the CaO modified sample showed an overall reduction peak at 731 °C, indicating that the generation of CaFe<sub>2</sub>O<sub>5</sub> can significantly improve the lattice oxygen release performance. In general, exogenous metal modification plays a significant role in improving reaction performance, reducing reduction temperature and enhancing the lattice oxygen transfer. Therefore, the improvement order of exogenous metal for lattice oxygen transfer of OCs can be obtained through the hydrogen reduction peak temperature of modified samples, which is Co<sub>2</sub>O<sub>3</sub> > NiO > CeO<sub>2</sub> > CaO.

### 3.2. Theoretical analysis of CLGCS reaction process

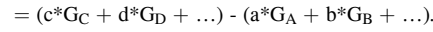
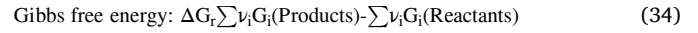
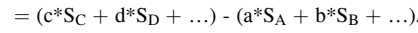
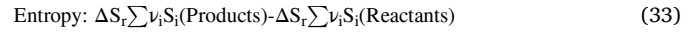
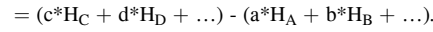
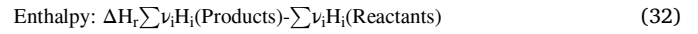
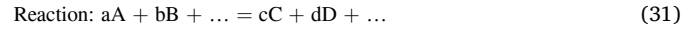
Since the lattice oxygen transfer of hematite can be improved by exogenous metal modification, the reaction equilibrium and reaction zone division of CLGCS process with the modified samples are further evaluated by thermodynamic calculation. The CLGCS reaction process is divided into two stages, the CLG stage and CO<sub>2</sub> splitting stage. The main reactions involved in CLG stage are shown as follows [42,43]:



Also, the major reactions involved in the CO<sub>2</sub> splitting stage are listed in equation (27) ~ equation (30), which mainly includes the CO<sub>2</sub> splitting reactions with oxygen carrier or biomass char.



The Ellingham diagrams from theoretical analysis of CLG stage and CO<sub>2</sub> splitting stage are shown in Fig. 4 and Fig. 5. The reaction equilibrium parameters are calculated based on the following formulas [42]:



Where, the abbreviations a, b and c are the stoichiometric coefficients of species A, B and C in reaction. The  $\nu_i$  represents the sum of stoichiometric coefficient of species in reaction (a, b, c, ...). The R is gas constant, 8.314 J/(Kmol) and T represents temperature, K.

As indicated in Fig. 4, there are three reaction zones in the Ellingham diagram of CLG stage, corresponding to the inert reaction zone, oxidation zone and CLG reaction zone [44]. In the inert reaction zone, the related reactions cannot be spontaneous occur due to the limitation of thermodynamics, where the Gibbs energy change of the reaction is positive. In the CLG reaction zone, the fuel reacts with OCs to generate syngas or terminal product, which are enhanced by the rising

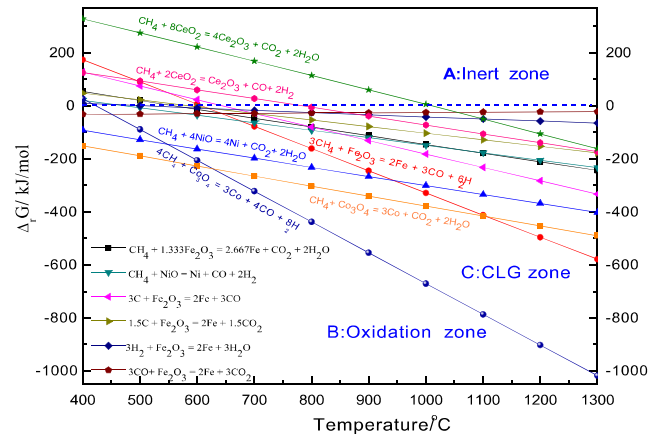


Fig. 4. Theoretical analysis of CLG in Ellingham diagram.



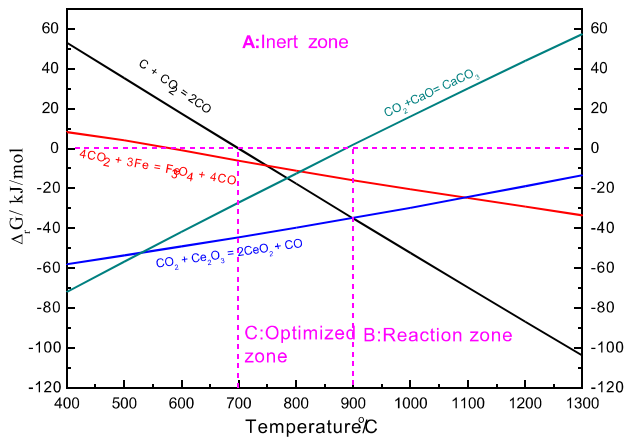


Fig. 5. Theoretical analysis of  $\text{CO}_2$  splitting in Ellingham diagram.

temperature. Also, the synergistic effect of different metals is exhibited in this reaction zone. Regarding the reaction of  $\text{Fe}_2\text{O}_3$  and  $\text{CH}_4$ , syngas consisting of  $\text{H}_2$  and  $\text{CO}$  is preferentially generated, locating in the CLG reaction zone. While, the subsequent reaction process is prone to form terminal product of  $\text{H}_2\text{O}$  and  $\text{CO}_2$ , being oriented in the oxidation zone. Therefore, the reactions between  $\text{Fe}_2\text{O}_3$  and fuel theoretically have a priority to generate syngas via CLG process than the terminal products though completely oxidation reaction [45]. Moreover, exogenous metal modification greatly expands the CLG reaction region of Fe-based OCs, resulting in lower Gibbs free energy change and easier reaction. In particular, the NiO and  $\text{Co}_3\text{O}_4$  display better CLG reaction performance based on the Gibbs free energy analysis. Considering the reaction of exogenous metals, the temperature range of  $750^\circ\text{C}$ – $1000^\circ\text{C}$  is preferable for the CLG process. Similarly, the sequential reduction of  $\text{CO}_2$  splitting appears three reaction regions, which are the inert zone, reaction zone and optimized reaction zone. The primary reactions (27,28) of  $\text{CO}_2$  splitting process are intensified by the rising temperature, locating in the inert reaction zone at temperature below  $700^\circ\text{C}$ . Whereas, high temperature inhibits the reaction (30) that promotes the  $\text{CO}_2$  conversion. Especially, the carbonation reaction is difficult to occur when the temperature is above  $900^\circ\text{C}$ . Therefore, an optimized reaction zone of  $700^\circ\text{C}$ – $1000^\circ\text{C}$  is achieved for the  $\text{CO}_2$  splitting stage.  $\text{Ce}_2\text{O}_3$  metal modification also contributes to the  $\text{CO}_2$  splitting process, as shown in reaction (29). In addition, though NiO cannot directly participate in the  $\text{CO}_2$  splitting process due to the thermodynamical limit, it takes a positive role in activation of  $\text{CO}_2$  molecular.

### 3.3. Reaction behavior of OCs in CLG stage

The CLGCS process were investigated in fixed bed with the B/O of 0.5, as shown in Fig. 6 and Fig. 7. The blank experiment with quartz sand indicated that small molecular gases such as  $\text{CO}$ ,  $\text{H}_2$ ,  $\text{CH}_4$ ,  $\text{CO}$  and  $\text{C}_2\text{H}_4$  generated from the pyrolysis of biomass with the carbon conversion efficiency 55.71%, gas yield  $0.74 \text{ m}^3/\text{kg}$  and syngas heating value  $15.80 \text{ MJ}/\text{m}^3$ , respectively. When the CLG stage occurred, lattice oxygen [O] in OCs escaped at high temperature and combined mainly with C/H elements in biomass to generate small molecule gas, improving biomass carbon conversion and syngas yield. The carbon conversion efficiency and syngas yield reached 63.64% and  $0.77 \text{ m}^3/\text{kg}$  by using hematite OCs, while the LHV of syngas declined to  $14.19 \text{ MJ}/\text{m}^3$  due to the input of external oxygen source. Small molecular gas  $\text{H}_2$  and  $\text{CO}$  from pyrolysis process were consumed in CLG stage with lattice oxygen, while  $\text{H}_2$  had lower activation energy and consumed more rapidly, resulting in the different  $\text{H}_2/\text{CO}$  ratio. The exogenous metals further enhanced the CLG reaction by catalytic cracking the  $\text{CH}_4$ ,  $\text{C}_2\text{H}_4$  and tar, which exhibited higher carbon conversion efficiency and syngas yield than the original hematite OC.

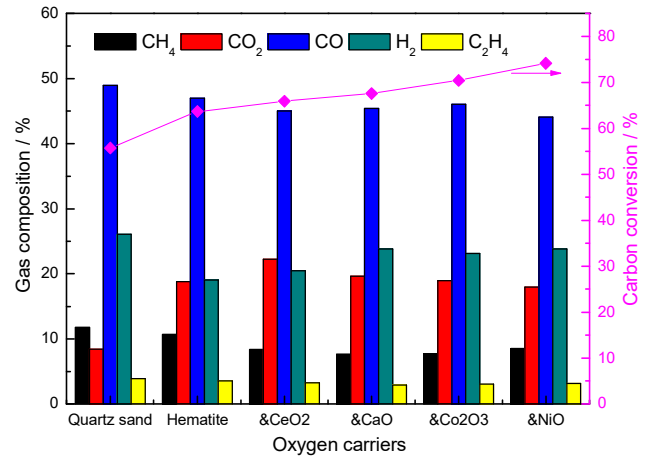


Fig. 6. Gas molecular composition in CLG with OCs.

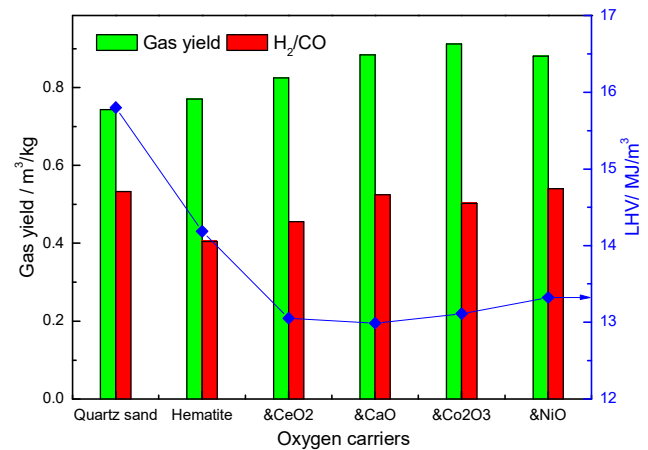


Fig. 7. Carbon conversion and syngas yield in CLG with OCs.

Among the exogenous metals, NiO-modified OC indicated the highest carbon conversion efficiency of 74.18% in CLG process, corresponding to the LHV of syngas  $13.32 \text{ MJ}/\text{m}^3$  and syngas yield  $0.88 \text{ m}^3/\text{kg}$ . In addition,  $\text{Co}_2\text{O}_3$  was reduced to low valent oxides or metal element in CLG stage, which provided good active sites for the catalytic cracking of tar and  $\text{CH}_4$  (equation 23, 26), promoting the conversion of biomass to syngas. The carbon conversion efficiency 70.44% with syngas LHV  $13.11 \text{ MJ}/\text{m}^3$  and gas yield  $0.91 \text{ Nm}^3/\text{kg}$  were achieved by using the  $\text{Co}_2\text{O}_3$  modified OCs. CaO modification reduced  $\text{CO}_2$  content in syngas due to formation reaction of  $\text{CaCO}_3$  (equation (30)), promoting the right shift of reaction equilibrium and improving carbon conversion of biomass. However, the  $\text{CO}_2$  molecular in syngas cannot be significantly reduced owing to the reversible carbonate reaction at high temperature. Moreover, CaO cannot directly participate in the CLG reaction to release lattice oxygen [O], which resulted in the inhibition of carbon conversion and syngas yield.  $\text{CeO}_2$  modification also displayed better reaction performance than hematite attributed to its more oxygen vacancy. In summary, NiO modified oxygen carrier exhibited excellent catalytic oxidation characteristics in CLG stage, reducing the content of tar molecules and improving syngas yield.

### 3.4. Reaction behavior of OCs in $\text{CO}_2$ splitting stage

After the CLG stage and  $\text{N}_2$  purging,  $\text{CO}_2$  was injected to perform the  $\text{CO}_2$  splitting reaction, which completed the CLGCS process. The molecular composition of gaseous products and  $\text{CO}_2$  conversion efficiency



with different OCs were shown in Fig. 8. The CO yield of 16.77 mmol/g and CO<sub>2</sub> conversion efficiency of 45.57% were achieved in blank experiment with quartz sand, which were mainly attributed to the reaction between CO<sub>2</sub> and biomass char from CLG stage (Equation (28)). In addition, the reduced hematite OC can also react with CO<sub>2</sub> to generate CO, from which the CO<sub>2</sub> conversion efficiency of 51.34% and CO yield of 18.90 mmol/g were obtained. The main reaction had been shown in equation (27).

Heterologous metals modification can significantly improve the CO<sub>2</sub> conversion efficiency and CO yield by catalytic cracking CO<sub>2</sub>. The CO<sub>2</sub> conversion efficiency 66.89% and 64.09%, corresponding to CO yield 24.62 mmol/g and 23.59 mmol/g were achieved by using CeO<sub>2</sub> and NiO modified OCs. The CaO and CO<sub>2</sub>O<sub>3</sub> modified OCs also revealed better CO<sub>2</sub> conversion and CO yield. The metallic Ni in the reduced OC sample indicated a great catalytic activity, which can synergistically interact with Fe in the OC to activate CO<sub>2</sub> molecule and promote the splitting reaction. Furthermore, the actual CO yield in splitting reaction was higher than the theoretical CO yield, which was ascribed to the reaction of CO<sub>2</sub> and biomass char from CLG stage. This experimental result also confirmed that the CLGCS process can realize the cascade conversion of biomass, where the residual biomass char from CLG stage continued to react with CO<sub>2</sub> in splitting stage to achieve CO product and higher carbon conversion efficiency. Co, Ni and other metals can also enhance the splitting reaction and promote CO<sub>2</sub> conversion. Calcium carbonate and CeO<sub>2</sub> formation reactions (equations (24), 29) were also beneficial to CO<sub>2</sub> conversion.

Considering the higher carbon conversion efficiency and less residual char in CLG stage, NiO modified sample revealed excellent comprehensive reaction performance for CLGCS process.

### 3.5. Reaction evolution of CLGCS as a function of temperature

Based on the above study, NiO-modified OC was adopted to further investigate reaction evolution of CLGCS as the function of temperature with a mass ratio of biomass to OC 0.5, as shown in Fig. 9. In CLG stage, the molecular composition of CO and C<sub>2</sub>H<sub>4</sub> in syngas increased from 40.82% and 2.67% to 46.83% and 2.83% as the rising temperature from 750 °C to 950 °C, while the molecular composition of CH<sub>4</sub> and CO<sub>2</sub> decreased. The H<sub>2</sub> content basically remained stable. According to the Le Chatelier's principle, high temperature intensifies the endothermic reactions, shifting the reaction equilibrium. The endothermic reactions of (9) ~ (10), (12), (15), (16) and (21) are enhanced, leading to the increase of CO and decrease of CH<sub>4</sub> in syngas. H<sub>2</sub> yield also increased based on the endothermic reactions, the reactions (14) and (16) were also strengthened, leading to a stable molecular content of H<sub>2</sub>. Owing to the CH<sub>4</sub> consumption reactions (12), (15), (17) and (21) were strongly

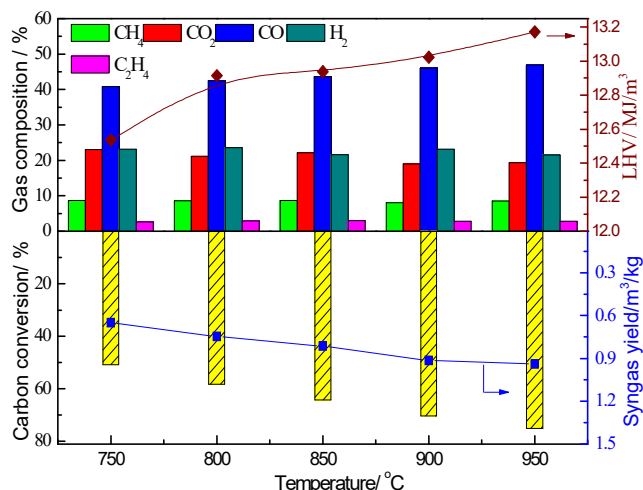


Fig. 9. CLG reaction of biomass as a function of temperature.

endothermic reactions, the CH<sub>4</sub> molecular component decreased with the rising temperature. The CO<sub>2</sub> decline was mainly attributed to the reaction between CO<sub>2</sub> and biomass char. The C<sub>2</sub>H<sub>4</sub> consumption reaction (25) was exothermic, being inhibited in the rising temperature process. The carbon conversion efficiency, syngas yield and syngas LHV of CLG stage were improved with the rising temperature, which increased from 50.84%, 12.54 MJ/m<sup>3</sup> and 0.65 m<sup>3</sup>/kg at 750 °C to 75.07%, 13.17 MJ/m<sup>3</sup> and 0.94 m<sup>3</sup>/kg at 950 °C, respectively. Therefore, high temperature indicated good strengthening effect on the endothermic reactions in CLG stage. In addition, NiO was conducive to the catalytic cracking of tar molecules into small molecule syngas products at high temperature, which also improved the carbon conversion efficiency and syngas yield.

The CO<sub>2</sub> splitting reaction as a function of temperature was shown in Fig. 10. The rising temperature can significantly promote the CO<sub>2</sub> conversion and CO generation. The CO<sub>2</sub> conversion and CO yield increased from 45.25% and 16.66 mmol/g to 63.90% and 23.52 mmol/g with the temperature from 750°C to 950°C. Since the CO<sub>2</sub> splitting reaction (27) was an endothermic reaction, the rising temperature shifted the reaction equilibrium and promoted the CO<sub>2</sub> conversion to CO. Considering that there were still some residual biomass chars from the CLG stage, which further reacted with CO<sub>2</sub> to generate CO in the splitting process. This reaction was also an endothermic reaction. Therefore, the rising temperature improved CO<sub>2</sub> splitting reaction, promoting the cascade conversion of biomass in CLGCS process.

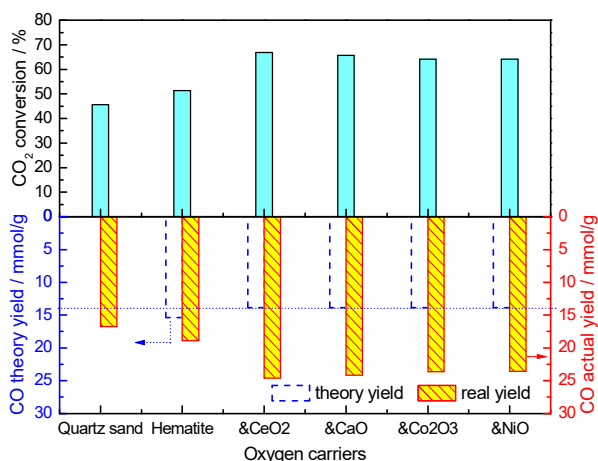


Fig. 8. CO<sub>2</sub> splitting behavior with different OCs.

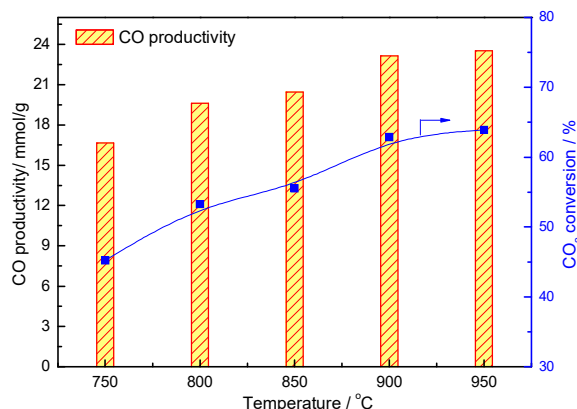
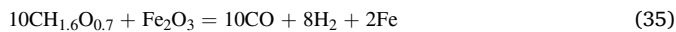


Fig. 10. CO<sub>2</sub> splitting reaction as a function of temperature.

### 3.6. Reaction evolution of CLGCS as a function of biomass occurrence ratio

The biomass mass ratio to OC (B/O) played an important role in CLGCS process. NiO modified OC was used to investigate the reaction evolution as the B/O variation from 0.2 to 1.5 with a step size 0.3. The result was indicated in Fig. 11 and Fig. 11. The molecular composition of H<sub>2</sub>, CO and CH<sub>4</sub> in syngas increased and became stable gradually with the rising biomass occurrence ratio, while the CO<sub>2</sub> composition revealed a downward trend and decreased rapidly when B/O exceeded 0.7. By contrast, the LHV of syngas exhibited an upward trend, while the carbon conversion efficiency was inhibited. The LHV of syngas increased from 11.42 MJ/m<sup>3</sup> to 13.65 MJ/m<sup>3</sup> with the B/O increasing from 0.5 to 1.5. Correspondingly, the carbon conversion declined from 75.34% to 64.84%. The maximum syngas yield 0.94 Nm<sup>3</sup>/kg was achieved at B/O of 0.5.



Theoretically, lattice oxygen supply can be sufficient to realize the CLG reaction with Fe<sub>2</sub>O<sub>3</sub> to generate syngas at the biomass/Fe<sub>2</sub>O<sub>3</sub> mass ratio of 0.5 according to Equation (35). However, due to the inert support in hematite and the limitation of solid-solid reaction mass transfer and reaction time, some OC particles did not participate in the CLG reaction, resulting in a substantial increase in the supply of OC for the CLG stage. Actually, when the B/O was less than 0.5, the lattice oxygen was supplied sufficiently in CLG process, which was conducive to the reforming of biomass pyrolysis gas and oxidation of biomass char by lattice oxygen [O] to produce small-molecule syngas, improving carbon conversion but reducing the LHV of syngas. With the rising of biomass supply, the lattice oxygen became insufficient gradually, where the biomass pyrolysis reaction was the main reaction in system. Correspondingly, the carbon conversion efficiency and syngas yield declined. when the B/O exceeded 1.2, the lattice oxygen supply was insufficient, the biomass pyrolysis was the main reaction system with a stable carbon conversion.

Fig. 12 indicated the CO<sub>2</sub> splitting reaction evolution as a function of biomass mass ratio to OC. The splitting reaction can be enhanced by the rising B/O. The CO<sub>2</sub> conversion rate and CO yield increased from 40.23% and 14.81 mmol/g to 77.68% and 28.9 mmol/g as the B/O rising from 0.2 to 1.5. This was mainly attributed to the increasing biomass in the CLG stage, leading to the lower valence of reacted oxygen carrier and more metallic Fe/Ni formation. On the other hand, the excessive biomass in reaction system cannot be completely transformed in CLG process, producing more biomass char. These two factors strengthened the CO<sub>2</sub> splitting process and improved CO yield.

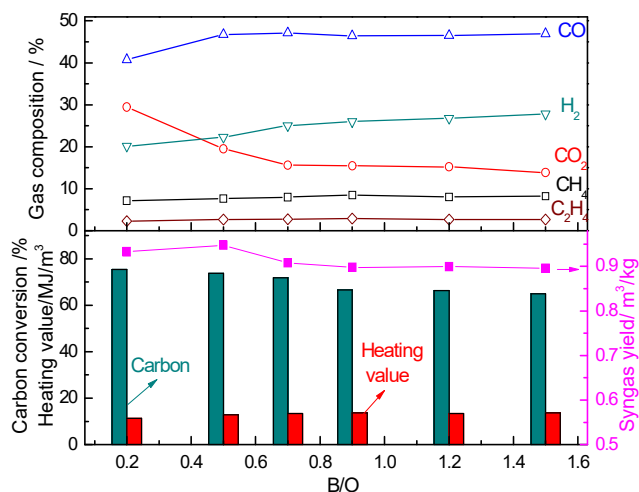


Fig. 11. The CLG reaction as a function of biomass occurrence ratio.

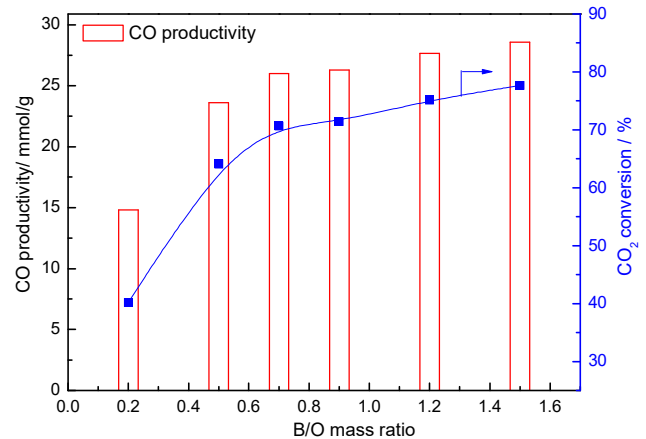


Fig. 12. The CO<sub>2</sub> splitting reaction as a function of B/O mass ratio.

However, the CO<sub>2</sub> conversion efficiency and CO yield tended to be stable attributed to the limited reactant in splitting reaction, although the biomass char in CLG stage still increased.

### 3.7. Reaction path analysis of OC in CLGCS process

To investigate the reaction path of NiO-modified OC in CLGCS process, the crystal evolution of OC in different reaction stages was analyzed and shown in Fig. 13. The fresh OC mainly consists of Fe<sub>2</sub>O<sub>3</sub> (00-019-0615), NiO (00-002-1216), NiFe<sub>2</sub>O<sub>4</sub> (00-044-1485) and SiO<sub>2</sub> (01-085-0796). NiFe<sub>2</sub>O<sub>4</sub> crystal phase generated from NiO and Fe<sub>2</sub>O<sub>3</sub> in the calcination process, which was beneficial to improve the lattice oxygen transfer and the catalytic activity of OC. The NiFe<sub>2</sub>O<sub>4</sub>, Fe<sub>2</sub>O<sub>3</sub> and NiO were reduced to metallic Fe (01-085-1410), metallic Ni (00-003-1043), SiO<sub>2</sub> (00-002-0459) and Fe<sub>0.963</sub>O (01-074-1882) in CLG reaction, releasing lattice oxygen to biomass. As shown in formulas 9 to 26, the CLG process of biomass involved gas-solid reaction (biomass pyrolysis gas reforming), solid-solid reaction (biomass char oxidation) and other heterogeneous reaction processes, which was relatively complex reaction system. Fe<sub>3</sub>O<sub>4</sub> (01-076-1849), FeO (01-089-7100), metallic Ni (01-088-2326) and SiO<sub>2</sub> (01-089-8938) were detected in the OC sample after CO<sub>2</sub> splitting reaction, revealing that metallic Fe was oxidized to Fe<sub>3</sub>O<sub>4</sub> in the splitting process. Metallic Ni played a catalytic role in catalyzing and activating CO<sub>2</sub> molecules [46–48], but did not directly participate in the splitting process. The Fe<sub>2</sub>O<sub>3</sub> (00-033-0664), NiO

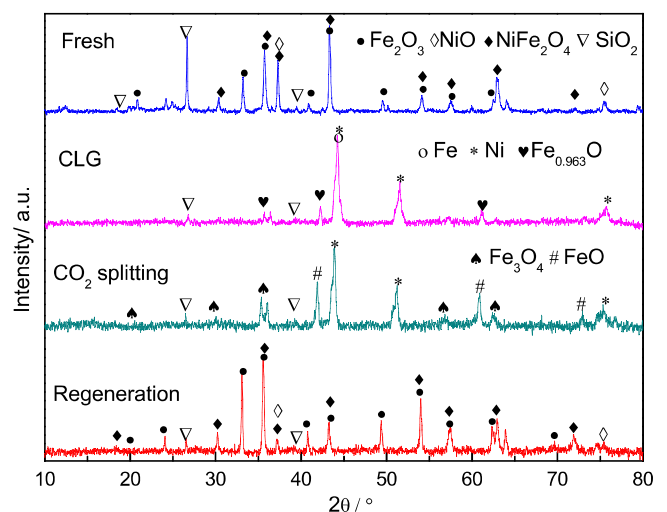


Fig. 13. Crystal structure of oxygen carrier in CLGCS process.

(03-065-6920),  $\text{NiFe}_2\text{O}_4$  (00-010-0325) and  $\text{SiO}_2$  (00-032-0993) were detected in the regeneration sample with air atmosphere, which were consistent with the main crystalline phase of original OC. The lattice oxygen and crystal structure were recovered, indicating the NiO modified hematite OC was suitable for CLGCS to produce high-quality syngas and CO. A reaction path of  $\text{Fe}_2\text{O}_3/\text{NiFe}_2\text{O}_4 \rightarrow \text{Fe}/\text{FeO}/\text{Ni} \rightarrow \text{Fe}_3\text{O}_4/\text{Ni} \rightarrow \text{Fe}_2\text{O}_3/\text{NiFe}_2\text{O}_4$  was also confirmed for the CLGCS process.

### 3.8. Micromorphology evolution of OC in CLGCS process

The microscopic morphology of NiO-modified OC in CLGCS process was characterized by SEM, as shown in Fig. 14. The fresh NiO modified sample exhibited an irregular block structure with the particle size of 20  $\mu\text{m}$  ~ 40  $\mu\text{m}$ . It was observed that NiO,  $\text{Fe}_2\text{O}_3$ ,  $\text{SiO}_2$  and  $\text{Al}_2\text{O}_3$  were combined and dispersed in OC particles. Pore channels distributed between the different block particles, which was conducive to the diffusion and infiltration of reactant molecules into the OC. After CLG stage, the particle size of OC decreased and the surface pulverization occurred, which were mainly caused by the transfer of lattice oxygen from oxygen carrier to biomass. Porous structure can still be observed between particles. Lattice oxygen of OC was partially regenerated in  $\text{CO}_2$  splitting process, and the particle size of OC was further reduced to 5  $\mu\text{m}$  ~ 10  $\mu\text{m}$ . Agglomeration phenomenon of OC particles appeared in this stage, but the pore structure was still maintained. In the air regeneration stage, the pores between the particles collapsed and reorganized due to the intense heat release and transfer in oxidation reaction process. Slightly sintering was observed in the OC particles after the regeneration process.

### 3.9. Multiple cyclic reaction of CLGCS process

Multiple cyclic reaction test of CLGCS were conducted in fixed-bed

reactor with NiO modified OC, as shown in Table 3. The results confirmed that the carbon conversion efficiency 73.72%, syngas yield 0.95  $\text{Nm}^3/\text{kg}$  and syngas LHV 12.86  $\text{MJ}/\text{m}^3$  were achieved in CLG stage of the first cycle. Correspondingly, the  $\text{CO}_2$  conversion 61.21% and CO yield 22.53 mmol/g were realized in  $\text{CO}_2$  splitting stage. After 5 cycles of reaction, the carbon conversion efficiency, syngas yield and LHV decreased slightly to 73.08%, 0.88  $\text{Nm}^3/\text{kg}$  and 12.81  $\text{MJ}/\text{m}^3$ , respectively. The CO yield and  $\text{CO}_2$  conversion increased to 23.00 mmol/g and 62.50% in splitting stage. Combined with SEM analysis, the declining carbon conversion efficiency and increasing  $\text{CO}_2$  conversion in cycle reaction are mainly attributed to particles sintering in regeneration stage, which also reduced the transfer of lattice oxygen in subsequent CLG process. Accordingly, the residual biomass char from CLG stage increased, enhancing the following  $\text{CO}_2$  splitting process and improving the  $\text{CO}_2$  conversion efficiency. The carbon conversion efficiency and syngas yield in CLG stage decreased respectively to 67.52% and 0.87  $\text{Nm}^3/\text{kg}$  after 20 cycle reaction, and the LHV of syngas basically remained stable. The CO yield and  $\text{CO}_2$  conversion in splitting stage reached 27.05 mmol/g and 73.50%, separately. The sintering of particles had negative effects on the reaction performance of OC, while the particle pore size and specific surface area were improved by the release lattice oxygen and regeneration alternately, which promoted the penetration and diffusion of reactants. Also, the oxygen vacancy concentration and catalytic activation also were strengthened in the cycle reaction. These factors offset the negative effects of sintering to a certain extent. The 20 cycle reaction tests indicated that the carbon conversion efficiency in CLG stage decreased by 6.2%, while the  $\text{CO}_2$  conversion in splitting stage increased by 12.3%. Therefore, the reaction performance of OC in CLGCS basically remained stable.

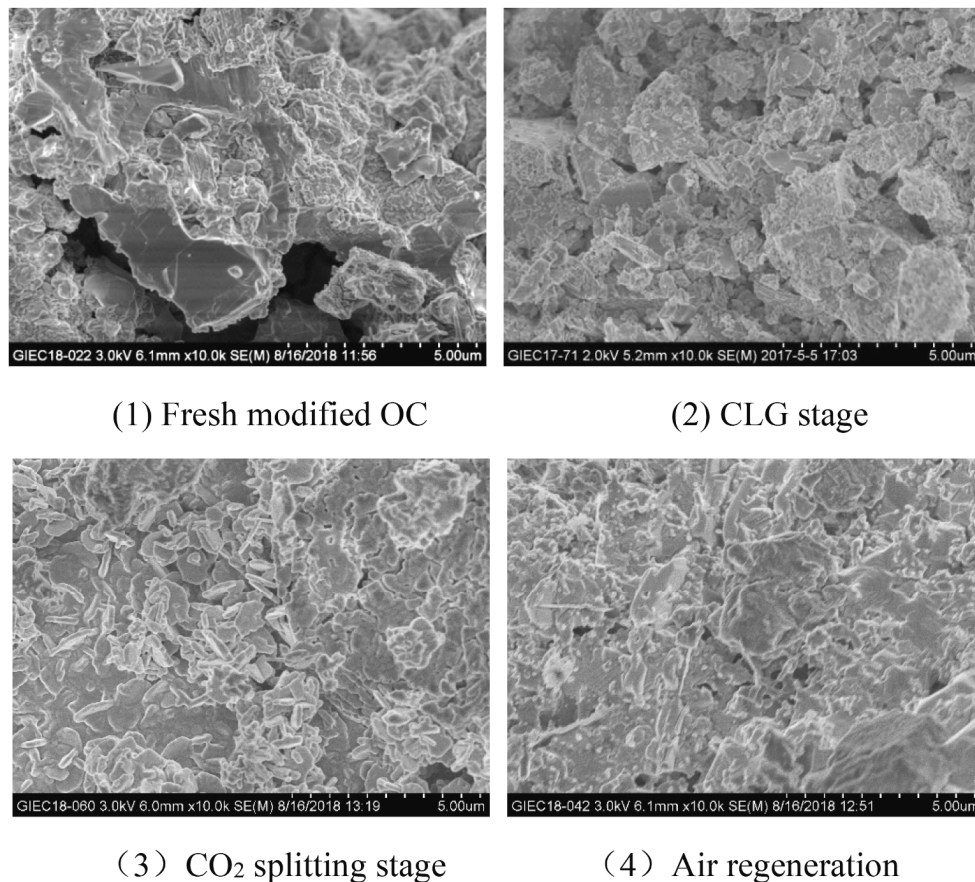


Fig. 14. SEM morphology evolution of NiO-modified OC.



**Table 3**  
Multiple cyclic tests of CLGCS process.

| Cycle No. | CLG stage |                 |                 |       |                | $\eta_c$ % | $Y_{\text{syngas}}$ m <sup>3</sup> /kg | LHV MJ/m <sup>3</sup> | CO <sub>2</sub> splitting stage |                        |
|-----------|-----------|-----------------|-----------------|-------|----------------|------------|--|-----------------------|---------------------------------|------------------------|
|           | $c_i$ %   | CH <sub>4</sub> | CO <sub>2</sub> | CO    | H <sub>2</sub> |            |  |                       | P <sub>co</sub> mmol/g          | $\eta_{\text{CO}_2}$ % |
| 1         | 7.67      | 19.55           | 46.74           | 22.31 | 2.72           | 73.72      | 0.95                                   | 12.86                 | 22.53                           | 61.21                  |
| 5         | 8.09      | 19.30           | 44.03           | 24.10 | 2.64           | 73.08      | 0.88                                   | 12.81                 | 23.00                           | 62.50                  |
| 10        | 9.39      | 18.01           | 45.23           | 20.87 | 3.23           | 69.31      | 0.76                                   | 13.47                 | 24.14                           | 65.58                  |
| 20        | 7.49      | 19.11           | 47.66           | 22.66 | 2.56           | 67.52      | 0.87                                   | 12.85                 | 27.05                           | 73.50                  |

#### 4. Conclusions

An enhanced CLGCS process with carbon negative emission was proposed to produce high quality syngas from biomass and split CO<sub>2</sub> to CO by using Fe-based mixed oxygen carriers. The reaction equilibrium and intermetallic synergy mechanism of CLGCS process were evaluated from the Ellingham diagrams based on the thermodynamic calculation. The heterologous metal modification played a significant role in improving reaction performance of OCs and enhancing the lattice oxygen transfer. The improvement order for lattice transfer of OCs was Co<sub>2</sub>O<sub>3</sub> > NiO > CeO<sub>2</sub> > CaO. Syngas with LHV 13.32 MJ/m<sup>3</sup> and carbon conversion 74.18% was achieved with NiO modified OC in CLG stage, corresponding to the CO<sub>2</sub> conversion 64.09% and CO yield 23.59 mmol/g in splitting, respectively. The reaction path of NiO modified OC was revealed for the CLGCS process, in which the Fe<sub>2</sub>O<sub>3</sub>/NiFe<sub>2</sub>O<sub>4</sub> were reduced to Fe/FeO/Ni in the CLG stage and then oxidized to Fe<sub>3</sub>O<sub>4</sub>/Ni in CO<sub>2</sub> splitting stage. The crystal phase of the modified OC was recovered after the regeneration process. Reaction temperature and biomass occurrence ratio had positive effects on the CLGCS process. Some OC particles were agglomerated in reaction process, but the pore structure and reactivity were still remained. In 20 cycles, the carbon conversion in CLG stage remained at 67.52% and the CO<sub>2</sub> conversion in splitting stage kept at 73.50%. The reaction performance of OC in CLGCS basically remained stable.

#### CRedit authorship contribution statement

**Guoqiang Wei:** Writing – original draft, Funding acquisition. **Lifang Deng:** Project administration. **Haoran Yuan:** Conceptualization, Supervision, Funding acquisition. **Xixian Yang:** . **Zhen Huang:** Methodology. **Anqing Zheng:** Writing – review & editing. **Li Xu:** Resources.

#### Declaration of Competing Interest

The authors declare that they have no known competing financial interests or personal relationships that could have appeared to influence the work reported in this paper.

#### Acknowledgements

The financial support of National Natural Science Foundation of China (Grant. 51976226, U1810125, 51776133) is gratefully acknowledged. This work is also supported by the Joint Fund of the Yulin University and the Dalian National Laboratory for Clean Energy (Grant. YLU-DNL Fund 2021021) and the Foundation of State Key Laboratory of High-efficiency Utilization of Coal and Green Chemical Engineering (Grant No. 2020-KF-04).

#### References

- [1] Zeng K, Yang X, Xie Y, Yang H, Li J, Zhong D, et al. Molten salt pyrolysis of biomass: The evaluation of molten salt. *Fuel* 2021;302:121103.
- [2] Li J, Xiong Z, Zeng K, Zhong D, Zhang X, Chen W, et al. Characteristics and evolution of nitrogen in the heavy components of algae pyrolysis bio-oil. *Environ Sci Technol* 2021;55(9):6373–85.

- [3] Wang X, Jin B, Zhu X, Liu H. Experimental evaluation of a novel 20 kW<sub>th</sub> in situ gasification chemical looping combustion unit with an iron ore as the oxygen carrier. *Ind Eng Chem Res* 2016;55(45):11775–84.
- [4] Yan J, Sun R, Shen L, Bai H, Jiang S, Xiao Y, et al. Hydrogen-rich syngas production with tar elimination via biomass chemical looping gasification (BCLG) using BaFe<sub>2</sub>O<sub>4</sub>/Al<sub>2</sub>O<sub>3</sub> as oxygen carrier. *Chem Eng J* 2020;387:124107.
- [5] Mendiara T, García-Labiano F, Abad A, Gayán P, de Diego LF, Izquierdo MT, et al. Negative CO<sub>2</sub> emissions through the use of biofuels in chemical looping technology: A review. *Appl Energy* 2018;232:657–84.
- [6] Lin Y, Wang H, Wang Y, Huo R, Huang Z, Liu M, et al. Review of biomass chemical looping gasification in China. *Energy Fuels* 2020;34(7):7847–62.
- [7] Wei G, Wang H, Zhao W, Huang Z, Yi Q, He F, et al. Synthesis gas production from chemical looping gasification of lignite by using hematite as oxygen carrier. *Energy Conv Manag* 2019;185:774–82.
- [8] Lin Y, Zhang Z, Wang H, Fang S, Huang Z, Chen T, et al. An evaluation of the reactivity of synthetic Fe-Ni oxygen carriers: CO oxidation, H<sub>2</sub>O reforming, and toluene cracking. *Energy Conv Manag* 2021;240:114263.
- [9] Wang S, Song T, Yin S, Hartge E-U, Dymala T, Shen L, et al. Syngas, tar and char behavior in chemical looping gasification of sawdust pellet in fluidized bed. *Fuel* 2020;270:117464.
- [10] Guene Lougou B, Shuai Y, Chaffa G, Xing H, Tan H, Du H. Analysis of CO<sub>2</sub> utilization into synthesis gas based on solar thermochemical CH<sub>4</sub>-reforming. *J Energy Chem* 2019;28:61–72.
- [11] Rafiee A, Khalilpour KR, Milani D. Chapter 8- CO<sub>2</sub> conversion and utilization pathways. In: *Polygeneration with Polystorage for Chemical and Energy Hubs*. Elsevier; 2019. p. 213–45.
- [12] Cormos CC. Energy and cost efficient manganese chemical looping air separation cycle for decarbonized power generation based on oxy-fuel combustion and gasification. *Energy* 2020;191:116579–93.
- [13] Zhu X, Imitiaz Q, Donat F, Müller CR, Li F. Chemical looping beyond combustion – a perspective. *Energy Environ Sci* 2020;13(3):772–804.
- [14] Chen L, Bao J, Kong L, Combs M, Nikolic HS, Fan Z, et al. Activation of ilmenite as an oxygen carrier for solid-fueled chemical looping combustion. *Appl Energy* 2017; 197:40–51.
- [15] Heng L, Xiao R, Zhang H. Life cycle assessment of hydrogen production via iron-based chemical-looping process using non-aqueous phase bio-oil as fuel. *Int J Greenh Gas Control* 2018;76:78–84.
- [16] Zhao F, Fan L, Xu K, Hua D, Zhan G, Zhou S-F. Hierarchical sheet-like Cu/Zn/Al nanocatalysts derived from LDH/MOF composites for CO<sub>2</sub> hydrogenation to methanol. *J CO<sub>2</sub> Util* 2019;33:222–32.
- [17] Qu M, Qin G, Du A, Fan J, Sun Q. B80 Fullerene: A promising metal-free photocatalyst for efficient conversion of CO<sub>2</sub> to HCOOH. *J Phys Chem C* 2019;123 (39):24193–9.
- [18] Alper E, Yuksel Orhan O. CO<sub>2</sub> utilization: Developments in conversion processes. *Petroleum* 2017;3(1):109–26.
- [19] Aresta M, Nobile CF, Albano VG, Forni E, Manassero M. New nickel–carbon dioxide complex: synthesis, properties, and crystallographic characterization of (carbon dioxide)-bis(tricyclohexylphosphine) nickel. *J Chem Soc Chem Commun* 1975;0 (15):636–7.
- [20] Paparo A, Okuda J. Carbon dioxide complexes: Bonding modes and synthetic methods. *Coord Chem Rev* 2017;334:136–49.
- [21] Kayaki Y, Yamamoto M, Ikariya T. N-heterocyclic carbenes as efficient organocatalysts for CO<sub>2</sub> fixation reactions. *Angew Chem Int Ed* 2009;48(23): 4194–7.
- [22] Kimura T, Kamata K, Mizuno N. A bifunctional tungstate catalyst for chemical fixation of CO<sub>2</sub> at atmospheric pressure. *Angew Chem Int Ed* 2012;51(27):6700–3.
- [23] Yang Z-Z, He L-N, Zhao Y-N, Li B, Yu B. CO<sub>2</sub> capture and activation by superbase/polyethylene glycol and its subsequent conversion. *Energy Environ Sci* 2011;4(10): 3971.
- [24] Wei G, Zhou H, Huang Z, Zheng A, Zhao K, Lin Y, et al. Reaction performance of Ce-enhanced hematite oxygen carrier in chemical looping reforming of biomass pyrolyzed gas coupled with CO<sub>2</sub> splitting. *Energy* 2021;215:119044.
- [25] Wei G-Q, Feng J, Hou Y-L, Li F-Z, Li W-Y, Huang Z, et al. Ce-enhanced hematite oxygen carriers for chemical looping reforming of biomass pyrolyzed gas coupled with CO<sub>2</sub> splitting. *Fuel* 2021;285:119125.
- [26] Li D, Xu R, Li X, Li Z, Zhu X, Li K. Chemical looping conversion of gaseous and liquid fuels for chemical production: a review. *Energy Fuels* 2020;34(5):5381–413.
- [27] Zhao H, Tian X, Ma J, Su M, et al. Development of tailor-made oxygen carriers and reactors for chemical looping processes at Huazhong University of Science & Technology. *Int J Greenh Gas Control* 2020;93:102898–922.
- [28] Wang X, Wang X, Kong Z, Shao Y, Jin B. Auto-thermal operation and optimization of coal-fueled separated gasification chemical looping combustion in a pilot-scale unit. *Chem Eng J* 2020;383:123159–70.

- [29] Qin Wu, Wang J, Luo L, Liu Lu, Xiao X, Zheng Z, et al. Chemical looping reforming of ethanol-containing organic wastewater for high ratio  $H_2/CO$  syngas with iron-based oxygen carrier. *Int J Hydrog Energy* 2018;43(29):12985–98.
- [30] Idziak K, Czakiert T, Krzywanski J, Zylka A, Kozłowska M, Nowak W. Safety and environmental reasons for the use of Ni-, Co-, Cu-, Mn- and Fe-based oxygen carriers in CLC/CLOU applications: An overview. *Fuel* 2020;268:117245.
- [31] Tijani MM, Aqsha A, Mahinpey N. Synthesis and study of metal-based oxygen carriers (Cu Co, Fe, Ni) and their interaction with supported metal oxides ( $Al_2O_3$ ,  $CeO_2$ ,  $TiO_2$ ,  $ZrO_2$ ) in a chemical looping combustion system. *Energy* 2017;138: 873–82.
- [32] Sun Z, Lu DY, Ridha FN, Hughes RW, Filippou D. Enhanced performance of ilmenite modified by  $CeO_2$ ,  $ZrO_2$ ,  $NiO$ , and  $Mn_2O_3$  as oxygen carriers in chemical looping combustion. *Appl Energy* 2017;195:303–15.
- [33] Zhu X, Zhang M, Li K, Wei Y, Zheng Y, Hu J, et al. Chemical-looping water splitting over ceria-modified iron oxide: Performance evolution and element migration during redox cycling. *Chem Eng Sci* 2018;179:92–103.
- [34] Zhou H, Wei G, Yi Q, Zhang Z, Zhao Y, Zhang Y, et al. Reactivity investigation on chemical looping gasification of coal with Iron-Manganese based oxygen carrier. *Fuel* 2022;307:121772.
- [35] Tian X, Niu P, Ma Y, Zhao H. Chemical-looping gasification of biomass: Part II. Tar yields and distributions Biomass Bioenergy 2018;108:178–89.
- [36] Chen J, Zhao K, Zhao Z, He F, Huang Z, Wei G, et al. Reaction schemes of barium ferrite in biomass chemical looping gasification for hydrogen-enriched syngas generation via an outer-inner looping redox reaction mechanism. *Energy Conv Manag* 2019;189:81–90.
- [37] Chang G, Wu W, Shi P, Ma J, Guo Q. A promising composite bimetallic catalyst for producing  $CH_4$ -rich syngas from bitumite one-step gasification. *Energy Conv Manag* 2020;205:112408.
- [38] Cuiping W, Hao Y, Yanbo Yu, Wenzheng L, Shirui Y, Weiwei C, et al. Chemical Looping Reforming of Coal Tar Vapor on the Surface of  $CaO$ -Modified Fe-Based Oxygen Carrier. *Energy Fuels* 2020;34(7):8534–42.
- [39] Huang Z, Zheng A, Deng Z, Wei G, Zhao K, Chen D, et al. In-situ removal of toluene as a biomass tar model compound using  $NiFe_2O_4$  for application in chemical looping gasification oxygen carrier. *Energy* 2020;190:116360.
- [40] Huang Z, He F, Zhu H, Chen D, Zhao K, Wei G, et al. Thermodynamic analysis and thermogravimetric investigation on chemical looping gasification of biomass char under different atmospheres with  $Fe_2O_3$  oxygen carrier. *Appl Energy* 2015;157: 546–53.
- [41] Hosseini SY, Khosravi-Nikou MR, Shariati A. Production of hydrogen and syngas using chemical looping technology via cerium-iron mixed oxides. *Chem Eng Process* 2019;139:23–33.
- [42] Wei G, He F, Zhao Z, Huang Z, Zheng A, Zhao K, et al. Performance of Fe–Ni bimetallic oxygen carriers for chemical looping gasification of biomass in a 10  $kW_{th}$  interconnected circulating fluidized bed reactor. *Int J Hydrog Energy* 2015;40(46): 16021–32.
- [43] Zhong D, Zeng K, Li J, Qiu Yi, Flamant G, Nzihou A, et al. Characteristics and evolution of heavy components in bio-oil from the pyrolysis of cellulose, hemicellulose and lignin. *Renew Sust Energy Rev* 2022;157:111989.
- [44] Porrazzo R, White G, Ocone R. Aspen plus simulations of fluidised beds for chemical looping combustion. *Fuel* 2014;136:46–56.
- [45] Wu J, Bai L, Tian H, Riley J, Siriwardane R, Wang Z, et al. Chemical looping gasification of lignin with bimetallic oxygen carriers. *Int J Greenh Gas Control* 2020;93:102897.
- [46] He F, Huang Z, Wei G, et al. Biomass chemical-looping gasification coupled with water/ $CO_2$ -splitting using  $NiFe_2O_4$  as an oxygen carrier. *Energy Conv Manag* 2019; 201:112157.
- [47] Cao Z, Zhu X, Li K, Wei Y, He F, Wang H. Moderate-temperature chemical looping splitting of  $CO_2$  and  $H_2O$  for syngas generation. *Chem Eng J* 2020;397:125393.
- [48] Huang Z, Jiang H, He F, et al. Evaluation of multi-cycle performance of chemical looping dry reforming using  $CO_2$  as an oxidant with Fe–Ni bimetallic oxides. *J Energy Chem* 2015;000:1–9.





## Contents

Volume 285

2021

Published 1 February 2021

## REVIEWS

A comprehensive review of physicochemical properties, production process, performance and emissions characteristics of 2nd generation biodiesel feedstock: *Jatropha curcas*  
*D. Singh, D. Sharma, S.L. Soni, C.S. Inda, S. Sharma, P.K. Sharma and A. Jhalani*

119110

2,5-Dimethylfuran (DMF) as a promising biofuel for the spark ignition engine application: A comparative analysis and review  
*A.T. Hoang, S. Nizetic and A.I. Öçer*

119140

## FULL LENGTH ARTICLES

Influence of pore structure and surface free energy on the contents of adsorbed and free methane in tectonically deformed coal  
*G. Lu, C. Wei, J. Wang, R. Meng and L. Soh Tamehe*

119087

Catalytic pyrolysis of microcrystalline cellulose extracted from rice straw for high yield of hydrocarbon over alkali modified ZSM-5  
*Nishu, R. Liu, M.M. Rahman, C. Li, M. Chai, M. Sarker, Y. Wang and J. Cai*

119038

Combustion and emission behavior of different waste fuel blends in a laboratory furnace  
*K. Vershinina, P. Strizhak, V. Dorokhov and D. Romanov*

119098

In-situ analysis of the effect of CaO/Fe<sub>2</sub>O<sub>3</sub> addition on ash melting and sintering behavior for slagging-type applications  
*W. Shi, M. Laabs, M. Reinmüller, J. Bai, S. Guhl, L. Kong, H. Li, B. Meyer and W. Li*

119090

Effect of sac-volume on the relationship among ball behavior, injection and initial spray characteristics of ultra-high pressure GDI injector  
*M. Chang, J. Park, B. Kim, J.H. Park, S. Park and S. Park*

119089

Biomass ash characterization, fusion analysis and its application in catalytic decomposition of methane  
*M. Assad Munawar, A. Hussain Khoja, M. Hassan, R. Liaquat, S. Raza Naqvi, M. Taqi Mehran, A. Abdullah and F. Saleem*

119107

Investigating the contribution of carbon nanotubes and diesel-biodiesel blends to emission and combustion characteristics of diesel engine  
*R.A. Alenezi, A.M. Norkhizan, R. Mamat, Erdiwansyah, G. Najafi and M. Mazlan*

119046

Mutually interacting SNG-air premixed flames  
*Y. Kang, K.M. Lee and J. Park*

119065

Unveiling needle lift dependence on near-nozzle spray dynamics of diesel injector  
*R.H. Pratama, W. Huang and S. Moon*

119088

Experimental investigation of the attachment of unburned carbon in coal fly ash to a stationary air bubble in aqueous solutions  
*J. Wu, L. Chen, N. Zheng and Z. Sun*

119080

Simultaneous needle lift and injection rate measurement for GDI fuel injectors by laser Doppler vibrometry and Zeuch method  
*A. Cavicchi and L. Postrioti*

119021

Experimental evaluation of diesel engine powered with waste mango seed biodiesel at different injection timings and EGR rates  
*S. Rami Reddy, G. Murali, A. Ahamad Shaik, V. Dhana Raju and M.B.S. Sreekara Reddy*

119047

(Contents continued on inside back cover)

INDEXED/ABSTRACTED IN: Current Contents, ISI SciSearch, Ei Compendex, Ei Engineering, American Petroleum Institute Abstracts, APILIT, Cambridge Abstract Services, Analytical Abstracts, Chemical Engineering Biotechnology Abstracts, EMBASE, Energy Science and Technology, Enviroline, Fuel and Energy Abstracts, International Petroleum Abstracts, Pollution Abstracts, Mass Spectrometry Index, Geo Archive, ANTE, PASCAL, TULSA. Also covered in the abstract and citation database Scopus®. Full text available on ScienceDirect®.



0016-2361(20210201)285:1-A

Printed by CPI Antony Rowe, Pegasus Way, Melksham, UK

268

FUEL Vol. 285 (1 February 2021)

ELSEVIER

96



Volume 285, 1 February 2021 ISSN 0016-2361



the science and technology of Fuel and Energy

Available online at [www.sciencedirect.com](http://www.sciencedirect.com)

ScienceDirect

*Fuel* is concerned with the nature, conservation, preparation, use, interconversion, physical and nuclear properties and chemical reactions, including combustion, of gaseous, liquid and solid fuels and associated mineral matter; with basic data determining the comparative economics of fuels, and with organic geochemistry.

#### Publishing Office

Elsevier Ltd, The Boulevard, Langford Lane, Kidlington, Oxford OX5 1GB, UK. Tel: +44(0)1865 843000, Fax: +44(0)1865 843010.

**Advertising information:** If you are interested in advertising or other commercial opportunities please e-mail [Commercialsales@elsevier.com](mailto:Commercialsales@elsevier.com) and your inquiry will be passed to the correct person who will respond to you within 48 hours.

#### Author inquiries

You can track your submitted article at <http://www.elsevier.com/track-submission>. You can track your accepted article at <http://www.elsevier.com/trackarticle>. You are also welcome to contact Customer Support via <http://service.elsevier.com>.

**Language (usage and editing services):** Please write your text in good English (American or British usage is accepted, but not a mixture of these). Authors who feel their English language manuscript may require editing to eliminate possible grammatical or spelling errors and to conform to correct scientific English may wish to use the English Language Editing service available from Elsevier's WebShop <http://webshop.elsevier.com/languageediting/> or visit our customer support site <http://service.elsevier.com> for more information.

**Illustration services:** Elsevier's WebShop (<http://webshop.elsevier.com/illustrationservices>) offers Illustration Services to authors preparing to submit a manuscript but concerned about the quality of the images accompanying their article. Elsevier's expert illustrators can produce scientific, technical and medical-style images, as well as a full range of charts, tables and graphs. Image 'polishing' is also available, where our illustrators take your image(s) and improve them to a professional standard. Please visit the website to find out more.

**Publication information:** *Fuel* (ISSN 0016-2361) is published bi-monthly by Elsevier (Radarweg 29, 1043 NX Amsterdam, The Netherlands) and distributed by Elsevier, 360 Park Avenue South, New York, NY 10010-1710, USA. Periodicals Postage Paid at New York, NY and at additional mailing offices (not valid for journal supplements). USA POSTMASTER: Send change of address to *Fuel*, Elsevier Customer Service Department, 3251 Riverport Lane, Maryland Heights, MO 63043, USA.

**Orders, claims, and journal inquiries:** please contact the Elsevier Customer Service Department nearest you:

**St. Louis:** Elsevier Customer Service Department, 3251 Riverport Lane, Maryland Heights, MO 63043, USA; phone: (877) 8397126 [toll free within the USA]; (+1) (314) 4478878 [outside the USA]; fax: (+1) (314) 4478077; e-mail: [JournalCustomerService-usa@elsevier.com](mailto:JournalCustomerService-usa@elsevier.com)

**Oxford:** Elsevier Customer Service Department, The Boulevard, Langford Lane, Kidlington, Oxford OX5 1GB, UK; phone: (+44) (1865) 843434; fax: (+44) (1865) 843970; e-mail: [JournalCustomerServiceEMEA@elsevier.com](mailto:JournalCustomerServiceEMEA@elsevier.com)

**Tokyo:** Elsevier Customer Service Department, 4F Higashi-Azabu, 1-Chome Bldg, 1-9-15 Higashi-Azabu, Minato-ku, Tokyo 106-0044, Japan; phone: (+81) (3) 5561 5037; fax: (+81) (3) 5561 5047; e-mail: [JournalCustomerServiceJapan@elsevier.com](mailto:JournalCustomerServiceJapan@elsevier.com)

**The Philippines:** Elsevier Customer Service Department, 2nd Floor, Building H, UP-Ayalalad Technohub, Commonwealth Avenue, Diliman, Quezon City, Philippines 1101; phone: (+65) 6349 0222; fax: (+63) 2 352 1394; e-mail: [JournalCustomerServiceAPAC@elsevier.com](mailto:JournalCustomerServiceAPAC@elsevier.com)

**Back Issues:** Back issues of all previously published volumes are available direct from Elsevier Offices (Oxford and New York). Complete volumes and single issues can be purchased for 2000–2006. Earlier issues are available in high quality photo-duplicated copies as complete volumes only. Back volumes on microfilm are available from UMI, 300 North Zeeb Road, Ann Arbor, MI 48106, USA.

#### Funding body agreements and policies

Elsevier has established agreements and developed policies to allow authors whose articles appear in journals published by Elsevier, to comply with potential manuscript archiving requirements as specified as conditions of their grant awards. To learn more about existing agreements and policies please visit <http://www.elsevier.com/fundingbodies>

#### © 2020 Elsevier Ltd.

This journal and the individual contributions contained in it are protected under copyright, and the following terms and conditions apply to their use in addition to the terms of any Creative Commons or other user license that has been applied by the publisher to an individual article:

#### Photocopying

Single photocopies of single articles may be made for personal use as allowed by national copyright laws. Permission is not required for photocopying of articles published under the CC BY license nor for photocopying for non-commercial purposes in accordance with any other user license applied by the publisher. Permission of the publisher and payment of a fee is required for all other photocopying, including multiple or systematic copying, copying for advertising or promotional purposes, resale, and all forms of document delivery. Special rates are available for educational institutions that wish to make photocopies for non-profit educational classroom use.

#### Derivative Works

Users may reproduce tables of contents or prepare lists of articles including abstracts for internal circulation within their institutions or companies. Other than for articles published under the CC BY license, permission of the publisher is required for resale or distribution outside the subscribing institution or company.

For any subscribed articles or articles published under a CC BY-NC-ND license, permission of the publisher is required for all other derivative works, including compilations and translations.

#### Storage or Usage

Except as outlined above or as set out in the relevant user license, no part of this publication may be reproduced, stored in a retrieval system or transmitted in any form or by any means, electronic, mechanical, photocopying, recording or otherwise, without prior written permission of the publisher.

#### Permissions

For information on how to seek permission visit [www.elsevier.com/permissions](http://www.elsevier.com/permissions)

#### Author rights

Author(s) may have additional rights in their articles as set out in their agreement with the publisher (more information at <http://www.elsevier.com/authorsrights>).

#### Notice

Practitioners and researchers must always rely on their own experience and knowledge in evaluating and using any information, methods, compounds or experiments described herein. Because of rapid advances in the medical sciences, in particular, independent verification of diagnoses and drug dosages should be made. To the fullest extent of the law, no responsibility is assumed by the publisher for any injury and/or damage to persons or property as a matter of products liability, negligence or otherwise, or from any use or operation of any methods, products, instructions or ideas contained in the material herein.

Although all advertising material is expected to conform to ethical (medical) standards, inclusion in this publication does not constitute a guarantee or endorsement of the quality or value of such product or of the claims made of it by its manufacturer.

© The paper used in this publication meets the requirements of ANSI/NISO Z39.48-1992 (Permanence of Paper)

Printed by CPI Antony Rowe, Pegasus Way, Melksham, UK

For a full and complete Guide for Authors, please go to: <http://www.journals.elsevier.com/fuel/>

(Contents continued from outside back cover)

Apparent permeability model for gas transport through micropores and microfractures in shale reservoirs

Q. Gao, S. Han, Y. Cheng, Y. Li, C. Yan and Z. Han

119086

Phase transitions involving Ca – The most abundant ash forming element – In thermal treatment of lignocellulosic biomass

M. Thyrel, R. Backman, D. Boström, U. Skyllberg and T.A. Lestander

119054

The effect of direct water injection on a diesel-gasoline reactivity controlled compression ignition engine

M. Kahnooji and K. Yazdani

119109

Extraction of shale oil with supercritical CO<sub>2</sub>: Effects of number of fractures and injection pressure

H. Yu, H. Xu, W. Fu, X. Lu, Z. Chen, S. Qi, Y. Wang, W. Yang and J. Lu

118977

Effect of hydrogen and 1-Hexanol on combustion, performance and emission characteristics of CRDI CI engine

K. Santhosh and G.N. Kumar

119100

High-temperature pyrolysis of biomass pellets: The effect of ash melting on the structure of the char residue

X. Wang, M. Zhai, H. Guo, A. Panahi, P. Dong and Y.A. Levendis

119084

Experimental & predicative analysis of engine characteristics of various biodiesels

U. Rajak, P. Nashine, P.K. Chaurasiya, T.N. Verma, D.K. Patel and G. Dwivedi

119097

Investigation of reactivities of bimetallic Cu-Fe oxygen carriers with coal in high temperature in-situ gasification chemical-looping combustion (IG-CLC) and chemical-looping with oxygen uncoupling (CLOU) using a fixed bed reactor

P. Wang, B. Howard and N. Means

119012

Gaseous emissions from freshly extracted coal in the inert and air atmosphere in terms of natural desorption and early coal oxidation

A. Dudzińska, J. Cygankiewicz and M. Włodarek

119066

Performance, emission and combustion characteristics of unmodified diesel engine with titanium dioxide (TiO<sub>2</sub>) nano particle along with water-in-diesel emulsion fuel

R. Vigneswaran, D. Balasubramanian and B.D.S. Sastha

119115

Chemo-rheological and morphology evolution of polymer modified bitumens under thermal oxidative and all-weather aging

G. Sun, B. Li, D. Sun, F. Yu and M. Hu

118989

Exhaust energy recovery via catalytic ammonia decomposition to hydrogen for low carbon clean vehicles

S. Sittichompoon, H. Nozari, J.M. Herreros, N. Serhan, J.A.M. da Silva, A.P.E. York, P. Millington and A. Tsolakis

119111

Investigation of product distribution from co-pyrolysis of side wall waste tire and off-shore oil sludge

N. Gao, K. Kamran, Z. Ma and C. Quan

119036

Synergic effect of manganese oxide on ceria based catalyst for direct conversion of CO<sub>2</sub> to green fuel additive: Catalyst activity and thermodynamics study

P. Kumar, L. Matoh, R. Kaur and U.L. Štangar

119083

Direct numerical simulation of DME auto-ignition with temperature and composition stratification under HCCI engine conditions

L. Su, M. Zhang, J. Wang and Z. Huang

119073

The petroleum-degrading bacteria *Alcaligenes aquatilis* strain YGD 2906 as a potential source of lipopeptide biosurfactant

D. Yalaoui-Guellal, S. Fella-Temzi, S. Djafri-Dib, S.K. Sahu, V.U. Irorere, I.M. Banat and K. Madani

119112

Microplasma ball reactor for JP-8 liquid hydrocarbon conversion to lighter fuels

K. Rathore, S.I. Bhuiyan, S.M. Slavens and D. Staack

118943

Fragmentation of dolomite bed material at pressurized conditions in the presence of H<sub>2</sub>O and CO<sub>2</sub>: Implications for pressurized fluidized bed gasification

C. Zhou, C. Rosén and K. Engvall

119061

Torrefaction of corn straw in oxygen and carbon dioxide containing gases: Mass/energy yields and evolution of gaseous species

Y. Liu, E. Rokni, R. Yang, X. Ren, R. Sun and Y.A. Levendis

119044

Insights into pyrolytic feedstock potential of date palm industry wastes: Kinetic study and product characterization

G. Bensidhom, A. Ben Hassen Trabelsi, M.A. mahmood and S. Ceylan

119096

Synergistic effect of dielectric barrier discharge plasma and Mn catalyst on CO<sub>2</sub> reforming of toluene

K. Xiao, X. Li, J. Santoso, H. Wang, K. Zhang, J. Wu and D. Zhang

119057

Low-cost additives to improve the fusion behaviour of hydrochar ash

V. Benavente and A. Fullana

119009

(Contents continued on back matter)

# ScienceDirect



## Improve the way you search

Discover ScienceDirect and experience fast and reliable access to a world of scientific, technical and health content.

[facebook.com/Elsevier.ScienceDirect](https://facebook.com/Elsevier.ScienceDirect)  
[@sciencedirect](https://twitter.com/sciencedirect)  
[www.sciencedirect.com](http://www.sciencedirect.com)

Start today at **ScienceDirect.com** and:

- Register
- Set up alerts
- Read articles on the go



(Contents continued from previous page)

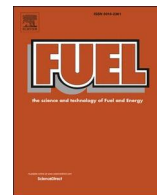
|   |        |   |        |
|---|--------|---|--------|
| Functional compounds of crude oil during low salinity water injection<br><i>M. Fattahi Mehraban, S.A. Farzaneh and M. Sohrabi</i>   | 119144 | Evaluation of surface diffusion in microporous/ mesoporous media using a numerical model applied to rate-of-adsorption data: Implications for improved gas permeability estimation in shales/tight rocks using drill cuttings<br><i>Z. Yang, B. Yuan, C.R. Clarkson and A. Ghanizadeh</i> | 118974 |
| Pilot scale production of fuel pellets from waste biomass leaves: Effect of milling size on pelletization process and pellet quality<br><i>P. Pradhan, S.M. Mahajani and A. Arora</i>   | 119145 | Modeling and optimization of a light-duty diesel engine at high altitude with a support vector machine and a genetic algorithm<br><i>J. Wang, L. Shen, Y. Bi and J. Lei</i>   | 119137 |
| Effect of ZnO nanoparticles concentration as additives to the epoxidized <i>Euphorbia Lathyris</i> oil and their tribological characterization<br><i>Y. Singh, N. Kumar Singh, A. Sharma, A. Singla, D. Singh and E. Abd Rahim</i>  | 119148 | DFT insights in to the hydrodenitrogenation behavior differences between indole and quinoline<br><i>X. Liu, S. Ding, Q. Wei, Y. Zhou, P. Zhang and Z. Xu</i>  | 119039 |
| Ca-enhanced hematite oxygen carriers for chemical looping reforming of biomass pyrolyzed gas coupled with CO <sub>2</sub> splitting<br><i>G.-q. Wei, J. Feng, Y.-L. Hou, F.-Z. Li, W.-Y. Li, Z. Huang, A.-q. Zheng and H.-b. Li</i> | 119125 | Modeling and numerical simulations of lignite char gasification with CO <sub>2</sub> : The effect of gasification parameters on internal transport phenomena<br><i>M. Karaca, D. Kaya, A. Yozgatligil and I. Gökalp</i>   | 119067 |
| Distilling small volumes of crude oil<br><i>G.F. Giordano, L.C.S. Vieira, A.O. Gomes, R.M. de Carvalho, L.T. Kubota, A. Fazio, G.R. Schleider, A.L. Gobbi and R.S. Lima</i>   | 119072 | Promotion effects of metallic iron on hydrothermal liquefaction of cornstalk in ethanol-water mixed solvents for the production of biocrude oil<br><i>B. Zhao, Y. Hu, L. Qi, J. Gao, G. Zhao, M.B. Ray and C.C. Xu</i>  | 119150 |
| A review of controlling strategies of the ignition timing and combustion phase in homogeneous charge compression ignition (HCCI) engine<br><i>X. Duan, M.-C. Lai, M. Jansons, G. Guo and J. Liu</i>                                 | 119142 | Construction of a novel cold-adapted oleaginous yeast consortium valued for textile azo dye wastewater processing and biorefinery<br><i>S.S. Ali, J. Sun, E. Koutra, N. El-Zawawy, T. Elsamahy and M. El-Shetehy</i>  | 119050 |
| Flame spread and combustion characteristics of two adjacent jatropha oil droplets<br><i>J. Wang, H. Zhang, Q. Zhang, X. Qiao, X. Wang, D. Ju and C. Sun</i>   | 119077 | Enhanced mercury control but increased bromine and sulfur trioxides emissions after using bromine injection technology based on full-scale experiment<br><i>Q. Wu, M. Wen, G. Li, D. Han, Y. Bai, J. Sun, H. Cao, Z. Li, L. Xu, Y. Tang and S. Wang</i>                                   | 119130 |
| Regeneration of alkali poisoned TiO <sub>2</sub> -based catalyst by various acids in NO selective catalytic reduction with NH <sub>3</sub><br><i>X. Wang, H. Ma, Y. Shi, Q. Wang, P. Xu, W. Li and S. Li</i>                        | 119069 | In situ experimental study of CO <sub>2</sub> gasification of petcoke particles on molten slag surface at high temperature<br><i>M. Liu, Z. Shen, Q. Liang, J. Xu and H. Liu</i>  | 119158 |
| Effect of hydrogen addition on the ionization of partially premixed methane flame<br><i>L. Guo, M. Zhai, Q. Shen, H. Guo and P. Dong</i>  | 119141 | Engineering Ni/SiO <sub>2</sub> catalysts for enhanced CO <sub>2</sub> methanation<br><i>R.-P. Ye, L. Liao, T.R. Reina, J. Liu, D. Chevella, Y. Jin, M. Fan and J. Liu</i>  | 119151 |
| Dynamic modeling and offset-free predictive control of LNG tank<br><i>Y.-P. Jo, M.S.F. Bangi, S.-H. Son, J.S.-I. Kwon and S.-W. Hwang</i>   | 119074 | A Cu doped TiO <sub>2</sub> catalyst mediated Catalytic Thermo Liquefaction (CTL) of polyolefinic plastic waste into hydrocarbon oil<br><i>T.M. Ukarde and H.S. Pawar</i>   | 119155 |
| Directed regulation of whole-cell catalysis for high-quality galactonic acid bio-preparation and characterization by Ca <sup>2+</sup><br><i>X. Hua, X. Zhou and Y. Xu</i>   | 119134 | Improvement of Buckley-Leverett equation and its solution for gas displacement with viscous fingering and gravity effects at constant pressure for inclined stratified heterogeneous reservoir<br><i>M.Y. Khan and A. Mandal</i>  | 119172 |
| Mechanistic insights into the thermal oxidative deposition of C10 hydrocarbon fuels<br><i>T. Jia, L. Pan, X. Wang, J. Xie, S. Gong, Y. Fang, H. Liu, X. Zhang and J.-J. Zou</i>   | 119136 |   |        |
| Investigation of kerosene supersonic combustion performance with hydrogen addition and fuel additive at low Mach inflow conditions<br><i>F. Luo, W. Song, W. Chen and Y. Long</i>   | 119139 |   |        |

(Contents continued on next page)



Contents lists available at ScienceDirect

Fuel

journal homepage: [www.elsevier.com/locate/fuel](http://www.elsevier.com/locate/fuel)

Full Length Article

# Ca-enhanced hematite oxygen carriers for chemical looping reforming of biomass pyrolyzed gas coupled with CO<sub>2</sub> splitting

Guo-qiang Wei<sup>a,b,c,d</sup>, Jie Feng<sup>a,\*</sup>, Ya-Lei Hou<sup>e</sup>, Fang-Zhou Li<sup>a</sup>, Wen-Ying Li<sup>a,\*</sup>, Zhen Huang<sup>b</sup>, An-qing Zheng<sup>b</sup>, Hai-bin Li<sup>b</sup>

<sup>a</sup> Training Base of State Key Laboratory of Coal Science and Technology Jointly Constructed by Shanxi Province and Ministry of Science and Technology, Taiyuan University of Technology, Taiyuan 030024, China

<sup>b</sup> Guangzhou Institute of Energy Conversion, Chinese Academy of Sciences (CAS), Guangzhou 510640, China

<sup>c</sup> CAS Key Laboratory of Renewable Energy, Guangzhou 510640, China

<sup>d</sup> Guangdong Provincial Key Laboratory of New and Renewable Energy Research and Development, Guangzhou 510640, China

<sup>e</sup> Guangdong Communication Polytechnic, Guangzhou 510800, China

## ARTICLE INFO

### Keywords:

Biomass pyrolyzed gases  
Chemical looping reforming  
Ca-modified hematite oxygen carriers  
Ca<sub>2</sub>Fe<sub>2</sub>O<sub>5</sub>  
CO<sub>2</sub> splitting

## ABSTRACT

Chemical looping reforming (CLR) of biomass pyrolyzed gases coupled with CO<sub>2</sub> splitting was proposed to improve the H<sub>2</sub>/CO ratio of gaseous product by using Ca-enhanced hematite oxygen carriers. The oxygen carriers mainly consist of Fe<sub>2</sub>O<sub>3</sub>, Ca<sub>2</sub>Fe<sub>2</sub>O<sub>5</sub>, CaO and SiO<sub>2</sub>. The impurity gas in biomass pyrolyzed gases is consumed in CLR stage, attributing to the dry reforming reaction over a catalytic effect of oxygen carriers. The highest CH<sub>4</sub> conversion 98.26% and CO<sub>2</sub> conversion 71.92% are realized in the CLR process with the crystal transformation of Fe<sub>2</sub>O<sub>3</sub> and Ca<sub>2</sub>Fe<sub>2</sub>O<sub>5</sub> to Fe and CaO. The improved reactivity of hematite oxygen carriers by CaO is mainly ascribed to the intermetallic synergistic effect in Ca<sub>2</sub>Fe<sub>2</sub>O<sub>5</sub>, which influences the lattice oxygen release and selectivity of gaseous products. The maximum H<sub>2</sub>/CO ratio of gaseous product in CLR process is nearly 3 times as high as the initial H<sub>2</sub>/CO ratio of biomass pyrolyzed gas. Moreover, up to 80.95% CO<sub>2</sub> conversion efficiency and 2.32 mmol/min/g CO yield are achieved in CO<sub>2</sub> splitting step with the generation of Fe<sub>3</sub>O<sub>4</sub> and CaFe<sub>3</sub>O<sub>5</sub> in oxygen carriers. The CO<sub>2</sub> conversion shows positive correlation with reaction temperature but negative correlation with weight hourly space velocity. The metallic synergistic effect between Ca/Fe are conducive to improve CO<sub>2</sub> conversion though shifting the reaction equilibrium and enhancing ion diffusion. Modest reactivity and stability of Ca-modified oxygen carriers are confirmed in 15 cycles reaction, which indicates that potentially application prospect in CLR of biomass pyrolyzed gases coupled with CO<sub>2</sub> splitting process.

## 1. Introduction

There is an increasing demand for the development of clean renewable energy, ascribing to the serious energy and environmental challenges caused by the combustion of fossil fuels, like coal and oil. On one hand, the fossil fuels may be in short supply in the near future based on the limited reservation. On the other hand, a lot of greenhouse gases are produced from the combustion of fossil fuels, leading to the global warming, sea level rise, land desertification, and so on [1]. Therefore, it is an effective approach to alleviate greenhouse effect by using clean renewable energy instead of fossil fuels together with pursuing novel technology for CO<sub>2</sub> utilization [2,3].

Biomass is a kind of clean, efficient, carbon neutral and renewable

energy. Traditionally, biomass gasification by using air, steam, oxygen as gasifying agent is an effective utilization method to produce synthesis gas which is used for power generation and F-T synthesis in subsequent process [4,5]. Moreover, the chemical looping gasification (CLG) is an emerging technology to generate synthesis gas via the lattice oxygen of oxygen carriers instead of molecular oxygen. The CLG reaction can be performed in fluidized bed reactors. The oxygen carriers react with biomass to produce synthesis gas (i.e. CO, H<sub>2</sub>, CH<sub>4</sub>) in fuel reactor, and then the reduced oxygen carriers are transferred to air reactor, recovering lattice oxygen [6]. Previous research has confirmed that CLG of biomass is a promising technology which reveals an advantage in avoiding gasification agent, reducing tar content and improving synthesis gas heating value [7]. High quality synthesis gas has been achieved via the CLG of biomass at 840 °C by Huang Zhen with synthesis gas

\* Corresponding authors.

E-mail addresses: [fengjie@tyut.edu.cn](mailto:fengjie@tyut.edu.cn) (J. Feng), [ying@tyut.edu.cn](mailto:ying@tyut.edu.cn) (W.-Y. Li).

<https://doi.org/10.1016/j.fuel.2020.119125>

Received 5 March 2020; Received in revised form 23 June 2020; Accepted 28 August 2020

Available online 13 September 2020

0016-2361/© 2020 Elsevier Ltd. All rights reserved.



| Notation list                                  |                                     |                                   |   |
|--|-------------------------------------|-----------------------------------|---|
| AR   | air reactor                         | Ca(NO <sub>3</sub> ) <sub>2</sub> | calcium nitrate                                 |
| Ar   | argon                               | CR                                | carbon reactor                                  |
| CaO  | calcium oxide                       | Fe <sup>3+</sup>                  | ferric ion                                      |
| CCS  | CO <sub>2</sub> capture and storage | Fe <sub>2</sub> O <sub>3</sub>    | iron oxide                                      |
| CH <sub>4</sub>                                | methane                             | Fe <sub>3</sub> O <sub>4</sub>    | ferroferric oxide                               |
| CLC  | chemical looping combustion         | FR                                | fuel reactor                                    |
| CLG  | chemical looping gasification       | H <sub>2</sub>                    | hydrogen  |
| CLR  | chemical looping reforming          | LHV                               | lower heating value                             |
| CO   | carbon monoxide                     | [O]                               | lattice oxygen                                  |
| CO <sub>2</sub>                                | carbon dioxide                      | TPR                               | H <sub>2</sub> temperature programmed reduction |
| Ca <sup>2+</sup>                               | calcium ion                         | WHSV                              | weight hourly space velocity                    |
| Ca <sub>2</sub> Fe <sub>2</sub> O <sub>5</sub> | calcium iron oxide                  | XRD                               | X-ray diffraction                               |
| CaFe <sub>3</sub> O <sub>5</sub>               | calcium iron oxide                  | XRF                               | X-ray fluorescence                              |
| CaFe <sub>2</sub> O <sub>4</sub>               | calcium iron oxide                  | η <sub>CH4</sub>                  | CH <sub>4</sub> conversion                      |
|  |                                     | η <sub>CO2</sub>                  | CO <sub>2</sub> conversion                      |
|  |                                     | ξ                                 | H <sub>2</sub> /CO molar ratio                  |

yield 1.06 Nm<sup>3</sup>/kg, carbon conversion 87.63%, lower heating value (LHV) 15.43 MJ/Nm<sup>3</sup> and tar content 10.25 g/Nm<sup>3</sup> [8]. The CLG process reveals a comparative advantage over the biomass steam gasification process with the syngas LHV 13.95 MJ/Nm<sup>3</sup> and tar content 16.88 g/Nm<sup>3</sup> [9]. Also, the CLG process displays superiority in syngas LHV, tar content or operation cost over the air gasification, oxygen rich gasification or oxygen-steam gasification [10]. While, there are still some challenges for the syngas product from biomass gasification when it is used directly for power generation or F-T synthesis. Some impurity gases (e.g. CO<sub>2</sub>, CH<sub>4</sub>) are still present in the syngas product. The presence of CO<sub>2</sub> will reduce the heating value of syngas product and the overall efficiency of power generation. While, the separation of CO<sub>2</sub> from the synthesis gas is an energy intensive process. Also, the H<sub>2</sub>/CO ratio of gaseous product from CLG process is difficult to meet the requirements of F-T synthesis. How to remove the impurity gases efficiently and adjust the H<sub>2</sub>/CO of gaseous product for power generation or F-T synthesis are the challenges needed to be further investigated and overcome. Our previous studies have shown that CLG process can be divided into two process, which are biomass pyrolysis stage and pyrolyzed gas reforming stage. Due to higher reaction rate of gas-solid reaction, the pyrolyzed gas reforming process with oxygen carrier reveals significant effects on the composition and H<sub>2</sub>/CO of gaseous product. Changing the ratio of oxygen carriers and feedstock of biomass pyrolyzed gas in CLR process are conducive to eliminate some impurity gases and adjust H<sub>2</sub>/CO ratio of gaseous product. Therefore, the in situ chemical looping reforming (CLR) of biomass pyrolyzed gas provides an attractive alternative [11] to remove impurity gas and adjust H<sub>2</sub>/CO ratio of gaseous product for the power generation or F-T synthesis.

Nowadays, several strategies have been taken to control the accumulation of CO<sub>2</sub>. The CO<sub>2</sub> Capture and Storage (CCS) technology is viewed as an effective option to reduce CO<sub>2</sub> emission. However, this technology requires additional energy consumption to capture and transport CO<sub>2</sub> as well as enough ocean or underground space to storage CO<sub>2</sub> [12,13]. Chemical Looping Combustion (CLC) technology contributes to CO<sub>2</sub> capture, while, it has not yet involved in the utilization of CO<sub>2</sub> in current research. In fact, CO<sub>2</sub> utilization technologies contribute not only to reducing the CO<sub>2</sub> accumulation amount, but also to producing valuable chemicals. Typical CO<sub>2</sub> utilization technologies can be classified into two categories, which are physical utilization technologies and chemical utilization technologies converting CO<sub>2</sub> into chemicals. For the physical utilization, CO<sub>2</sub> has been applied in fire extinguisher, dry ice, refrigerant, solvent, process fluid, welding medium, or in algae farms for photosynthesis, etc. However, these CO<sub>2</sub> physical applications are limited in the scale and have slight impacted on the total accumulation amount of CO<sub>2</sub>. As for the chemical conversion of CO<sub>2</sub> into chemicals, CO<sub>2</sub> is used as feedstock for the F-T synthesis

or other chemical processes, which have positively impact on the global carbon balance with enormous potential rewards by recycling CO<sub>2</sub> into usable fuels or other chemicals. While, the CO<sub>2</sub> molecules are extremely stable, which causes a fundamental challenge in activation or decomposition of CO<sub>2</sub> to the useful intermediate components (e.g. CO, C). Traditionally, this process requires intense energy input and appropriate catalysts [14,15]. The chemical looping process reveals advantage in splitting CO<sub>2</sub> and generating CO with low cost and high efficiency. Therefore, the in situ CLR of biomass pyrolyzed gases coupled with CO<sub>2</sub> splitting process was proposed to improve H<sub>2</sub>/CO of biomass pyrolyzed gases and achieve CO from the greenhouse gas CO<sub>2</sub> simultaneously with lower energy input. The schematic for this system is shown in Fig. 1.

As illustrated in Fig. 1, the CLR of biomass pyrolyzed gases coupled with CO<sub>2</sub> splitting system consists of three reactors, which are FR (fuel reactor), CR (carbon reactor), AR (air reactor). The oxygen carriers firstly react with biomass pyrolyzed gases in FR to remove some of impurity gas (CH<sub>4</sub>, CO<sub>2</sub>) and adjust H<sub>2</sub>/CO ratio, where the oxygen carriers are reduced. Then, the reduced oxygen carriers are transferred to the CR, splitting CO<sub>2</sub> and generating CO. Finally, the oxygen carriers are delivered to the AR to recover lattice oxygen. The three reactions occur alternately in the whole system to generate higher H<sub>2</sub>/CO gaseous product and CO product successively. This reaction system reveals better advantages in improving biomass pyrolyzed gases H<sub>2</sub>/CO ratio and CO<sub>2</sub> utilization with low cost, high efficiency and simple operation.

Obviously, oxygen carriers play a critical role in the whole reaction system as the function of transferring reaction heat, lattice oxygen and catalytic splitting CO<sub>2</sub>. In recent years, various oxygen carriers including Ni, Fe, Mn, Cu, Co and nonmetallic oxygen carriers (e.g. CaSO<sub>4</sub>) have been tested in chemical looping conversion process [16–20]. Among these kinds of oxygen carriers, Fe-based oxygen carriers have attracted people's attention due to the advantages of low cost, non-toxicity, anti-sintering and high oxygen carrying capacity [21]. The Fe-based oxygen carriers used in chemical looping process can be classified into two major categories, which are nature iron ore oxygen carriers and synthetic iron-based oxygen carriers [22–24]. In fact, the synthetic iron-based oxygen carriers usually display better reactivity and selectivity than the natural ore oxygen carriers [25,26]. Whereas, there are still challenges for the synthetic oxygen carriers in industrial application due to the high preparation cost and low particle mechanical strength [27]. By contrast, the natural ore oxygen carriers exhibit better advantage in industrial application prospects with low cost, high particle mechanical strength and moderate reactivity. Furthermore, the reactivity and selectivity of the nature ore oxygen carriers can be improved by the modification of exogenous metal ions [24,28,29]. Liao investigates the reactivity of Fe<sub>2</sub>O<sub>3</sub> oxygen carriers with CaO additive in the chemical looping conversion of microalgae. The results indicate that CaO addition

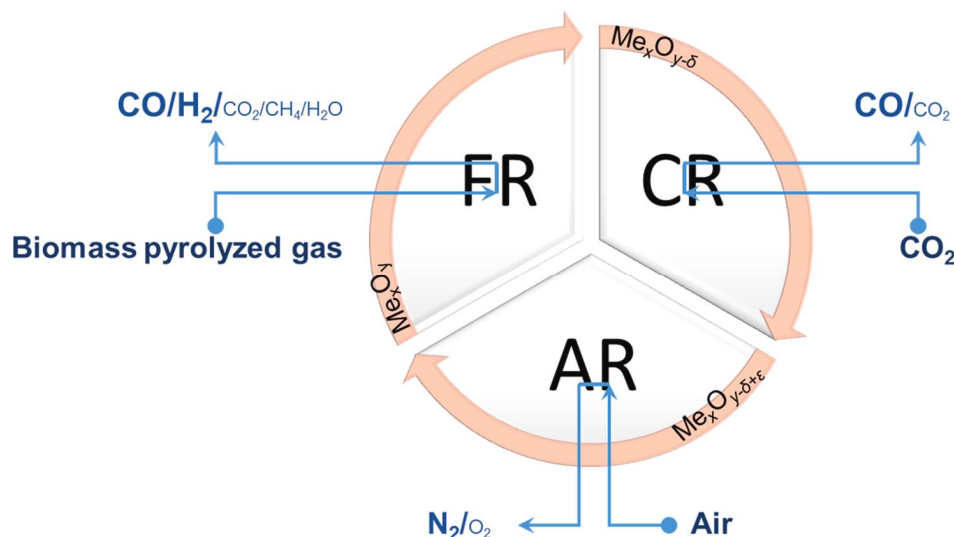


Fig. 1. Schematic for the CLR of biomass pyrolyzed gases coupled with CO<sub>2</sub> splitting process.

can efficiently depress CO<sub>2</sub> release and increase the yield of CO and H<sub>2</sub> as well as improve the gasification efficiency and gaseous products LHV. In particular, CaO plays a role of CO<sub>2</sub> absorbent and catalyst in the CLG process [30]. Also, there are limited literatures report that CaO addition can improve the carbon conversion and gasification rate in chemical looping process [31].

Therefore, the CLR of biomass pyrolyzed gas coupled with CO<sub>2</sub> splitting process is proposed in this study and hematite oxygen carriers enhanced by CaO are used in this reaction process to achieve higher H<sub>2</sub>/CO gaseous product and recycle CO<sub>2</sub>.

## 2. Experimental and apparatus

### 2.1. Materials

Natural hematite from China was crushed and screened into the particles with size of 0.18–0.25 mm. The major elements content of the hematite ore is shown in Table 1. Next, Ca(NO<sub>3</sub>)<sub>2</sub>·4H<sub>2</sub>O analytical pure sample was dissolved by deionized water to prepare solution. The hematite ore particles were incipient impregnated by the Ca(NO<sub>3</sub>)<sub>2</sub> solution with the CaO/hematite mass ratio of 5 wt%, 10 wt%, 15 wt% and 20 wt%. The water in impregnated mixture was evaporated in a thermostatic oscillator at 60 °C, and then the resulting particles was dried in air atmosphere for 12 h. Finally, the hematite oxygen carriers modified with CaO were achieved by calcining the impregnated hematite particles at 950 °C in a muffle furnace for 4 h. Correspondingly, the hematite oxygen carriers and the samples modified by CaO with mass ratio of 5 wt%, 10 wt%, 15 wt%, 20 wt% were marked as HC0, HC5, HC10, HC15 and HC20, respectively. Also, the volume content of model biomass pyrolyzed gases consisting of 15 vol% H<sub>2</sub>, 30 vol% CO, 12.5 vol% CH<sub>4</sub>, 5 vol% CO<sub>2</sub>, 37.5 vol% N<sub>2</sub> were used as reactant gas in CLR stage. The pyrolysis temperature had an important influence on the composition of biomass pyrolyzed gases. The composition of biomass pyrolyzed gases used in this study was derived from our previous pyrolysis experiments with biomass raw material at 850 °C. The volume fraction of CO<sub>2</sub> used in CR experiment was more than 99.99 vol%.

### 2.2. Method and apparatus

The reactivity of lattice oxygen in oxygen carriers was evaluated by H<sub>2</sub> temperature programmed reduction (TPR, ASIQAIV200-2) with gas flow rate of 120 ml/min (5 vol% H<sub>2</sub>/He) and heating rate of 10 °C/min. Moreover, the crystalline evolution of oxygen carriers in the reaction process was characterized by X-ray diffraction (XRD, X'Pert PRO MPD) with Cu Kα radiation (40 kV, 40 mA) at scan rate 2°/min and step of 0.0167°. The elements content of nature hematite ore was analyzed by X-ray fluorescence (XRF, AXIOSMAX- PETRO). Fixed bed reactor system consisting of electric furnace, quartz tube, temperature control system, gas flow control system and clarification unit was used to investigate the CLR coupled with CO<sub>2</sub> splitting process. The flowsheet of experimental apparatus was shown in Fig. 2. The parameters of quartz tube used in this experiment were 800 mm length and 23 mm inner diameter.

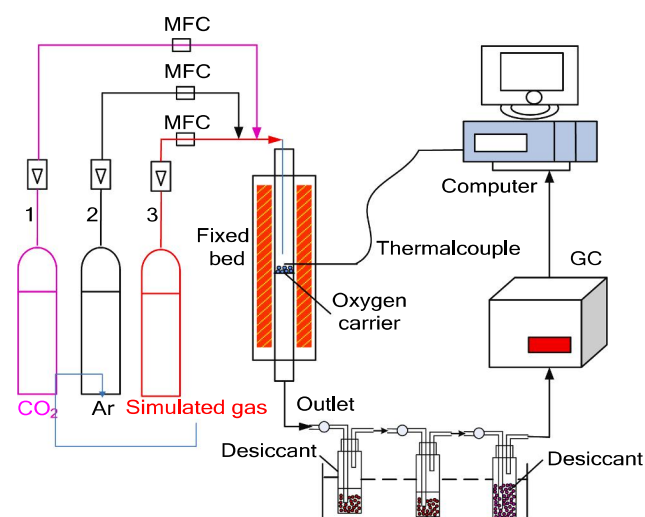


Fig. 2. Flowsheet of the experimental apparatus.

Table 1

The elements content of nature hematite ore.

| Elements | Fe    | O     | Si   | Al   | Zn   | Na   | P    | Ca   | Mg   | Mn   | Ti   | K    |
|----------|-------|-------|------|------|------|------|------|------|------|------|------|------|
| Conc. %  | 64.61 | 30.10 | 2.83 | 1.40 | 0.53 | 0.10 | 0.10 | 0.09 | 0.08 | 0.05 | 0.03 | 0.02 |

Before the experiments, 1 g oxygen carriers were played on the sieve plate of quartz tube, where quartz cotton was spread on the sieve plate in advance. Then the fixed bed reactor was heated up with an Ar gas replacing air in quartz tube simultaneously. When the reactor temperature reaches the set data, the model biomass pyrolyzed gases was introduced to perform the CLR process with gas flow rate of 60 ml/min. The CLR process lasted for 30 min. Then high purity CO<sub>2</sub> was introduced fixed bed reactor at a gas flow rate of 50 ml/min to carry out the CO<sub>2</sub> splitting process after 20 min Ar purge. After the CO<sub>2</sub> splitting reaction, the used oxygen carriers were regenerated in air atmosphere for 60 min to complete a cycle redox reaction. Agilent gas chromatograph (7890A) was used to analyzed the gaseous products composition.

### 2.3. Data analysis

Gas composition was calculated with Eq. (1):

$$c_i = \frac{\int_0^t v x_i dt}{\int_0^t v (x_{CO} + x_{CO_2} + x_{H_2} + x_{CH_4} + x_{N_2}) dt} \quad (1)$$

where,  $v$  was gas flow rate and  $x_i$  indicated volume fraction of species  $i$ . The total amount of each gaseous product was evaluated on the basis of Ar balance. The conversion ( $\eta$ , %) of CO<sub>2</sub> and CH<sub>4</sub> in CLR stage are presented as:

$$\eta_{CO_2} = \frac{\int_0^t v \times x_{CO_2} dt - c_{CO_2} \times G_{out}}{\int_0^t v x_{CO_2} dt} \quad (2)$$

$$\eta_{CH_4} = \frac{\int_0^t v \times x_{CH_4} dt - c_{CH_4} \times G_{out}}{\int_0^t v x_{CH_4} dt} \quad (3)$$

The H<sub>2</sub>/CO molar ratio ( $\xi$ ) in the gas products is defined as:

$$\xi = \frac{c_{H_2}}{c_{CO}} \quad (4)$$

The conversion ( $\eta$ , %) of CO<sub>2</sub> in splitting stage is also calculated by the Eq. (2) and the CO yield is achieved by the gas products amount analysis.

## 3. Results and discussion

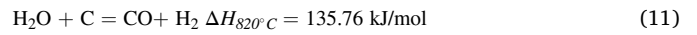
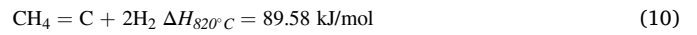
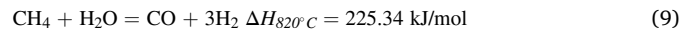
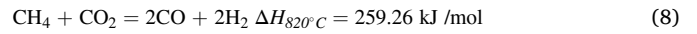
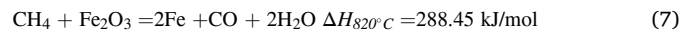
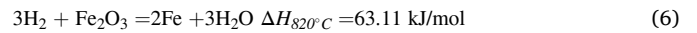
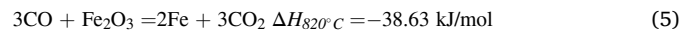
### 3.1. Mass and heat balances analysis

Before the experiment, the mass balance and heat balance analysis of the CLR of biomass pyrolyzed gas coupled with CO<sub>2</sub> splitting reaction system were performed to achieve chemical reaction equilibrium limit and thermodynamic parameter. The following assumptions were adopted:

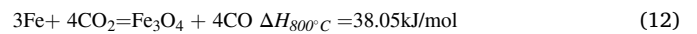
- The calculations were performed by using Aspen Plus simulation software based on the Gibbs free energy minimum principle without considering reaction kinetics, mass transfer and other factors.
- All the reactors in this system have been in chemical reaction equilibrium state.
- Fe<sub>2</sub>O<sub>3</sub> modified by CaO (molar ratio: 85.7% Fe<sub>2</sub>O<sub>3</sub>, 14.3% Ca<sub>2</sub>Fe<sub>2</sub>O<sub>5</sub>) was used as oxygen carrier in the calculation and model gas consisting of 15 vol% H<sub>2</sub>, 30 vol% CO, 12.5 vol% CH<sub>4</sub>, 5 vol% CO<sub>2</sub>, 37.5 vol% N<sub>2</sub> was used as reactant gas in FR.
- The temperature of AR, FR and CR were set at 840 °C, 820 °C and 800 °C in order to guarantee suitable reaction rate and heat transfer.
- The feeding rates of biomass pyrolyzed gases in FR were 1 kmol/hr. Also, the gas flow rate of CO<sub>2</sub> in CR and air in AR were set as 0.2 kmol/hr and 0.75 kmol/hr, respectively.

Main reactions of the three reactors under atmospheric pressure were shown as below.

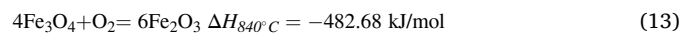
### Fuel Reactor (FR)



### Carbon Reactor (CR)



### Air Reactor (AR)



The Aspen Plus simulation flowsheet of CLR coupled with CO<sub>2</sub> splitting system was shown in Fig. 3. Table 2 summarized the calculation results of mass balance and heat balance analysis. It was observed from the table that oxygen carriers can react with biomass pyrolyzed gases in FR to convert CH<sub>4</sub> and generate H<sub>2</sub>. The mole flow of CH<sub>4</sub> decreased from 0.125 kmol/hr to nearly 0, while the mole flow of H<sub>2</sub> increased from 0.15 kmol/hr to 0.25 kmol/hr. The CLR process in FR indicates good potential to reduce the CH<sub>4</sub> content and adjust the H<sub>2</sub>/CO in biomass pyrolyzed gas. The reduced oxygen carriers of Fe and CaO can spilt CO<sub>2</sub> to generate CO in CR at 800 °C, where the oxygen carriers are oxidized to Fe<sub>3</sub>O<sub>4</sub> and Ca<sub>2</sub>Fe<sub>2</sub>O<sub>5</sub>. Finally, the reacted oxygen carrier including Fe<sub>3</sub>O<sub>4</sub>, Fe and Ca<sub>2</sub>Fe<sub>2</sub>O<sub>5</sub> are transferred to AR, recovering lattice oxygen and releasing reaction heat. The mass recovery of Fe and Ca elements in the whole reaction process were 100%.

Moreover, the heat duty of FR, CR and AR three reactors in CLR coupled with CO<sub>2</sub> splitting process were 72.30 kW, -1.70 kW and -10.72 kW, respectively, which were also presented in Table. 2. The reactions in FR were strongly endothermic while the reactions in CR and AR were weakly exothermic, which can realize partial heat complementation between the three reactors though the circulating of oxygen carrier. Overall, the CLR coupled with CO<sub>2</sub> splitting process requires an additional heat to maintain operation under the current conditions. Actually, the following three measures can be adopted to improve the system thermal efficiency and reduce the additional heat: (a) The circulation of oxygen carrier in system can be increased to supply more lattice oxygen in FR and improve the exothermic reactions. This process is easy to be performed, while the active composition of biomass pyrolyzed gas in FR will be partially consumed. (b) The feedstock of reactant gases in the inlets of three reactors were preheated by using sensible heat from the outlet gases of three reactors. (c) The CLR coupled with CO<sub>2</sub> splitting process were operated at lower temperatures based on the feasible temperature region from reaction thermodynamics and kinetics.

### 3.2. Characterization of Ca-modified hematite oxygen carriers

The crystalline phases of fresh hematite oxygen carriers (HC0) and CaO modified sample (HC10) were characterized by XRD analysis, as illustrated in Fig. 4. It is observed that Fe<sub>2</sub>O<sub>3</sub>, Al<sub>2</sub>O<sub>3</sub> and SiO<sub>2</sub> are mainly composed of hematite oxygen carriers, which are well correspond to JCPDS standard card. Moreover, The Ca-modified hematite oxygen carriers consist of Fe<sub>2</sub>O<sub>3</sub>, Al<sub>2</sub>O<sub>3</sub>, SiO<sub>2</sub> and Ca<sub>2</sub>Fe<sub>2</sub>O<sub>5</sub> (JCPDS: 01-071-2108). For hematite oxygen carriers, Fe<sub>2</sub>O<sub>3</sub> is the main active component to release lattice oxygen in chemical looping conversion process, while, the Al<sub>2</sub>O<sub>3</sub> and SiO<sub>2</sub> are regarded as inert carrier to prevent sintering of FeO<sub>x</sub> phase. Actually, the unit cell parameters of Fe<sub>2</sub>O<sub>3</sub>, Al<sub>2</sub>O<sub>3</sub>, SiO<sub>2</sub> display complementarity in hematite crystalline phase system [18]. The new

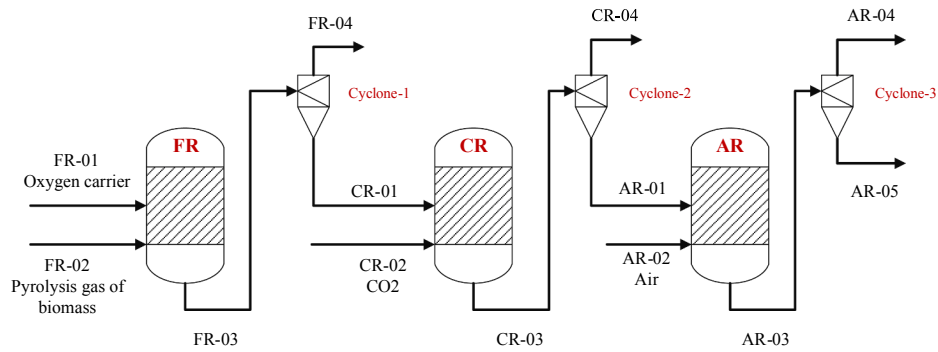


Fig. 3. Aspen plus simulation flowsheet of CLR coupled with CO<sub>2</sub> splitting system.

Table 2

Mass and heat balance analysis of CLR coupled with CO<sub>2</sub> splitting process.

| FR inlet                                       |                   | FR outlet                                      |                   | FR heat duty /kW |
|--|-------------------|--|-------------------|------------------|
| Species  | Mole flow/kmol/hr | Species  | Mole flow/kmol/hr |                  |
| H <sub>2</sub>                                 | 0.150             | H <sub>2</sub>                                 | 0.250             | 72.30            |
| CH <sub>4</sub>                                | 0.125             | CH <sub>4</sub>                                | ~0                |                  |
| CO   | 0.300             | CO   | 0.295             |                  |
| CO <sub>2</sub>                                | 0.050             | CO <sub>2</sub>                                | 0.180             |                  |
| N <sub>2</sub>                                 | 0.375             | H <sub>2</sub> O                               | 0.150             |                  |
|  |                   | N <sub>2</sub>                                 | 0.375             |                  |
|  |                   | Fe   | 0.053             |                  |
| Fe <sub>2</sub> O <sub>3</sub>                 | 0.841             | Fe <sub>3</sub> O <sub>4</sub>                 | 0.649             |                  |
| Ca <sub>2</sub> Fe <sub>2</sub> O <sub>5</sub> | 0.159             | CaO  | 0.318             |                  |
| CR inlet                                       |                   | CR outlet                                      |                   |                  |
| Species  | Mole flow/kmol/hr | Species  | Mole flow/kmol/hr | CR heat duty /kW |
| CO <sub>2</sub>                                | 0.200             | CO <sub>2</sub>                                | 0.077             | -1.70            |
| Fe   | 0.053             | CO   | 0.123             |                  |
| Fe <sub>3</sub> O <sub>4</sub>                 | 0.649             | Fe   | 0.001             |                  |
| CaO  | 0.318             | Fe <sub>3</sub> O <sub>4</sub>                 | 0.560             |                  |
|  |                   | Ca <sub>2</sub> Fe <sub>2</sub> O <sub>5</sub> | 0.159             |                  |
| AR inlet                                       |                   | AR outlet                                      |                   | -10.72           |
| Species  | Mole flow/kmol/hr | Species  | Mole flow/kmol/hr |                  |
| O <sub>2</sub>                                 | 0.158             | O <sub>2</sub>                                 | 0.017             |                  |
| N <sub>2</sub>                                 | 0.592             | N <sub>2</sub>                                 | 0.592             |                  |
| Fe   | 0.001             |  |                   |                  |
| Fe <sub>3</sub> O <sub>4</sub>                 | 0.560             | Fe <sub>2</sub> O <sub>3</sub>                 | 0.841             |                  |
| Ca <sub>2</sub> Fe <sub>2</sub> O <sub>5</sub> | 0.159             | Ca <sub>2</sub> Fe <sub>2</sub> O <sub>5</sub> | 0.159             |                  |

phase of Ca<sub>2</sub>Fe<sub>2</sub>O<sub>5</sub> is detected in the Ca-modified hematite, which reveals that CaO and Fe<sub>2</sub>O<sub>3</sub> in hematite are dispersed evenly to form new active compound. It reports that Ca<sub>2</sub>Fe<sub>2</sub>O<sub>5</sub> plays a major role in chemical looping process, promoting lattice oxygen release [32,33]. Also, the Ca<sub>2</sub>Fe<sub>2</sub>O<sub>5</sub> generation in calcination can be described as Eq. (14):



In addition, some trace elements, such as Zn, Na, Ca and Mn verified by X-ray fluorescence (XRF) analysis are too little to be neglected.

The reactivity of lattice oxygen in fresh hematite oxygen carriers (HC0) and modified sample (HC10) were characterized by the TPR analysis, as shown in Fig. 5. There are three H<sub>2</sub> absorption peaks at 476.3 °C, 625.2 °C and 845.5 °C in the TPR profile of hematite oxygen carriers, which can be ascribed to the crystal phase transformation process of Fe<sub>2</sub>O<sub>3</sub> → Fe<sub>3</sub>O<sub>4</sub> → FeO → Fe. By contrast, two H<sub>2</sub> consumption peaks are observed at 596.8 °C and 627.8 °C in the decorated hematite sample reaction curve. Based on XRD analysis, the H<sub>2</sub> reduced peaks can be summarized as the reduction of CaFe<sub>2</sub>O<sub>5</sub> to FeO, Fe and CaO in H<sub>2</sub> atmosphere at 557.2 °C, 728.7 °C respectively [34]. Apparently, the reduction temperature of Fe species in modified sample was lower than that in hematite oxygen carriers due to the synergistic effect between CaO and iron species in Ca<sub>2</sub>Fe<sub>2</sub>O<sub>5</sub>. Since the lattice oxygen in modified sample has a better reactivity, the Ca-modified hematite oxygen carriers exhibit the better advantage for the CLR of biomass pyrolyzed gas coupled with CO<sub>2</sub> splitting process [35].

### 3.3. Investigation on the CLR coupled with CO<sub>2</sub> splitting process

#### 3.3.1. Gas production as a function of reaction time in CLR stage

Ca-modified hematite oxygen carriers was used to further investigate

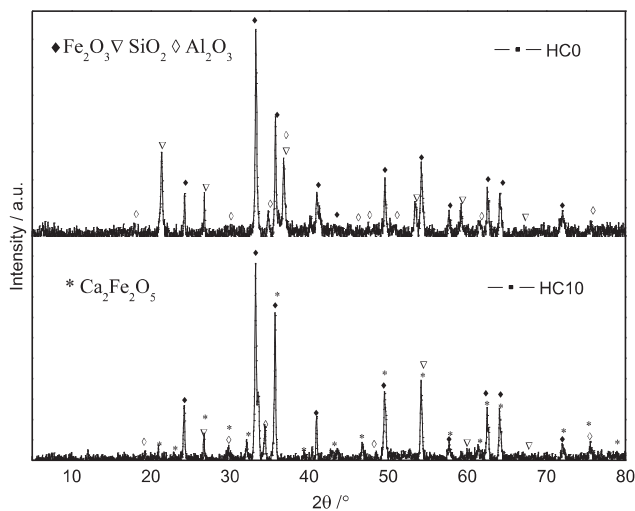


Fig. 4. XRD patterns of hematite and Ca-modified hematite oxygen carriers.

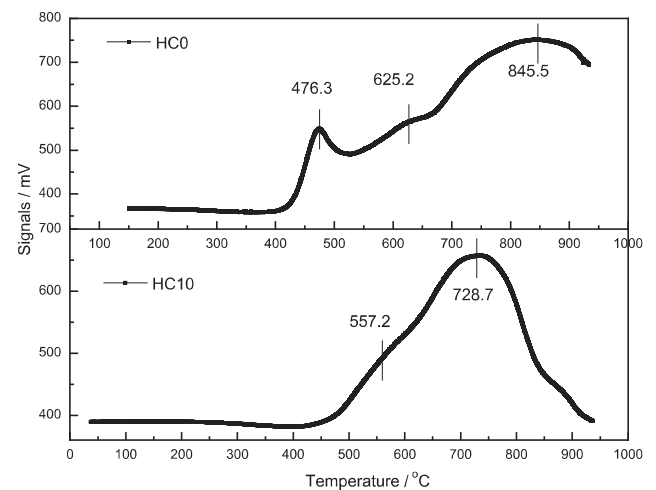
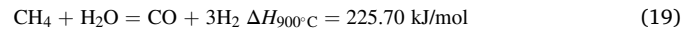
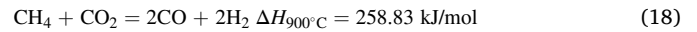
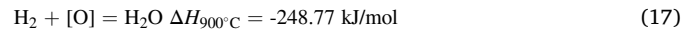
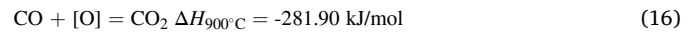
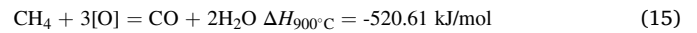


Fig. 5. TPR profiles of hematite and Ca-modified hematite oxygen carriers.



the CLR of biomass pyrolyzed gases coupled with CO<sub>2</sub> splitting process in fixed bed reactor. The gas product evolution and impurity gas (CO<sub>2</sub>, CH<sub>4</sub>) conversion with HC10 sample in CLR stage as function of reaction time at 900 °C are presented in Fig. 6. The CLR stage continued for 30 min. The composition of CO in gaseous products reveals a descending tendency within 6 minutes of reaction time then gradually ascends to a stable state. The H<sub>2</sub> composition increases as the proceeding of reaction. The maximum H<sub>2</sub>/CO ratio 1.47 of gaseous product appears at the 6<sup>th</sup> minute, which is nearly 3 times as high as the initial H<sub>2</sub>/CO ratio 0.5 of biomass pyrolyzed gas. The highest CH<sub>4</sub> conversion 98.26% and CO<sub>2</sub> conversion 71.92% were realized in the CLR process. These phenomena are ascribed to the oxidization reactions of lattice oxygen [O] from oxygen carriers at the initial stage and the dry reforming reaction of CH<sub>4</sub> in the later stage. The gas product yield and generation rate (productivity) display rising tendency with the reaction time, while, the CH<sub>4</sub> and CO<sub>2</sub> conversion indicate an opposite trend which decrease and then reach stability as the reaction time. The main CLR reactions are listed as Eqs. (15)–(19). Obviously, the oxygen carriers promote the CLR reactions at the early stage of reaction by releasing lattice oxygen [O] and takes catalytic effect on the conversion of impurity gas in biomass pyrolyzed gas at the later stage reaction. The reaction (16) contributes to CO<sub>2</sub> generation in CLR reaction process, leading to the negative value of CO<sub>2</sub> conversion after 19 min of CLR reaction. Moreover, the CLR total

efficiency of biomass pyrolyzed gas to biomass-based syngas can be calculated with the total syngas production and model gas input in Fig. 6, which is 70.44% in this process.



### 3.3.2. Effect of CaO content in oxygen carriers on the CLR process

To further investigate the effect of CaO addition in hematite oxygen carriers on the gas yield and composition of CLR process, a set of comparative experiments were conducted on the fixed bed reactor at 900 °C, as displayed in Fig. 7. Also, the reaction time of CLR process lasted for 30 min. It is found that the composition of H<sub>2</sub> and CO as well as the H<sub>2</sub>/CO (ξ) in syngas increase gradually then remain stable with the addition of CaO in hematite oxygen carriers. Nevertheless, the CH<sub>4</sub> and CO<sub>2</sub> volume fraction in gaseous product decline from 11.7 vol%, 6.84 vol% to 8.04 vol%, 6.04 vol%, respectively. Correspondingly, the gas productivity shows a similar trend to the gas composition with the addition of CaO in oxygen carriers. The generation rates of CO, H<sub>2</sub> increase from 0.64 mmol/min/g, 0.27 mmol/min/g to 0.67 mmol/min/g, 0.38 mmol/min/g, respectively. In comparison, the CH<sub>4</sub> and CO<sub>2</sub> productivity decrease from 0.26 mmol/min/g, 0.15 mmol/min/g to 0.18 mmol/min/g, 0.14 mmol/min/g severally. The CaO modified hematite oxygen carriers exhibit advantage in promoting the generation of CO and H<sub>2</sub>, but disadvantage in improving CH<sub>4</sub> and CO<sub>2</sub> conversion. Combined with XRD and TPR analysis, CaO improves the reactivity of hematite oxygen carriers mainly attributed to the intermetallic synergistic effect in Ca<sub>2</sub>Fe<sub>2</sub>O<sub>5</sub>. The previous study has indicated that Ca<sub>2</sub>Fe<sub>2</sub>O<sub>5</sub> plays important role in chemical looping process, enhancing the lattice oxygen release [36,37]. The reduced outer layers of Ca<sub>2</sub>Fe<sub>2</sub>O<sub>5</sub> is beneficial to oxygen ion movement, which influences the lattice oxygen transfer and selectivity of the products. Actually, 5 wt% CaO modified hematite oxygen carriers reveals better gas product yield and productivity with higher H<sub>2</sub>/CO (ξ). With more addition CaO addition in oxygen carriers, more Ca<sub>2</sub>Fe<sub>2</sub>O<sub>5</sub> generation improves the lattices oxygen release and gas production in chemical looping process. However, when the mass content of CaO in oxygen carriers is more than 10 wt%, the improvement effect is not obvious, because the CaO content is more than that generated Ca<sub>2</sub>Fe<sub>2</sub>O<sub>5</sub> in oxygen carriers based on the atomic mole ratio. The

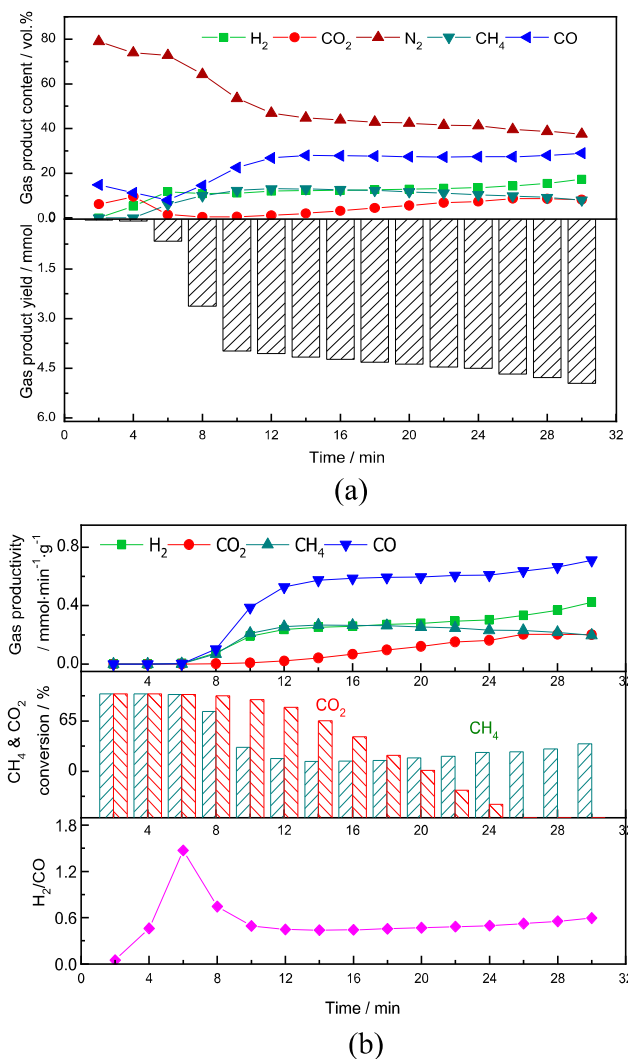


Fig. 6. Biomass pyrolyzed gases evolution as the function of reaction time in CLR stage: (a) Gas composition evolution and yield in the CLR stage; (b) Gas productivity and impurity gas conversion.

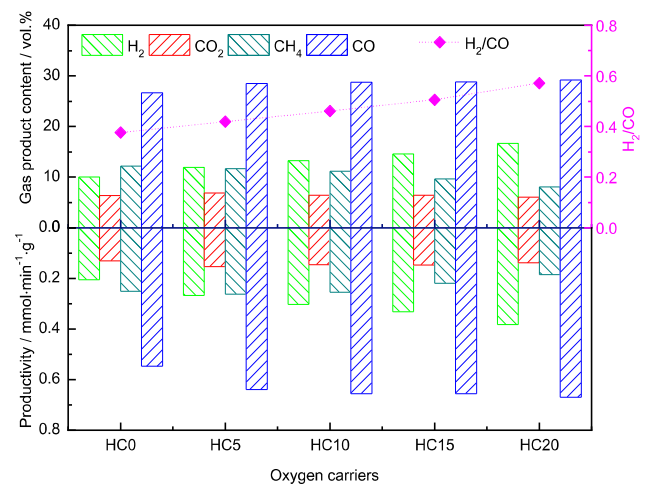


Fig. 7. The effect of CaO content in oxygen carriers on the CLR process.



surplus CaO is difficult to participate in the chemical looping process at 900 °C, leading to the slight improvement of oxygen carriers' reactivity. Considering the reaction performance and preparation cost, it is advantageous that the content of CaO in oxygen carriers is less than 15 wt. %.

Following the CLR process, CO<sub>2</sub> splitting reaction was carried out in fixed bed at 900 °C to utilize the greenhouse gas and achieve high purity CO with 10 wt% CaO modified oxygen carriers (HC10). The CO<sub>2</sub> conversion and CO productivity as the function of reaction time are shown in Fig. 8. It is noted that CO<sub>2</sub> reacts with the reduced oxygen carriers to generate CO following the Eq. (24). The CO instantaneous productivity reaches the maximum value 2.32 mmol/min/g at the initial 3 min of reaction then decreases gradually to 0.017 mmol/min/g as the proceeding of reaction time. Similarly, the CO<sub>2</sub> conversion decreases from 80.95% to 0.59% as the function of reaction time. As previously said, the CaFe<sub>2</sub>O<sub>5</sub> and Fe<sub>2</sub>O<sub>3</sub> were reduced by biomass pyrolyzed gases to consume lattice oxygen and create surface oxygen vacancies. CO<sub>2</sub> reacts with the reduced oxygen carriers to recover the oxygen vacancies from surface to the bulk phase. This reaction process is not only limited by mass transfer or diffusional but also in kinetically controlling regimes. As the lattice oxygen migration from the surface to the bulk phase in reaction process, the CO<sub>2</sub> conversion and CO productivity decline due to the decrease in oxygen deficiencies. Also, the formation of Fe<sub>3</sub>O<sub>4</sub> reorients the oxygen vacancies arrangement of oxygen carriers, which makes the lattice oxygen reaction more difficult. In addition, there is an equilibrium for the reversible reaction between CaO and CO<sub>2</sub> at high temperature. Small amount of CO<sub>2</sub> promotes the generation of CaCO<sub>3</sub>, whereas, with the increasing of CO<sub>2</sub>, the reaction tends to equilibrium gradually and the CO productivity descends until the reaction is accomplished at 40 min.

Moreover, Fig. 9 presents the XRD analysis of Ca modified oxygen carriers at different reaction stage. There are crystal phases of CaO (JCPDS: 01-087-0722), Fe (JCPDS: 01-074-1226) and SiO (JCPDS: 01-083-2466) in the reduced oxygen carriers after CLR process. This indicates that the CaFe<sub>2</sub>O<sub>5</sub> and Fe<sub>2</sub>O<sub>3</sub> in oxygen carriers are reduced to metallic Fe and CaO in CLR process. Moreover, the crystal phases of CaFe<sub>3</sub>O<sub>5</sub> (00-031-0274), CaO (JCPDS: 00-028-0775), CaCO<sub>3</sub> (JCPDS: 00-013-0192) and Fe<sub>3</sub>O<sub>4</sub> (JCPDS: 00-003-0862) are detected in the oxygen carriers after CO<sub>2</sub> splitting stage. Obviously, the metallic Fe was oxidized to Fe<sub>3</sub>O<sub>4</sub> in CO<sub>2</sub> splitting stage. Also, there is a reaction equilibrium between CaO and CaCO<sub>3</sub> in the reaction process with high CO<sub>2</sub> concentration atmosphere. Combined crystalline phase and TPR analysis, the reaction process of oxygen carriers in CLR coupled with CO<sub>2</sub> splitting process can be summarized as the reactions (20)–(26).

CLR stage

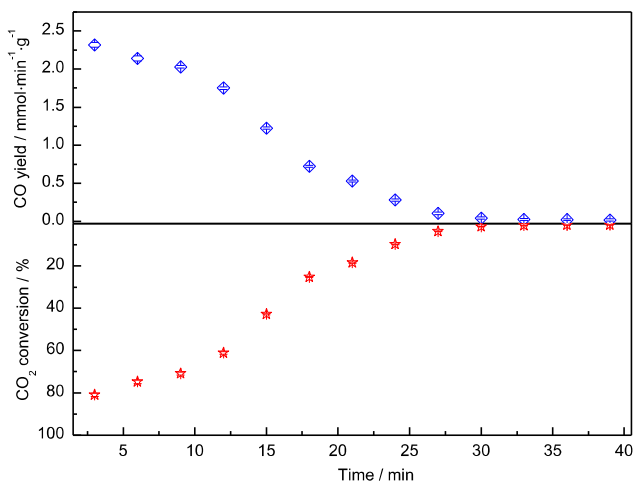


Fig. 8. CO<sub>2</sub> conversion and CO productivity as the function of reaction time.

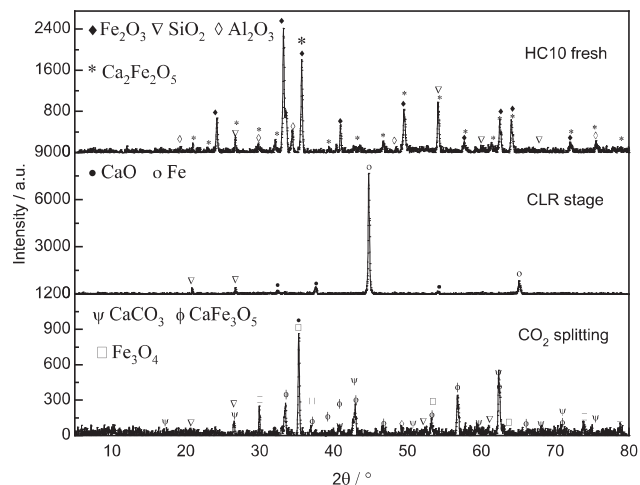
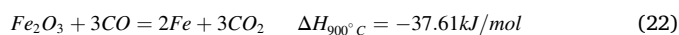
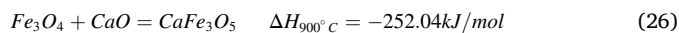
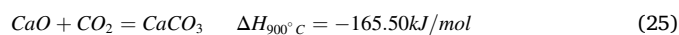


Fig. 9. XRD analysis of CaO modified oxygen carriers at different reaction stage.



CO<sub>2</sub> splitting stage



Furthermore, the whole reaction path for the CLR of biomass pyrolyzed gases coupled with CO<sub>2</sub> splitting process can be summarized as Ca<sub>2</sub>Fe<sub>2</sub>O<sub>5</sub> → CaO/Fe → Fe<sub>3</sub>O<sub>4</sub>/CaFe<sub>3</sub>O<sub>5</sub>, achieving syngas with a high H<sub>2</sub>/CO ratio.

### 3.3.3. Effect of temperature and WHSV on CO<sub>2</sub> splitting process

The effect of temperature and weight hourly space velocity (WHSV) on CO<sub>2</sub> splitting process were also evaluated in the fixed-bed reactor, as presented in Fig. 10. The reaction time was set at 30 min. HC10 oxygen carrier sample which was reduced by biomass pyrolyzed gases at 900 °C for 30 minutes with gas flow rate 60 ml/min was used in this study. It is observed that the increasing temperature enhances CO<sub>2</sub> conversion and CO generation due to the endothermic reaction between CO<sub>2</sub> and Fe. The CO<sub>2</sub> conversion and CO productivity rate increase from 48.99%, 1.00 mmol/min/g to 61.10%, 1.25 mmol/min/g, respectively in the temperature range of 750 °C to 950 °C. The reactivity of reduced oxygen carriers with CO<sub>2</sub> at various temperature follows the line of 750 °C < 800 °C < 850 °C < 900 °C, though the reaction equilibrium of CaO and CO<sub>2</sub> (Eq. (25)) shifts to the direction of reactant gas at high temperature. Fig. 10(b) presents the effect of WHSV on CO<sub>2</sub> splitting reaction. The WHSV represents the mass of reactant gas flow though per mass of oxygen carriers in per hour, which indicates the reaction efficiency of oxygen carriers. As for the reaction process of CO<sub>2</sub>, high WHSV of CO<sub>2</sub> leads to the increase in amount of CO<sub>2</sub> introduced and decrease of CO<sub>2</sub> conversion. To realize the CO<sub>2</sub> splitting process, it is necessary to make the CO<sub>2</sub> diffuse into the internal pores of oxygen carriers. As the WHSV increasing gradually from 4.32/h to 9.72/h, more CO<sub>2</sub> gas flows directly through the surface of oxygen carriers without reaction occurrence, resulting in the decrease of CO<sub>2</sub> conversion and CO productivity from 67.99%, 1.39 mmol/min/g to 27.51%, 0.56 mmol/min/g, separately.

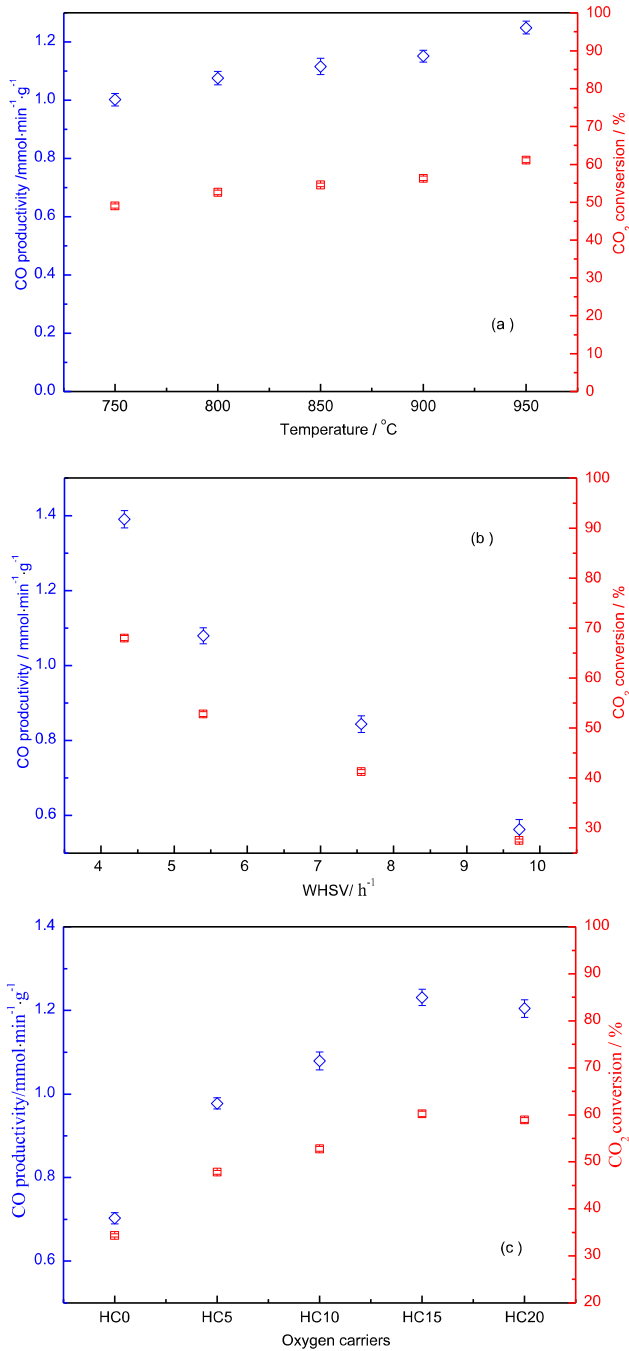
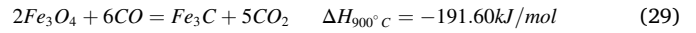
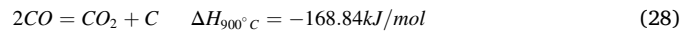
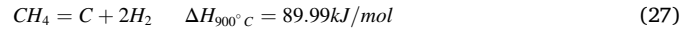


Fig. 10. Effect of operation conditions on the CO<sub>2</sub> spitting process: (a) temperature; (b) WHSV; (c) CaO content.

### 3.3.4. Effect of CaO content in oxygen carriers on CO<sub>2</sub> splitting process

Also, the influence of CaO content in oxygen carriers on CO<sub>2</sub> splitting process was investigated in fixed bed reactor with the 30 min reaction time, which is illustrated in Fig. 10(c). There is a similar trend for the CO<sub>2</sub> splitting reaction to the CLR process of biomass pyrolyzed gases with CaO addition in hematite oxygen carriers. The CO<sub>2</sub> conversion and CO productivity increase steadily to the maximum values 60.20% and 1.08 mmol/min/g at 15% CaO content in hematite oxygen carriers and then falls. Apparently, CaO plays a significant role in promoting CO<sub>2</sub> conversion in reaction compared with the unmodified hematite oxygen carriers. It has been confirmed by XRD analysis that the Ca<sub>2</sub>Fe<sub>2</sub>O<sub>5</sub> in oxygen carriers is first reduced to CaO/Fe in CLG stage and then oxidized to Fe<sub>3</sub>O<sub>4</sub>/CaFe<sub>3</sub>O<sub>5</sub> in CO<sub>2</sub> splitting process, producing CO gas.

With the addition of CaO in modified oxygen carriers, more CaO appears in the reduced oxygen carriers after CLR process, which further participates in the CO<sub>2</sub> splitting reaction. Accordingly, more CaO reacts with CO<sub>2</sub> to generate CaCO<sub>3</sub>, contributing to the CO<sub>2</sub> conversion in reaction. Also, the synergistic effect between CaO and metallic Fe are conducive to improve the CO<sub>2</sub> conversion reaction though the enhancing ion movement in oxygen carriers [37]. In addition, the reactions between CO<sub>2</sub> and carbon deposition in the CLR stage are another factor to increase the CO productivity, which are shown in the following reactions:



Therefore, the CO<sub>2</sub> conversion and CO yield in CO<sub>2</sub> spitting process show an upward trend with the CaO addition in oxygen carriers. Whereas, higher percentage of CaO in oxygen carriers corresponds to lower content of Fe species in oxygen carriers. It is obvious that Fe needs more CO<sub>2</sub> reactant than CaO based on the reactions (24) and (25). Consequently, the CO<sub>2</sub> conversion and CO productivity descend when the content of CaO exceeds 15% in oxygen carriers.

### 3.4. Successive cycle tests for the CLR coupled with CO<sub>2</sub> splitting process

Multiple cycle tests of 10 wt% CaO modified hematite oxygen carriers (HC10) were carried out in fixed bed at 900 °C with introducing the atmosphere of biomass pyrolyzed gases, CO<sub>2</sub> and air alternately. Each cyclic redox reaction consists of five steps, which are (1) CLR stage, 30 min; (2) Ar purge, 20 min; (3) CO<sub>2</sub> splitting, 30 min; (4) Ar purge, 20 min; (5) Air regeneration, 60 min. The cyclic reaction results are shown in Fig. 11. For the CLR stage, the productivity of H<sub>2</sub>, CO, CO<sub>2</sub> as well H<sub>2</sub>/CO (ξ) reveal upward trends in the first 5 cycles and then keep stability at the values of 0.52 mmol/min/g, 0.72 mmol/min/g, 0.16 mmol/min/g, 0.72 mmol/min/g separately in the later 10 cycles. Also, the generation rate of CH<sub>4</sub> exhibits a decreasing trend from 0.23 mmol/min/g to 0.13 mmol/min/g, which further indicates the rising conversion of CH<sub>4</sub> impurity gas in biomass pyrolyzed gases in CLR stage. Moreover, the CO<sub>2</sub> conversion and CO productivity in CO<sub>2</sub> splitting stage display similar trends, increasing from 52.78%, 1.07 mmol/min/g to 66.76%, 1.36 mmol/min/g, respectively. The rising conversion of CH<sub>4</sub> in CLR stage and CO<sub>2</sub> in splitting process are mainly attributed to the increasing of oxygen vacancy and catalytic active site in oxygen carriers caused by oxygen ion movement alternately in cyclic reaction process. Also, the increase of pore diameter and surface area of oxygen carriers in cyclic reaction is beneficial to the diffusion of reactant gas, improving the reaction efficiency. The CO<sub>2</sub> conversion 67.2% with CO generation rate

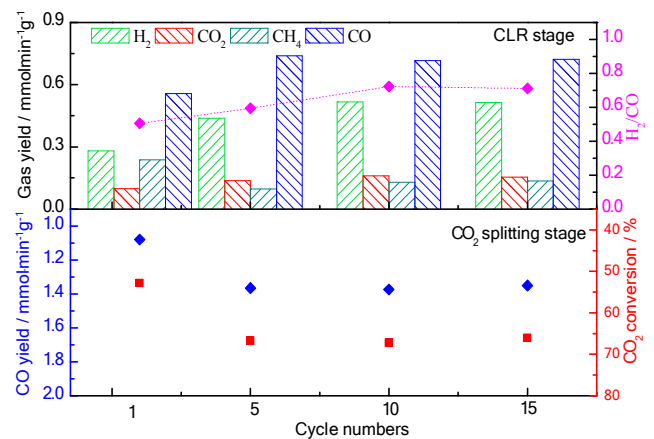


Fig. 11. Multiple cyclic reaction performances of Ca-modified oxygen carriers.

1.37 mmol/min/g is still achieved during the cyclic reaction, displaying the stable cyclic reaction performance of the Ca-modified hematite oxygen carriers.

### 3.5. Reaction path of oxygen carriers in the CLR coupled with CO<sub>2</sub> splitting

Also, the crystalline phase evolution of oxygen carriers at multiple redox cycles reactions is displayed in Fig. 12. The main crystalline phase of CaO modified oxygen carriers remains stable during the 15 cyclic reactions. The crystalline phase of oxygen carriers after 5 cyclic reaction is basically consistent with the fresh oxygen carriers, consisting of Ca<sub>2</sub>Fe<sub>2</sub>O<sub>5</sub> (JCPDS:00–018-0286), Fe<sub>2</sub>O<sub>3</sub> (JCPDS:00–033-0664) and SiO<sub>2</sub> (JCPDS:01–089-8937). Furthermore, Fe<sub>2</sub>O<sub>3</sub> and SiO<sub>2</sub> can still be detected after 15 cycles redox reaction, though CaFe<sub>2</sub>O<sub>4</sub> (JCPDS: 01–072-1199) generated from Ca<sub>2</sub>Fe<sub>2</sub>O<sub>5</sub> presents as the main crystalline phase of oxygen carriers. It is inferred that CaFe<sub>2</sub>O<sub>4</sub> indicates higher stability in cyclic reaction process, following the generation process (30) [38]:



Compared with the CaFe<sub>2</sub>O<sub>4</sub> production from Eq. (30), Ca<sub>2</sub>Fe<sub>2</sub>O<sub>5</sub> is easier to generated from the Eq. (14) on the basis of reaction thermodynamics, resulting in the appearance of Ca<sub>2</sub>Fe<sub>2</sub>O<sub>5</sub> in fresh oxygen carriers and used sample after 5 cycles reaction. As the proceeding of cyclic reaction, lattice oxygen continues to escape and migrate into the bulk phase of oxygen carriers alternately, which leads to an increase of oxygen deficiencies and ion diffusion based on reaction kinetics. Accordingly, It has confirmed by Hedvall and R. Freer [39] that the diffusion of Fe<sup>3+</sup> in CaFe<sub>2</sub>O<sub>4</sub> ( $D = 3.20 \times 10^{-8} \text{ cm}^2/\text{s}$ , 1100 °C) is more intensity than that of Ca<sup>2+</sup> in Ca<sub>2</sub>Fe<sub>2</sub>O<sub>5</sub> ( $D = 8.31 \times 10^{-10} \text{ cm}^2/\text{s}$ , 1140 °C) at high temperature, contributing to the transition of CaFe<sub>2</sub>O<sub>4</sub> from Ca<sub>2</sub>Fe<sub>2</sub>O<sub>5</sub> and Fe<sub>2</sub>O<sub>3</sub>. Consequently, the whole redox reaction path of the oxygen carriers is summarized as Ca<sub>2</sub>Fe<sub>2</sub>O<sub>5</sub> → CaO/Fe → Fe<sub>3</sub>O<sub>4</sub>/CaFe<sub>3</sub>O<sub>5</sub> → Ca<sub>2</sub>Fe<sub>2</sub>O<sub>5</sub>/CaFe<sub>2</sub>O<sub>4</sub>. The Ca-modified oxygen carriers manifests modest reactivity and stability during the cyclic redox reaction, which is suitable to the CLR coupled with CO<sub>2</sub> splitting process.

## 4. Conclusions

Hematite oxygen carriers modified by CaO were successfully used in the CLR of biomass pyrolyzed gases coupled with CO<sub>2</sub> splitting process to improve the H<sub>2</sub>/CO ratio of gaseous product. Ca-modified hematite oxygen carriers consist of Fe<sub>2</sub>O<sub>3</sub>, Al<sub>2</sub>O<sub>3</sub>, SiO<sub>2</sub> and Ca<sub>2</sub>Fe<sub>2</sub>O<sub>5</sub> that generates from the reaction CaO and Fe<sub>2</sub>O<sub>3</sub>. The CaO addition exhibits advantages in promoting the CO and H<sub>2</sub> generation while improving the impurity gas conversion due to the enhancement of O ion transfer by the new crystalline phase Ca<sub>2</sub>Fe<sub>2</sub>O<sub>5</sub>. The impurity gas CH<sub>4</sub> and CO<sub>2</sub> are consumed in the CLR stage by the oxidation reactions of lattice oxygen [O] and the dry reforming reaction. High temperature plays a role in promoting CO<sub>2</sub> splitting reaction, but high WHSV shows negative correlation with CO<sub>2</sub> conversion. The production of CaCO<sub>3</sub> and synergistic effect between CaO and metallic Fe are conducive to improve CO<sub>2</sub> conversion reaction in CO<sub>2</sub> splitting stage.

### CRedit authorship contribution statement

**Guo-qiang Wei:** Conceptualization, Data curation, Writing - original draft. **Jie Feng:** Supervision. **Ya-Lei Hou:** Resources. **Fang-Zhou Li:** Formal analysis. **Wen-Ying Li:** Methodology, Writing - review & editing. **Zhen Huang:** Project administration. **An-qing Zheng:** Resources. **Hai-bin Li:** Funding acquisition.

### Declaration of Competing Interest

The authors declare that they have no known competing financial interests or personal relationships that could have appeared to influence

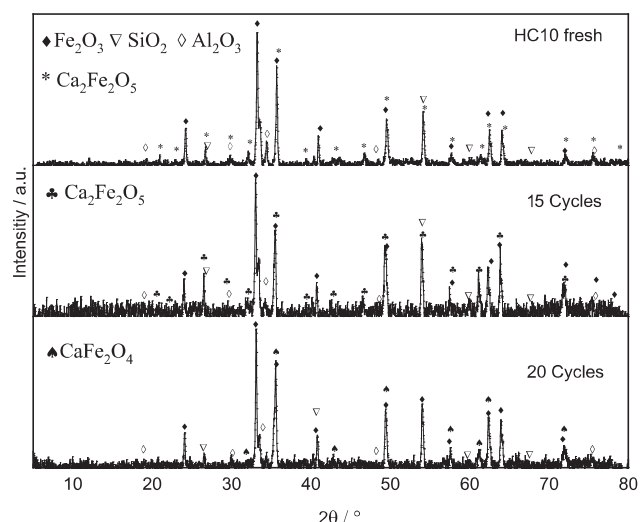


Fig. 12. Crystalline phase evolution of oxygen carriers at multiple redox cycles.

the work reported in this paper.

### Acknowledgements

The financial support of National Natural Science Foundation of China (Grant No. 51976226; No. 51776133) is gratefully acknowledged. This work is also supported by Cooperation fund of Dalian National Laboratory for Clean Energy, Chinese Academy of Sciences (DNL180205), Natural Science Foundation of Guangdong Province (2018A0303130012), Science & Technology Research Project of Guangdong Province (2015A020215023), and Science & Technology Project of Guangzhou (201707010202).

### References

- [1] Martins F, Felgueiras C, Smítková M, Caetano N. Analysis of fossil fuel energy consumption and environmental impacts in European countries. *Energies* 2019;12(6):964–74. <https://doi.org/10.3390/en12060964>.
- [2] Blumberg T, Morosuk T, Tsatsaronis G. CO<sub>2</sub>-utilization in the synthesis of methanol: Potential analysis and exergetic assessment. *Energy* 2019;175:730–44. <https://doi.org/10.1016/j.energy.2019.03.107>.
- [3] Lougou BG, Shuai Y, Chaffa G, Xing H, Tan HP, Du HB. Analysis of CO<sub>2</sub> utilization into synthesis gas based on solar thermochemical CH<sub>4</sub>-reforming. *J Energy Chem* 2019;28:61–72. <https://doi.org/10.1016/j.jchem.2018.01.011>.
- [4] Saebea D, Authayanun S, Arpornwichanop A. Process simulation of bio-dimethyl ether synthesis from tri-reforming of biogas: CO<sub>2</sub> utilization. *Energy* 2019;175:36–45. <https://doi.org/10.1016/j.energy.2019.03.062>.
- [5] Chen KF, Zhang L, Ai N, Zhang S, Song Y, Song YC, et al. Feasibility of direct utilization of biomass gasification product gas fuels in tubular solid oxide fuel cells for on-site electricity generation. *Energy Fuels* 2015;30(3):1849–57. <https://doi.org/10.1021/acs.energyfuels.5b02458>.
- [6] Wei GQ, He F, Huang Z, Zheng AQ, Zhao K, Li HB. Continuous operation of a 10 kW (th) chemical looping integrated fluidized bed reactor for gasifying biomass using an iron-based oxygen carriers. *Energy Fuels* 2015;29:233–41. <https://doi.org/10.1021/ef5021457>.
- [7] Boot-Handford ME, Florin N, Fennell PS. Investigations into the effects of volatile biomass tar on the performance of Fe-based CLC oxygen carriers materials. *Environ Res Lett* 2016;11(11):115001–10. <https://doi.org/10.1088/1748-9326/11/11/115001>.
- [8] Huang Z, He F, Feng YP, Zhao K, Zheng AQ, Chang S, Li HB. Synthesis gas production through biomass direct chemical looping conversion with natural hematite as an oxygen carriers. *Bioresour Technol* 2013;140:138–45. <https://doi.org/10.1016/j.biortech.2013.04.055>.
- [9] Huang Z, He F, Feng YP, Liu RD, Zhao K, Zheng AQ, et al. Characteristics of biomass gasification using chemical looping with iron ore as an oxygen carriers. *Int J Hydrog Energy* 2013;38:14568–75. <https://doi.org/10.1016/j.ijhydene.2013.09.022>.
- [10] AlNouss A, McKay G, Al-Ansari T. Production of syngas via gasification using optimum blends of biomass. *J Cleaner Prod* 2020;242:1–15. <https://doi.org/10.1016/j.jclepro.2019.118499>.
- [11] Wei GQ, Huang J, Fan YY, Huang Z, Zheng AQ, He F, et al. Chemical looping reforming of biomass based pyrolysis gas coupling with chemical looping hydrogen

- by using Fe/Ni/Al oxygen carriers derived from LDH precursors. *Energy Conv Manag* 2019;179:304–13. <https://doi.org/10.1016/j.enconman.2018.10.065>.
- [12] Galina NR, Arce GLAF, Ávila I. Evolution of carbon capture and storage by mineral carbonation: Data analysis and relevance of the theme. *Miner Eng* 2019;142: 105879–89. <https://doi.org/10.1016/j.mineng.2019.105879>.
- [13] Zhang S, Zhuang Y, Liu LL, Zhang L, Du J. Risk management optimization framework for the optimal deployment of carbon capture and storage system under uncertainty. *Renewable Sustainable Energy Rev* 2019;113:109280–92. <https://doi.org/10.1016/j.rser.2019.109280>.
- [14] Zhao FG, Fan LL, Xu KJ, Hua D, Zhan GW, Zhou SF. Hierarchical sheet-like Cu/Zn/Al nanocatalysts derived from LDH/MOF composites for CO<sub>2</sub> hydrogenation to methanol. *J CO<sub>2</sub> Util* 2019;33:222–32. <https://doi.org/10.1016/j.jcou.2019.05.021>.
- [15] Qu MN, Qin GQ, Du AJ, Fan JF, Sun Q. B80 Fullerene: A promising metal-free photocatalyst for efficient conversion of CO<sub>2</sub> to HCOOH. *J Phys Chem C* 2019;123 (39):24193–9. <https://doi.org/10.1021/acs.jpcc.9b07562>.
- [16] Ma JC, Wang JX, Tian X, Zhao HB. In-situ gasification chemical looping combustion of plastic waste in a semi-continuously operated fluidized bed reactor. *Proc Combust Inst* 2019;37(4):4389–97. <https://doi.org/10.1016/j.proci.2018.07.032>.
- [17] Zhu X, Li KZ, Neal L, Li FX. Perovskites as geo-inspired oxygen storage materials for chemical looping and three-way catalysis: a perspective. *ACS Catal* 2018;8(9): 8213–36. <https://doi.org/10.1021/acscatal.8b01973>.
- [18] Wei GQ, Wang H, Zhao WN, Huang Z, Yi Q, He F, Zhao K, Zheng AQ, Meng JG, Deng ZB, Chen J, Zhao ZL, Li HB. Synthesis gas production from chemical looping gasification of lignite by using hematite as oxygen carriers. *Energy Convers Manage* 2019;185:774–82. <https://doi.org/10.1016/j.enconman.2019.01.096>.
- [19] Wang BW, Li J, Ding N, Mei DF, Zhao HB, Zheng CG. Chemical looping combustion of a typical lignite with a CaSO<sub>4</sub>–CuO mixed oxygen carriers. *Energy Fuels* 2017;31 (12):13942–54. <https://doi.org/10.1021/acs.energyfuels.7b02584>.
- [20] Zhao X, Zhou H, Sikarwar VS, Zhao M, Park AA, Fennell PS, et al. Biomass-based chemical looping technologies: the good, the bad and the future. *Energy Environ Sci* 2017;10(9):1885–910. <https://doi.org/10.1039/C6EE03718F>.
- [21] Zhu M, Chen SY, Soomro A, Hu J, Sun Z, Ma SW, et al. Effects of supports on reduction activity and carbon deposition of iron oxide for methane chemical looping hydrogen generation. *Appl Energy* 2018;225:912–21. <https://doi.org/10.1016/j.apenergy.2018.05.082>.
- [22] Chen J, Zhao K, Zhao ZL, He F, Huang Z, Wei GQ. Identifying the roles of MFe<sub>2</sub>O<sub>4</sub> (M=Cu, Ba, Ni, and Co) in the chemical looping reforming of char, pyrolysis gas and tar resulting from biomass pyrolysis. *Int J Hydrogen Energy* 2019;44(10): 4674–87. <https://doi.org/10.1016/j.ijhydene.2018.12.216>.
- [23] Wei GQ, Zhao WN, Meng JG, Feng J, Li WY, He F, et al. Hydrogen production from vegetable oil via a chemical looping process with hematite oxygen carriers. *J Cleaner Prod* 2018;200:588–97. <https://doi.org/10.1016/j.jclepro.2018.07.263>.
- [24] Wang LL, Shen LH, Liu WD, Jiang SX. Chemical looping hydrogen generation using synthesized hematite-based oxygen carriers comodified by potassium and copper. *Energy Fuels* 2017;31(8):8423–33. <https://doi.org/10.1021/acs.energyfuels.7b01190>.
- [25] Huang Z, Deng ZB, He F, Chen DZ, Wei GQ, Zhao K, et al. Reactivity investigation on chemical looping gasification of biomass char using nickel ferrite oxygen carriers. *Int J Hydrogen Energy* 2017;42(21):14458–70. <https://doi.org/10.1016/j.ijhydene.2017.04.246>.
- [26] Miller DD, Smith M, Shekhawat D. Interaction of manganese with aluminosilicate support during high temperature (1100° C) chemical looping combustion of the Fe-Mn-based oxygen carrier. *Fuel* 2020;263:116738–47. <https://doi.org/10.1016/j.fuel.2019.116738>.
- [27] Zhang S, Xiao R. Comparison of pyrite cinder with synthetic and natural iron-based oxygen carriers in coal-fueled chemical-looping combustion. *Greenhouse Gases: Sci Technol* 2018;8(1):106–19. <https://doi.org/10.1002/ghg.1724>.
- [28] Sun ZK, Lu DY, Ridha FN, Hughes RW, Filippou D. Enhanced performance of ilmenite modified by CeO<sub>2</sub>, ZrO<sub>2</sub>, NiO, and Mn<sub>2</sub>O<sub>3</sub> as oxygen carriers in chemical looping combustion. *Appl Energy* 2017;195:303–15. <https://doi.org/10.1016/j.apenergy.2017.03.014>.
- [29] Feng YC, Wang N, Guo X, Zhang SX. Dopant screening of modified Fe<sub>2</sub>O<sub>3</sub> oxygen carriers in chemical looping hydrogen production. *Fuel* 2020;262:116489–97. <https://doi.org/10.1016/j.fuel.2019.116489>.
- [30] Liu G, Liao YF, Wu YT, Ma XQ. Synthesis gas production from microalgae gasification in the presence of Fe<sub>2</sub>O<sub>3</sub> oxygen carriers and CaO additive. *Appl Energy* 2018;212:955–65. <https://doi.org/10.1016/j.apenergy.2017.12.110>.
- [31] Guo QJ, Hu XD, Liu YZ, Jia WH, Yang MM, Wu M, et al. Coal chemical-looping gasification of Ca-based oxygen carriers decorated by CaO. *Powder Technol* 2015; 275:60–8. <https://doi.org/10.1016/j.powtec.2015.01.061>.
- [32] Yang SX, Zhang XD, Chen L, Sun LZ, Xie XP, Zhao BF. Production of syngas from pyrolysis of biomass using Fe/CaO catalysts: Effect of operating conditions on the process. *J Anal Appl Pyrolysis* 2017;125:1–8. <https://doi.org/10.1016/j.jaap.2017.05.007>.
- [33] Sun Z, Chen SY, Hu J, Chen AM, Rony AH, Russell CK, et al. Ca<sub>2</sub>Fe<sub>2</sub>O<sub>5</sub>: A promising oxygen carriers for CO/CH<sub>4</sub> conversion and almost-pure H<sub>2</sub> production with inherent CO<sub>2</sub> capture over a two-step chemical looping hydrogen generation process. *Appl Energy* 2018;211:431–42. <https://doi.org/10.1016/j.apenergy.2017.11.005>.
- [34] Miller DD, Siriwardane R. CaFe<sub>2</sub>O<sub>4</sub> oxygen carriers characterization during the partial oxidation of coal in the chemical looping gasification application. *Appl Energy* 2018;224:708–16. <https://doi.org/10.1016/j.apenergy.2018.05.035>.
- [35] Hafizi A, Rahimpour MR, Hassanajili S. Hydrogen production via chemical looping steam methane reforming process: Effect of cerium and calcium promoters on the performance of Fe<sub>2</sub>O<sub>3</sub>/Al<sub>2</sub>O<sub>3</sub> oxygen carriers. *Appl Energy* 2016;165:685–94. <https://doi.org/10.1016/j.apenergy.2015.12.100>.
- [36] Riley J, Siriwardane R, Tian HJ, Benincosa W, Poston J. Kinetic analysis of the interactions between calcium ferrite and coal char for chemical looping gasification applications: Identifying reduction routes and modes of oxygen transfer. *Appl Energy* 2017;201:94–110. <https://doi.org/10.1016/j.apenergy.2017.05.101>.
- [37] Zhang JS, Haribal V, Li FX. Perovskite nanocomposites as effective CO<sub>2</sub>-splitting agents in a cyclic redox scheme. *Sci Adv* 2017;3(e1701184):1–8. <https://doi.org/10.1126/sciadv.1701184>.
- [38] Xue B j, Luo J, Zhang F, Fang Z. Biodiesel production from soybean and Jatropha oils by magnetic CaFe<sub>2</sub>O<sub>4</sub>–Ca<sub>2</sub>Fe<sub>2</sub>O<sub>5</sub>-based catalyst. *Energy* 2014;68:584–91. <https://doi.org/10.1016/j.energy.2014.02.082>.
- [39] Freer R. Self-diffusion and impurity diffusion in oxides. *J Mater Sci* 1980;15(4): 803–24.



## CONTENTS

## Full Length Articles

Property-based biomass feedstock grading using *k*-Nearest Neighbour technique

O.O. Olatunji, S. Akinlabi, N. Madushele and P.A. Adediji

116346

Emotional responses to energy projects: A new method for modeling and prediction beyond self-reported emotion measure

E. Buah, L. Linnanen and H. Wu

116210

Perspectives for 700 °C ultra-supercritical power generation: Thermal safety of high-temperature heating surfaces

Z. Zhang, R. Zhou, X. Ge, J. Zhang and X. Wu

116411

Assessment of the effects of chemical and physical parameters in the fluidization of biomass and sand binary mixtures through statistical analysis

E.S. Ocanha, F.S.F. Zinani, R.C.E. Modolo and F.A. Santos

116401

Performance evaluation of single slope solar still augmented with the ultrasonic fogger

P. Dumka and D.R. Mishra

116398

Bioethanol production from rice straw through an enzymatic route mediated by enzymes developed in-house from *Aspergillus fumigatus*

X. Jin, J. Song and G.-Q. Liu

116395

Investigation on the performance of a novel forward-folding rotor used in a downwind horizontal-axis turbine

H. Meng, Z. Ma, B. Dou, P. Zeng and L. Lei

116384

Restoring the natural flow regime of a large hydroelectric complex: Costs and considerations

J. Opgrand, P.V. Preckel, F.T. Sparrow, G. Thomas and D.P. Loucks

116260

Assessment of cost and energy effectiveness of modified technologies for production of young fruit trees, taking into account the use of waste biomass for energy and soil amendment related purposes

N. Matlok and J. Gorzelany

116428

Evaluation of hydrogen production via electrolysis with ion exchange membranes

B. Yuzer, H. Selcuk, G. Chehade, M.E. Demir and I. Dincer

116420

Indonesian electricity load forecasting using singular spectrum analysis, fuzzy systems and neural networks

W. Sulandari, Subanar, M.H. Lee and P.C. Rodrigues

116408

Modelling geothermal resource utilization by incorporating resource dynamics, capacity expansion, and development costs

N. Spittler, E. Shafiei, B. Davidsdottir and E. Juliusson

116407

A comprehensive investigation of finding the best location for hot steam injection into the wet steam turbine blade cascade

M.A.F. Aliabadi, E. Lakzian, I. Khazaei and A. Jahangiri

116397

In-situ performance and degradation of three different photovoltaic module technologies installed in arid climate of Morocco

A. Bouaichi, A. El Amrani, M. Ouhadou, A. Lfakir and C. Messaoudi

116368

*In-situ* removal of toluene as a biomass tar model compound using  $\text{NiFe}_2\text{O}_4$  for application in chemical looping gasification oxygen carrier

Z. Huang, A. Zheng, Z. Deng, G. Wei, K. Zhao, D. Chen, F. He, Z. Zhao, H. Li and F. Li

116360

CONTENTS—continued on inside back cover

Abstracted/indexed in: Applied Sci. & Tech. Index, Biosis Data, Cam. Sci. Abstr. Chem. Abstr. Serv. Curr. Cont. Eng. Tech. & Applied Sci., Elsevier BIOBASE/Current Awareness in Biological Sciences, Eng. Ind., Environ. Per. Biol., INSPEC Data, Res. Alert, Curr. Cont. Sci. Cit. Ind., Curr. Cont. SCISEARCH Data. Also covered in the abstract and citation database SCOPUS®. Full text available on ScienceDirect®



ELSEVIER

Printed by Henry Ling in the United Kingdom



0360-5442(20200101)190;1-X

ISSN 0360-5442

483



TECHNOLOGIES

RESOURCES

RESERVES

DEMAND



IMPACT

CONSERVATION

MANAGEMENT

POLICY

The International Journal

Available online at [www.sciencedirect.com](http://www.sciencedirect.com)

ScienceDirect



## AIMS AND SCOPE

*Energy* is an international, multi-disciplinary journal in energy engineering and research. The journal aims to be a leading peer-reviewed platform and an authoritative source of information for analyses, reviews and evaluations related to energy. The journal covers research in mechanical engineering and thermal sciences, with a strong focus on energy analysis, energy modelling and prediction, integrated energy systems, energy planning and energy management. The journal also welcomes papers on related topics such as energy conservation, energy efficiency, biomass and bioenergy, renewable energy, electricity supply and demand, energy storage, energy in buildings, and on economic and policy issues, provided such topics are within the context of the broader multi-disciplinary scope of *Energy*.

© 2019 Elsevier Ltd. All rights reserved.

This journal and the individual contributions contained in it are protected under copyright by Elsevier Ltd., and the following terms and conditions apply to their use:

### Photocopying

Single photocopies of single articles may be made for personal use as allowed by national copyright laws. Permission of the Publisher and payment of a fee is required for all other photocopying, including multiple or systematic copying, copying for advertising or promotional purposes, resale, and all forms of document delivery. Special rates are available for educational institutions that wish to make photocopies for non-profit educational classroom use.

For information on how to seek permission visit [www.elsevier.com/permissions](http://www.elsevier.com/permissions) or call: (+44) 1865 843830 (UK)/(+1) 215 239 3804 (USA).

### Derivative works

Subscribers may reproduce tables of contents or prepare lists of articles including abstracts for internal circulation within their institutions. Permission of the Publisher is required for resale or distribution outside the institution. Permission of the Publisher is required for all other derivative works, including compilations and translations (please consult [www.elsevier.com/permissions](http://www.elsevier.com/permissions)).

### Electronic storage or usage

Permission of the Publisher is required to store or use electronically any material contained in this journal, including any article or part of an article (please consult [www.elsevier.com/permissions](http://www.elsevier.com/permissions)).

Except as outlined above, no part of this publication may be reproduced, stored in a retrieval system or transmitted in any form or by any means, electronic, mechanical, photocopying, recording or otherwise, without prior written permission of the Publisher.

### Notice

No responsibility is assumed by the Publisher for any injury and/or damage to persons or property as a matter of products liability, negligence or otherwise, or from any use or operation of any methods, products, instructions or ideas contained in the material herein. Because of rapid advances in the medical sciences, in particular, independent verification of diagnoses and drug dosages should be made.

Although all advertising material is expected to conform to ethical (medical) standards, inclusion in this publication does not constitute a guarantee or endorsement of the quality or value of such product or of the claims made of it by its manufacturer.

**Funding body agreements and policies:** Elsevier has established agreements and developed policies to allow authors who publish in Elsevier journals to comply with potential manuscript archiving requirements as specified as conditions of their grant awards. To learn more about existing agreements and policies please visit <http://www.elsevier.com/funding-bodies>.

**Publication information:** *Energy* (ISSN 0360-5442). For 2020 volumes 190-213 (24 issues) are scheduled for publication. Subscription prices are available upon request from the Publisher or from the Elsevier Customer Service Department nearest you or from this journal's website (<http://www.elsevier.com/locate/energy>). Further information is available on this journal and other Elsevier products through Elsevier's website (<http://www.elsevier.com>). Subscriptions are accepted on a prepaid basis only and are entered on a calendar year basis. Issues are sent by standard mail (surface within Europe, air delivery outside Europe). Priority rates are available upon request. Claims for missing issues should be made within six months of the date of dispatch.

**Orders, claims, and journal inquiries:** Please visit our Support Hub page <https://service.elsevier.com> for assistance.

### Author inquiries:

You can track your submitted article at <http://www.elsevier.com/track-submission>. You can track your accepted article at <http://www.elsevier.com/trackarticle>. You are also welcome to contact Customer Support via <http://support.elsevier.com>.

### Advertising information:

If you are interested in advertising or other commercial opportunities please e-mail [Commercialsales@elsevier.com](mailto:Commercialsales@elsevier.com) and your inquiry will be passed to the correct person who will respond to you within 48 hours.

### Language (usage and editing services)

Please write your text in good English (American or British usage is accepted, but not a mixture of these). Authors who feel their English language manuscript may require editing to eliminate possible grammatical or spelling errors and to conform to correct scientific English may wish to use the English Language Editing service available from Elsevier's WebShop <http://webshop.elsevier.com/languageediting/> or visit our customer support site <http://support.elsevier.com> for more information.

### Illustration services

Elsevier's WebShop (<http://webshop.elsevier.com/illustrationservices>) offers Illustration Services to authors preparing to submit a manuscript but concerned about the quality of the images accompanying their article. Elsevier's expert illustrators can produce scientific, technical and medical-style images, as well as a full range of charts, tables and graphs. Image 'polishing' is also available, where our illustrators take your image(s) and improve them to a professional standard. Please visit the website to find out more.

For a full and complete Guide for Authors, please go to: <http://www.elsevier.com/locate/energy>

Printed by Henry Ling in the United Kingdom

© The paper used in this publication meets the requirements of ANSI/NISO Z39.48-1992 (Permanence of Paper)

## CONTENTS—continued from outside back cover

Understanding energy efficiency and its drivers: An empirical analysis of China's 14 coal intensive industries

X. Qi, P. Guo, Y. Guo, X. Liu and X. Zhou

116354

Optimal scheduling of distribution systems considering multiple downward energy hubs and demand response programs

A. Bostan, M.S. Nazar, M. Shafic-khah and J.P.S. Catalão

116349

Influence of ultrasonic pretreatment on the co-pyrolysis characteristics and kinetic parameters of municipal solid waste and paper mill sludge

S. Fang, Y. Lin, Y. Lin, S. Chen, X. Shen, T. Zhong, L. Ding and X. Ma

116310

Modeling and experimental verification of a fractional damping quad-stable energy harvesting system for use in wireless sensor networks

M. Gao, Y. Wang, Y. Wang, Y. Yao, P. Wang, Y. Sun and J. Xiao

116301

Urban models enrichment for energy applications: Challenges in energy simulation using different data sources for building age information

M. Zirak, V. Weiler, M. Hein and U. Eicker

116292

Exergetic life cycle assessment of hydrogen production from biomass staged-gasification

Q. Li, G. Song, J. Xiao, J. Hao, H. Li and Y. Yuan

116416

1st Edition, in: Achim Brunnengräber, Maria Rosaria Di Nucci (Eds.), Conflicts, Participation and Acceptability in Nuclear Waste Governance - An International Comparison, Vol. III (2019), ISBN: 978-3658271060

E. Laes

116406

Microwave-induced carbon-CO<sub>2</sub> gasification for energy conversion

Y.N. Chun and H.G. Song

116386

Investigation of agro-byproduct pellet properties and improvement in pellet quality through mixing

S. Park, S.J. Kim, K.C. Oh, L. Cho, M.J. Kim, I.S. Jeong, C.G. Lee and D. Kim

116380

Impact factors of the real-world fuel consumption rate of light duty vehicles in China

T. Wu, X. Han, M.M. Zheng, X. Ou, H. Sun and X. Zhang

116388

A two-level approach for three-dimensional micro-siting optimization of large-scale wind farms

M. Song, K. Chen and J. Wang

116340

A sharing economy market system for private EV parking with consideration of demand side management

F. Xu, X. Chen, M. Zhang, Y. Zhou, Y. Cai, Y. Zhou, R. Tang and Y. Wang

116321

Catalytic pyrolysis of biomass with potassium compounds for Co-production of high-quality biofuels and porous carbons

Y. Shen, N. Zhang and S. Zhang

116431

Typical Meteorological Year methodologies applied to solar spectral irradiance for PV applications

J. Polo, M. Alonso-Abella, N. Martin-Chivelet, J. Alonso-Montesinos, G. López, A. Marzo, G. Nofuentes and N. Vela-Barriounevo

116453

Day-ahead optimal bidding strategy of microgrid with demand response program considering uncertainties and outages of renewable energy resources

S. Das and M. Basu

116441

Energy and thermal storage in clusters of grid-independent buildings

M.K. DeValeria, E.E. Michaelides and D.N. Michaelides

116440

Energy storage and management system design optimization for a photovoltaic integrated low-energy building

J. Liu, X. Chen, H. Yang and Y. Li

116424

Thermodynamic and economic analysis of a gas turbine set coupled with a turboexpander in a hierarchical gas-gas system

R. Bartnik, A. Hnydiuk-Stefan and Z. Buryń

116394

An optical mechanism for detecting the whole pyrolysis process of oil shale

H. Zhan, Y. Wang, M. Chen, R. Chen, K. Zhao and W. Yue

116343

Experimental investigation on the performance of a very high temperature heat pump with water refrigerant

D. Wu, J. Jiang, B. Hu and R.Z. Wang

116427

Improvement of magnetic and cryogenic energy preservation performances in a feeding-power-free superconducting magnet system for maglevs

F. Dong, Z. Huang, X. Xu, L. Hao, N. Shao and Z. Jin

116403

Investigation on the effect of bluff body ball on the combustion characteristics for methane/oxygen in micro combustor

J. Pan, C. Zhang, Z. Pan, D. Wu, Y. Zhu, Q. Lu and Y. Zhang

116465

CONTENTS— continued on Back Matter



# *In-situ* removal of toluene as a biomass tar model compound using $\text{NiFe}_2\text{O}_4$ for application in chemical looping gasification oxygen carrier

Zhen Huang<sup>a, b</sup>, Anqing Zheng<sup>a</sup>, Zhengbing Deng<sup>a</sup>, Guoqiang Wei<sup>a, \*</sup>, Kun Zhao<sup>a</sup>,  
Dezhen Chen<sup>b</sup>, Fang He<sup>a, c, d, \*\*</sup>, Zengli Zhao<sup>a</sup>, Haibin Li<sup>a</sup>, Fanxing Li<sup>d</sup>

<sup>a</sup> Key Laboratory of Renewable Energy, Chinese Academy of Sciences (CAS), Guangzhou Institute of Energy Conversion, CAS, No.2 Nengyuan Road, Wushan, Tianhe District, Guangzhou, 510640, China

<sup>b</sup> Thermal & Environmental Engineering Institute, Tongji University, No.4800 Caoan Road, Jiading District, Shanghai, 201804, China

<sup>c</sup> College of Chemistry and Bioengineering, Guilin University of Technology, No.12 Jiangnan Road, Qixing District, Guilin, 541004, China

<sup>d</sup> Department of Chemical and Biomolecular Engineering, North Carolina State University, 911 Partners Way, Raleigh, NC, 27695-7905, United States

## ARTICLE INFO

### Article history:

Received 22 July 2019

Received in revised form

28 September 2019

Accepted 13 October 2019

Available online 16 October 2019

### Keywords:

Chemical looping gasification (CLG)

$\text{NiFe}_2\text{O}_4$  oxygen carrier

Toluene

Oxidation-catalysis

Biomass tar model compound

## ABSTRACT

Efficient removal of tar is a major challenge for biomass gasification. A scheme based on chemical looping gasification (CLG) provides a promising alternative for converting biomass into syngas with low tar content. The current study investigates the reactivity of  $\text{NiFe}_2\text{O}_4$  oxygen carrier for toluene (biomass tar model compound) removal. The  $\text{NiFe}_2\text{O}_4$  oxygen carrier shows a dual-function of oxidation-catalysis for toluene cracking and significantly promotes toluene cracked into carbon and  $\text{H}_2$ . A suitable temperature for toluene cracking is determined at  $850^\circ\text{C}$ . As the weight hourly space velocity (WHSV) increases by approximately a factor of nine, the toluene removal decreases slightly by 2.78%. The toluene removal does not significantly decrease with the crystal phase transformation of the oxygen carrier. Addition of steam significantly eliminates the carbon deposition, which decreases to 4.97% at S/C (steam/toluene) ratio of 1.20. The catalytic activity of  $\text{NiFe}_2\text{O}_4$  initially remained stable for a long time, and then started showing a slight decrease after transitory activation during the long-term experiment (82 h). These results fully demonstrate that the  $\text{NiFe}_2\text{O}_4$  is a good oxygen carrier for tar removal in biomass CLG.

© 2019 Elsevier Ltd. All rights reserved.

## 1. Introduction

Biomass gasification has proved itself as a promising biomass energy utilization technique converting bulky biomass of low energy density into gaseous products with high energy density, suitable for storage, transportation and use. This is done through the use of lattice oxygen as the gasifying agents, thereby improving the quality, utilization efficiency and utilization range of biomass energy [1]. Since biomass contains high amount of volatiles, tar (organic pollutants with a molecular weight greater than benzene) is an inevitable by-product during the gasification process [2]. As a product of biomass gasification, the tar content is generally between  $1\text{ g/Nm}^3$  and  $100\text{ g/Nm}^3$  and its energy accounts for 5%–15%

of the total energy of the products [3]. Thus, the generation of tar not only reduces the gasification efficiency resulting in a loss in efficiency, but tar formation also not favorable for the subsequent use of syngas. Additionally, tar condenses at low temperature, causing many problems such as pipeline blockage and equipment corrosion [4]. Therefore, tar formation limits further application of the gasification technology. As such, efficient removal of tar becomes a major challenge during biomass gasification. Compared with the physical purification [5–7] and thermal cracking methods [8,9] for tar removal, the catalytic cracking method can decompose the large molecules into small molecules with relatively low energy consumption using catalysts [10–12]. The catalytic cracking method can remove significant amounts of tar, which not only improves the gasification efficiency, but also adjusts the composition of the synthesis gas. The catalytic cracking method involves *in-situ* catalytic cracking and secondary catalytic cracking depending on the loading position of the catalyst [13]. Compared with the secondary catalytic cracking, the *in-situ* catalytic cracking of the tar possesses some advantages of short process flow, simple operation

\* Corresponding author.

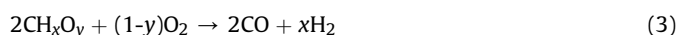
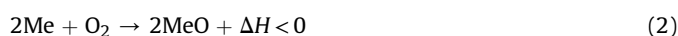
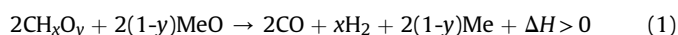
\*\* Corresponding author. Key Laboratory of Renewable Energy, Chinese Academy of Sciences (CAS), Guangzhou Institute of Energy Conversion, CAS, No.2 Nengyuan Road, Wushan, Tianhe District, Guangzhou, 510640, China.

E-mail addresses: [weigq@ms.giec.ac.cn](mailto:weigq@ms.giec.ac.cn) (G. Wei), [hufang@glut.edu.cn](mailto:hufang@glut.edu.cn) (F. He).

and low cost [13,14]. Therefore, *in-situ* catalytic cracking of biomass tar can effectively reduce the tar content in the crude gas, resulting in an increase in gasification efficiency, reduction in downstream equipment loss, and a lower operating cost, thus achieving clean and efficient gasification of biomass.

Currently, the catalysts used in catalytic cracking of tar mainly include natural ores [15,16], alkali metals [17,18], transition metals [2,19,20], and carbon-based catalysts [21,22]. Although natural ore catalysts are widely available, cheap, and environmentally friendly, they have low catalytic activity [23]. Alkali metal catalysts are cheap and show high catalytic cracking of biomass tar, but their thermal stability is poor, they are easily deactivated at high temperatures due to sintering [24], and are difficult to recycle and regenerate [11]. Carbon-based catalysts display good reactivity for catalytic cracking of biomass/polyethylene tar because of their developed pore structure [16,25], and are also cheap and easy to produce. However, carbon deposition during tar cracking blocks pores causing the catalysts to deactivate [26]. Transition metal catalysts are viewed as excellent catalysts for tar removal due to lots of active sites on the surface of catalysts, allowing tar molecules to be easily adsorbed and catalytically cracked into small molecular gases [27,28]. Different metals play different roles during catalytic cracking of tar, and the synergistic effect of two different metals can effectively compensate for the shortcomings of the single metal, improving the reactivity of catalyst. Hence, the bimetallic catalysts have extensively attracted attention in recent years [29–31]. Nickel-based catalysts have a high tar cracking capacity, but are relatively expensive and harmful to the environment [32]. Although the iron-based catalysts have a relatively lower reactivity, they are easy to obtain, relatively cheap, and environmentally friendly [33]. Therefore, the bimetallic Fe–Ni catalysts can reduce the cost and toxicity of single Ni-based catalyst and improve the reactivity of single Fe-based catalyst, which is already considered an excellent tar cracking catalyst.

A biomass gasification technology, named chemical looping gasification (CLG) [34,35] was proposed to overcome the shortcomings of traditional gasification technologies. CLG of biomass uses lattice oxygen in oxygen carrier instead of molecular oxygen in gas phase to partially oxidize biomass into syngas, followed by the reduced oxygen carrier to be re-oxidized by air to bring it back to its initial state. Thereby, CLG of biomass involves in two steps. In the fuel reactor, biomass ( $\text{CH}_x\text{O}_y$ ) is gasified by the lattice oxygen in oxygen carrier ( $\text{MeO}$ ) and converted into high-quality synthesis gas. The oxygen carrier is reduced into its metallic state ( $\text{Me}$ ) (and low-valent metal oxide ( $\text{MeO}_{1-\beta}$ )), as shown in reaction (1). The overall reaction is endothermic. In the air reactor, the reduced oxygen carrier ( $\text{Me}/\text{MeO}_{1-\beta}$ ) is then re-oxidized into its initial state ( $\text{MeO}$ ) by reacting with air in order to start the next cycle. This reaction provides sensible heat for the fuel reactor, as shown in reaction (2). In this process, biomass can be continuously converted into high quality synthesis gas by the continuous circulation of oxygen carrier between the two reactors as shown in reaction (3). Hence, the oxygen carrier plays the key roles in biomass CLG. In addition to providing oxygen and heat, the oxygen carrier can also catalytically crack biomass tar, thus improving the quality of synthesis gas.



At present, the transition metal oxides are generally used as oxygen carriers of biomass CLG. Using an ilmenite oxygen carrier

( $\text{FeTiO}_3$ ), the tar content reduced by ~35% and the branched hydrocarbons and phenols in tar were completely cracked [36]. It was found that the catalytic performance of iron-based catalysts to crack biomass tar gradually decreased with increasing oxygen content [2]. Compared with the Fe-based oxygen carrier (the tar removal was only 60%), the Ni-based oxygen carrier demonstrated excellent biomass tar cracking performance and the tar removal exceeded 95% [37,38]. Tar removal further improved using the bimetallic oxygen carrier due to the synergistic effect, especially the use of Fe–Ni spinel structure oxygen carrier [31,39]. The  $\text{NiFe}_2\text{O}_4$  sample showed a higher catalytic performance of cracking tar comparing with similar spinel oxides ( $\text{CuFe}_2\text{O}_4$  and  $\text{CoFe}_2\text{O}_4$ ) [40]. These results fully indicate that the Fe–Ni oxygen carrier can be used as a catalyst to achieve *in-situ* removal of tar. Therefore, the bimetallic Fe–Ni oxide with spinel structure (i.e.  $\text{NiFe}_2\text{O}_4$ ) has the potential to be a good oxygen carrier for biomass CLG.

The composition of biomass tar is quite complex and includes more than 100 components [3], which is also affected by biomass feedstock, gasifier type and gasification conditions, making it difficult to study the cracking of tar. In order to simplify the analysis, toluene, is often chosen as a model compound. Toluene accounts for about 15–25% of the total biomass tar [41,42] and is a widely investigated as a tar model compound.

The current studies generally discussed the removal effects of oxygen carrier for tar or its model compound removal. There are rare studies reported how the oxygen carrier cracks the tar and the effects of the state of oxygen carrier on tar removal during the reduction process, which are very important for understanding the reaction paths. At the same time, the removal effects of oxygen carrier on tar during long-term operation (>72 h) are rarely explored. Therefore, investigating the roles of the oxygen carrier in tar removal, especially the effects of phase change and long time performance of oxygen carrier are the key to understand the reaction mechanisms of tar removal.

The objective of this work is to explore the *in-situ* removal of toluene using  $\text{NiFe}_2\text{O}_4$  oxygen carrier. The role of active  $\text{NiFe}_2\text{O}_4$  on toluene removal was firstly conducted. Using the  $\text{NiFe}_2\text{O}_4$  oxygen carrier, the effects of reaction temperature, weight hourly space velocity (WHSV) and steam/toluene ratio (S/C) on toluene removal were also performed. Especially, different reduced species of oxygen carrier to remove toluene was mainly discussed to understand the reaction paths of toluene removal and the toluene removal during long-term operation was also explored to evaluate the sustainable capacity of  $\text{NiFe}_2\text{O}_4$  oxygen carrier.

## 2. Experimental section

### 2.1. Sample preparation

The  $\text{NiFe}_2\text{O}_4$  oxygen carrier was prepared through a sol-gel method (SG) and the preparation procedures were reported in the previous work [43].

### 2.2. Experimental setup and procedure

A fixed bed reactor was used to investigate the catalytic performance of  $\text{NiFe}_2\text{O}_4$  oxygen carrier for toluene removal. The diagram of the reaction equipment is shown in Fig. 1.

The fixed bed is mainly composed of an electric heating furnace (including a temperature control system), a quartz tube reactor, a gas distribution system, and a sampling system. During the experiment, the  $\text{NiFe}_2\text{O}_4$  sample adhering on quartz wool (~0.2 g) was placed in a porous plate located in the middle of the quartz tube reactor with a length of 800 mm and inner diameter of 15 mm. The end of the reactor was sealed by stainless steel joints. The

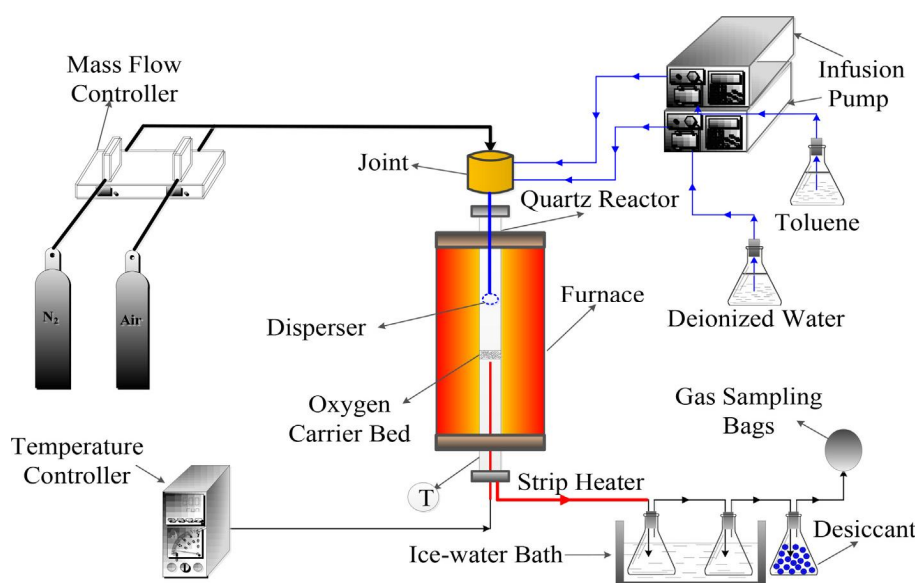


Fig. 1. The diagram of the fixed bed equipment.

sample was then heated in an inert atmosphere of nitrogen (carrier gas) to a desired reaction temperature. The reaction temperature was measured by a K-type thermocouple inside the quartz tube reactor (near the perforated plate). The volumetric flow of air and carrier gas (high purity N<sub>2</sub>) were controlled by mass flow controllers. After the experimental temperature reaching the desired reaction temperature, a certain amount of toluene was directly injected into the reactor through a high-pressure infusion pump (Surwit Technology Inc., STI501, 0–10 mL/min, accuracy = 1%) and the toluene was vaporized at the internal component of the reactor under high temperature. The toluene vapor carried by carrier gas (N<sub>2</sub>) smoothly penetrated the oxygen carrier bed for the cracking reactions of toluene to take place. Additionally, deionized water was directly injected into the reactor using a high-pressure infusion pump to suppress the formation of carbon deposition during toluene steam reforming (The deionized water was also vaporized at the internal component of the reactor under high temperature). The generated gas product was absorbed by an isopropanol solution (placed in Mengshi washing bottles) placed in an ice brine to absorb the residual toluene and its cracked products. The pipe section between the reactor outlet to the Mengshi washing bottle inlet was heated to 180 °C with an electric heating belt to prevent condensation of toluene and its cracked products. After being treated with purifying and drying processes (using color-changing silica gel), the gas product was collected by sampling bags for the gas chromatograph (Agilent Refinery Gas Chromatograph, 7890A) analysis. The inert gas of N<sub>2</sub> continued to purge the system to avoid back mixing between reduction (toluene cracking period) and oxidation period when the toluene cracking was finished. The N<sub>2</sub> was switched to air for the oxidation of the reduced oxygen carrier and the combustion of the carbon deposition. After the experiment, the oxygen carrier was cooled to room temperature under N<sub>2</sub> atmosphere then collected for analysis (various phase characterization).

In section 3.1, the feeding rate of toluene was controlled at 0.05 mL/min, the mass of oxygen carrier was fixed at 0.5 g, the reaction time was set at 60 min, the reaction temperature was maintained at 850 °C, and the carrier gas (N<sub>2</sub>) flow rate was assigned at 100 mL/min. In section 3.2, the reaction temperature increased from 700 °C to 900 °C in 50 °C increment while the other

parameters remained constant. In section 3.3, the weight hourly space velocity (WHSV) was altered by changing the feeding rate of toluene. In section 3.4, in order to explore the effect of the reduced species of oxygen carrier on toluene removal, the feeding rate of toluene was controlled at 0.02 mL/min, the reaction time was fixed at 15 min, and the mass of oxygen carrier was varied between 0.11 g and 5 g to obtain the different reduced species. In section 3.5, the effect of steam (water vapor) on the catalytic cracking of toluene was studied by changing the amount of water vapor (the feeding rate of deionized water) while maintaining the toluene feeding rate at 0.05 mL/min (i.e. steam (water vapor)/carbon (toluene) mass ratio, S/C). In section 3.6, the WHSV and S/C were set at 4.98 and 1.20, respectively. The other experimental conditions in other sections were the same as those in section 3.1.

### 2.3. Material characterization

An X-ray diffractometer (XRD, X'Pert Pro MPD) with Cu K<sub>α</sub> radiation (40 kV, 40 mA) was used to analyze the crystal structure of fresh and reacted oxygen carrier samples. The sample was scanned at a rate of 2°/min from 2θ = 5°–80° at a step of 0.02°. The pore structure analysis of the samples was measured by N<sub>2</sub> physisorption at 77 K using an automatic specific surface area and pore size distribution analyzer (Quantachrome, SI-MP-10). The samples were degassed under vacuum at 473 K for 10 h before measurement. The amount of residual toluene in isopropanol solution was analyzed by gas chromatography (Agilent Gas Chromatograph, 7890A).

### 2.4. Data evaluation

Toluene conversion ( $\eta_t$ , %) is defined as the mass ratio of the cracked toluene to the injected toluene during the toluene cracking, which is calculated using Eq. (4). Where  $m_t$  represents the mass of injected toluene (kg) and  $m_t'$  represents the mass of residual toluene (kg).

$$\eta_t = (m_t - m_t') / m_t \times 100\% \quad (4)$$

Weight hourly space velocity (WHSV, h<sup>-1</sup>) refers to the mass of reactants per unit mass of catalyst per unit time [39], which is



calculated using Eq. (5). Where  $Q_t$  represents the feeding rate of toluene (kg/h) and  $m_o$  represents the mass of the oxygen carrier (kg).

$$WHSV = Q_t / m_o \quad (5)$$

Carbon deposition ( $\eta_d$ , %) is defined as the ratio of the mass of carbon deposition ( $m'_c$ , kg) to the mass of carbon in injected toluene ( $m_c$ , kg) during the toluene cracking process, which is calculated using Eq. (6). The carbon deposition attains a maximum of 1 when all of the toluene is completely cracked into carbon deposition and  $H_2$ .

$$\eta_d = m'_c / m_c \times 100\% \quad (6)$$

Carbon deposition mass ( $m'_c$ , kg) refers to the mass of generated carbon originated from toluene cracking, which is calculated by the mass of generated carbon-containing gas during the air oxidation, as shown in Eq. (7). Where  $F_{in}$  is the volume flow rate of the gas in the inlet,  $x_{in, N_2}$  and  $x_{out, N_2}$  are the actual concentrations of  $N_2$  in the inlet and outlet, respectively,  $x_{CO}$  and  $x_{CO_2}$  are the actual concentrations of the CO and  $CO_2$  components during the air oxidation process, respectively.

$$m'_c = (273.15 / 300.15) \times (F_{in} \cdot x_{in, N_2} / x_{out, N_2}) \times (x_{CO} + x_{CO_2}) \times (12 / 22.4) \quad (7)$$

Gas relative concentration ( $C_i$ , %) is calculated using Eq. (8). Where  $x_i$  is the actual concentration of the component  $i$  (i.e.  $H_2/CH_4/CO/CO_2/C_2H_m$ ), given by the gas chromatograph.

$$C_i = (x_i / \sum x_i) \times 100\% \quad (8)$$

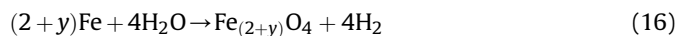
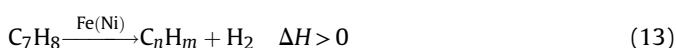
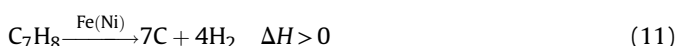
Gas yield ( $G_i$ ,  $m^3/kg$ ) refers to the volume of gas component  $i$  generated by per unit mass of fuel during the toluene cracking, which is calculated according to Eq. (9). Where  $M_t$  is the mass of the toluene fuel (kg). The theoretical  $H_2$  yield refers to the  $H_2$  produced from the H atoms present in toluene, which is completely cracked into  $H_2$  and carbon deposition.

$$G_i = (F_{in} \cdot x_{in, N_2} / x_{out, N_2}) \times x_i / M_t \quad (9)$$

## 2.5. Methodology

In this work, in order to explore the *in-situ* removal of toluene, the role of  $NiFe_2O_4$  oxygen carrier was first highlighted, and then the effects of operation parameters (i.e. temperature,  $WHSV$ , reduced species, steam/toluene ratio, and reaction time) on toluene removal were discussed in detail to better understand the reaction mechanisms of tar removal.

The main chemical reactions involved in this work include reactions (10)–(18), as follows.



Several terminologies are used to qualitatively illuminate the reasons, as shown in section 3.5. The gas velocity (m/s) is the ratio of volumetric flow of gas ( $m^3/s$ ) to the cross-sectional area of reactor ( $m^2$ ), including the carrier gas ( $N_2$ ) velocity and the steam velocity. The gas-solid residence time (s) is defined as the ratio of length of the reactor (m) to the gas velocity (m/s).

## 3. Results and discussions

### 3.1. The role of oxygen carrier

In order to highlight the role of oxygen carrier, the toluene cracking over  $NiFe_2O_4$  sample was first conducted. The results are shown in Table 1 and Fig. 2.

Using  $NiFe_2O_4$  oxygen carrier, the toluene conversion attains to 96.83% and the  $H_2$  yield ( $0.91 m^3/kg$ ) is close to the theoretical  $H_2$  yield of  $0.97 m^3/kg$ . Meanwhile, it is observed that CO and  $CO_2$  are generated in the early stage of toluene cracking (as shown in Fig. 2). These results fully manifests that there are mainly two reactions for toluene removal. In the first reaction, the toluene is oxidized into small molecule gases (e.g.  $CO/CO_2/H_2O$ ) with lattice oxygen from  $NiFe_2O_4$  via the reaction (10). The donation of oxygen results in the reduction of oxygen carrier to  $Fe(Ni)$  alloy. In the second reaction, the reduced oxygen carrier (i.e.  $Fe(Ni)$  alloy) catalytically cracks toluene to generate  $H_2$  and carbon deposition via the reaction (11). Additionally, some of the deposited carbon reacts with  $H_2$  to form  $CH_4$  in the presence of catalysts ( $Fe(Ni)$  alloy), as shown in reaction (12). Thus, the  $H_2$  concentration shows a slight decreasing trend and  $CH_4$  concentration displays an uptrend in the final stage of toluene cracking, as shown in Fig. 2.

These results demonstrate that  $NiFe_2O_4$  acts as an oxidant for toluene removal in the absence of gaseous oxygen and exhibits catalytic performance after reduction. Hence, the  $NiFe_2O_4$  sample shows two functions of oxidation-catalysis and can be used as an excellent oxygen carrier for biomass CLG.

### 3.2. Effect of reaction temperature

The reaction temperature is an important factor for the conversion of hydrocarbon compounds. The effect of reaction temperature on toluene cracking is shown in Figs. 3 and 4.

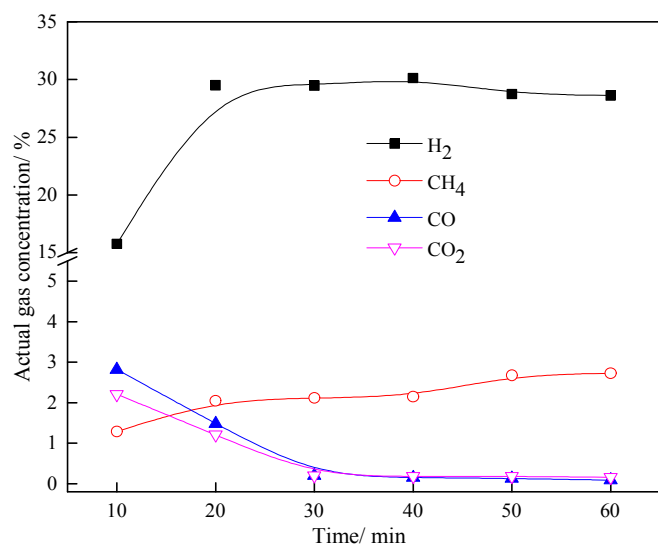
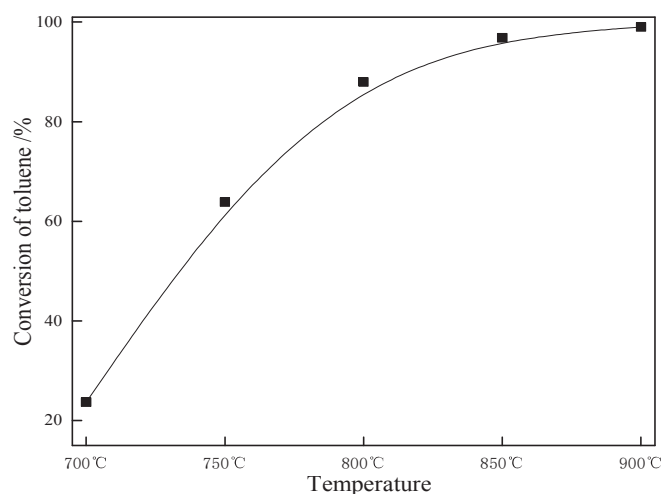
As the reaction temperature increases, the toluene conversion and  $H_2$  yield increases from 23.70% to 0.29  $m^3/kg$  at  $700^\circ C$  to 99.04% and  $0.93 m^3/kg$  at  $900^\circ C$ , respectively. This result can be explained by the fact that the oxidation reaction of toluene (10) and the catalytic cracking reactions of toluene (11) and (13) are strong endothermic reactions, as a result higher temperatures can promote toluene conversion and the  $H_2$  generation.

There are mainly two reactions (11) and (13) during the toluene catalytic cracking. The reaction (11) represents that the toluene is almost completely cracked into carbon and  $H_2$ . Differently, the reaction (13) reveals that the toluene is only partially cracked to  $H_2$  and hydrocarbons ( $C_nH_m$ ), which include the smaller hydrocarbons

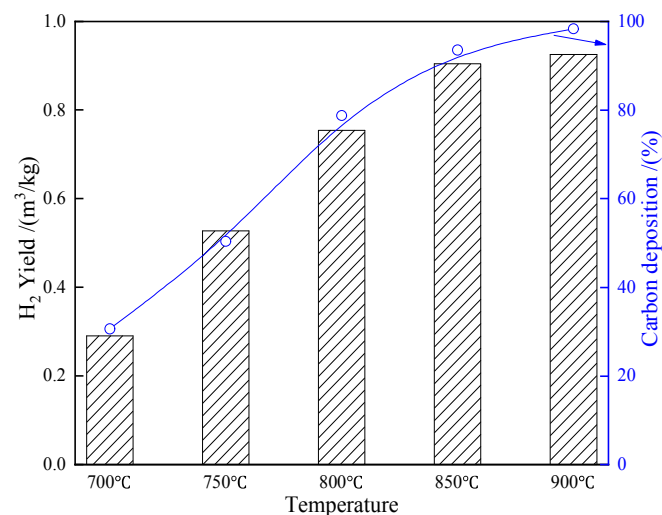


**Table 1**The characteristics of toluene conversion over  $\text{NiFe}_2\text{O}_4$  oxygen carrier.

| $\text{H}_2$ (%) <sup>a</sup> | $\text{CH}_4$ (%) <sup>a</sup> | $\text{CO}$ (%) <sup>a</sup> | $\text{CO}_2$ (%) <sup>a</sup> | Toluene conversion (%) | $\text{H}_2$ yield ( $\text{m}^3/\text{kg}$ ) | Theoretical value of $\text{H}_2$ yield ( $\text{m}^3/\text{kg}$ ) |
|-------------------------------|--------------------------------|------------------------------|--------------------------------|------------------------|---|--|
| 27.04                         | 2.17                           | 0.81                         | 0.69                           | 96.83                  | 0.91  | 0.97   |

<sup>a</sup> Actual concentration of gas.**Fig. 2.** The actual gas concentration with reaction time during the toluene cracking.**Fig. 3.** The conversion of toluene with reaction temperature.

than toluene formed through the direct cracking (e.g.  $\text{C}_1\text{--C}_6$ ) and the larger hydrocarbons than toluene polymerized by the intermediate products ( $>\text{C}_7$ ). In other words, the carbon deposition is close to one and  $\text{H}_2$  yield is near to the theoretical  $\text{H}_2$  yield when the reaction (11) is dominated. If the reactions (11) and (13) coexist, the carbon deposition would be below one and  $\text{H}_2$  yield would be less than the theoretical  $\text{H}_2$  yield. Below  $800^\circ\text{C}$ , the  $\text{H}_2$  yield is much lower than the theoretical  $\text{H}_2$  yield of  $0.97 \text{ m}^3/\text{kg}$ , and the corresponding carbon deposition is also far less than one. These results are ascribed to the incomplete decomposition of toluene at low temperatures. A large amount of toluene is only partially cracked into  $\text{C}_n\text{H}_m$ , inhibiting the generation of  $\text{H}_2$ . Thus, the main reaction (11) and the side reaction (13) coexist at relatively low temperatures ( $\leq 800^\circ\text{C}$ ). Above  $800^\circ\text{C}$ , the  $\text{H}_2$  yield is closer to the

**Fig. 4.**  $\text{H}_2$  yield and carbon deposition with reaction temperature.

theoretical  $\text{H}_2$  yield and the corresponding carbon deposition is close to one, indicating that the main reaction (11) is more dominated, therefore more  $\text{H}_2$  and carbon deposition are produced at higher temperatures.

Furthermore, it is observed that toluene conversion,  $\text{H}_2$  yield and carbon deposition are stable when the reaction temperature exceeds  $850^\circ\text{C}$ . This is attributed to the near complete conversion of toluene above  $850^\circ\text{C}$ . Therefore, in order to explore the effect of other operating parameters on the toluene conversion, the reaction temperature is kept at  $850^\circ\text{C}$ .

### 3.3. Effect of weight hourly space velocity (WHSV)

The weight hourly space velocity ( $\text{WHSV}, \text{h}^{-1}$ ) is a key parameter to evaluate the catalytic performance and its effect on the toluene catalytic cracking is shown in Fig. 5.

The oxygen carrier for biomass CLG needs to have a high catalytic activity even at a high  $\text{WHSV}$ . As shown in Fig. 5, although the  $\text{WHSV}$  increases approximately nine times (from  $0.92 \text{ h}^{-1}$  to  $7.97 \text{ h}^{-1}$ ), the toluene conversion only decreases by 2.78% (from 98.76% to 95.98%). The results preliminarily indicate that the  $\text{NiFe}_2\text{O}_4$  oxygen carrier is an excellent catalyst for toluene cracking.

### 3.4. Effect of different reduced species of oxygen carrier

The reduced oxygen carrier acts as a catalyst in promoting toluene cracking through reactions (11) and (13). The composite oxygen carrier can form various crystalline phases during the reduction process, and the capability of each phase to catalytically crack toluene may differ. Therefore, the effect of different reduced species of oxygen carrier on the catalytic cracking of toluene was investigated through changing the  $\text{WHSV}$  value.

The change on crystalline phase of  $\text{NiFe}_2\text{O}_4$  oxygen carrier during reaction testing is shown in Fig. 6. The  $\text{NiFe}_2\text{O}_4$  oxygen carrier is initially reduced to  $\text{Ni}_{0.6}\text{Fe}_{2.4}\text{O}_4$  and then is further reduced to

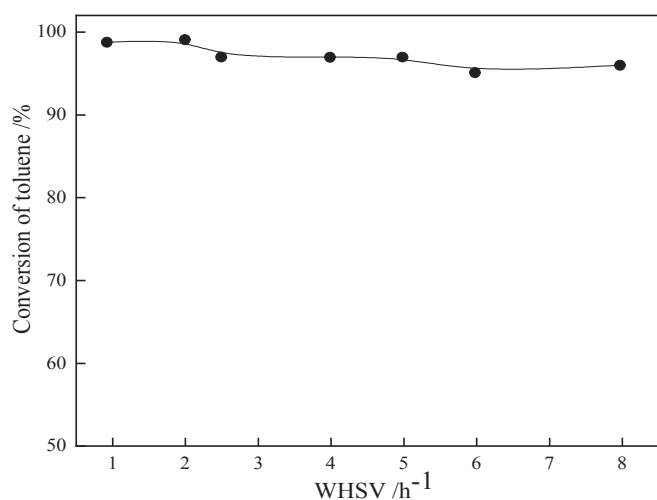


Fig. 5. The conversion of toluene with WHSV.

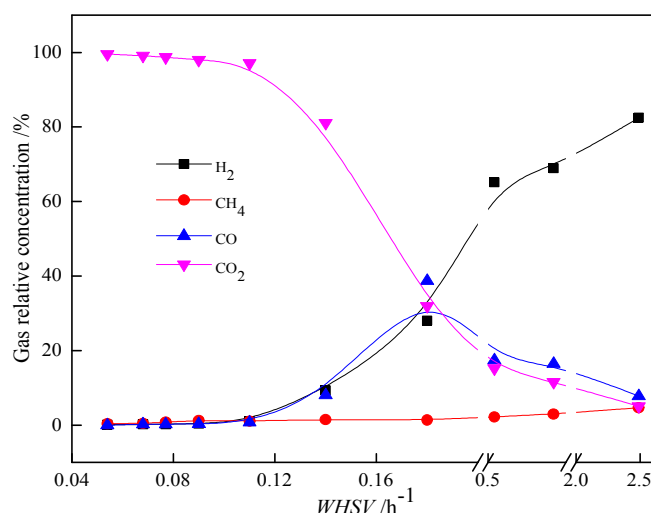


Fig. 7. The change on gas relative concentration with oxygen carrier species.

$\text{Fe}_{0.64}\text{Ni}_{0.36}$  at higher WHSV values. A distinct graphite carbon species is observed at a WHSV value greater than  $0.18 \text{ h}^{-1}$  due to carbon deposition.

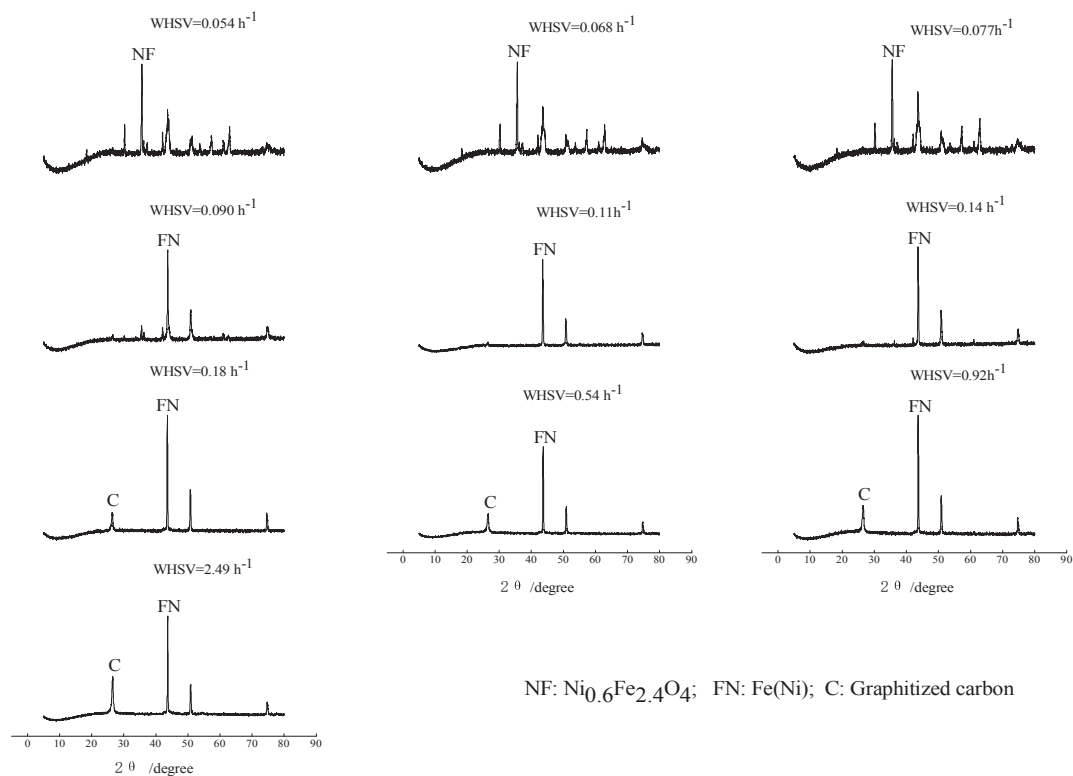
According to the reduction products of oxygen carrier, the process of toluene cracking can be divided into four stages. The experimental results are shown in Fig. 7 and Table 2.

When the WHSV value is below  $0.077 \text{ h}^{-1}$ , the  $\text{NiFe}_2\text{O}_4$  oxygen carrier is reduced to  $\text{Ni}_{0.6}\text{Fe}_{2.4}\text{O}_4$ . The donated lattice oxygen converts ~99% of the toluene and produces large amounts of  $\text{CO}_2$  and  $\text{H}_2\text{O}$ . Between WHSV values of  $0.077 \text{ h}^{-1}$  and  $0.11 \text{ h}^{-1}$ , additional lattice oxygen is donated and the  $\text{NiFe}_2\text{O}_4$  oxygen carrier is reduced to  $\text{Fe}(\text{Ni})$  alloy species besides a small number of oxygen-containing

Table 2

The effect of oxygen carrier species on toluene conversion.

| WHSV/ $\text{h}^{-1}$ | Oxygen carrier species  | Toluene conversion/% |
|-----------------------|---|----------------------|
| 0.054                 | $\text{Ni}_{0.6}\text{Fe}_{2.4}\text{O}_4$ ; $\text{Fe}_{0.64}\text{Ni}_{0.36}$ ; $\text{Fe}_{3-x}\text{O}_4$ ; $\text{Fe}_x\text{O}$ ; C | 99.86                |
| 0.068                 | $\text{Ni}_{0.6}\text{Fe}_{2.4}\text{O}_4$ ; $\text{Fe}_{0.64}\text{Ni}_{0.36}$ ; $\text{Fe}_{3-x}\text{O}_4$ ; $\text{Fe}_x\text{O}$ ; C | 99.85                |
| 0.077                 | $\text{Ni}_{0.6}\text{Fe}_{2.4}\text{O}_4$ ; $\text{Fe}_{0.64}\text{Ni}_{0.36}$ ; $\text{Fe}_{3-x}\text{O}_4$ ; $\text{Fe}_x\text{O}$ ; C | 99.74                |
| 0.090                 | $\text{Fe}_{0.64}\text{Ni}_{0.36}$ ; $\text{Ni}_{0.4}\text{Fe}_{2.6}\text{O}_4$ ; $\text{Fe}_x\text{O}$ ; C                               | 99.86                |
| 0.11                  | $\text{Fe}_{0.64}\text{Ni}_{0.36}$ ; $\text{Ni}_{0.4}\text{Fe}_{2.6}\text{O}_4$ ; $\text{Fe}_x\text{O}$ ; C                               | 99.85                |
| 0.14                  | $\text{Fe}_{0.64}\text{Ni}_{0.36}$ ; C  | 99.86                |
| 0.18                  | $\text{Fe}_{0.64}\text{Ni}_{0.36}$ ; C  | 99.48                |
| 0.54                  | $\text{Fe}_{0.64}\text{Ni}_{0.36}$ ; C  | 98.80                |
| 0.92                  | $\text{Fe}_{0.64}\text{Ni}_{0.36}$ ; C  | 98.76                |
| 2.49                  | $\text{Fe}_{0.64}\text{Ni}_{0.36}$ ; C  | 97.11                |



NF:  $\text{Ni}_{0.6}\text{Fe}_{2.4}\text{O}_4$ ; FN:  $\text{Fe}(\text{Ni})$ ; C: Graphitized carbon

Fig. 6. The change on crystalline phase of oxygen carrier.

species ( $\text{Ni}_{0.4}\text{Fe}_{2.6}\text{O}_4$  and  $\text{Fe}_x\text{O}$ ). In this stage, the toluene conversion is still as high as ~99% and the complete oxidation of toluene is still the dominant reaction. As the *WHSV* value further increases ( $0.11\text{ h}^{-1} < \text{WHSV} \leq 0.18\text{ h}^{-1}$ ), the lattice oxygen to toluene molar ratio decreases, resulting in the partial oxidation of toluene (to  $\text{CO}$  and  $\text{H}_2$ ) and some of toluene is catalytically cracked on the reduced oxygen carrier to  $\text{H}_2$  and carbon. This results in a decrease in  $\text{CO}_2$  concentration and an increase in  $\text{CO}$  and  $\text{H}_2$  concentrations. As the *WHSV* value exceeds  $0.18\text{ h}^{-1}$ , the  $\text{NiFe}_2\text{O}_4$  oxygen carrier quickly releases all of its available oxygen and is reduced to  $\text{Fe}(\text{Ni})$  alloy species. This further increases the catalytic cracking of toluene to form  $\text{H}_2$  and carbon deposition, resulting in a decrease in the concentrations of  $\text{CO}_2$  and  $\text{CO}$ , and a significant increase in  $\text{H}_2$  concentration. In the stage, the toluene conversion shows a slight decrease to ~97%. This is likely the result of carbon deposition deactivating the catalyst. The  $\text{CH}_4$  concentration is very low and shows a slightly increasing trend as the oxygen carrier is reduced, which is caused by the catalytic reaction (12). It is worth noting that the diffraction peak of graphitic carbon is always observed and the intensity increases with an increase in *WHSV*, as shown in Table 2. The result indicates that a small part of carbon deposition is in the form of graphitized carbon during the catalytic cracking of toluene. The increase in graphitized carbon degree may be ascribed to the fact that the benzene ring is more liable to be partially broken in the case of a high *WHSV* value.

The above results show that there is no significant decrease in the conversion of toluene cracked by the  $\text{NiFe}_2\text{O}_4$  oxygen carrier regardless of the change in the crystal phase of the oxygen carrier during the reduction process. Previous literature [2,44–46] reported that the ability of metal oxide catalyst to crack tar decreased as oxygen capacity increased. However, the  $\text{NiFe}_2\text{O}_4$  is able to convert toluene in both its oxidized and reduced states. These results may be attributed to the excellent oxidation-catalytic performance of the  $\text{NiFe}_2\text{O}_4$  oxygen carrier with a unique spinel structure.

Therefore, according to the above analysis, the  $\text{NiFe}_2\text{O}_4$  sample exhibits good application potential as an excellent biomass tar cracking catalyst and can be used as a good oxygen carrier candidate for biomass CLG.

### 3.5. Effect of steam/toluene ratio (S/C)

The reduced oxygen carrier catalytically cracks toluene while produces a large amount of carbon deposition. The continuous accumulation of carbon deposition could cover the active sites on the surface of the catalyst, which deactivates the catalyst. The introduction of water vapor can suppress the formation of carbon deposition through the water-gas shift reactions (14) and (15), therefore increasing the lifetime of the catalyst [28].

The experimental results are shown in Figs. 8–10. The toluene conversion gradually decreases from 98.51% at an S/C of 0.24–63.05% at an S/C of 1.92, as shown in Fig. 8. This result is attributed to the following three aspects.

Within the S/C range of interest, the above mentioned three reasons sufficiently show that the toluene conversion gradually decreases with an increasing S/C. However, the toluene conversion is 96.83% at S/C of 0, which is slightly lower than the toluene conversion at  $\text{S/C} \leq 0.36$  (~98%). This indicates that the minor introduction of steam is beneficial to the toluene conversion, which may be due to the promotion of steam reforming reactions of toluene (17) and (18). Although the reaction (16) inhibits toluene conversion due to the addition of steam, the steam reforming reactions (17) and (18) are more predominant during the competition. Therefore, it is important to properly control the amount of steam.

A large amount of  $\text{H}_2$  and  $\text{CO}$  is generated, and a small amount of

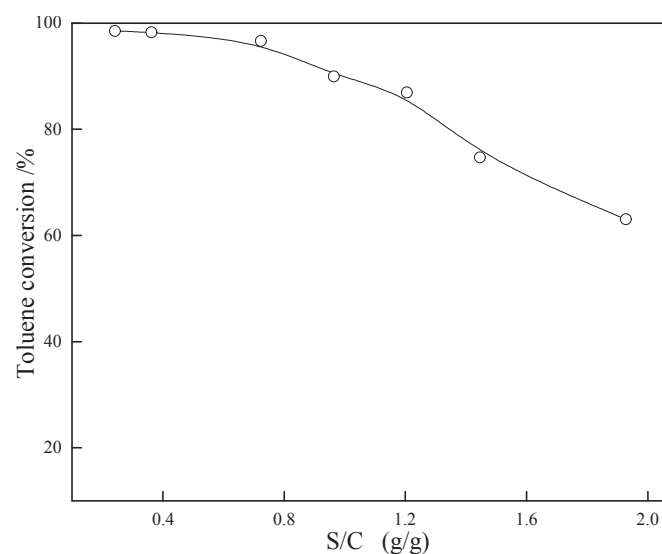


Fig. 8. Effect of S/C on toluene conversion.

$\text{CO}_2$  and  $\text{CH}_4$  is also observed during toluene steam reforming (Fig. 9). Despite the re-oxidation of the oxygen carrier by steam, the production of  $\text{H}_2$  and  $\text{CO}$  is not inhibited due to the promotion of steam reforming reactions. The  $\text{H}_2$  and  $\text{CO}$  yields increase from  $1.09\text{ m}^3/\text{kg}$  and  $0.32\text{ m}^3/\text{kg}$  at an S/C of 0.24– $2.08\text{ m}^3/\text{kg}$  and  $1.24\text{ m}^3/\text{kg}$  at an S/C of 1.20, respectively. However, as the S/C ratio further increases, the  $\text{H}_2$  and  $\text{CO}$  yields significantly decrease to  $1.08\text{ m}^3/\text{kg}$  and  $0.46\text{ m}^3/\text{kg}$  at an S/C of 1.93, respectively. This is primary because the excessive steam lowers the temperature of the effective reaction space and shortens the gas solid residence time.

The addition of steam primarily inhibits the formation of carbon deposition and prolongs the service life of the oxygen carrier during catalytic cracking of toluene. The effect of S/C on the formation of carbon deposition is shown in Fig. 10.

The amount of carbon deposition decreases significantly with an increasing S/C due to the oxidation of carbon by steam. The carbon deposition reduces to ~5% at an S/C of 1.20 and does not significantly change as S/C increases. Additionally, during the air oxidation, the  $\text{CO}/\text{CO}_2$  concentration significantly decreases and the  $\text{O}_2$  concentration significantly increases, but they are stable after  $\text{S/C} \geq 1.20$ .

These results indicate that the S/C ratio should be assigned to 1.20 to obtain the lowest carbon deposition of 4.97% in the present study, in which the toluene conversion is 86.93% and the effective gas ( $\text{CO} + \text{H}_2$ ) yield attains to the highest value ( $3.32\text{ m}^3/\text{kg}$ ). It is worth noting that most of carbon deposition is partially oxidized to  $\text{CO}$  during air oxidation. Therefore, it is speculated that the main carbonaceous gas product is also  $\text{CO}$  during oxidation of carbon deposition by steam and the chemical equilibrium (14) is more dominant during toluene steam reforming, which is in good agreement with the experimental results.

### 3.6. Effect of reaction time

The cyclic performance and stability are important parameters for the evaluation of the oxygen carrier. Therefore, the effect of reaction time on the catalytic cracking of toluene by  $\text{NiFe}_2\text{O}_4$  oxygen carrier was tested.

In order to avoid the deactivation of the catalyst caused by the long-term accumulation of carbon deposition, the air oxidation procedure was carried out for 1 h to eliminate carbon deposition at 28th, 56th, 61st, 74th and 81<sup>st</sup>h of the experiment. It was purged

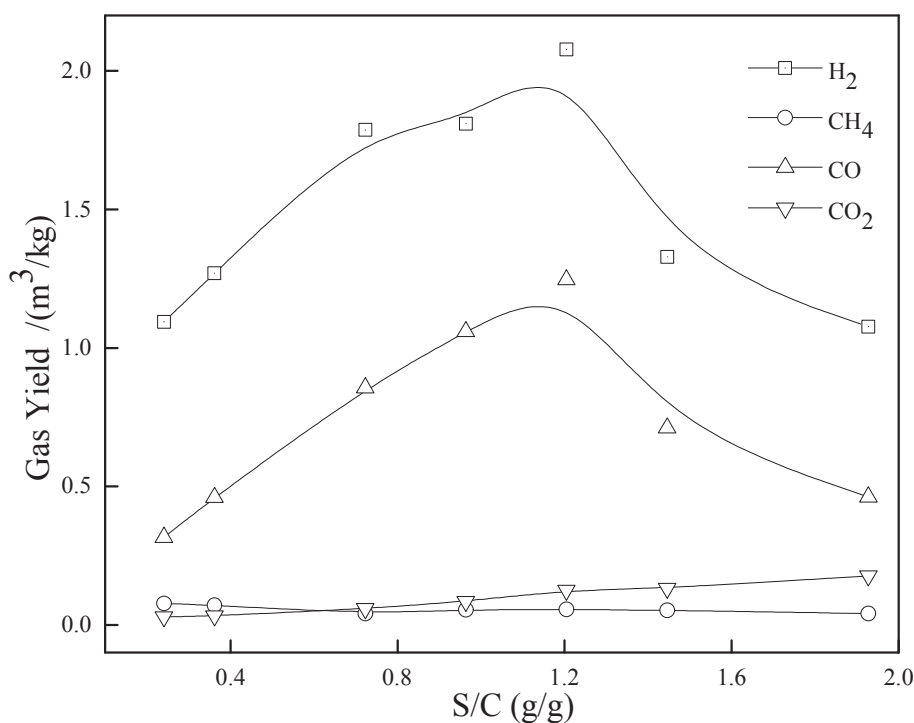


Fig. 9. Effect of S/C on gas yield.

with N<sub>2</sub> for 0.5 h to discharge the air in the reactor after oxidation of carbon deposition. The sampling of the gas and liquid products in the experiment was intermittently collected and the cumulative sampling time was 15.33 h, 10 h, 2.33 h, 3.67 h and 3.33 h, respectively. The sampling distribution during toluene cracking is shown in Fig. 11 and the experimental results are shown in Figs. 12–15.

No significant change is observed for the relative concentration of various gases (H<sub>2</sub>/CH<sub>4</sub>/CO/CO<sub>2</sub>) during continuously catalytic cracking experiment of toluene within 82 h. The H<sub>2</sub>, CO, CO<sub>2</sub>, and CH<sub>4</sub> concentrations are approximately 60%, 36%, 2.5% and 1.5%, respectively, as shown in Fig. 12. At the same time, it is also observed that the toluene conversion shows a general downward trend and there is a short-term ascending process during the continuous experiment of 82 h. As shown in Fig. 13, the toluene conversion is stable at approximately 85% within the first 27 h, but then increases to 89% at the 30<sup>th</sup> h after the first air oxidation (at the 28<sup>th</sup> h). It then gradually decreases to approximately 81% at the 55<sup>th</sup> h. After the second air oxidation (at the 56<sup>th</sup> h), the toluene conversion increases to approximately 90% (at the 57<sup>th</sup> h) which is maintained until the third air oxidation (at the 61<sup>st</sup> h). Afterwards, the toluene conversion is stable at approximately 87% until the fourth air oxidation (at the 74<sup>th</sup> h). After 74 h, the toluene conversion decreases from approximately 85% at the 75<sup>th</sup> h to approximately 81% at the 80<sup>th</sup> h. After the fifth air oxidation (at the 81<sup>st</sup> h), the toluene conversion is maintained at approximately 81%. The results indicate that the catalytic activity of the NiFe<sub>2</sub>O<sub>4</sub> oxygen carrier is declining, but still active for 82 h. Additionally, an activated process of catalyst is observed in the course of the experiment.

The activation process of the catalyst is further illustrated in Figs. 14–15. Initially, the overall conversion of toluene is 84.74% and the carbon deposition is 0.80% within the first 15.33 h. In the following 10 h, the overall conversion of toluene decreases to 83.63% and carbon deposition increases to 3.28%. A distinct change is not observed, indicating that the catalytic activity of the oxygen carrier can be maintained stably. However, the overall conversion of

toluene increases to 90.87% and 86.83%, and the carbon deposition increases significantly to 35.26% and 35.08% in the following 2.33 h and 3.67 h, respectively, which indicates that there is a transitory activation process for the catalyst. During the last 3.33 h, the overall conversion of toluene and carbon deposition decrease significantly to 82.52% and 4.99%, respectively, which indicates an evident decline in the catalytic activity of the oxygen carrier. It is also observed that there is a significant increase in the relative concentration of H<sub>2</sub> between the 56<sup>th</sup> h and 73<sup>rd</sup> h, which again indicates that the catalytic activity of the oxygen carrier is enhanced during toluene catalytic cracking, as seen in Fig. 15. The improvement in the reactivity of the oxygen carrier facilitates more toluene to be catalytically cracked into H<sub>2</sub> and carbon deposition, thus the H<sub>2</sub> concentration and carbon deposition evidently increase.

At the same time, the comparisons between the catalytic cracking of toluene by the used oxygen carrier at the 1<sup>st</sup> h and at the 82<sup>nd</sup> h were performed, as shown in Table 3. It is observed that toluene conversion and carbon deposition decrease from 86.93% to 4.97% at the 1<sup>st</sup> h to 81.12% and 4.27% at the 82<sup>nd</sup> h, respectively. Additionally, there is a slight decrease in various gas concentrations during toluene cracking after 80 h. The results also show a decline in catalytic activity after 80 h.

It can be roughly concluded that the catalytic activity of NiFe<sub>2</sub>O<sub>4</sub> oxygen carrier is stable for a long time, followed by a transient activation, and finally a slight decrease during the long-term experiment based on the above discussions. The main reasons for the change in the catalytic activity of the oxygen carrier are attributed to the competition of the following two reasons. On the one hand, there is a positive correlation between the catalytic activity of the oxygen carrier and its specific surface area [49,50], i.e., the larger specific surface area of the catalyst implies the more active sites existed on the surface of the catalyst, thereby it is easier to activate the reactants to improve the reactivity of the catalyst. After 82 h, the specific surface area of the oxygen carrier increases

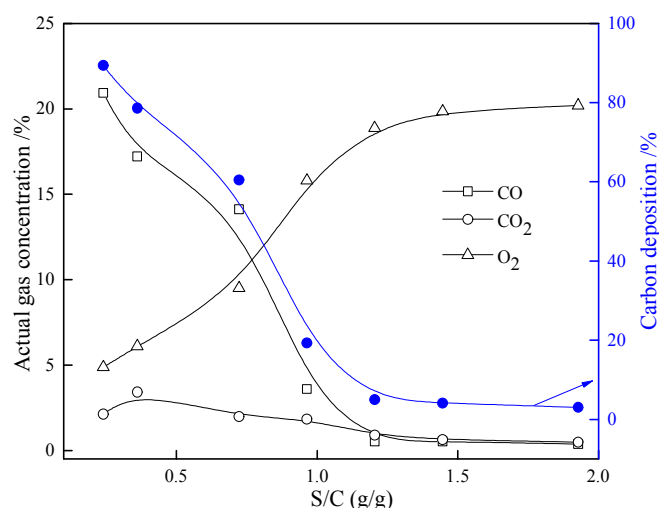


Fig. 10. Effect of S/C on gas concentration of air oxidation and carbon deposition.

- 1) The  $\text{NiFe}_2\text{O}_4$  oxygen carrier is reduced into Fe(Ni) alloy phase under high WHSV value of 4.98. It is found that the complete reduction product of  $\text{NiFe}_2\text{O}_4$  sample, i.e. the Fe(Ni) alloy species, can be oxidized by steam and a large amount of  $\text{Fe}_{2+y}\text{O}_4$  species is generated via reaction (16) [43,47,48]. Additionally, the catalytic performance of iron oxide species in tar cracking presented a negative relationship with its oxygen content, the metallic Fe showed the strongest catalytic activity and the complete oxidation species ( $\text{Fe}_2\text{O}_3$ ) displayed the lowest catalytic activity [2]. The chemical equilibrium (16) proceeds towards the right with the increase of S/C, more metallic Fe is oxidized into  $\text{Fe}_{2+y}\text{O}_4$  with steam addition. Thus, the catalytic activity of the reduced oxygen carrier gradually decreases with an increase in S/C. At the same time, the oxidation performance of  $\text{Fe}_{2+y}\text{O}_4$  species is relatively low. Therefore, the toluene conversion shows a downtrend with an increase in S/C.
- 2) Although the toluene cracking reactions (11) and (13) occur over the  $\text{NiFe}_2\text{O}_4$  bed (i.e. reactor bed), the reforming reactions (17) and (18) occur over the reactor bed and the upper section of reactor due to the diffusion of water vapor and toluene vapor. Hence, the effective reaction space of toluene conversion includes the reactor bed and the upper section of reactor. Because of the introduction of excess steam, it requires a large amount of sensible heat to maintain the reaction temperature, resulting in the uneven distribution of temperature in the reactor. The temperature of the reactor bed is higher than that of the upper section of the reactor, thus resulting in a decrease in temperature in the effective reaction space to inhibit the catalytic cracking of toluene. This result further indicates that the toluene conversion gradually decreases with the increase in S/C, especially at high S/C. (as shown in Fig. 3, the temperature is an important factor for the catalytic cracking of toluene).
- 3) Qualitatively, at a certain temperature (e.g. 850 °C), the velocity of carrier gas ( $\text{N}_2$ ) is constant because the flow rate of carrier gas is fixed at 100 mL/min and the cross-sectional area of reactor is constant. However, the steam velocity increases with the increase in water vapor amount. Hence, the addition of excess steam results in a high superficial gas velocity, thereby shortening the gas-solid two-phase residence time to further decrease the toluene conversion.

from 4.12  $\text{m}^2/\text{g}$  to 5.32  $\text{m}^2/\text{g}$ , which is beneficial to increase the catalytic activity of the oxygen carrier to promote toluene conversion. On the other hand, the crystal phase of  $\text{NiFe}_2\text{O}_4$  is changed

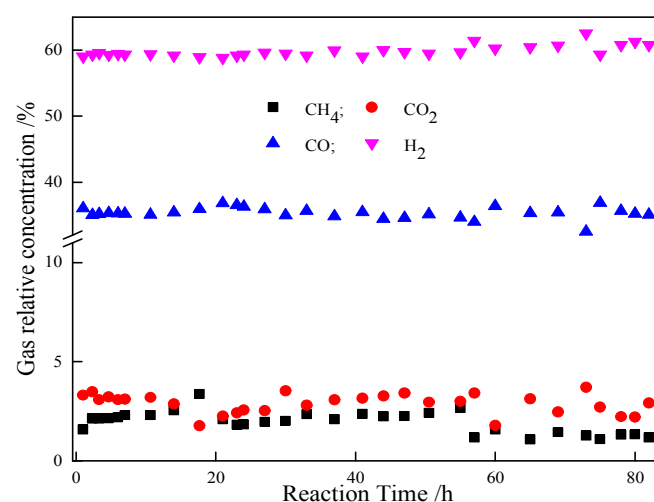


Fig. 12. The gas relative concentration with the reaction time.

significantly after a long period of reaction (as seen in Fig. 16). The presence of  $\text{Fe}_2\text{O}_3$  species reduces the catalytic activity of the oxygen carrier, thereby inhibiting the toluene conversion. Therefore, the catalytic activity of the oxygen carrier is first maintained for a long time under the combined effect of the above two aspects, and then is transiently activated due to the increase in the specific surface area of the oxygen carrier, and finally slightly decreases because of the appearance of  $\text{Fe}_2\text{O}_3$  species.

A significant change for the crystal phase of the oxygen carrier is observed after continuous experiment of 82 h, as shown in Fig. 16. Compared with the fresh oxygen carrier with complete spinel structure, a new crystal phase of  $\text{Fe}_2\text{O}_3$ , derived from some Fe element divorced from the Fe–Ni spinel structure appears in the used oxygen carrier, which is the main reason for the decrease in catalytic activity of  $\text{NiFe}_2\text{O}_4$  oxygen carrier.

Therefore, based on the above discussions, it can be concluded that the  $\text{NiFe}_2\text{O}_4$  oxygen carrier can be used as a good tar cracking catalyst for long-term use during biomass CLG.

#### 4. Conclusions

The characteristics of *in-situ* removal of toluene (biomass tar model compound) on  $\text{NiFe}_2\text{O}_4$  oxygen carrier were investigated in the work.

The  $\text{NiFe}_2\text{O}_4$  oxygen carrier presents a dual-function of oxidation-catalysis for toluene removal and the toluene conversion and  $\text{H}_2$  yield attain to 96.83% and 0.91  $\text{m}^3/\text{kg}$ , respectively. The increasing trend of toluene removal gradually slows down above 850 °C. Although the WHSV increases approximately nine times, the toluene conversion only reduces by 2.78%. The crystal phase is

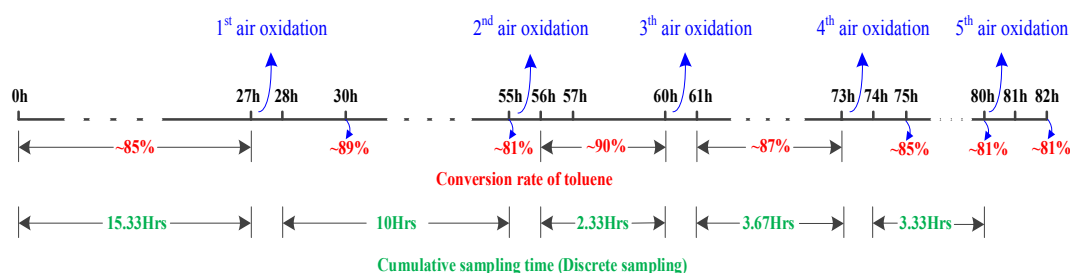


Fig. 11. The sampling distribution during the toluene catalytic cracking.



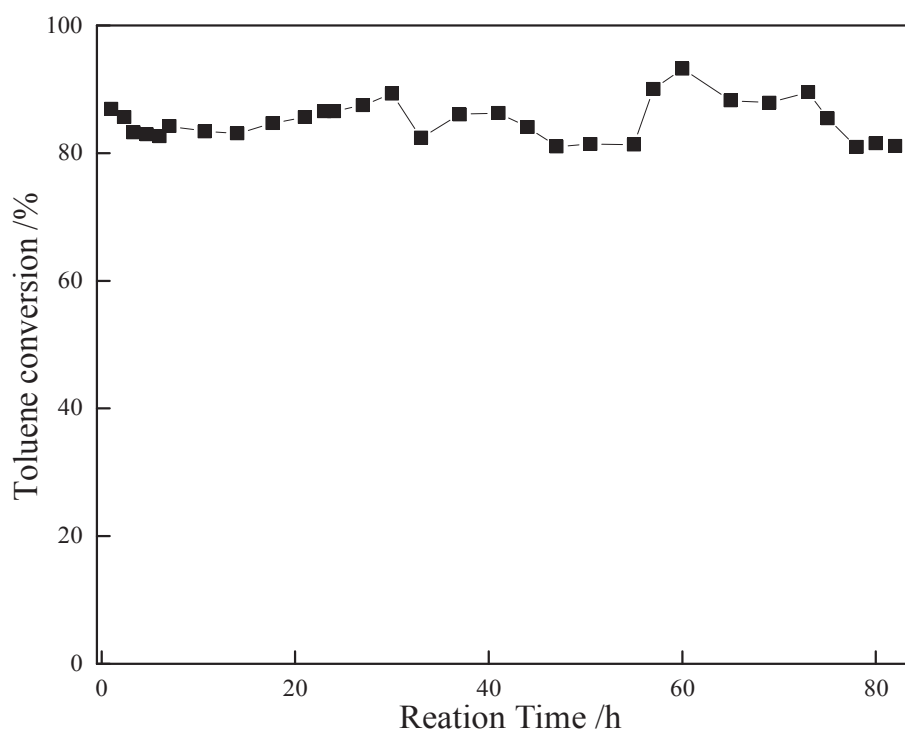


Fig. 13. The toluene conversion with the reaction time.

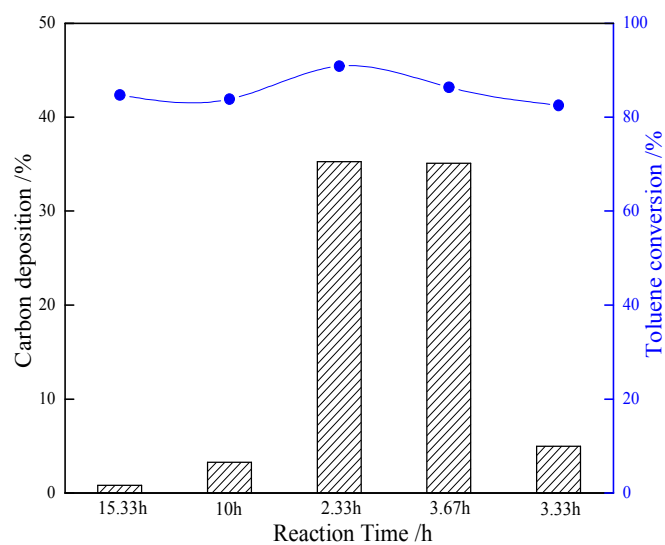


Fig. 14. Toluene conversion and carbon deposition within different reaction periods.

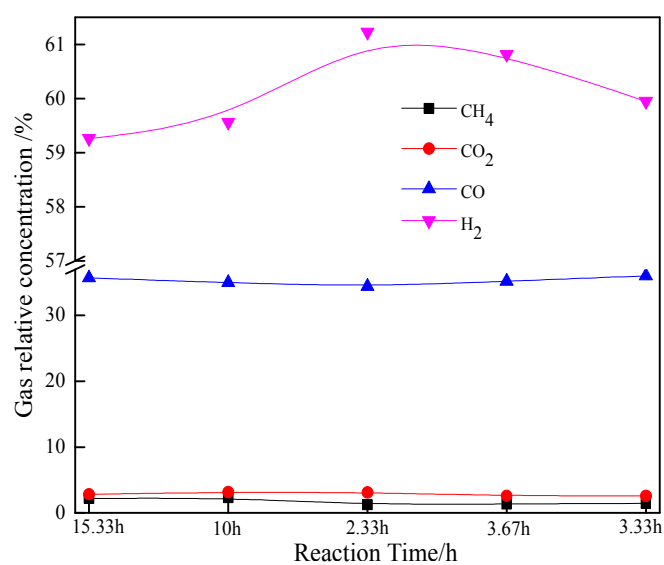


Fig. 15. Gas relative concentration within different reaction periods.

Table 3

The comparisons on characteristics of catalytic cracking of toluene at the 1<sup>st</sup>h and 82<sup>nd</sup>h.

| Time               | Cracking stage (Actual gas concentration, %) |                 |       |                 | Oxidation stage (Actual gas concentration, %) |                 |                | Conversion (%) | Carbon deposition (%) | S <sub>BET</sub> (m <sup>2</sup> /g) |
|--------------------|--|-----------------|-------|-----------------|---|-----------------|----------------|----------------|-----------------------|--------------------------------------|
|                    | H <sub>2</sub>                               | CH <sub>4</sub> | CO    | CO <sub>2</sub> | CO  | CO <sub>2</sub> | O <sub>2</sub> |                |                       |                                      |
| 1st h              | 34.27  | 0.92            | 20.95 | 1.92            | 0.52  | 0.89            | 18.88          | 86.93          | 4.97                  | 4.12                                 |
| 82 <sup>th</sup> h | 32.56  | 0.63            | 18.80 | 1.56            | 0.32  | 0.90            | 19.37          | 81.12          | 4.27                  | 5.32                                 |

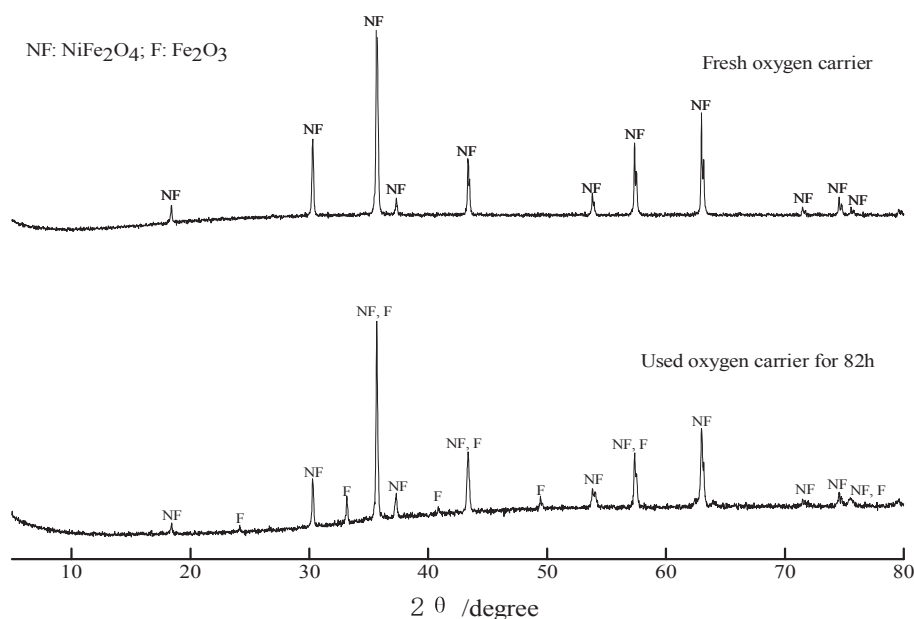


Fig. 16. XRD patterns of fresh oxygen carrier and used oxygen carrier.

transformed from initial state (NiFe<sub>2</sub>O<sub>4</sub>) to intermediate transition state (Ni<sub>0.6</sub>Fe<sub>2.4</sub>O<sub>4</sub>, Fe<sub>3-x</sub>O<sub>4</sub> and Fe<sub>x</sub>O), until its completely reduced state (Fe<sub>0.64</sub>Ni<sub>0.36</sub>), the toluene conversion is as high as ~98%. A suitable S/C ratio is chosen to be 1.20, where the maximum effective gas yield is attained. Moreover, the introduction of steam greatly eliminates the carbon deposition, with the lowest carbon deposition (4.97%) found at the S/C ratio of 1.20. The catalytic activity of NiFe<sub>2</sub>O<sub>4</sub> oxygen carrier maintained stabilized for a long time, followed by a transient activation, and finally a slight decrease during the long-term experiment of toluene cracking (82 h).

## Acknowledgments

The authors gratefully acknowledge the financial support by the National Natural Science Foundation of China (51776210), the National Key Research and Development Program of China (2018YFB0605405), DNL Cooperation Fund, Chinese Academy of Sciences (DNL180205), the Major International (Regional) Joint Research Project of the National Natural Science Foundation of China (51661145011), and the Youth Innovation Promotion Association, Chinese Academy of Sciences (2018384).

## References

- [1] Wang ZQ, He T, Li JQ, Wu JL, Qin JG, Liu GB, et al. Design and operation of a pilot plant for biomass to liquid fuels by integrating gasification, DME synthesis and DME to gasoline. *Fuel* 2016;186:587–96.
- [2] Nordgreen T, Liliedahl T, Sjöström K. Metallic iron as a tar breakdown catalyst related to atmospheric, fluidised bed gasification of biomass. *Fuel* 2006;85(5–6):689–94.
- [3] Li CS, Suzuki K. Tar property, analysis, reforming mechanism and model for biomass gasification—An overview. *Renew Sustain Energy Rev* 2009;13(3):594–604.
- [4] Chen G, Andries J, Luo Z, Spliethoff H. Biomass pyrolysis/gasification for product gas production: the overall investigation of parametric effects. *Energy Convers Manag* 2003;44(11):1875–84.
- [5] de Jong W, Unal O, Andries J, Hein KRG, Spliethoff H. Biomass and fossil fuel conversion by pressurised fluidised bed gasification using hot gas ceramic filters as gas cleaning. *Biomass Bioenergy* 2003;25(1):59–83.
- [6] Bhave AG, Vyas DK, Patel JB. A wet packed bed scrubber-based producer gas cooling-cleaning system. *Renew Energy* 2008;33(7):1716–20.
- [7] Nakamura S, Kitano S, Yoshikawa K. Biomass gasification process with the tar removal technologies utilizing bio-oil scrubber and char bed. *Appl Energy* 2016;170:186–92.
- [8] Claude V, Courson C, Kohler M, Lambert SD. Overview and essentials of biomass gasification technologies and their catalytic cleaning methods. *Energy Fuel* 2016;30(11):8791–814.
- [9] Ahmad AA, Zawawi NA, Kasim FH, Inayat A, Khasri A. Assessing the gasification performance of biomass: a review on biomass gasification process conditions, optimization and economic evaluation. *Renew Sustain Energy Rev* 2016;53:1333–47.
- [10] Han J, Kim H. The reduction and control technology of tar during biomass gasification/pyrolysis: an overview. *Renew Sustain Energy Rev* 2008;12(2):397–416.
- [11] Sutton D, Kelleher B, Ross JRH. Review of literature on catalysts for biomass gasification. *Fuel Process Technol* 2001;73(3):155–73.
- [12] Ashok J, Kawi S. Nickel-iron alloy supported over iron-alumina catalysts for steam reforming of biomass tar model compound. *ACS Catal* 2014;4(1):289–301.
- [13] Shen YF, Fu YH. Advances in in situ and ex situ tar reforming with biochar catalysts for clean energy production. *Sustain Energy Fuels* 2018;2(2):326–44.
- [14] Shen YF, Wang JF, Ge XL, Chen MD. By-products recycling for syngas cleanup in biomass pyrolysis - an overview. *Renew Sustain Energy Rev* 2016;59:1246–68.
- [15] Yung MM, Jablonski WS, Magrini-Bair KA. Review of catalytic conditioning of biomass-derived syngas. *Energy Fuel* 2009;23(3–4):1874–87.
- [16] Anis S, Zainal ZA. Tar reduction in biomass producer gas via mechanical, catalytic and thermal methods: a review. *Renew Sustain Energy Rev* 2011;15(5):2355–77.
- [17] Mitsuoka K, Hayashi S, Amano H, Kayahara K, Sasaoaka E, Uddin MA. Gasification of woody biomass char with CO<sub>2</sub>: the catalytic effects of K and Ca species on char gasification reactivity. *Fuel Process Technol* 2011;92(1):26–31.
- [18] Berghel J, Frodeson S, Granström K, Renström R, Stahl M, Nordgren D, et al. The effects of kraft lignin additives on wood fuel pellet quality, energy use and shelf life. *Fuel Process Technol* 2013;112:64–9.
- [19] Furusawa T, Saito K, Kori Y, Miura Y, Sato M, Suzuki N. Steam reforming of naphthalene/benzene with various types of Pt- and Ni-based catalysts for hydrogen production. *Fuel* 2013;103:111–21.
- [20] Cui H, Turn SQ, Keffer V, Evans D, Tran T, Foley M. Contaminant estimates and removal in product gas from biomass steam gasification. *Energy Fuels* 2010;24(2):1222–33.
- [21] Min ZH, Yimsiri P, Asadullah M, Zhang S, Li CZ. Catalytic reforming of tar during gasification. Part II. Char as a catalyst or as a catalyst support for tar reforming. *Fuel* 2011;90(7):2545–52.
- [22] Bhandari PN, Kumar A, Bellmer DD, Huhnke RL. Synthesis and evaluation of biochar-derived catalysts for removal of toluene (model tar) from biomass-generated producer gas. *Renew Energy* 2014;66:346–53.
- [23] Rapagna S, Jand N, Kiennemann A, Foscolo PU. Steam-gasification of biomass in a fluidised-bed of olivine particles. *Biomass Bioenergy* 2000;19(3):187–97.
- [24] Lizzio AA, Radovic LR. Transient kinetics study of catalytic char gasification in carbon-dioxide. *Ind Eng Chem Res* 1991;30(8):1735–44.
- [25] Jeong YS, Choi YK, Kim JS. Three-stage air gasification of waste polyethylene: in-situ regeneration of active carbon used as a tar removal additive. *Energy*

- 2019;166:335–42.
- [26] El-Rub ZA. Biomass char as an in-situ catalyst for tar removal in gasification systems. PhD thesis. Enschede, The Netherlands: Twente University; 2008.
- [27] Meng JG, Wang XB, Zhao ZL, Zheng AQ, Huang Z, Wei GQ, et al. Highly abrasion resistant thermally fused olivine as in-situ catalysts for tar reduction in a circulating fluidized bed biomass gasifier. *Bioresour Technol* 2018;268:212–20.
- [28] Meng JG, Zhao ZL, Wang XB, Wu XS, Zheng AQ, Huang Z, et al. Effects of catalyst preparation parameters and reaction operating conditions on the activity and stability of thermally fused Fe-olivine catalyst in the steam reforming of toluene. *Int J Hydrogen Energy* 2018;43(1):127–38.
- [29] Zhang RQ, Wang YC, Brown RC. Steam reforming of tar compounds over Ni/olivine catalysts doped with CeO<sub>2</sub>. *Energy Convers Manag* 2007;48(1):68–77.
- [30] Hu X, Lu GX. Investigation of steam reforming of acetic acid to hydrogen over Ni-Co metal catalyst. *J Mol Catal A Chem* 2007;261(1):43–8.
- [31] Meng JG, Zhao ZL, Wang XB, Zheng AQ, Zhang DY, Huang Z, et al. Comparative study on phenol and naphthalene steam reforming over Ni-Fe alloy catalysts supported on olivine synthesized by different methods. *Energy Convers Manag* 2018;168:60–73.
- [32] Ryden M, Lyngfelt A, Mattisson T. Chemical-looping combustion and chemical-looping reforming in a circulating fluidized-bed reactor using Ni-based oxygen carriers. *Energy Fuel* 2008;22(4):2585–97.
- [33] Adanez J, Abad A, Garcia-Labiano F, Gayan P, de Diego LF. Progress in chemical-looping combustion and reforming technologies. *Prog Energy Combust* 2012;38(2):215–82.
- [34] Huang Z, He F, Feng YP, Zhao K, Zheng AQ, Chang S, et al. Synthesis gas production through biomass direct chemical looping conversion with natural hematite as an oxygen carrier. *Bioresour Technol* 2013;140:138–45.
- [35] Huang Z, Zhang Y, Fu JJ, Yu LH, Chen M, Liu S, et al. Chemical looping gasification of biomass char using iron ore as an oxygen carrier. *Int J Hydrogen Energy* 2016;41(40):17871–83.
- [36] Lind F, Seemann M, Thunman H. Continuous catalytic tar reforming of biomass derived raw gas with simultaneous catalyst regeneration. *Ind Eng Chem Res* 2011;50(20):11553–62.
- [37] Berguerand N, Lind F, Israelsson M, Seemann M, Biollaz S, Thunman H. Use of nickel oxide as a catalyst for tar elimination in a chemical-looping reforming reactor operated with biomass producer gas. *Ind Eng Chem Res* 2012;51(51):16610–6.
- [38] Lind F, Berguerand N, Seemann M, Thunman H. Ilmenite and nickel as catalysts for upgrading of raw gas derived from biomass gasification. *Energy Fuel* 2013;27(2):997–1007.
- [39] Meng JG, Wang XB, Zhao ZL, Wu XS, Zheng AQ, Wei GQ, et al. A highly carbon-resistant olivine thermally fused with metallic nickel catalyst for steam reforming of biomass tar model compound. *RSC Adv* 2017;7(62):39160–71.
- [40] Wang X, Chen ZH, Hu M, Tian YF, Jin XY, Ma S, et al. Chemical looping combustion of biomass using metal ferrites as oxygen carriers. *Chem Eng J* 2017;312:252–62.
- [41] Coll R, Salvado J, Farriol X, Montane D. Steam reforming model compounds of biomass gasification tars: conversion at different operating conditions and tendency towards coke formation. *Fuel Process Technol* 2001;74(1):19–31.
- [42] Caballero MA, Corella J, Aznar MP, Gil J. Biomass gasification with air in fluidized bed. Hot gas cleanup with selected commercial and full-size nickel-based catalysts. *Ind Eng Chem Res* 2000;39(5):1143–54.
- [43] Liu S, He F, Huang Z, Zheng AQ, Feng YP, Shen Y, et al. Screening of NiFe<sub>2</sub>O<sub>4</sub> nanoparticles as oxygen carrier in chemical looping hydrogen production. *Energy Fuel* 2016;30(5):4251–62.
- [44] Matsuoka K, Shimbori T, Kuramoto K, Hatano H, Suzuki Y. Steam reforming of woody biomass in a fluidized bed of iron oxide-impregnated porous alumina. *Energy Fuel* 2006;20(6):2727–31.
- [45] Virginie M, Courson C, Kiennemann A. Toluene steam reforming as tar model molecule produced during biomass gasification with an iron/olivine catalyst. *Cr Chimia* 2010;13(10):1319–25.
- [46] Swierczynski D, Courson C, Bedel L, Kiennemann A, Vilminot S. Oxidation reduction behavior of iron-bearing olivines (Fe<sub>x</sub>Mg<sub>1-x</sub>)(2)SiO<sub>4</sub> used as catalysts for biomass gasification. *Chem Mater* 2006;18(4):897–905.
- [47] Sturzenegger M, D'Souza L, Struis RPWJ, Stucki S. Oxygen transfer and catalytic properties of nickel iron oxides for steam reforming of methane. *Fuel* 2006;85(10–11):1599–602.
- [48] Aston VJ, Evanko BW, Weimer AW. Investigation of novel mixed metal ferrites for pure H<sub>2</sub> and CO<sub>2</sub> production using chemical looping. *Int J Hydrogen Energy* 2013;38(22):9085–96.
- [49] Keller M, Leion H, Mattisson T, Thunman H. Investigation of natural and synthetic bed materials for their utilization in chemical looping reforming for tar elimination in biomass-derived gasification gas. *Energy Fuel* 2014;28(6):3833–40.
- [50] Uddin MA, Tsuda H, Wu SJ, Sasaoka E. Catalytic decomposition of biomass tars with iron oxide catalysts. *Fuel* 2008;87(4–5):451–9.

## Review Article

A review of thermo-fluidic performance and application of shellless phase change slurry: Part 2 – Flow and heat transfer characteristics

F. Ma and P. Zhang

116602

Quantitative evaluation of thermal performance and energy saving potential of the building integrated with PCM in a subarctic climate

S. Kenzhekanov, S.A. Memon and

I. Adilkhanova

116607

## Full Length Articles

Development of a numerical model for performance prediction of an integrated microcombustor-thermoelectric power generator

K. Hiranandani, B. Aravind, V. Ratna Kishore and S. Kumar

116624

An efficient optimization framework of cyclic steam stimulation with experimental design in extra heavy oil reservoirs

E. Luo, Z. Fan, Y. Hu, L. Zhao, B. Bo, W. Yu, H. Liang, M. Liu, Y. Liu, C. He and J. Wang

116601

Heat transfer of supercritical CO<sub>2</sub> in vertical round tube: A considerate turbulent Prandtl number modification

X. Du, Z. Lv, X. Yu, M. Cao, J. Zhou, Y. Ren, Q. Qiu and X. Zhu

116612

Investigation of water co-adsorption on the energy balance of solid sorbent based direct air capture processes

C. Drechsler and D.W. Agar

116587

Optimal scheduling of resources and appliances in smart homes under uncertainties considering participation in spot and contractual markets

A. Mohammadi Rad and T. Barforoushi

116548

Assessing temporal complementarity between three variable energy sources through correlation and compromise programming

F.A. Canales, J. Jurasz, A. Beluco and A. Kies

116637

Energy and uncertainty management through domestic demand response in the residential building

H. Mehrjerdi and R. Hemmati

116647

B-matching-based optimization model for energy allocation in sea surface monitoring

L. Dong, X. Kang, M. Pan, M. Zhao, F. Zhang and H. Yao

116618

Thermo-economic modeling and analysis of an NG-fueled SOFC-WGS-TSA-PEMFC hybrid energy conversion system for stationary electricity power generation

Z. Wu, P. Zhu, J. Yao, P. Tan, H. Xu, B. Chen, F. Yang, Z. Zhang and M. Ni

116613

Improvement of energy supply configuration for telecommunication system in remote area s based on improved chaotic world cup optimization algorithm

H. Li, K. Li, N. Zafetti and J. Gu

116614

Utilization of biomass ash for upgrading petroleum coke gasification: Effect of soluble and insoluble components

Q. He, J. Yu, X. Song, L. Ding, J. Wei and G. Yu

116642

Energy solutions for producing shale oil: Characteristics of energy demand and economic analysis of energy supply options

C. Huang, H. Hou, G. Yu, L. Zhang and E. Hu

116603

Optimal charging infrastructure planning based on a charging convenience buffer

S. Davidov

116655

CONTENTS—continued on inside back cover

Abstracted/indexed in: Applied Sci. & Tech. Index, Biosis Data, Cam. Sci. Abstr, Chem. Abstr. Serv. Curr. Cont. Eng. Tech. & Applied Sci., Elsevier BIOBASE/Current Awareness in Biological Sciences, Eng. Ind., Environ. Per. Bibl, INSPEC Data., Res. Alert, Curr. Cont. Sci. Cit. Ind., Curr. Cont. SCISEARCH Data. Also covered in the abstract and citation database SCOPUS®. Full text available on ScienceDirect®



ELSEVIER

Printed by Henry Ling in the United Kingdom



ISSN 0360-5442

483



Available online at [www.sciencedirect.com](http://www.sciencedirect.com)

ScienceDirect

## AIMS AND SCOPE

*Energy* is an international, multi-disciplinary journal in energy engineering and research. The journal aims to be a leading peer-reviewed platform and an authoritative source of information for analyses, reviews and evaluations related to energy. The journal covers research in mechanical engineering and thermal sciences, with a strong focus on energy analysis, energy modelling and prediction, integrated energy systems, energy planning and energy management. The journal also welcomes papers on related topics such as energy conservation, energy efficiency, biomass and bioenergy, renewable energy, electricity supply and demand, energy storage, energy in buildings, and on economic and policy issues, provided such topics are within the context of the broader multi-disciplinary scope of *Energy*.

### © 2020 Elsevier Ltd. All rights reserved.

This journal and the individual contributions contained in it are protected under copyright by Elsevier Ltd., and the following terms and conditions apply to their use:

#### Photocopying

Single photocopies of single articles may be made for personal use as allowed by national copyright laws. Permission of the Publisher and payment of a fee is required for all other photocopying, including multiple or systematic copying, copying for advertising or promotional purposes, resale, and all forms of document delivery. Special rates are available for educational institutions that wish to make photocopies for non-profit educational classroom use.

For information on how to seek permission visit [www.elsevier.com/permissions](http://www.elsevier.com/permissions) or call: (+44) 1865 843830 (UK)/(+1) 215 239 3804 (USA).

#### Derivative works

Subscribers may reproduce tables of contents or prepare lists of articles including abstracts for internal circulation within their institutions. Permission of the Publisher is required for resale or distribution outside the institution. Permission of the Publisher is required for all other derivative works, including compilations and translations (please consult [www.elsevier.com/permissions](http://www.elsevier.com/permissions)).

#### Electronic storage or usage

Permission of the Publisher is required to store or use electronically any material contained in this journal, including any article or part of an article (please consult [www.elsevier.com/permissions](http://www.elsevier.com/permissions)).

Except as outlined above, no part of this publication may be reproduced, stored in a retrieval system or transmitted in any form or by any means, electronic, mechanical, photocopying, recording or otherwise, without prior written permission of the Publisher.

#### Notice

No responsibility is assumed by the Publisher for any injury and/or damage to persons or property as a matter of products liability, negligence or otherwise, or from any use or operation of any methods, products, instructions or ideas contained in the material herein. Because of rapid advances in the medical sciences, in particular, independent verification of diagnoses and drug dosages should be made.

Although all advertising material is expected to conform to ethical (medical) standards, inclusion in this publication does not constitute a guarantee or endorsement of the quality or value of such product or of the claims made of it by its manufacturer.

**Funding body agreements and policies:** Elsevier has established agreements and developed policies to allow authors who publish in Elsevier journals to comply with potential manuscript archiving requirements as specified as conditions of their grant awards. To learn more about existing agreements and policies please visit <http://www.elsevier.com/funding-bodies>.

**Publication information:** *Energy* (ISSN 0360-5442). For 2020 volumes 190-213 (24 issues) are scheduled for publication. Subscription prices are available upon request from the Publisher or from the Elsevier Customer Service Department nearest you or from this journal's website (<http://www.elsevier.com/locate/energy>). Further information is available on this journal and other Elsevier products through Elsevier's website (<http://www.elsevier.com>). Subscriptions are accepted on a prepaid basis only and are entered on a calendar year basis. Issues are sent by standard mail (surface within Europe, air delivery outside Europe). Priority rates are available upon request. Claims for missing issues should be made within six months of the date of dispatch.

**Orders, claims, and journal inquiries:** Please visit our Support Hub page <https://service.elsevier.com> for assistance.

#### Author inquiries

You can track your submitted article at <http://www.elsevier.com/track-submission>. You can track your accepted article at <http://www.elsevier.com/trackarticle>. You are also welcome to contact Customer Support via <http://support.elsevier.com>.

#### Advertising information

If you are interested in advertising or other commercial opportunities please e-mail [Comercialsales@elsevier.com](mailto:Comercialsales@elsevier.com) and your inquiry will be passed to the correct person who will respond to you within 48 hours.

#### Language (usage and editing services)

Please write your text in good English (American or British usage is accepted, but not a mixture of these). Authors who feel their English language manuscript may require editing to eliminate possible grammatical or spelling errors and to conform to correct scientific English may wish to use the English Language Editing service available from Elsevier's WebShop <http://webshop.elsevier.com/languageediting/> or visit our customer support site <http://support.elsevier.com> for more information.

#### Illustration services

Elsevier's WebShop (<http://webshop.elsevier.com/illustrationservices>) offers Illustration Services to authors preparing to submit a manuscript but concerned about the quality of the images accompanying their article. Elsevier's expert illustrators can produce scientific, technical and medical-style images, as well as a full range of charts, tables and graphs. Image 'polishing' is also available, where our illustrators take your image(s) and improve them to a professional standard. Please visit the website to find out more.

For a full and complete Guide for Authors, please go to: <http://www.elsevier.com/locate/energy>

Printed by Henry Ling in the United Kingdom

Ⓢ The paper used in this publication meets the requirements of ANSI/NISO Z39.48-1992 (Permanence of Paper)

## CONTENTS—continued from outside back cover

|  |        |  |        |
|--|--------|--|--------|
| Concept of hydrogen fired gas turbine cycle with exhaust gas recirculation: Assessment of process performance<br><b>M. Ditaranto, T. Heggset and D. Berstad</b>  | 116646 | Numerical analysis of aerodynamic performance of a floating offshore wind turbine under pitch motion<br><b>Y. Fang, L. Duan, Z. Han, Y. Zhao and H. Yang</b>   | 116621 |
| Performance improvement of a PV/T system utilizing Ag/CoSO <sub>4</sub> -propylene glycol nanofluid optical filter<br><b>X. Han, X. Chen, Y. Sun and J. Qu</b>   | 116611 | Fuel consumption at the oversaturated signalized intersection considering queue effects: A case study in Harbin, China<br><b>L. Wu, Y. Ci, Y. Wang and P. Chen</b>   | 116654 |
| Distribution characteristics of salt-out particles in steam turbine stage<br><b>P. Hu, L. Cao, J. Su, Q. Li and Y. Li</b>  | 116626 | Effect of flame interaction on swirl-stabilized mesoscale burner array performance<br><b>J. Choi, R. Rajasegar, C.M. Mitsingas, Q. Liu, T. Lee and J. Yoo</b>  | 116661 |
| Adaptive selective catalytic reduction model development using typical operating data in coal-fired power plants<br><b>Y. Lv, X. Lv, F. Fang, T. Yang and C.E. Romero</b>  | 116589 | Investigation on specific milling energy and energy efficiency in high-speed milling based on energy flow theory<br><b>T. Zhang, Z. Liu, X. Sun, J. Xu, L. Dong and G. Zhu</b>   | 116596 |
| Numerical research on combining flue gas recirculation sintering and fuel layered distribution sintering in the iron ore sintering process<br><b>X.-H. Zhang, P. Feng, J.-R. Xu, L.-B. Feng and S. Qing</b>                  | 116660 | Machine learning-based optimal design of a phase change material integrated renewable system with on-site PV, radiative cooling and hybrid ventilations—study of modelling and application in five climatic regions<br><b>Y. Zhou, S. Zheng and G. Zhang</b> | 116608 |
| Scenario analysis for promoting clean cooking in Sub-Saharan Africa: Costs and benefits<br><b>A.G. Dagnachew, A.F. Hof, P.L. Lucas and D.P. van Vuuren</b>   | 116641 | An experimental study on energy and exergy performance of a spiral tube receiver for solar parabolic dish concentrator<br><b>V. Thirunavukkarasu and M. Cheralathan</b>  | 116635 |
| Analytical modelling of counter-flow non-premixed combustion of coal particles under non-adiabatic conditions taking into account trajectory of particles<br><b>M. Nematollahi, S. Sadeghi, H. Rasam and M. Bidabadi</b>     | 116650 | Prediction of the NO <sub>x</sub> emissions from thermal power plant using long-short term memory neural network<br><b>G. Yang, Y. Wang and X. Li</b>  | 116597 |
| Performance evaluation of μDMFCs based on porous-silicon electrodes and methanol modification<br><b>C.-R. Yang, C.-W. Lu, P.-C. Fu, C. Cheng, Y.-C. Chiou, R.-T. Lee and S.-F. Tseng</b>                                     | 116666 | Potential of coastal headlands for tidal energy extraction and the resulting environmental effects along Negeri Sembilan coastlines: A numerical simulation study<br><b>H.-B. Goh, S.-H. Lai, M. Jameel and H.-M. Teh</b>                                    | 116656 |
| Operation characteristics of a bubbling fluidized bed heat exchanger with internal solid circulation for a 550-MWe ultra-supercritical CFB boiler<br><b>D. Li, R. Cai, M. Zhang, H. Yang, K. Choi, S. Ahn and C.-H. Jeon</b> | 116503 | Thermal efficiency enhancement of direct absorption parabolic trough solar collector (DAPTSC) by using nanofluid and metal foam<br><b>M.M. Heyhat, M. Valizade, Sh. Abdolhazade and M. Maerefat</b>  | 116662 |
| Cost-benefit analysis of integrated energy system planning considering demand response<br><b>Y. Xiang, H. Cai, C. Gu and X. Shen</b>   | 116632 | Energy management and control strategy for a DFIG wind turbine/fuel cell hybrid system with super capacitor storage system<br><b>A. Kadri, H. Marzougui, A. Aouiti and F. Bacha</b>  | 116518 |
| Day ahead powerful probabilistic wind power forecast using combined intelligent structure and fuzzy clustering algorithm<br><b>L. Li, X.-L. Yin, X.-C. Jia and B. Sobhani</b>  | 116498 | Design and optimization of bio-inspired wave-like channel for a PEM fuel cell applying genetic algorithm<br><b>G. Cai, Y. Liang, Z. Liu and W. Liu</b>   | 116670 |
| Gas turbine performance prediction via machine learning<br><b>Z. Liu and I.A. Karimi</b>   | 116627 |  |        |

CONTENTS— continued on Back Matter



CONTENTS– continued from inside back cover

An experimental examination of the effects of *n*-hexane and *n*-heptane fuel blends on combustion, performance and emissions characteristics in a HCCI engine

**B. Aydoğan**

Co-gasification of biomass blends: Performance evaluation in circulating fluidized bed gasifier

**D. Mallick, P. Mahanta and V.S. Moholkar**

Coordinated allocation of distributed generation resources and electric vehicle charging stations in distribution systems with vehicle-to-grid interaction

**L. Luo, Z. Wu, W. Gu, H. Huang, S. Gao and J. Han**

Flexible power and hydrogen production: Finding synergy between CCS and variable renewables

**S. Cloete and L. Hirth**

Modeling condensate throttling to improve the load change performance of cogeneration units

**Z. Han and P. Xiang**

Achievement in ultra-low-load combustion stability for an anthracite- and down-fired boiler after applying novel swirl burners: From laboratory experiments to industrial applications

**Q. Wang, Z. Chen, L. Li, L. Zeng and Z. Li**

Spatiotemporal analysis of industrial excess heat supply for district heat networks in Switzerland

**J. Chambers, S. Zuberi, M. Jibran, K. Narula and M.K. Patel**

Support schemes adapting district energy combined heat and power for the role as a flexibility provider in renewable energy systems

**A.N. Andersen and P.A. Østergaard**

Feasibility study on the year-round operation of PCM based free cooling systems in tropical climatic conditions

**K. Panchabikesan, M.M. Joybari, F. Haghighat, V. Ramalingam and Y. Ding**

Entropy and exergy analysis of an internally-cooled membrane liquid desiccant dehumidifier

**C.-H. Liang, N.-F. Li and S.-M. Huang**

Robust operation of a multicarrier energy system considering EVs and CHP units

**H. Zafarani, S.A. Taher and M. Shahidehpour**

Optimized energy management strategy for grid connected double storage (pumped storage-battery) system powered by renewable energy resources

**A.M. Abdelshafy, J. Jurasz, H. Hassan and A.M. Mohamed**

Power load demand response potential of secondary sectors in China: The case of western Inner Mongolia

**Y. Pang, Y. He, J. Jiao and H. Cai**

Load response potential evaluation for distribution networks: A hybrid decision-making model with intuitionistic normal cloud and unknown weight information

**P. Du, Z. Chen and X. Gong**

Risk evaluation and retail electricity pricing using downside risk constraints method

**T. Deng, W. Yan, S. Nojavan and K. Jemsittiparsert**

Reducing emission of NO<sub>x</sub> and SO<sub>x</sub> precursors while enhancing char production from pyrolysis of sewage sludge by torrefaction pretreatment

**A. Zheng, L. Li, N. Tippayawong, Z. Huang, K. Zhao, G. Wei, Z. Zhao and H. Li**

Techno-economic performance study of stand-alone wind/diesel/battery hybrid system with different battery technologies in the cold region of China

**C. Li, D. Zhou, H. Wang, Y. Lu and D. Li**

Hydrogen storage properties and cycling degradation of single-phase La<sub>0.60</sub>R<sub>0.15</sub>Mg<sub>0.25</sub>Ni<sub>3.45</sub> alloys with A<sub>2</sub>B<sub>7</sub>-type superlattice structure

**J. Liu, H. Cheng, S. Han, H. Liu and J. Huot**

Effect of rapid combustion on engine performance and knocking characteristics under different spark strategy conditions

**L. Chen, J. Pan, C. Liu, G. Shu and H. Wei**

Drying of untreated *Musa nendra* and *Momordica charantia* in a forced convection solar cabinet dryer with thermal storage

**K.R. Arun, G. Kunal, M. Srinivas, C.S.S. Kumar, M. Mohanraj and S. Jayaraj**

Cooperation or rivalry? Impact of alternative development pathways on India's long-term electricity generation and associated water demands

**V. Chaturvedi, P.N. Koti, R. Sugam, K. Neog and M. Hejazi**

Performance and emission analysis of a dual fuel variable compression ratio (VCR) CI engine utilizing producer gas derived from walnut shells

**M. Sharma and R. Kaushal**

Mitigation of high pressure rise rate by varying IVC timing and EGR rate in an RCCI engine with high premixed fuel ratio

**J. Li, X. Yu, J. Xie and W. Yang**

CONTENTS– continued on Next Page



# Reducing emission of NO<sub>x</sub> and SO<sub>x</sub> precursors while enhancing char production from pyrolysis of sewage sludge by torrefaction pretreatment



Anqing Zheng<sup>a, b, c</sup>, Luwei Li<sup>a, b, c</sup>, Nakorn Tippayawong<sup>d</sup>, Zhen Huang<sup>a, b, c</sup>,  
Kun Zhao<sup>a, b, c, \*</sup>, Guoqiang Wei<sup>a, b, c, \*\*</sup>, Zengli Zhao<sup>a, b, c</sup>, Haibin Li<sup>a, b, c</sup>

<sup>a</sup> Guangzhou Institute of Energy Conversion, Chinese Academy of Sciences, Guangzhou, 510640, PR China

<sup>b</sup> CAS Key Laboratory of Renewable Energy, Guangzhou, 510640, PR China

<sup>c</sup> Guangdong Provincial Key Laboratory of New, Renewable Energy Research and Development, Guangzhou, 510640, PR China

<sup>d</sup> Department of Mechanical Engineering, Chiang Mai University, Chiang Mai, 50200, Thailand

## ARTICLE INFO

### Article history:

Received 29 August 2019

Received in revised form

5 November 2019

Accepted 23 November 2019

Available online 29 November 2019

### Keywords:

Torrefaction

Sewage sludge

Pyrolysis behaviors

NO<sub>x</sub> and SO<sub>x</sub> precursors

Char

## ABSTRACT

This study aims to explore the possibility of reducing emission of NO<sub>x</sub> and SO<sub>x</sub> precursors while enhancing char production from pyrolysis of sewage sludge by torrefaction pretreatment. The influence of torrefaction severity on structural alterations of sewage sludge and resulting pyrolysis behaviors was systematically studied. The experimental results show that 33.3% of N and 52.8% of S in sewage sludge can be removed by torrefaction pretreatment, leading to the evident reduction in the emission of NO<sub>x</sub> and SO<sub>x</sub> precursors (e.g. NH<sub>3</sub>, HCNO, H<sub>2</sub>S, COS and CS<sub>2</sub>) during subsequent pyrolysis of torrefied sewage sludge. Moreover, the yield and specific surface area of char from pyrolysis of sewage sludge can be improved by torrefaction. The char obtained from pyrolysis of sewage sludge torrefied at 300 °C exhibited the highest yield of 61.0 wt% and the maximum BET surface areas of 26.5 m<sup>2</sup>/g. These results could be ascribed to the devolatilization, polycondensation and charring of sewage sludge during torrefaction to form torrefied sewage sludge with stable aromatic and heterocyclic structure. These findings suggest that torrefaction is an effective pretreatment method prior to pyrolysis of sewage sludge for reducing emission of NO<sub>x</sub> and SO<sub>x</sub> precursors while enhancing yield and specific surface area of char.

© 2019 Elsevier Ltd. All rights reserved.

## 1. Introduction

Sewage sludge is a byproduct generated from municipal wastewater treatment plants. The production of sewage sludge has been sharply increased owing to enhanced handling capacity of wastewater caused by rapidly growing urban populations and stringent environmental regulation [1]. In China, the production of sewage sludge with a moisture content of 80% is approximately 35 million tons from about 4000 municipal wastewater treatment plants in 2015 [1]. Sewage sludge mainly contains moisture, proteins, lipids, carbohydrates, nucleic acids, detergents, phenols and

ash, as well as harmful substances, such as pathogens, heavy metals, polychlorinated biphenyls and dioxins. The release of large quantities of sewage sludge into the environment has been considered as one of the most challenging issues [2]. Increasingly stringent environmental regulations have forced the industries to seek efficient technologies for sewage sludge disposal [3]. Many methods have been adopted to dispose sewage sludge, including landfilling, composting and incineration [4]. Currently, landfilling and composting are the main disposal methods for sewage sludge in China, accounting for about 60–65% and 10–15% of the total amounts of sewage sludge, respectively [1]. Landfilling and composting of sewage sludge can result in serious environmental issues, such as spread of pathogens, transferring leachate and heavy metals to soil and groundwater, and uncontrolled release of CH<sub>4</sub> [5,6]. Thermochemical conversion of sewage sludge (pyrolysis, gasification and incineration) appears to be the most promising method for solving these issues [7,8]. Among them, pyrolysis of sewage sludge has received great attentions since it can

\* Corresponding author. Guangzhou Institute of Energy Conversion, Chinese Academy of Sciences, Guangzhou, 510640, PR China.

\*\* Corresponding author. Guangzhou Institute of Energy Conversion, Chinese Academy of Sciences, Guangzhou, 510640, PR China.

E-mail addresses: [zhaokun@ms.giec.ac.cn](mailto:zhaokun@ms.giec.ac.cn) (K. Zhao), [weigq@ms.giec.ac.cn](mailto:weigq@ms.giec.ac.cn) (G. Wei).

simultaneously provide solid, liquid and gaseous products at the lowest cost [9–11]. However, the high content of nitrogen and sulfur in sewage sludge can result in the formation of large amounts of  $\text{NO}_x$  and  $\text{SO}_x$  precursors, such as  $\text{NH}_3$ ,  $\text{HCN}$ ,  $\text{H}_2\text{S}$  and  $\text{COS}$ , during pyrolysis of sewage sludge. These  $\text{NO}_x$  and  $\text{SO}_x$  precursors could be further converted into  $\text{NO}_x$ ,  $\text{N}_2\text{O}$ , and  $\text{SO}_x$  after being combusted, which are responsible for the formation of acid rain, photochemical smog, tropospheric ozone, the enhancement of greenhouse effects, and the increased depletion of stratospheric ozone [12,13]. In addition, considering the inherent drawbacks of sewage sludge, such as low bulk density, high moisture content, hydrophilic nature, and heterogeneous composition, It is necessary to develop a promising pretreatment method to achieve the clean and efficient pyrolytic disposal of sewage sludge [14].

Torrefaction is a thermal pretreatment method which is carried out at a temperature range of 200–320 °C under an oxygen-free atmosphere [15–23]. Torrefaction is typically applied to lignocellulosic biomass for improving its unfavorable properties, such as low bulk density, high moisture content, hydrophilic nature, tenacious and fibrous structure, and heterogeneous composition, thus providing technical and economic benefits for grinding, storage, transportation, feed handling and conversion of lignocellulosic biomass [24–27]. Our previous works demonstrated that torrefaction can effectively promote the char yield from fast pyrolysis of biomass [20,28]. Torrefaction can also serve as an effective pretreatment method applied to sewage sludge. The pioneering works by Atienza-Martínez et al. showed that the grindability, energy density and higher heating value of sewage sludge was improved by torrefaction [29]. They also found that torrefaction reduced the yields of water and the liquid aqueous phase in subsequent fast pyrolysis of torrefied sewage sludge [14]. Oh et al. demonstrated that the chemical exergy and carbon content of sewage sludge were enhanced by torrefaction and the optimal torrefaction temperature was 250–300 °C [30]. Chen et al. developed a nonisothermal torrefaction kinetic of sewage sludge using the simplified distributed activation energy model [31]. Chiueh et al. found that there was a synergistic effect during microwave co-torrefaction of sewage sludge and *Leucaena* [32].

However, to date, the existing literatures have mostly focused on the effect of torrefaction severity on the physicochemical properties of sewage sludge. The structural alterations of torrefied sewage sludge and resulting pyrolysis behaviors, particularly the formation of  $\text{NO}_x$  and  $\text{SO}_x$  precursors and char from pyrolysis of torrefied sewage sludge, have not been vigorously discussed. In the present study, the effect of torrefaction severity, as well as the structural alterations of sewage sludge, on the formation of volatile products, char and  $\text{NO}_x$  and  $\text{SO}_x$  precursors from pyrolysis of torrefied sewage sludge were systematically studied.

## 2. Experimental section

### 2.1. Torrefaction of sewage sludge

Sewage sludge was obtained from Datansha wastewater treatment plant in Guangzhou, P. R. China. Prior to experiments, sewage sludge was crushed to a particle size of 0.18–0.25 mm, and then dried at 105 °C for 36 h until it reached a constant weight. Torrefaction of sewage sludge was carried out in a fixed bed reactor (as shown in Fig. 1). Sewage sludge was torrefied at different torrefaction temperature (240–320 °C) with a constant residence time of 40 min under inert atmosphere.

### 2.2. Characterization of untreated and torrefied sewage sludge

The proximate analysis of untreated and torrefied sewage

sludge was performed in a muffle furnace according to the method in the national standard (GB/T28731–2012). The elemental analysis (C, H, N and S) of untreated and torrefied sewage sludge was conducted on an elemental analyzer (Vario EL, Elementar Analysensysteme GmbH, Germany). The higher heating value (HHV) of untreated and torrefied sewage sludge was measured by using a bomb calorimeter (WZR-1T-CII, Changsha Bente, China). The structural alterations of sewage sludge before and after torrefaction was characterized by a solid-state nuclear magnetic resonance (NMR) spectrometer (Ascend™ 300WB, Bruker, Germany). The relative energy density and energy yield of torrefied sewage sludge were calculated as follows:

$$\text{The relative energy density} = \frac{\text{HHV of torrefied sewage sludge}}{\text{HHV of untreated sewage sludge}} \quad (1)$$

$$\begin{aligned} \text{The energy yield} &= \text{Mass yield of torrefied sewage sludge} \\ &\times \frac{\text{HHV of torrefied sewage sludge}}{\text{HHV of untreated sewage sludge}} \end{aligned} \quad (2)$$

The removal efficiency of N or S was calculated as follows:

$$\begin{aligned} \text{The removal efficiency of N or S} &= 100\% \\ &- \frac{\text{Mass yield of torrefied sewage sludge}}{\text{N or S content of torrefied sewage sludge}} \\ &\times \frac{\text{N or S content of untreated sewage sludge}}{\text{N or S content of untreated sewage sludge}} \end{aligned} \quad (3)$$

### 2.3. Pyrolysis of untreated and torrefied sewage sludge

The pyrolysis behaviors of untreated and torrefied sewage sludge were examined in a thermogravimetric analyzer (STA449F3, Netzsch, Germany) coupled with a Fourier transform infrared spectrophotometer (Tensor 27, Bruker Optik, Germany) and a mass spectrometer (MS) (OmniStar™, Pfeiffer Vacuum, Germany) (TG-

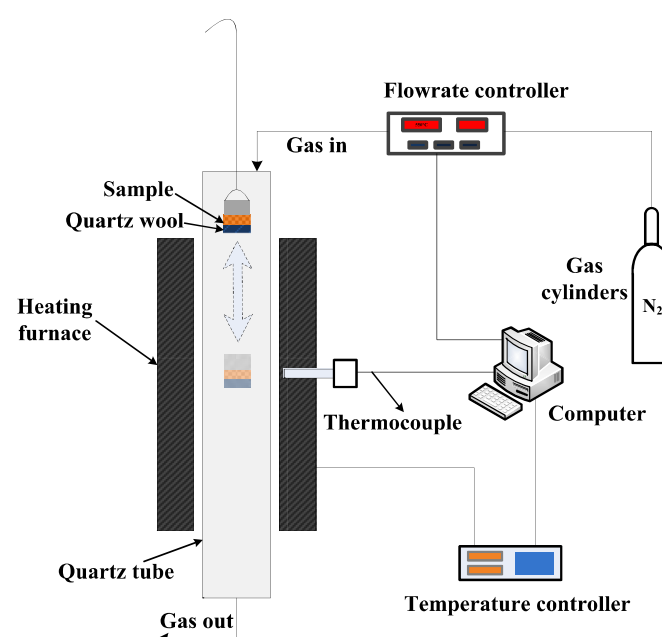


Fig. 1. Schematic diagram of the fixed bed reactor for torrefaction of sewage sludge.

FTIR-MS). The sample (About 10 mg) was heated from 30 to 900 °C at a heating rate of 10 °C/min. High-purity argon was used as carrier gas with a flow rate of 40 ml/min. The fast pyrolysis of untreated and torrefied sewage sludge was performed in a semibatch pyroprobe reactor (CDS 5200, Oxford, USA) coupled with a 7890A gas chromatograph and a 5975C mass spectrometer (Agilent Technologies, USA) (Py-GC-MS). The samples were accurately weighed and subsequently pyrolyzed at 500 °C with a heating rate of 10 °C/ms and a residence time of 20 s. The GC column was an Agilent J&W DB-1701. The char from pyrolysis of untreated and torrefied sewage sludge at a reaction temperature of 500 or 600 °C with a residence time of 60 min was conducted in the same fixed bed reactor mentioned above. The yield of char from pyrolysis of torrefied sewage were based on the mass of untreated sewage sludge used (dry basis). The textural properties of char obtained from pyrolysis of torrefied sewage sludge were determined by N<sub>2</sub> adsorption at 77.35 K on an Autosorb-iQ2 instrument (Quantachrome, USA). The carbon content of char was conducted on an elemental analyzer (Vario EL, Elementar Analysensysteme GmbH, Germany).

### 3. Results and discussion

#### 3.1. Characterization of untreated and torrefied sewage sludge

To determine the effect of torrefaction on the physicochemical properties of sewage sludge, the mass and energy yields, ultimate and proximate analysis and the higher heating value (HHV) of torrefied sewage sludge were measured and compared with those of untreated sewage sludge. Fig. 2A and B shows the mass yields, relative energy densities and energy yields of torrefied sewage sludge as a function of torrefaction temperature. As the torrefaction temperature increased from 240 to 320 °C, the mass yields of torrefied sewage sludge decreased steadily from 86.30 to 76.30%, while the relative energy densities and energy yields of torrefied sewage sludge declined gradually. During torrefaction, sewage sludge predominantly underwent devolatilization reactions, including dehydration, decarbonylation, decarboxylation, depolymerization and cracking reactions [33]. The van krevelen diagram of untreated and torrefied sewage sludge is presented in Fig. 2C. It is found that both the atomic O/C and H/C ratios of torrefied sewage sludge dropped consistently with increasing torrefaction temperature. The atomic H/C ratio of torrefied sewage was a linearly increasing function of its atomic O/C ratio. The results indicate that dehydration was the dominant reaction during torrefaction of sewage sludge. Atienza-Martínez reported that water was the major liquid product from torrefaction of sewage sludge [34]. Fig. 2D gives the removal efficiency of N, S in sewage sludge by torrefaction pretreatment. The contents of N and S in untreated sewage sludge were 3.97 and 0.61 wt%, respectively. As torrefaction increased from 240 to 320 °C, the removal efficiency of N, S increased continuously, indicating that the N and S-containing fractions in sewage sludge can be effectively removed by torrefaction. The results were in line with those reported in literature [14]. When the torrefaction temperature reached 320 °C, the removal efficiency of N and S achieved the maximum value of 33.3 and 52.8 wt%, respectively. The proximate analysis of untreated and torrefied sewage sludge is shown in Fig. 2E. The proximate analysis show that the content of fixed carbon and ash increased, whereas the content of volatile matter declined with the increase in torrefaction temperature. These results are caused by the release of organic matter during torrefaction of sewage sludge. The higher heating value of untreated and torrefied sewage sludge is shown in Fig. 2F. The higher heating value of torrefied sewage sludge gradually dropped with increasing torrefaction temperature. The HHV

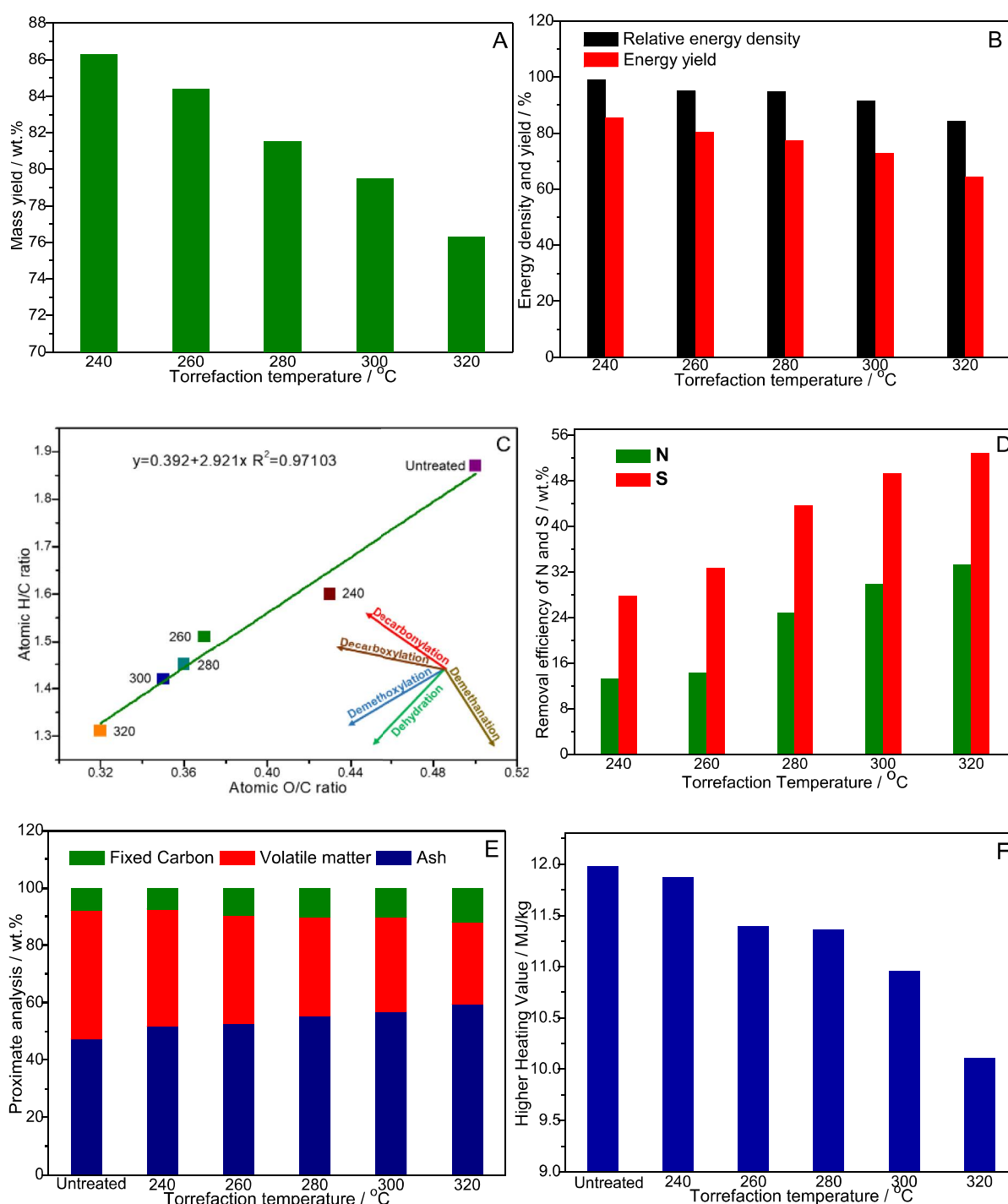
decreased from 12.0 MJ/kg for untreated sewage sludge to 10.1 MJ/kg for that torrefied at 320 °C. The reduction in HHV is mainly ascribed to the release of volatile matter and the preservation of ash during torrefaction of sewage sludge.

To investigate the structural alterations of sewage sludge before and after torrefaction, the structure of untreated and torrefied sewage sludge was characterized by solid <sup>13</sup>C NMR. As shown in Fig. 3, it is evident that the structure of sewage sludge was altered significantly by torrefaction. The peak at 160–185 ppm is attributed to the carbonyl carbons in carboxylic acids, esters and amide [35]. These carbonyl carbons in sewage sludge mainly exist in the form of protein, lipid and carbohydrate. After torrefaction of sewage sludge at 280 and 320 °C, the peak intensity of carbonyl carbons decreased drastically until it completely disappeared. These carbonyl carbons were removed by the thermal decomposition of sewage sludge via decarbonylation, decarboxylation, deacetylation and so on. The peak at 145–160 ppm is ascribed to the carbons in oxygen or nitrogen substituted aromatic rings [35]. And the peak at 112–145 ppm is associated with the carbons in aromatic rings. The peak at 50–110 ppm is related to the oxygen or nitrogen substituted aliphatic carbons [35]. Among them, the peak centered at around 78 ppm is assigned to the carbons in carbohydrates. As increasing torrefaction severity, the peak intensity of the oxygen or nitrogen substituted aliphatic carbons decreased obviously until it disappeared, whereas the significant increase was observed in the peak intensity of the carbons in carbon, oxygen or nitrogen substituted aromatic rings. These results suggest that the oxygen or nitrogen substituted aliphatic carbons in sewage sludge underwent severe devolatilization, polycondensation and charring reactions during torrefaction to significantly improve the content of aromatic and heterocyclic carbons in torrefied sewage sludge. The peak at 17–37 ppm is ascribed to the carbons in CH<sub>2</sub> and CH<sub>3</sub> [35,36]. Its peak intensity first increased at the torrefaction temperature of 280 °C, and then declined at the torrefaction temperature of 320 °C. The increase in its peak intensity might be due to the increasing content of CH<sub>2</sub> and CH<sub>3</sub> attached to aromatic ring caused by the polycondensation and charring of sewage sludge during torrefaction. The decrease in its peak intensity might be attributed to the thermal scission of CH<sub>2</sub> and CH<sub>3</sub> at the torrefaction temperature of 320 °C.

#### 3.2. TG-FTIR-MS analysis of untreated and torrefied sewage sludge

To compare the pyrolysis behaviors of untreated and torrefied sewage sludge, the thermal decomposition of untreated and torrefied sewage sludge under inert atmosphere was investigated by TGA. The weight loss (TG) curves and weight loss rate (DTG) curves for the pyrolysis of untreated and torrefied sewage sludge are illustrated in Fig. 4. It can be seen that the devolatilization of sewage sludge was mainly taken place in the temperature range of 150–600 °C. The sharp peak centered at 150–400 °C is mainly ascribed to the devolatilization of biodegradable organic matter in sewage sludge [37]. The shoulder peak centered at 400–600 °C is predominantly attributed to the decomposition of non-biodegradable organic matter in sewage sludge [37]. As torrefaction temperature increased from 240 to 320 °C, the intensity of first sharp peak declined and its peak temperature shifted to higher temperature. The first peak finally merged with the shoulder peak, and the intensity of the shoulder peak increased gradually, indicating that, during torrefaction of sewage sludge, the biodegradable organic matter proceeded serious devolatilization and polycondensation reactions to form non-biodegradable organic matter with stable aromatic and heterocyclic structure.

The characteristic parameters obtained from TG/DTG curves are tabulated in Table 1. The initial pyrolysis temperature for sewage



**Fig. 2.** Characterization of untreated and torrefied sewage sludge on dry basis. A: the mass yields of torrefied sewage sludge obtained at different torrefaction temperature, B: the relative energy density and energy yields of torrefied sewage sludge obtained at different torrefaction temperature, C: the van Krevelen diagram of untreated and torrefied sewage sludge, D: the removal efficiency of N, S at different torrefaction temperature, E: the proximate analysis of untreated and torrefied sewage sludge, F: the higher heating value of untreated and torrefied sewage sludge.

sludge was obviously improved by torrefaction. It increased gradually with elevating torrefaction temperature, whereas the maximum weight loss rate for sewage sludge decreased steadily. At the same time, the temperature ( $T_{max}$ ) corresponding to the maximum weight loss rate was progressively shifted to higher temperature. Hence, the comprehensive pyrolysis index of sewage sludge was reduced by torrefaction. The reduction in the

comprehensive pyrolysis index indicated that the torrefied sewage sludge were decomposed more slowly and hardly when compared with untreated sewage sludge. These results suggest that torrefaction played negative roles on the pyrolysis reactivity of sewage sludge.

To investigate the effect of torrefaction on the evolution of N and S-containing compounds and permanent gases from pyrolysis of



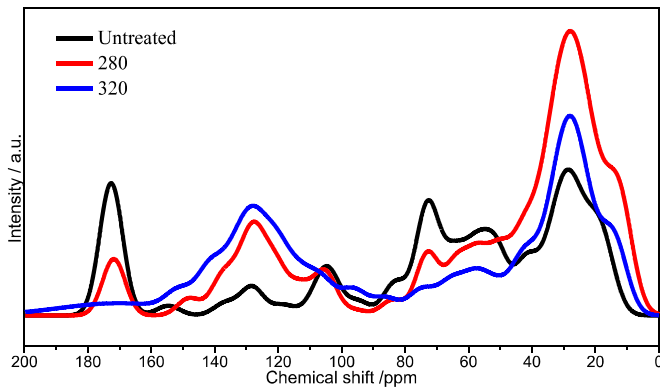


Fig. 3. Solid-state  $^{13}\text{C}$  NMR spectra of untreated and torrefied sewage sludge obtained at different torrefaction temperature.

sewage sludge, the volatile products from pyrolysis of untreated and torrefied sewage sludge was online-monitored by FTIR and MS. The 3D FTIR spectra for the release of volatile products from pyrolysis of untreated and torrefied sewage sludge are drawn in Fig. 5A–E. FTIR spectra for the evolution of volatile products from pyrolysis of untreated and torrefied sewage sludge at the maximum weight loss peak are given in Fig. 5F. The characteristic absorption bands at  $4000\text{--}3400\text{ cm}^{-1}$ ,  $3050\text{--}2650\text{ cm}^{-1}$ ,  $2400\text{--}2240\text{ cm}^{-1}$ , and  $2230\text{--}2000\text{ cm}^{-1}$  are assigned to  $\text{H}_2\text{O}$ ,  $\text{CH}_4$ ,  $\text{CO}_2$ , and  $\text{CO}$ , respectively. And the bands at  $1890\text{--}1630\text{ cm}^{-1}$  are related to  $\text{C=O}$  stretching in organic acids, ketones, and aldehydes [38]. It is obvious that the intensity of most of the bands decreased with increasing torrefaction temperature. The N and S-containing compounds from pyrolysis, such as  $\text{NH}_3$ ,  $\text{HCN}$ ,  $\text{H}_2\text{NCN}$ ,  $\text{H}_2\text{S}$ ,  $\text{COS}$  and  $\text{CS}_2$ , has been considered as  $\text{NO}_x$  and  $\text{SO}_x$  precursors. The

evolution profiles of N and S-containing compounds from pyrolysis of untreated and torrefied sewage sludge are drawn in Fig. 6. Nitrogen in the sewage sludge predominantly exists in the form of amine-N, protein-N, pyrrolic-N and pyridinic-N. During pyrolysis of sewage sludge, the major N-containing compounds were  $\text{NH}_3$ ,  $\text{HCN}$ ,  $\text{HCNO}$  and  $\text{H}_2\text{NCN}$ , which had the characteristic peak centered at  $963$ ,  $714$ ,  $2274$  and  $2251\text{ cm}^{-1}$ , respectively [39–41].  $\text{NH}_3$  was produced by the decomposition of ammonium salts and amine-N in sewage sludge.  $\text{HCNO}$  and  $\text{H}_2\text{NCN}$  were mainly produced from protein-N and other N-containing organic matter in sewage sludge. It is observed that the peak intensity of  $\text{NH}_3$ ,  $\text{HCNO}$  and  $\text{H}_2\text{NCN}$  was effectively reduced by torrefaction. And their peak intensity dropped steadily with increasing torrefaction temperature. During torrefaction, the decomposition of ammonium salts, amine-N and protein-N occurred, resulting in the reduction in the emission of  $\text{NH}_3$ ,  $\text{HCNO}$  and  $\text{H}_2\text{NCN}$  during subsequent pyrolysis of torrefied sewage sludge. However, the peak intensity of  $\text{HCN}$  exhibited opposite trends. Its peak intensity was promoted by torrefaction.  $\text{HCN}$  is predominantly obtained from the pyrolysis of nitrile-N or heterocyclic-N. It is inferred that polycondensation of amine-N, protein-N, pyrrolic-N and pyridinic-N during torrefaction can lead to the formation of the aromatic nitrile-N and heterocyclic-N in torrefied sewage sludge. The S-containing compounds from pyrolysis of untreated and torrefied sewage sludge contained  $\text{H}_2\text{S}$ ,  $\text{CS}_2$ ,  $\text{COS}$  and  $\text{SO}_2$ , which had the characteristic peak centered at  $2703$ ,  $1541$ ,  $2072$  and  $1375\text{ cm}^{-1}$ , respectively [40,42].  $\text{CS}_2$ ,  $\text{COS}$  and  $\text{H}_2\text{S}$  were generated from the thermal decomposition of S-containing organic matter (e.g. protein) in sewage sludge.  $\text{SO}_2$  was derived from the thermal cracking of sulfonates and sulfates in sewage sludge. Pyrolysis of torrefied sewage sludge produced less  $\text{H}_2\text{S}$ ,  $\text{CS}_2$ ,  $\text{COS}$  and  $\text{SO}_2$  than untreated sewage sludge. It could be attributed to the pre-decomposition of S-containing organic matter, sulfonates and sulfates during torrefaction of sewage sludge. These results

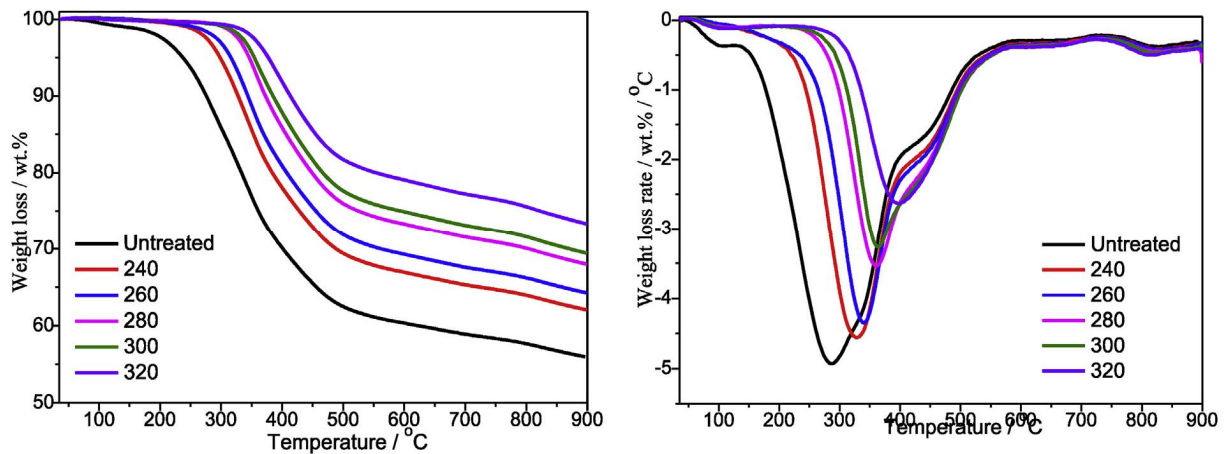


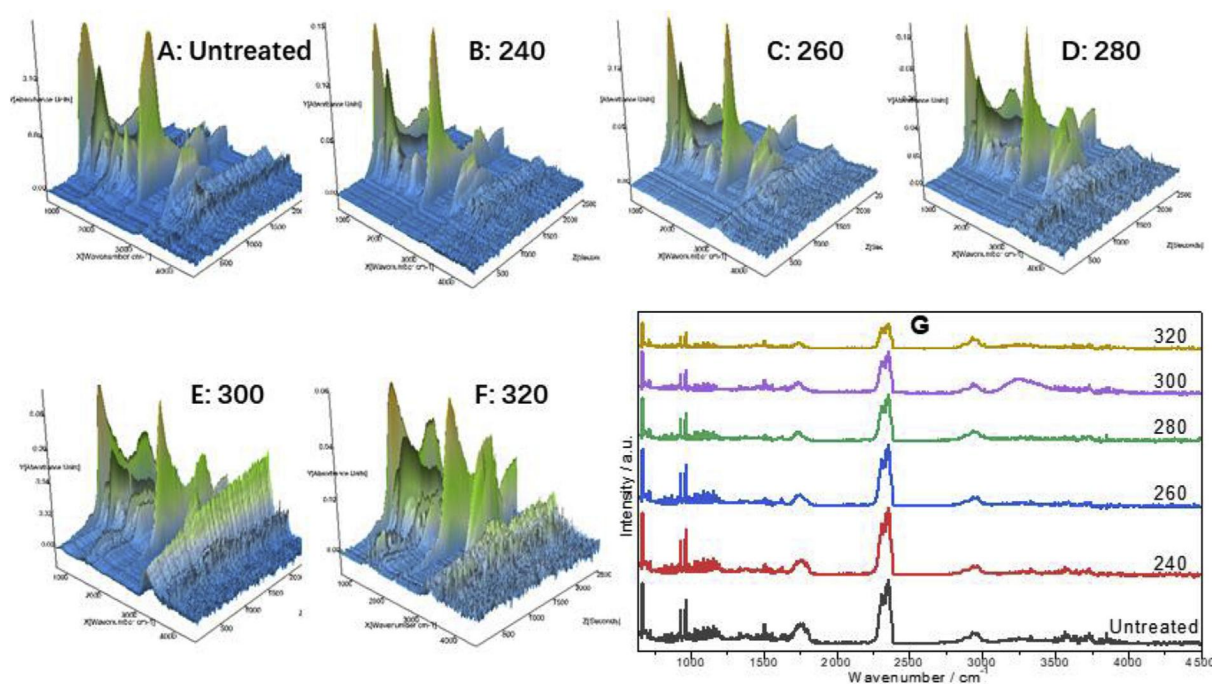
Fig. 4. TG/DTG curves for the pyrolysis of untreated and torrefied sewage sludge obtained at different torrefaction temperature.

Table 1

The characteristic parameters for pyrolysis of untreated and torrefied sewage sludge obtained at different torrefaction temperature.

| Samples   | $T_i/^\circ\text{C}$ | $T_f/^\circ\text{C}$ | $\text{DTG}_{\text{max}}/\text{wt.}\% \cdot \text{min}^{-1}$ | $T_{\text{max}}/^\circ\text{C}$ | $D/10^{-5} \text{ wt.}\% \cdot \text{min}^{-1} \cdot ^\circ\text{C}^{-2}$ |
|-----------|----------------------|----------------------|--|---------------------------------|---|
| Untreated | 135.6                | 581.0                | 4.949  | 286.1                           | 3.88  |
| 240       | 149.5                | 581.1                | 4.557  | 327.6                           | 3.22  |
| 260       | 153.9                | 585.7                | 4.341  | 339.8                           | 2.96  |
| 280       | 215.2                | 611.2                | 3.539  | 359.5                           | 2.49  |
| 300       | 235.9                | 597.4                | 3.254  | 362.9                           | 2.48  |
| 320       | 263.9                | 590.3                | 2.617  | 397.6                           | 2.02  |

$$D = \text{DTG}_{\text{max}} / [T_{\text{max}}(T_f - T_i)].$$



**Fig. 5.** FTIR spectra for the release of volatile products from pyrolysis of untreated and torrefied sewage sludge. A, B, C, D, E, F: 3D FTIR spectra for the release of volatile products from pyrolysis of untreated and torrefied sewage sludge obtained at different torrefaction temperature. G: FTIR spectra for the release of volatile products from pyrolysis of untreated and torrefied sewage sludge at the maximum weight loss peak.

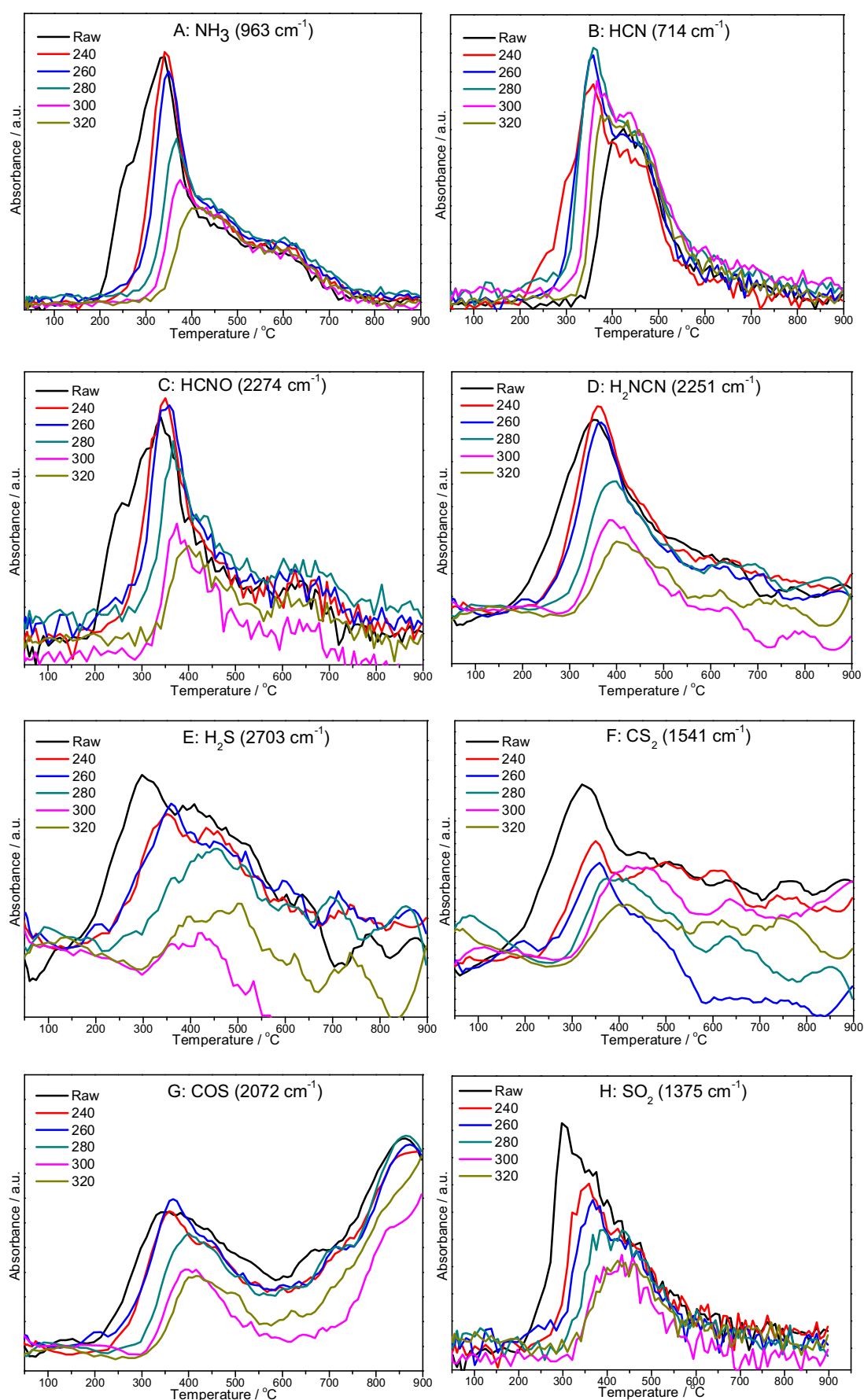
were in line with the increasing removal efficiency of N and S with elevating torrefaction temperature (as shown in Fig. 2D). It can be concluded that torrefaction is an effective pretreatment method to reduce the emission of various  $\text{NO}_x$  and  $\text{SO}_x$  precursors, except HCN.

The evolution profiles of the ions of 18, 16, 44, and 28  $m/z$  corresponding to  $\text{H}_2\text{O}$ ,  $\text{CH}_4$ ,  $\text{CO}_2$  and CO from pyrolysis of untreated and torrefied sewage sludge is plotted in Fig. 7. As shown in Fig. 7A, it is obvious that the first shoulder peak centered at 50–85 °C is related to the evaporation of moisture. The second peak centered at 230–368 °C and the third peak centered at 460 °C are respectively ascribed to the dehydration of biodegradable and non-biodegradable organic matter. The dehydration of bio-degradable organic matter during pyrolysis of untreated sewage sludge reached a maximum peak intensity at about 230 °C. As elevating torrefaction temperature, its peak intensity decreased and its peak temperature shift toward higher temperature. The results could be due to the pre-dehydration reactions associated with the polycondensation and charring of biodegradable organic matter during torrefaction of sewage sludge. It is well accepted that the polycondensation and charring reactions are frequently accompanied by the elimination of water and other small molecules (e.g.  $\text{CH}_4$  and  $\text{CO}_2$ ). It is found that the dehydration of non-biodegradable organic matter was enhanced by torrefaction. Its highest peak intensity was found for torrefied sewage sludge obtained at 280 °C. The polycondensation and charring of biodegradable organic matter during torrefaction can result in the formation of more non-biodegradable organic matter with stable aromatic and heterocyclic structure. The similar trend was also observed for the release of  $\text{CH}_4$ . The release of  $\text{CH}_4$  from pyrolysis of untreated and torrefied sewage sludge is depicted in Fig. 7B. The first shoulder peak centered at 210 °C and the second sharp peak centered at 290–370 °C are attributed to the demethylation of biodegradable organic matter during pyrolysis of untreated and torrefied sewage sludge. After torrefaction, the first shoulder peak disappeared, and the intensity of the second peak

first increased and then decreased gradually with increasing torrefaction severity. These results could be explained by the pre-methylation of biodegradable organic matter during torrefaction of sewage sludge. The peak located at approximately 460 °C is related to the demethylation of non-biodegradable organic matter during pyrolysis of untreated and torrefied sewage sludge. It is worthy of note that its peak intensity was obviously enhanced by torrefaction. The torrefied sewage sludge obtained at 280 °C exhibited the highest peak intensity. These results are consistent with the NMR analysis in Fig. 3. The polycondensation and charring of sewage sludge during torrefaction could cause the increase in the content of  $\text{CH}_3$  attached to aromatic ring, thus resulting in the improvement in the release of  $\text{CH}_4$  at higher temperature. The evolution of  $\text{CO}_2$  from pyrolysis of untreated and torrefied sewage sludge is illustrated in Fig. 7C. The intensity of the first peak declined with elevating torrefaction temperature and its peak temperature shifted toward higher temperature. The reduction in its peak intensity is mainly due to the pre-decarboxylation and polycondensation of biodegradable organic matter during torrefaction of sewage sludge. The maximum peak intensity of the second peak was found for torrefied sewage sludge obtained at 280 °C. The release of CO from pyrolysis of untreated and torrefied sewage sludge is shown in Fig. 7D. The intensities of all peaks were reduced by torrefaction, since sewage sludge underwent pre-decarbonylation and polycondensation reactions during torrefaction.

### 3.3. The organic compounds from fast pyrolysis of untreated and torrefied sewage sludge

To compare the formation of organic compounds from fast pyrolysis of untreated and torrefied sewage sludge, the volatile products from fast pyrolysis of untreated and torrefied sewage sludge was online-analyzed by GC/MS. The major organic compounds obtained from fast pyrolysis of untreated and torrefied



**Fig. 6.** The evolution profiles of N and S-containing compounds from pyrolysis of untreated and torrefied sewage sludge.

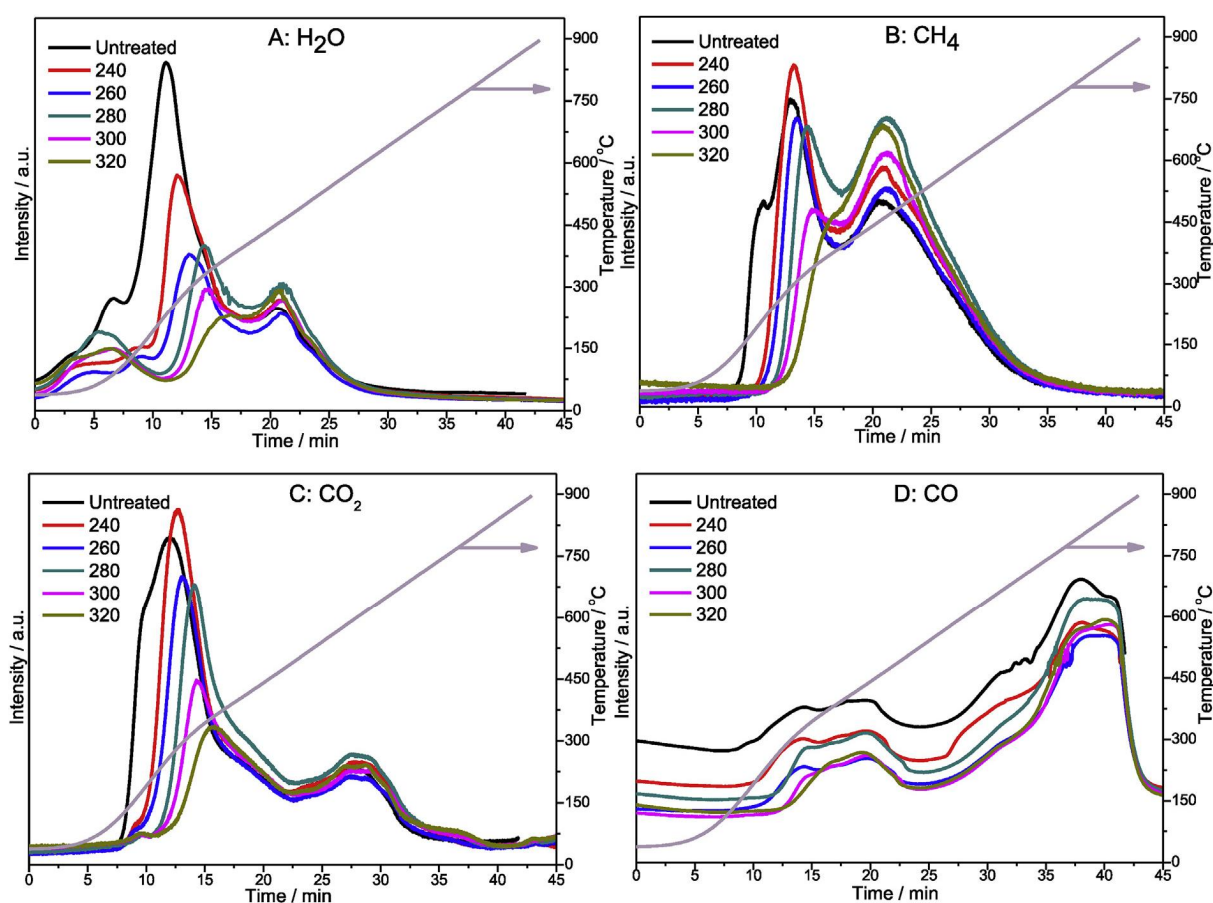


Fig. 7. The evolution profiles of  $\text{H}_2\text{O}$ ,  $\text{CH}_4$ ,  $\text{CO}_2$  and  $\text{CO}$  from pyrolysis of untreated and torrefied sewage sludge.

Table 2

The yields of major organic compounds obtained from fast pyrolysis of untreated and torrefied sewage sludge at 500 °C.

| Compounds                                | Absolute peak area of each compound per mg sample ( $10^6/\text{mg}$ ) |        |        |        |        |        |
|--|--|--------|--------|--------|--------|--------|
|  | Untreated  | 240 °C | 260 °C | 280 °C | 300 °C | 320 °C |
| Acetic acid                              | 2.15   | 1.20   | 0.48   | N.D.   | N.D.   | N.D.   |
| Methanethiol                             | 9.67   | 3.58   | 2.89   | 1.92   | 1.90   | 1.97   |
| Pyrrole                                  | 1.57   | 2.79   | 1.53   | 0.91   | 1.34   | 0.53   |
| Indole                                   | 1.97   | 1.25   | 1.48   | 1.26   | 1.11   | 0.42   |
| Toluene                                  | 2.87   | 2.52   | 2.62   | 2.11   | 3.17   | 0.97   |
| Styrene                                  | 2.35   | 3.08   | 1.57   | 1.07   | 0.88   | 0.72   |
| Naphthalene, 2,6-bis(1,1-dimethylethyl)- | N.D.   | 1.63   | 1.74   | 1.52   | 1.44   | 0.74   |
| Phenol                                   | 1.72   | 1.76   | 1.65   | 1.15   | 1.35   | 0.52   |
| p-Cresol                                 | 2.33   | 2.97   | 2.35   | 1.92   | 2.35   | 1.02   |
| 2,3-Diphenylindole                       | N.D.   | 1.70   | 1.86   | 1.92   | N.D.   | N.D.   |

N.D.: not detected.

Table 3

The characterization of char from pyrolysis of torrefied sewage sludge at 500 and 600 °C.

| Number | Torrefaction temperature/°C | Pyrolysis temperature/°C | Char yield <sup>a</sup> /wt.% | Carbon content/wt.% | BET/(m <sup>2</sup> /g) | Total pore volume/(cm <sup>3</sup> /g) | Average pore size/nm |
|--------|-----------------------------|--------------------------|-------------------------------|---------------------|-------------------------|--|----------------------|
| 1      | 240                         | 500                      | 57.8                          | 16.2                | 13.96                   | 0.10                                   | 13.73                |
| 2      |                             | 600                      | 57.1                          | 16.0                | 14.67                   | 0.10                                   | 14.09                |
| 3      | 260                         | 500                      | 59.3                          | 16.9                | 15.87                   | 0.09                                   | 11.75                |
| 4      |                             | 600                      | 57.9                          | 16.8                | 14.04                   | 0.11                                   | 15.22                |
| 5      | 280                         | 500                      | 60.1                          | 17.0                | 20.27                   | 0.11                                   | 22.33                |
| 6      |                             | 600                      | 57.7                          | 17.9                | 14.05                   | 0.12                                   | 16.65                |
| 7      | 300                         | 500                      | 61.0                          | 16.8                | 26.45                   | 0.10                                   | 7.48                 |
| 8      |                             | 600                      | 58.1                          | 17.1                | 13.66                   | 0.10                                   | 14.68                |
| 9      | 320                         | 500                      | 59.9                          | 17.4                | 19.32                   | 0.11                                   | 11.60                |
| 10     |                             | 600                      | 58.0                          | 17.1                | 16.06                   | 0.10                                   | 12.71                |

<sup>a</sup> The char yield was based on the initial mass of untreated sewage sludge used (dry basis).



sewage sludge at 500 °C are identified and listed in Table 2. Acetic acid was mainly produced by the deacylation of sewage sludge. The result is consistent with the solid NMR analysis. The yield of acetic acid from pyrolysis of sewage sludge decreased when applying torrefaction. And it declined with elevating torrefaction temperature. Acetic acid was not detected when the torrefaction temperature was equal to or greater than 280 °C. These results indicate that the acetyl groups of sewage sludge can be effectively removed by torrefaction. The yields of aromatic and phenolic compounds, such as toluene, styrene, phenol and p-Cresol, from pyrolysis of sewage sludge were reduced by torrefaction. Their lowest yields were obtained at the highest torrefaction temperature of 320 °C. These results suggest that the aromatic and phenolic groups in sewage sludge can be pre-removed during torrefaction. The yields of S and N-containing compounds, such as methanethiol, pyrrole and indole, can also be lowered by torrefaction, indicating that S and N-containing matter can be decomposed during torrefaction. These results were in accordance with the results in Fig. 2D. It should be noted that 2,6-bis(1,1-dimethylethyl)-naphthalene and 2,3-diphenylindole were only found for the fast pyrolysis of torrefied sewage sludge, since sewage sludge underwent polycondensation reactions during torrefaction to yield torrefied sewage sludge with heterocyclic-N and polycyclic aromatic structure, thus resulting in the formation of 2,6-bis(1,1-dimethylethyl)-naphthalene and 2,3-diphenylindole in subsequent fast pyrolysis.

#### 3.4. The char production from pyrolysis of torrefied sewage sludge

The char obtained from pyrolysis of sewage sludge can be used as carbon materials, catalyst supports, absorbents and so on. The physicochemical and textural properties of char produced from pyrolysis of torrefied sewage sludge are shown in Table 3. At the pyrolysis temperature of 500 °C, it is observed that the yield of char first increased with elevating torrefaction temperature, and then decreased. It reached the highest value of 61.0% at the torrefaction temperature of 300 °C. The sewage sludge proceeded devolatilization, polycondensation and charring reactions during torrefaction to form torrefied sewage sludge with more stable aromatic and heterocyclic structure, thus resulting in the improvement in the yield of char and the reduction in the formation of volatile products during subsequent pyrolysis at high temperature. The variation trend of char yield caused by torrefaction was obviously different from that reported in literature [14]. Atienza-Martínez reported that torrefaction had no significant effect on the yield of char from fast pyrolysis of sewage sludge. The textural properties of char, such as BET surface area, total pore volume and average pore size, were significantly influenced by the torrefaction temperature. As the torrefaction temperature increased from 240 to 300 °C, the BET surface area of char increased gradually with elevating torrefaction temperature. When the torrefaction temperature further increased from 300 to 320 °C, the BET surface area of char started to decrease. The char obtained from pyrolysis of sewage sludge torrefied at 300 °C exhibited the maximum BET surface areas of 26.5 m<sup>2</sup>/g and the minimum average pore size of 7.5 nm. It is inferred that the moderate devolatilization of sewage sludge during torrefaction was beneficial for the formation of micropores and mesopores in char when the torrefaction temperature was less than 300 °C. However, the severe torrefaction of sewage sludge at 320 °C caused the collapse of the structure of micropores and mesopores in sewage sludge, resulting in the increase in the average pore size of char from pyrolysis of sewage sludge at 500 °C. These results suggest that the yield and surface area of char from pyrolysis of sewage sludge can be promoted by torrefaction. As the pyrolysis temperature of torrefied sewage sludge increased from 500 to 600 °C, the char yield, carbon content and BET surface area

decreased, indicating that higher pyrolysis temperatures can cause the further decomposition of char as well as the collapse of pore structure.

#### 4. Conclusion

As the torrefaction temperature increased from 240 to 320 °C, the mass yields of torrefied sewage sludge decreased steadily from 86.30 to 76.30%. And up to 33.3% of N and 52.8% of S in sewage sludge were removed by torrefaction pretreatment. By comparing the pyrolysis behaviors of untreated and torrefied sewage sludge, it is found that the formation of H<sub>2</sub>O, CH<sub>4</sub>, CO<sub>2</sub> and CO from the decomposition of biodegradable organic matter decreased as increasing torrefaction temperature, whereas the formation of H<sub>2</sub>O, CH<sub>4</sub> and CO<sub>2</sub> from the cracking of non-biodegradable organic matter was promoted by torrefaction. Moreover, the emission of NO<sub>x</sub> and SO<sub>x</sub> precursors (e.g. NH<sub>3</sub>, HCNO, H<sub>2</sub>S, COS, CS<sub>2</sub>, methanethiol, pyrrole and indole) from pyrolysis of sewage sludge was evidently reduced by torrefaction. These results could be ascribed to the devolatilization and polycondensation, and charring of biodegradable organic matter during torrefaction of sewage sludge to form non-biodegradable organic matter with stable aromatic and heterocyclic structure. As increasing torrefaction temperature, the yield and BET surface area of char from pyrolysis of sewage sludge first increased gradually and then decreased. The char obtained from pyrolysis of sewage sludge torrefied at 300 °C exhibited the highest yield of 61.0%, the maximum BET surface areas of 26.5 m<sup>2</sup>/g and the minimum average pore size of 7.5 nm. These results suggest that torrefaction can serve as an effective pretreatment method prior to pyrolysis of sewage sludge for reducing emission of NO<sub>x</sub> and SO<sub>x</sub> precursors and enhancing char production. The quantitative analyses of the liquid and gaseous products, including the concentrations of various NO<sub>x</sub> and SO<sub>x</sub> precursors, from pyrolysis of untreated and torrefied sewage sludge were not provided in this manuscript. We will consider it in our next study.

#### Acknowledgements

The authors acknowledge the Major International (Regional) Joint Research Project of the National Natural Science Foundation of China (Grant 51661145011), National Natural Science Foundation of China (Grants 51776209, 51876208 and 51606204), National Key R&D Program of China (Grant 2017YFE0124200), Science and Technology Planning Project of Guangdong Province, China (Grants 2014B020216004 and 2015A020215024), Youth Innovation Promotion Association, CAS (2018383), and Pearl River S&T Nova Program of Guangzhou (Grant 201806010061) for their financial supports of this work.

#### Appendix A. Supplementary data

Supplementary data to this article can be found online at <https://doi.org/10.1016/j.energy.2019.116620>.

#### References

- [1] Sun S-J, Zhao Z-B, Li B, Ma L-X, Fu D-L, Sun X-Z, et al. Occurrence, composition profiles and risk assessment of polycyclic aromatic hydrocarbons in municipal sewage sludge in China. *Environ Pollut* 2019;245:764–70.
- [2] Zandi S, Nemati B, Jahaniannard D, Davarazar M, Sheikhnajad Y, Mostafaie A, et al. Industrial biowastes treatment using membrane bioreactors (MBRs) - a scientometric study. *J Environ Manag* 2019;247:462–73.
- [3] Kamali M, Costa ME, Aminabhavi TM, Capela I. Sustainability of treatment technologies for industrial biowastes effluents. *Chem Eng J* 2019;370: 1511–21.
- [4] Yang G, Zhang G, Wang H. Current state of sludge production, management, treatment and disposal in China. *Water Res* 2015;78:60–73.



- [5] Kim J-H, Oh J-I, Lee J, Kwon EE. Valorization of sewage sludge via a pyrolytic platform using carbon dioxide as a reactive gas medium. *Energy* 2019;179:163–72.
- [6] Matsakas L, Gao Q, Jansson S, Rova U, Christakopoulos P. Green conversion of municipal solid wastes into fuels and chemicals. *Electron J Biotechnol* 2017;26:69–83.
- [7] Naqvi SR, Tariq R, Hameed Z, Ali I, Naqvi M, Chen W-H, et al. Pyrolysis of high ash sewage sludge: kinetics and thermodynamic analysis using Coats-Redfern method. *Renew Energy* 2019;131:854–60.
- [8] Feng Y, Yu T, Chen D, Xu G, Wan L, Zhang Q, et al. Effect of hydrothermal treatment on the steam gasification behavior of sewage sludge: reactivity and nitrogen emission. *Energy Fuel* 2018;32(1):581–7.
- [9] Inguanzo M, Domínguez A, Menéndez JA, Blanco CG, Pis JJ. On the pyrolysis of sewage sludge: the influence of pyrolysis conditions on solid, liquid and gas fractions. *J Anal Appl Pyrolysis* 2002;63(1):209–22.
- [10] Fonts I, Gea G, Azuara M, Abrego J, Arauzo J. Sewage sludge pyrolysis for liquid production: a review. *Renew Sustain Energy Rev* 2012;16(5):2781–805.
- [11] Lin Y, Liao Y, Yu Z, Fang S, Ma X. A study on co-pyrolysis of bagasse and sewage sludge using TG-FTIR and Py-GC/MS. *Energy Convers Manag* 2017;151:190–8.
- [12] Chen H, Namioka T, Yoshikawa K. Characteristics of tar, NOx precursors and their absorption performance with different scrubbing solvents during the pyrolysis of sewage sludge. *Appl Energy* 2011;88(12):5032–41.
- [13] Liu H, Zhang Q, Hu H, Xiao R, Li A, Qiao Y, et al. Dual role of conditioner CaO in product distributions and sulfur transformation during sewage sludge pyrolysis. *Fuel* 2014;134:514–20.
- [14] Atienza-Martínez M, Fonts I, Lázaro L, Ceamanos J, Gea G. Fast pyrolysis of torrefied sewage sludge in a fluidized bed reactor. *Chem Eng J* 2015;259:467–80.
- [15] Chen W-H, Cheng W-Y, Lu K-M, Huang Y-P. An evaluation on improvement of pulverized biomass property for solid fuel through torrefaction. *Appl Energy* 2011;88(11):3636–44.
- [16] Wang S, Dai G, Ru B, Zhao Y, Wang X, Zhou J, et al. Effects of torrefaction on hemicellulose structural characteristics and pyrolysis behaviors. *Bioresour Technol* 2016;218:1106–14.
- [17] Chen D, Gao A, Cen K, Zhang J, Cao X, Ma Z. Investigation of biomass torrefaction based on three major components: hemicellulose, cellulose, and lignin. *Energy Convers Manag* 2018;169:228–37.
- [18] Chen Y, Yang H, Wang X, Zhang S, Chen H. Biomass-based pyrolytic poly-generation system on cotton stalk pyrolysis: influence of temperature. *Bioresour Technol* 2012;107:411–8.
- [19] Zeng K, Yang Q, Che Q, Zhang Y, Wang X, Yang H, et al. Effects of temperature and Mg-based additives on properties of cotton stalk torrefaction products. *Energy Fuel* 2018;32(9):9640–9.
- [20] Zheng A, Zhao Z, Chang S, Huang Z, He F, Li H. Effect of torrefaction temperature on product distribution from two-staged pyrolysis of biomass. *Energy Fuel* 2012;26(5):2968–74.
- [21] Prins MJ, Ptasiński KJ, Janssen FJJG. Torrefaction of wood: Part 2. Analysis of products. *J Anal Appl Pyrolysis* 2006;77(1):35–40.
- [22] Zhang S, Hu B, Zhang L, Xiong Y. Effects of torrefaction on yield and quality of pyrolysis char and its application on preparation of activated carbon. *J Anal Appl Pyrolysis* 2016;119:217–23.
- [23] Wang S, Dai G, Yang H, Luo Z. Lignocellulosic biomass pyrolysis mechanism: a state-of-the-art review. *Prog Energy Combust* 2017;62:33–86.
- [24] Li L, Huang Y, Zhang D, Zheng A, Zhao Z, Xia M, et al. Uncovering Structure–Reactivity Relationships in pyrolysis and gasification of biomass with varying severity of torrefaction. *ACS Sustainable Chem Eng* 2018;6(5):6008–17.
- [25] Chen W-H, Peng J, Bi XT. A state-of-the-art review of biomass torrefaction, densification and applications. *Renew Sustain Energy Rev* 2015;44:847–66.
- [26] Wang S, Ru B, Dai G, Lin H, Zhang L. Influence mechanism of torrefaction on softwood pyrolysis based on structural analysis and kinetic modeling. *Int J Hydrogen Energy* 2016;41(37):16428–35.
- [27] van der Stelt MJC, Gerhauser H, Kiel JHA, Ptasiński KJ. Biomass upgrading by torrefaction for the production of biofuels: a review. *Biomass Bioenergy* 2011;35(9):3748–62.
- [28] Zheng A, Zhao Z, Chang S, Huang Z, Wang X, He F, et al. Effect of torrefaction on structure and fast pyrolysis behavior of corn cobs. *Bioresour Technol* 2013;128:370–7.
- [29] Atienza-Martínez M, Fonts I, Abrego J, Ceamanos J, Gea G. Sewage sludge torrefaction in a fluidized bed reactor. *Chem Eng J* 2013;222:534–45.
- [30] Poudel J, Ohm T-I, Lee S-H, Oh SC. A study on torrefaction of sewage sludge to enhance solid fuel qualities. *Waste Manag* 2015;40:112–8.
- [31] Huang YW, Chen MQ, Luo HF. Nonisothermal torrefaction kinetics of sewage sludge using the simplified distributed activation energy model. *Chem Eng J* 2016;298:154–61.
- [32] Huang Y-F, Sung H-T, Chiueh P-T, Lo S-L. Microwave torrefaction of sewage sludge and leucaena. *J Taiwan Inst Chem E* 2017;70:236–43.
- [33] Zheng A, Jiang L, Zhao Z, Huang Z, Zhao K, Wei G, et al. Impact of torrefaction on the chemical structure and catalytic fast pyrolysis behavior of hemicellulose, lignin, and cellulose. *Energy Fuel* 2015;29(12):8027–34.
- [34] Atienza-Martínez M, Mastral JF, Abrego J, Ceamanos J, Gea G. Sewage sludge torrefaction in an auger reactor. *Energy Fuel* 2015;29(1):160–70.
- [35] Amir S, Jouraiphy A, Meddich A, El Gharous M, Winterton P, Hafidi M. Structural study of humic acids during composting of activated sludge-green waste: elemental analysis, FTIR and <sup>13</sup>C NMR. *J Hazard Mater* 2010;177(1):524–9.
- [36] Baccile N, Falco C, Titirici M-M. Characterization of biomass and its derived char using <sup>13</sup>C-solid state nuclear magnetic resonance. *Green Chem* 2014;16(12):4839–69.
- [37] Zhai Y, Peng W, Zeng G, Fu Z, Lan Y, Chen H, et al. Pyrolysis characteristics and kinetics of sewage sludge for different sizes and heating rates. *J Therm Anal Calorim* 2012;107(3):1015–22.
- [38] Chen D, Wang Y, Liu Y, Cen K, Cao X, Ma Z, et al. Comparative study on the pyrolysis behaviors of rice straw under different washing pretreatments of water, acid solution, and aqueous phase bio-oil by using TG-FTIR and Py-GC/MS. *Fuel* 2019;252:1–9.
- [39] Tian K, Liu W-J, Qian T-T, Jiang H, Yu H-Q. Investigation on the evolution of N-containing organic compounds during pyrolysis of sewage sludge. *Environ Sci Technol* 2014;48(18):10888–96.
- [40] Madarász J, Pokol G. Comparative evolved gas analyses on thermal degradation of thiourea by coupled TG-FTIR and TG/DTA-MS instruments. *J Therm Anal Calorim* 2007;88(2):329–36.
- [41] Peng X, Ma X, Lin Y, Guo Z, Hu S, Ning X, et al. Co-pyrolysis between microalgae and textile dyeing sludge by TG-FTIR: kinetics and products. *Energy Convers Manag* 2015;100:391–402.
- [42] Madarász J, Brăileanu A, Pokol G. Comprehensive evolved gas analysis of amorphous precursors for S-doped titania by in situ TG-FTIR and TG/DTA-MS: Part 1. Precursor from thiourea and titanium (IV)-isopropoxide. *J Anal Appl Pyrolysis* 2008;82(2):292–7.

证书号第6841145号



# 发明专利证书

发明名称：一种垃圾填埋气化学链重整制备低碳烯烃联产高纯一氧化碳的方法

发明人：魏国强;曹晋曾;姚炜珊;武小燕;张声森;杨希贤

专利号：ZL 2023 1 0740352.X

专利申请日：2023年06月20日

专利权人：华南农业大学

地址：510642 广东省广州市天河区五山路483号

授权公告日：2024年03月29日

授权公告号：CN 116983996 B

国家知识产权局依照中华人民共和国专利法进行审查，决定授予专利权，颁发发明专利证书并在专利登记簿上予以登记。专利权自授权公告之日起生效。专利权期限为二十年，自申请日起算。

专利证书记载专利权登记时的法律状况。专利权的转移、质押、无效、终止、恢复和专利权人的姓名或名称、国籍、地址变更等事项记载在专利登记簿上。



局长  
申长雨

申长雨

2024年03月29日

证书号第7103674号



专利公告信息

# 发明专利证书

发明名称：一种废塑料耦合碱木质素制备低碳烯烃联产高纯氢气的方法

专利权人：华南农业大学

地址：510642 广东省广州市天河区五山路483号

发明人：魏国强;袁浩然;王亚琢;顾菁;陈勇

专利号：ZL 2022 1 1427005.3

授权公告号：CN 115895736 B

专利申请日：2022年11月15日

授权公告日：2024年06月14日

申请日时申请人：华南农业大学

申请日时发明人：魏国强;袁浩然;王亚琢;顾菁;陈勇

国家知识产权局依照中华人民共和国专利法进行审查，决定授予专利权，并予以公告。  
专利权自授权公告之日起生效。专利权有效性及专利权人变更等法律信息以专利登记簿记载为准。

局长  
申长雨

申长雨

2024年06月14日





证书号第7316009号



专利公告信息

# 发明专利证书

发明名称：一种碱木质素化学链氧化偶联制备低碳烯烃的方法

专利权人：华南农业大学

地址：510642 广东省广州市天河区五山路483号

发明人：魏国强;袁浩然;王亚琢;顾菁;陈勇

专利号：ZL 2022 1 1427025.0

授权公告号：CN 115894144 B

专利申请日：2022年11月15日

授权公告日：2024年08月23日

申请日时申请人：华南农业大学

申请日时发明人：魏国强;袁浩然;王亚琢;顾菁;陈勇

国家知识产权局依照中华人民共和国专利法进行审查，决定授予专利权，并予以公告。  
专利权自授权公告之日起生效。专利权有效性及专利权人变更等法律信息以专利登记簿记载为准。

局长  
申长雨

申长雨



证书号第 13539855 号



# 实用新型专利证书

实用新型名称：一种化学链处理污泥制合成气及高纯  $H_2$  同时回收磷的装置

发 明 人：魏国强;黄振;郑安庆;王小波;赵坤;赵增立

专 利 号：ZL 2020 2 2102051.9

专利申请日：2020 年 09 月 22 日

专 利 权 人：中国科学院广州能源研究所

地 址：510640 广东省广州市天河区五山能源路 2 号

授权公告日：2021 年 06 月 29 日

授权公告号：CN 213570344 U

国家知识产权局依照中华人民共和国专利法经过初步审查，决定授予专利权，颁发实用新型专利证书并在专利登记簿上予以登记。专利权自授权公告之日起生效。专利权期限为十年，自申请日起算。

专利证书记载专利权登记时的法律状况。专利权的转移、质押、无效、终止、恢复和专利权人的姓名或名称、国籍、地址变更等事项记载在专利登记簿上。



局长  
申长雨

申长雨

2021 年 06 月 29 日